A Validated Shape Optimization Approach for Maximizing the Convective Heat Transfer from Generic Heat Sink Geometries

---

Quentin Pelletier

Department of Mechanical & Manufacturing Engineering
Parsons Building
University of Dublin, Trinity College
Dublin 2, Ireland

October 2016

A dissertation submitted to the University of Dublin for the Degree of Doctor of Philosophy.

Declaration

I declare that this thesis has not been submitted as an exercise for a degree at this or any other university and it is entirely my own work.

I agree to deposit this thesis in the University's open access institutional repository or allow the library to do so on my behalf, subject to Irish Copyright Legislation and Trinity College Library conditions of use and acknowledgment.

Signed,

Quentin Pelletier,

October 2016

Abstract

Improving the effectiveness of heat transfer devices is one of the most challenging and determinant processes for industrial situations involving energy transformation. Thermal simulations can enable engineers to try and assess different approaches to deal with a heat transfer situation, at a very early stage in the design process of a device. The enhancement of the heat transfer potential of a device, based on the optimization of its shape, has been reported by many authors. This thesis presents the development of a shape optimization procedure for maximizing the heat transfer from complex geometries by (i) establishing and validating a robust and low-cost computational fluid dynamics (CFD) method to predict the fluid flow and heat transfer of steady and unsteady convective heat transfer phenomena, and by (ii) incorporating the CFD model in an optimization loop which aims at searching for the optimal design that maximizes the heat transfer, using a genetic algorithm. In parallel, this study could enable the improvement of our understanding of coral growth as these living organisms rely on mass transfer processes to develop. In order to achieve the development of a shape optimization procedure that can be applied to complex geometries, and additionally, that can provide results comparable to situations specific to the living environment of corals, the investigation was done progressively. The idea is to study flow and heat transfer configurations around geometries of increasing complexity resulting in a shape optimization methodology applicable to a wide range of shape complexities. A genetic algorithm is used to search for optimal solutions over a high-dimension search-space that represents all the possible designs of a complex geometry. The study of how genetic algorithms operate in combination with CFD simulations is conducted in order to assess the shape optimization methodology.

Acknowledgements

First and foremost, I would like to thank my main supervisor Prof. Tim Persoons who has been a real pleasure to work with. I have learned so much from his knowledge in the areas of heat transfer, thermodynamics and fluid mechanics. He has always been available to give clever suggestions and ideas concerning this research work, but moreover, he has been very understanding and helpful in many other situations. I also would like to give my gratitude to Prof. Carlos Rocha. I have not had the chance to see him as often as it could have been but our meetings were rewarding. I have been impressed by his knowledge in the areas of fluid mechanics and mass transfer related to corals, and above all, his enthusiasm concerning this scientific branch. I have also had the chance to work with Prof. Darina Murray and Prof. Henry Rice. They have been very generous with their time and offered their interest and help many times.

A special thank to Prof. Craig Meskell, who gave me valuable advice on CFD modeling and who accepted to be my confirmation report's internal examiner.

I would like to thank all the technical staff who has been a great help with the tutorials and laboratories I conducted.

To all my colleagues and friends: Sajad Alimohammadi, Nicolas Baudin, Daniel Keogh, Alberto Pellegrino, KunZhao, Jason Botha, Patrick N. Okolo and Eleonora Neri, thank you all for providing a friendly working atmosphere and for the stimulating discussions and helpful suggestions throughout these three years.

Thanks to Judith Lee for her unbeatable good mood and more generally all the administrative staff for their mindful help.

Thank you Maman, Papa, Camille and Véro, for your support during my studies and for enabling me getting there. To my family and close friends, thank you for your support and for helping me keep my sanity. To my love Laura, for her amazing support, proof-reading and endless understanding and patience. I could not have done it without you all.

Finally I would like to acknowledge the financial support of the School of Engineering that granted me an E3 Scholarship for these three years, and the Cooling Technologies Research Centre at Purdue University, USA, without which this research would not have been possible.

Table of Contents

Nomenclature

Symbol	Units	Description
A	$[m^2]$	Surface's area
D	$[m]$	Circle's diameter
D_ϕ	$[m^2s^{-1}]$	Mass diffusivity
f	$[Hz]$	Frequency
g	$[ms^{-2}]$	Acceleration due to Earth's gravity
Gr	[-]	Grashof number $Gr = (\rho^2\beta gL^3\Delta T)/\mu^2$
h	$[Wm^{-2}K^{-1}]$	Heat transfer coefficient
H	$[m]$	Height
$\vec{J}$	$[molm^{-2}s^{-1}]$	Diffusion flux
k	$[m^2s^{-2}]$	Turbulent kinetic energy $k = 1/2(\overline{u'^2} + \overline{v'^2} + \overline{w'^2})$
k	$[Wm^{-1}K^{-1}]$	Thermal conductivity
K	$[ms^{-1}]$	Mass transfer coefficient
L	$[m]$	Length
n	[-]	Population size
Nu	[-]	Nusselt number $Nu = hL/k$
p	[-]	Search-space dimension
p_c	[-]	Cross-over probability
p_m	[-]	Mutation probability
P	$[Pa]$	Pressure
Pr	[-]	Prandtl number $Pr = \nu/\alpha$
$\vec{q}$	$[Js^{-1}m^{-2}]$	Local heat flux
q'	$[W]$	Heat transfer rate
Q_{cond}	$[J]$	Amount of heat transferred by conduction
Q_{conv}	$[J]$	Amount of heat transferred by convection
Ra	[-]	Rayleigh number $Ra = Gr \cdot Pr$
Re	[-]	Reynolds number $Re = UL/\nu$
Ri	[-]	Richardson number $Ri = Gr/Re^2$

S	$[m]$	Spacing between bodies
Sc	[-]	Schmidt number $Sc = \nu/D_\phi$
Sh	[-]	Sherwood number $Sh = KL/D_\phi$
Sr	[-]	Strouhal number $Sr = fD/V_{ref}$
t	$[s]$	Time
T	$[K]$	Temperature
T_{bulk}	$[K]$	Bulk temperature
T_f	$[K]$	Fluid's temperature
T_S	$[K]$	Surface temperature
T_w	$[K]$	Wall temperature
u_i	$[ms^{-1}]$	Velocity component
u_τ	$[ms^{-1}]$	Shear velocity
U, V	$[ms^{-1}]$	Velocity
y^+	[-]	Wall coordinate $y^+ = yu_\tau/\nu$
Greek		
α	$[m^2s^{-1}]$	Thermal diffusivity
β	$[K^{-1}]$	Coefficient of thermal expansion
ϵ	$[m^2s^{-3}]$	Turbulence dissipation rate
μ	$[Pas^{-1}]$	Dynamic viscosity
ν	$[m^2s^{-1}]$	Kinematic viscosity
ω	$[s^{-1}]$	Turbulence specific dissipation rate
ϕ	$[molm^{-3}]$	Concentration of particles
ρ	$[kgm^{-3}]$	Fluid's density
τ	$[Nm^{-2}]$	Shear stress
θ	$[rad, ^\circ]$	Angle
σ	$[Nm^{-2}]$	Stress tensor
Subscripts		
∞		Free-stream
m		Mean value over a surface
max		Maximum value
min		Minimum value
w		Wall values

List of Figures

Chapter 1

Introduction: Lessons for Engineering from Natural Sciences

Convective heat transfer is found in many technical applications such as heat exchangers, boiler devices, air cooling systems, etc. According to the International Energy Agency [1], apart from hydro, wind and photovoltaic energy generation technologies, more than 75% of the world's electricity is produced in heat source power plants such as fossil-fuel, nuclear, geothermal, biomass or solar power stations. The heat is transferred from these primary energy sources to water which is transformed into steam and drive a rotor in order to produce electricity. But electricity is not the only production that requires heat transfer; oil, which is the most used fossil fuel for transportation, generates power in a car engine by converting heat energy into mechanical energy (the piston's movement). Heat transfer processes are literally involved everywhere, from the industry and huge power plants to the small heat sink of everyone's computer.

This PhD research is a study inspired by the well-known parallel between convective heat and mass transfer; we aim at examining the similarities between optimal design of heat exchange structures (e.g., heat sinks and heat exchangers in engineering applications) and the evolutionary development and growth patterns of biological organisms in response to convective mass transfer from nutrient streams (e.g., deep water coral growth).

1.1 Nature-inspired shapes in engineering

The choice that has been made to turn toward biological organisms in order to study the physics and enhance the performance of an engineering device is not new in human history. In order to understand why, one has to understand first the importance of the parallel between engineering and Nature.

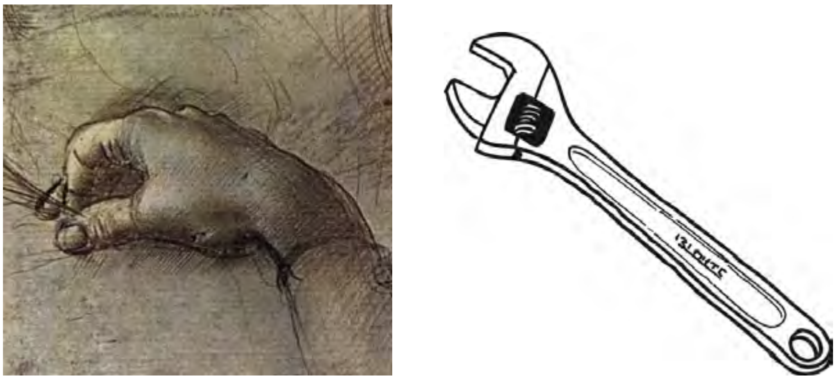

(a) Nature (b) Engineering

Figure 1.1: Principle of biomimetics[1]

The seminal book of Adrian Bejan, *Shape and structure, from engineering to Nature* [2] has been very useful in the understanding of Nature: its relation with engineering, and the study of laws that drive Nature's design. This relation with Nature has always been of importance, especially in the engineering field; the biomimetics is the basis of tools creation as illustrated in Fig. 1.1. It seems that humans have always tried to mimic Nature because Nature's shapes appear to be the most efficient for their task. In other words, Nature is optimal.

Nature seems to find its way, always being the most favorable for its development. But why is it so? Where does this come from? Why are leaves distributed this way? How a nautilus shell, a cyclone and a galaxy come up to have the same logarithmic spiral shape? The main idea developed in A. Bejan's book [2] is that Nature designs itself as a result of a global process of optimization subject to global and local constraints.

---

[1] `http://www.art.com/gallery/id--a32178/leonardo-da-vinci-posters_p5.htm`

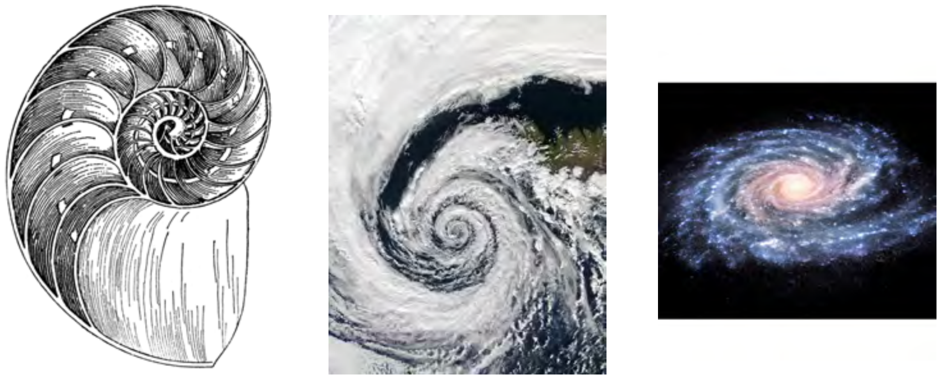

(a) Nautilus shell (b) Cyclone (c) Galaxy

Figure 1.2: Logarithmic spiral shapes in Nature, references: [2]

(a) Lungs (b) Tree (c) River delta

Figure 1.3: "Tree shapes" in Nature, references: [3]

In order to understand how Nature creates these patterns, we need to investigate what are the constraints it is subjected to, and finally, what is this optimization process, this universal law, that makes the trees, the river deltas and our lung's bronchi look the same.

In the framework of heat transfer enhancement and the parallel between heat and mass transfer, the attention should be drawn to corals because of their capacity to absorb nutrients efficiently. This has already been noticed by engineers who

---

[2] `http://www.123rf.com/stock-photo/nautilus_shell.html`, `https://en.wikipedia.org/wiki/Cyclone`, `https://apod.nasa.gov/apod/archivepix.html`

[3] `http://drawingimage.com/art/21862`, `http://www.drodd.com/html7/tree-drawing.html`, `http://www.dfiles.me/delta-river-definition.html`

built cooling devices inspired by these organisms as illustrated in Fig. 1.4.

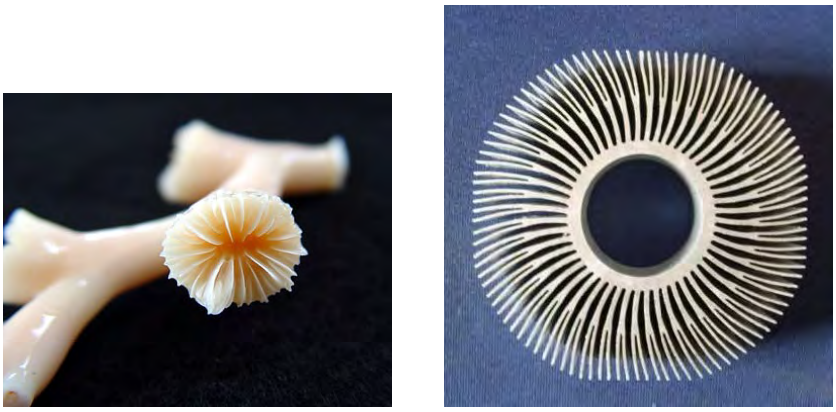

(a) Deep-sea coral (b) Axi-symmetrical heat sink

Figure 1.4: Principle of biomimetics, references: [4]

The ability of corals to grow and reproduce using the energy of nutrients absorbed from the surrounding fluid deserves as many studies as there are different corals and this goes beyond the scope of the present work. Some studies have investigated the growth of corals by accretion, considering the advection and diffusion of nutrients only [3]. However, the effects of wave driven flows inside coral colonies that could enhance the mass transfer compared to a steady flow situation are reported in [4]. And more recently, studies present some features of corals that help enhance the mass transfer: small polyps at the coral's surface, called cilia, can create vortices to improve the mixing and therefore increase the mass transfer between the coral and the water [5].

Obviously the full understanding of corals growth dynamic and how efficiently they absorb nutrients from the surrounding water covers a wide range of disciplines.

---

[4] `http://www.marinebio.net/marinescience/04benthon/index.htm`

1.2 Universal design laws

In the case of the tree-shaped natural structures (the tree, the river delta, the lungs), it is important to notice that they are all traversed by internal currents. These networks are meant to transport sap for the trees, water for the river, and air for the bronchi. In the case of a coral, the structure is surrounded by an external current.

From these observations, a question arises: how does Nature optimize the design of these structures so that the internal or external currents can flow efficiently?

1.2.1 Constructal law: minimum travel time

The first approach comes from the field of optics [6] with the Fermat Law which states that when light travels between two points (A, B) located in two different media, it must choose the path that minimizes the time of travel between these two points (which is often not a straight line!).

In our case and in contrast to the point-to-point flow of Fermat, the constructal law applies to a finite-size system in which the current flows from one point (M) toward several points (P) contained in a fixed area (A_0) [7]. In 2D, $A_0 = L_0 \times H_0$ as shown on Fig. 1.5. (A_0) is fixed but (L_0) and (H_0) are not; they define the system's external shape.

The system is composed of two media; a small medium where the movement occurs at high speed and a low-speed medium which mainly composes the system A_0, that is to say, $V_1 \gg V_0$. If A_0 is assumed to be small enough, it contains only one channel of high-speed material (V_1) and the rest of the volume contains the low-speed material (V_0). These two media and how they are distributed in (A_0) define the internal structure of the system.

The idea of the constructal law is to find the external shape and the internal structure so that the access between all the points $(P) \in (A_0)$ and (M) is maximized. The maximization of volume-to-point access is obtained using the minimization of travel-time [8, 9].

For this simple 2D case, the best way to distribute the high-speed material is a straight line along the longer of the two axes of symmetry as it is already the case in Fig. 1.5. The internal structure is thus defined.

In terms of external shape; two different approaches are possible in order to

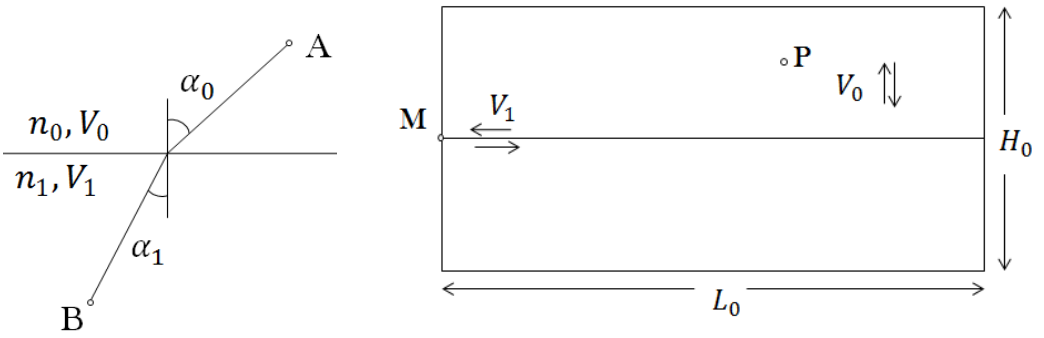

(a) Fermat law, point-to-point flow

(b) Constructal law, volume-to-point flow

Figure 1.5: Minimization of travel time: between two points (a) and between a volume and one point (b).

optimize (A_0) and surprisingly they provide identical results [7,8]. The first one is the "altruistic" mode. The idea is to minimize the travel-time between the furthest point (top right corner in Fig. 1.5) to point (M). All the other travel-times will be shorter since the points are closer to point (M). The optimization is done in order to benefit the most disadvantaged traveler. In this case, the maximal travel-time is $t_{max} = H_0/(2V_0) + L_0/V_1$. This time is minimal with $(H_0/L_0)_{opt} = 2V_0/V_1$, which defines the external shape of our system.

The second approach is to calculate the time-travel between any point $(P) \in (A_0)$ to (M), average it over the whole domain (A_0) and minimize it. It can be found [2] that the mean travel-time in this scenario is $t_{\bar{A_0}} = H_0/(4V_0) + L_0/(2V_1)$ which can be minimized with $(H_0/L_0)_{opt} = 2V_0/V_1$. The same optimized external shape is obtained.

1.2.2 Minimum entropy generation

The general idea of entropy minimization comes directly from the second law of thermodynamics. Indeed, in a heat exchanger design for example, there is no first law efficiency metric since energy is only transferred. The second law on the other hand pinpoints all losses including those associated with energy transfer. As such, there is a second law efficiency for components like heat sinks and heat exchangers. Therefore, entropy generation minimization is a popular objective function to design heat sinks and heat exchangers with.

As described by Adrian Bejan [10], Entropy Generation Minimization (EGM) consists of modeling and optimizing real devices that owe their imperfections to heat transfer, mass transfer and fluid flow. Multiple objectives can be achieved using this method, such as, minimization of entropy generation in heat exchangers, maximization of power output in power plants, minimization of costs, etc.

Let us consider a general system which is enclosed in space (real finite device) and operates at an unsteady state. The first and second law of thermodynamics enable us to compute the net work rate, the heat transfer rate, or any quantity we are interested in as well as the total entropy generation rate (which can not be negative). The whole idea of EGM is to minimize this entropy generation and get as close as possible to the hypothetical case of an entropy generation of zero, that is to say, the reversible, and most effective, case.

For example, considering the flow of a single-phase stream of mass flow rate $\dot{m}$ through a heat exchanger tube of internal diameter D the entropy generation rate per unit tube's length $\dot{S}_{gen}$ is, according to A. Bejan [11, 12];

$$\dot{S}_{gen} = \frac{q'^2}{\pi k T^2 Nu} + \frac{32 \dot{m} f}{\pi^2 \rho 2 T D^5} \tag{1.1}$$

where q' is the heat transfer rate per unit length of the tube from the wall to the fluid, $Nu = hD/k$ is the Nusselt number - h being the heat transfer coefficient between the wall and the fluid - and f is the friction factor which accounts for the frictional pressure drop along the tube. ρ, T and k are the bulk density, temperature and thermal conductivity of the fluid, respectively.

The optimal tube diameter that minimizes the $\dot{S}_{gen}$ expression 1.1 is given by [12];

$$Re_{D,opt} = 2.023 B_0^{0.36} Pr^{-0.007} \tag{1.2}$$

where B_0 is a heat and fluid flow "‘duty"’ parameter that accounts for the constraints (q', $\dot{m}$):

$$B_0 = \frac{q' \dot{m}}{(kT)^{1/2} \mu^{5/2} / \rho} \tag{1.3}$$

This is a quick example of a simple situation of heat transfer but illustrates the concept; minimizing the entropy generation in order to optimize the performances. The EGM method is well described and extensively documented by A. Bejan in many of his papers, especially in [10].

1.2.3 Asymptotic Analysis

A different approach from the Minimum Travel Time (MTT) and the Entropy Generation Minimization (EGM) theories described in this section, is the Asymptotic Analysis (AA) which has been developed in order to estimate approximately the optimal design of a system under constraints.

In order to illustrate the concept of asymptotic analysis, an example can be considered; what is the optimal spacing S_{opt} between the cylinders of an array of cylinders of diameter D contained in a volume $V_0 = L \times H \times W$, which maximizes the overall thermal conductance $q/(T_w - T_\infty)$? This example is from the study of Stanescu et al. [13];

To optimize the spacing S is equivalent to determining the optimal number of cylinders n in the fixed volume HLW, namely $n = HW/(S+D)^2 cos(30^\circ)$, or the optimal porosity of the HLW space;

$$\phi = 1 - \frac{n(\pi/4)D^2}{HW} \tag{1.4}$$

In the small-spacing limit, the cylinders almost touch, the fluid spends a long time in the HLW volume and the fluid outlet temperature is practically the same as the cylinder temperature. The total heat transfer rate between the volume and the fluid is;

$$q_{smallS} = \dot{m}c_p(T_w - T_\infty) \tag{1.5}$$

where $\dot{m} = \rho WLU$ is the total mass flow rate. The volume averaged longitudinal velocity U can be estimated by assuming Darcy flow;

$$U = \frac{K}{\mu}\frac{\Delta p}{H} \tag{1.6}$$

where the permeability of the equilateral triangle array is represented adequately by the Carman-Kozeny model [14]

$$K = \frac{D^2\phi^3}{C(1-\phi)^2} \tag{1.7}$$

where $C \approx 100$ in an order of magnitude sense. In the small-S limit the pressure difference between the front and back planes of the fixed volume, Δp, is controlled by the dynamic pressure of the approaching stream, $\Delta p = 1/2\rho U_\infty^2$. Combining these equations we find that in the small-S limit the volume averaged velocity U behaves as

$$U \cong \frac{\rho U_\infty}{200\mu H} \frac{\phi^3}{(1-\phi)^2} \tag{1.8}$$

where

$$\phi = 1 - \frac{0.907}{(1+S/D)^2} \tag{1.9}$$

The asymptotic behavior for the small spacing is determined by assuming $S/D \ll 1$ and combining all these equations gives;

$$\left(\frac{q}{T_w - T_\infty}\right)_{smallS} \cong \frac{1}{25}\rho c_p \nu \frac{WL}{H} Re_D^2 \left(\frac{S}{D}\right)^3 \tag{1.10}$$

In the opposite extreme, $S \gg D$, each cylinder is bathed by free-stream fluid and the total heat flux is the sum of each individual cylinder's $q_{single} = Nu_D k/D\pi DL(T_w - T_\infty)$ and finally;

$$\left(\frac{q}{T_w - T_\infty}\right)_{largeS} \cong 1.89k\frac{HWL}{D^2} Pr^{0.37} Re_D^{1/2} \left(\frac{S}{D}\right)^{-2} \tag{1.11}$$

The overall thermal conductance increases with S/D when S/D is small and decreases when S/D is large, so there is a maximum thermal conductance which can be estimated approximately by intersecting equations 1.10 and 1.11.

1.2.4 Evolutionary computation techniques

In the early 50's, the science of computing machines and artificial intelligence was booming and at this time appeared the premises of evolutionary algorithms. Such algorithms are based on the Darwinian evolutionary theory. The "survival of the fittest" concept that describes the mechanism of natural selection perfectly summarizes the idea of evolutionary computing. The basic principle is to start from a certain solution to the posed optimization problem and modify it randomly: this procedure is referred to a mutation. The new solution, the offspring, is then compared to its "parent" solution and the best solution between parent and child, is conserved. The process is repeated until it is told to stop (for example, after a fixed number of mutations, or when no better solution is discovered for a given number of consecutive mutations, etc.)

Several different versions of such evolutionary algorithms have been developed, among which is the Genetic Algorithm (GA). In a GA, not only one but several different solutions are mutated, mixed and compared through successive generations in order to find solutions that are progressively fitter to the problem. The history and principles of genetic algorithms will be presented and discussed in detail in Section 3.3.3 and Chapter 6.

The two previous sections aimed at highlighting that the improvement of heat transfer structures can be explored by combining the knowledge from

- An effective optimization technique.
- Certain aspects of efficient mass transfer structures like corals.

The choice of this optimization technique is twofold:

- When searching for possible optimization methods to deal with shape optimization involving CFD simulations, evolutionary computation techniques appeared to be interesting tools as evolution, in the Darwinist sense, is the process that describes how Nature searches for optimal solutions by mean of natural selection. To apply this survival-of-the-fittest process to a complex optimization problem seems promising and is worth investigating.

- For complex optimization problems, classical optimization techniques such as hill-climbing or gradient methods are inefficient or too time-consuming compared to GAs [15–18]. According to many scientists, genetic algorithms seem best suited to deal with noisy, non-linear, complex optimization problems [15, 19–21]. For those reasons, genetic algorithms appear to be a strong choice if one wants to deal with non-trivial phenomena that are encountered in fluid mechanics and heat/mass transfer situations.

The potential to deal with complex problems and the puzzling process of evolution that genetic algorithms represent, are promising as it will be highlighted in Section 3.3.3 and Chapter 6.

1.3 Research objectives and outline of this thesis

This PhD thesis intends to make a contribution towards setting up a theoretical and numerical framework for shape optimization of convective heat and mass transfer structures and can be divided in two stages;

- To develop a numerical methodology to model convective heat transfer from complex geometries, which is (i) experimentally validated, (ii) capable of modeling transient phenomena, and (iii) computationally efficient enough[5] to be used as part of a numerical optimization procedure.

- To derive an optimal design methodology for two-dimensional heat sinks in a stream, in an attempt to mimic the conditions inspired by deep sea corals.

Several optimization methods can be considered such as the ones introduced in the previous section: minimization of entropy generation, minimization of travel time [2, 22] or the asymptotic method [13, 23, 24], among many others including genetic algorithms.

The present work aims at developing a numerical method of design optimization of two-dimensional structures subjected to mixed convection heat transfer.

By studying the mass transfer dynamics and evolutionary optimization in nature [25], this cross-disciplinary research aims at providing new ways of improving energy efficiency and minimizing material usage of cooling systems, e.g. for large-scale ICT infrastructures such as data centers and telecommunication systems [26].

Chapter 2 presents an overview of the theoretical background necessary to the understanding of the processes involved in heat transfer phenomena and to the development of a numerical method which aims at optimizing the shape of a device subjected to heat transfer.

Chapter 3 reviews the literature on the work done in the area of thermal convection and genetic algorithms that are the core of this study.

---

[5] The difficulty to define "enough" must be noticed as this mainly depends on the optimization procedure itself

Chapter 4 presents the numerical methodology that has been developed on the simulation of the interaction between two two-dimensional vertically aligned horizontal cylinders in natural convection and the optimization method used to optimize the geometry of a two-dimensional heat sink in a stream.

The results of the simulation of two horizontal cylinders in natural convection are presented and discussed in Chapter 5 while the results of the numerical shape optimization of the heatsink in cross-flow are presented in Chapter 6.

A final conclusion is drawn and some possible improvements are suggested in Chapter 7.

Chapter 2

Theoretical background: Convective heat and mass transfer

2.1 Convective heat transfer

This thesis mainly deals with numerical simulations dedicated to heat transfer problems, that is to say, situations where heat is transferred from a medium to another as encountered in many engineering situations. The most interesting situation (from the engineering field's point of view) is when heat is transferred from a solid structure to a surrounding fluid as for the examples shown in Fig. 2.1. A schematic of this process (the cooling of a computer chip) is shown in Fig. 2.2. The equations describing the heat transfer presented in this section can be found in any handbook about heat transfer such as the the one from Bejan & Kraus [27].

Heat is first transferred by conduction as shown in Fig. 2.2. The conductive heat flux through the structure's boundary can be computed using the Fourier's law eq. 2.1 and its one dimensional form 2.2.

$$\vec{q} = -k\nabla T \tag{2.1}$$

---

[2] `http://www.coltinfo.co.uk/data-centre-climate-control.html`

(a) Air-cooled data centre

(b) Axi-symmetrical heat sink

Figure 2.1: Heat transfer from a solid to a fluid encountered in everyday engineering applications, reference:[2]

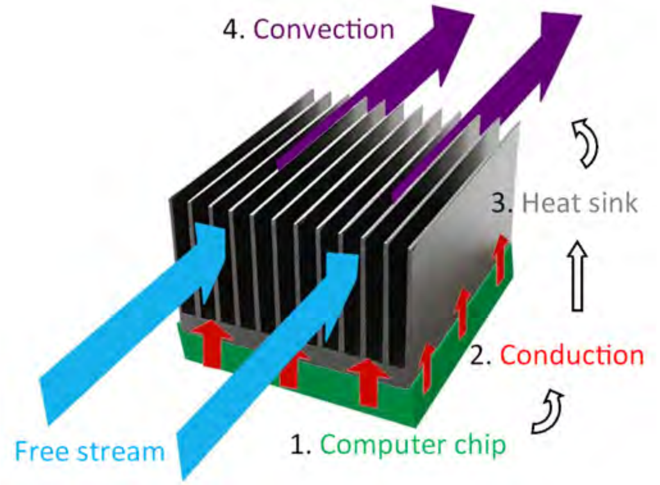

Figure 2.2: Schematic of the cooling process of a chip in a computer.

$$\frac{\Delta Q_{cond,x}}{\Delta t} = -kA\frac{\Delta T}{\Delta x} \tag{2.2}$$

where $\vec{q}$ is the local heat flux $Js^{-1}m^{-2}$, $Q_{cond,x}$ is the amount of heat transferred by conduction through a surface perpendicular to the x-direction (J), k is the material's conductivity $(Wm^{-1}K^{-1})$, A is the surface area (m^2), ∇T is the temperature gradient (Km^{-1}) and $\Delta T = T_s - T_f$ is the difference between the solid's and the fluid's local temperatures (K).

Heat is then carried from one place to another by the fluid's movement: this phenomenon is known as convection, or advection and is shown in Fig. 2.2. Newton's law of cooling, as shown in eq. 2.3 in its one-dimensional form, is used to compute the convective heat transfer.

$$\frac{\Delta Q_{conv}}{\Delta t} = hA\Delta T \tag{2.3}$$

where Q_{conv} is the amount of heat energy transferred by convection (J), h is the fluid's heat transfer coefficient (assumed independent of T here) $(Wm^{-2}K^{-1})$ and $\Delta T = T_f - T_{bulk}$ is the difference between the fluid's local temperature and the bulk temperature (K).

The ratio between convective and conductive heat transfer across the boundary of the structure is non-dimensionalized using eq. 2.4 in order to obtain the Nusselt number Nu. This number characterizes the heat transfer structure; the higher the Nusselt number, the more effectively heat is evacuated since the fluid carries heat away by convection at a higher rate than heat comes in the fluid by conduction within the thermal boundary layer.

This parameter, which is used to compare the different situations and geometries, is expressed as follows:

$$Nu = \frac{\text{Convective heat transfer}}{\text{Conductive heat transfer}} = \frac{hL}{k} \tag{2.4}$$

with L the characteristic length of the system (m).

The Nusselt number is one of the several dimensionless numbers that are used. The second one is the Prandtl number Pr, which is a fluid's property parameter:

$$Pr = \frac{\nu}{\alpha} \tag{2.5}$$

In the absence of external pressure gradient, the temperature of the fluid close to the heated surface will increase, which leads to a decrease of its density. This difference in density creates an imbalance in the buoyancy forces near the surface, and leads to advective currents, if they overcome the viscous forces which tend to maintain the fluid at rest. This leads to the third dimensionless parameter, the Grashof number Gr, which is the ratio of buoyancy over viscous forces:

$$Gr = \frac{\rho^2 \beta g L^3 \Delta T}{\mu^2} \tag{2.6}$$

The Rayleigh number Ra, which is a modified version of the Grashof number, takes the thermal diffusivity of the fluid into account:

$$Ra = \frac{g\beta}{\nu\alpha} \Delta T L^3 = Gr \cdot Pr \tag{2.7}$$

When the flow is driven externally by forces (pressure gradient or any other external force field) which overpower buoyancy forces, the main parameter characterizing the flow is the Reynolds number Re, which relates the momentum in the flow to the viscous dissipation:

$$Re = \frac{\rho U L}{\mu} \tag{2.8}$$

If both buoyancy and pressure gradient forces affect the flow, it cannot be characterized by only one parameter, and both the Reynolds number and the Rayleigh number have to be considered. This phenomenon is called mixed convection and is described in the next section.

2.1.1 Mixed convection heat transfer

The real-life situation of heat transfer is called mixed convection and takes into account both natural - or free - convection as well as forced convection. Natural convection is the convection of heat where the fluid's motion is driven by density differences created by temperature gradients, that is to say, by heat itself. Forced convection refers to a phenomenon in which the fluid is set in motion by another process - for example, when a heat exchanger is placed inside an existing stream flow. In this case, the general form of the Navier-Stokes equations have to be considered. The Navier-Stokes equations are written using the Einstein notation as 2.9, 2.10 and 2.11

Continuity:

$$\frac{\partial \rho}{\partial t} + \frac{\partial \rho u_i}{\partial x_i} = 0 \tag{2.9}$$

Momentum:

$$\frac{\partial \rho u_i}{\partial t} + \frac{\partial \rho u_i u_j}{\partial x_j} = \frac{\partial \sigma_{ij}}{\partial x_j} + \rho g_i \tag{2.10}$$

Energy:

$$\frac{\partial \rho e}{\partial t} + \frac{\partial \rho u_i e}{\partial x_i} = \sigma_{ij}\frac{\partial u_i}{\partial x_j} + \frac{\partial q_i}{\partial x_i} \tag{2.11}$$

where ρ is the density, u_i the velocity vector and $\sigma_{ij} = \tau_{ij} - p\delta_{ij}$ the stress tensor, split into the deviatoric stress tensor (which contains the shear stresses) τ_{ij} and the normal stress tensor $-p\delta_{ij}$ (with $\delta_{ij} = 1$ if $i = j$ and 0 otherwise, the Kronecker delta). g_i is the gravitational acceleration, e is the internal energy and q_i is the heat flux.

The Einstein notation is used in this thesis because of its simplicity; a vector is noted with one subscript such as $\vec{u} = u_i$ and then $u_1 = u$, $u_2 = v$ and $u_3 = w$. A tensor is noted with two subscripts such as $\vec{\vec{\tau}} = \tau_{ij}$. The particularity of this notation is that when a term presents two equal subscripts, the sum of this term over this subscript have to be taken such as: $\frac{\partial \rho u_i u_j}{\partial x_j} = \frac{\partial \rho u_i u}{\partial x} + \frac{\partial \rho u_i v}{\partial y} + \frac{\partial \rho u_i w}{\partial z}$, which is valid for $u_i = u$, v or w, corresponding to the three momentum equations.

Two important assumptions are often used:

(i) The fluid is Newtonian. In this case, the Newton's law describes the stress tensor σ_{ij} and the Fourier's law describes the heat flux q_i;

$$\sigma_{ij} = \left(-p + \lambda\frac{\partial u_l}{\partial x_l}\right)\delta_{ij} + 2\mu S_{ij} \tag{2.12}$$

where $S_{ij} = \frac{1}{2}\left(\frac{\partial u_i}{\partial x_j} + \frac{\partial u_j}{\partial x_i}\right)$, and δ_{ij} is the identity tensor, or Kronecker's delta.

$$q_i = -k\frac{\partial T}{\partial x_i} \tag{2.13}$$

(ii) The fluid is incompressible. In this case, the density is considered constant (except for the buoyancy term in some particular cases explained later in this chapter).

When the fluid is considered Newtonian and incompressible, the Navier-Stokes equations reduce to Eq. 2.14 - 2.16;

Continuity:

$$\frac{\partial u_i}{\partial x_i} = 0 \tag{2.14}$$

Momentum:

$$\frac{\partial u_i}{\partial t} + u_j \frac{\partial u_i}{\partial x_j} = -\frac{1}{\rho}\frac{\partial p}{\partial x_i} + g_i + \nu \frac{\partial^2 u_i}{\partial x_j^2} \tag{2.15}$$

Temperature:

$$\frac{\partial T}{\partial t} + u_i \frac{\partial T}{\partial x_i} = \alpha \frac{\partial^2 T}{\partial x_i^2} + \frac{2\mu}{\rho C_v} S_{ij} S_{ij} \tag{2.16}$$

The main dimensionless parameter which comes into play when considering mixed convection is the Richardson number Ri which represents the importance of natural convection relative to the forced convection:

$$Ri = \frac{\text{Buoyancy}}{\text{Inertia}} = \frac{g\beta L \Delta T}{U^2} = \frac{Gr}{Re^2} \tag{2.17}$$

Typically, the natural convection is negligible for $Ri < 0.1$, the forced convection is negligible for $Ri > 10$, and both natural and forced convection have to be taken into account for $0.1 < Ri < 10$.

2.1.2 Forced convection heat transfer

In many heat transfer situations encountered in the engineering field, the fluid carrying the heat evolves at high speed, that is to say, high Re compared to the buoyancy term ($\sqrt{Gr}$). It moves at speed high enough so that generally, the corresponding Richardson number is below 0.1 and only forced convection can be considered. Basically, considering only forced convection simply means that the convection due to temperature differences - or density differences - is neglected, that is to say, gravity is neglected. The Navier-Stokes equations thus become;

Continuity:

$$\frac{\partial \rho}{\partial t} + \frac{\partial \rho u_i}{\partial x_i} = 0 \tag{2.18}$$

Momentum:

$$\frac{\partial \rho u_i}{\partial t} + \frac{\partial \rho u_i u_j}{\partial x_j} = \frac{\partial \sigma_{ij}}{\partial x_j} \tag{2.19}$$

Energy:

$$\frac{\partial \rho e}{\partial t} + \frac{\partial \rho u_i e}{\partial x_i} = \sigma_{ij} \frac{\partial u_i}{\partial x_j} + \frac{\partial q_i}{\partial x_i} \tag{2.20}$$

As it can be noted, only the momentum equation (Eq. 2.19) is modified. Indeed the term ρg_i has been removed from Eq. 2.10 and inertial forces are significantly larger than buoyancy forces.

As the result of the assumption of forced convection is the removal of a term in one of the equation of fluid mechanics, one can assume that this particular case of forced convection is relatively easier to treat than the natural situation.

2.1.3 Natural convection heat transfer

Let us assume now a fluid subject to density differences and gravity so that buoyancy forces overpower viscous forces. In this case the Grashof and Rayleigh numbers are larger than one. In contrast with the previous section, if the device is placed in a medium where the free stream flows at a velocity, so that these buoyancy forces are greater than the upstream advective forces, then the Richardson number of such a flow is above 10. Consequently, the buoyancy forces affect the flow in a greater extent than the free stream. This is natural convection.

In this case, the buoyancy term cannot be neglected and the general form of the Navier-Stokes equations apply (Eq. 2.9 - 2.11).

As only natural convection is considered and the flow velocity is relatively low compared to forced convection, it can be safely assumed (if not dealing with acous-

tic problems) that the fluid is incompressible, that is to say, that the density does not depend on the pressure but on the temperature only.
very common approximation, when the temperature differences are significantly small, is the *Boussinesq approximation*, named after Boussinesq [28] but certainly introduced by Oberbeck [29]. As the density depends on the temperature only, the Taylor series expansion of the density evaluated for any temperature T is given in Eq. 2.1.3;equation $\rho(T) = \rho(T_0) + \frac{d\rho}{dT}\Big|_{T_0} (T - T_0) + \dots$

Now, neglecting higher order terms and defining the thermal expansion coefficient $\beta = -\dfrac{1}{\rho_0}\dfrac{\partial\rho}{\partial T}$, where $\rho_0 = \rho(T = T_0)$, we obtain the Boussinesq's approximation in its common form;

$$\rho(T) = \rho_0(1 - \beta\Delta T) \tag{2.21}$$

which is valid for small changes in density, that is to say, for $\beta(T - T_0) \ll 1$.

In this case, only the zeroth order term is kept in the Navier-Stokes equations ($\rho = \rho_0$), but the first order term is used for the buoyancy term; $\rho g_i = \rho_0 g_i(1 - \beta\Delta T)$, in order to reproduce the effects of the temperature variations in the flow.

2.2 Convective mass transfer

The analogies between heat transfer and mass transfer mechanisms can be observed by considering their governing equations. While the heat transfer governing equations have been presented in the previous section, their mass transfer equivalents are described in the present section [30].

The mechanism which drives how particles are moving inside a fluid medium, such as the way nutrients are carried in the ocean, is a combination of advection and diffusion. Advection is the phenomenon which leads to the movement of particles in a medium, as a consequence of the medium motion. The moving medium (the stream created by the movement of a spoon in a cup of coffee for example) will carry particles it contains (the dissolved sugar in this example). Diffusion is the mechanism which drives the particles' motion as a consequence of a gradient of these particles's concentration in the medium (just like this same sugar will eventually mix with water even if nobody stirs the coffee).

The advection can be directly related to the heat transfer convection as the movement of the entity of interest (heat for heat transfer and particles for mass transfer phenomena) is driven by the surrounding fluid's motion.

The analogy between mass diffusion and heat conduction is not straightforward but can be observed using the Fourier's law 2.1, describing the heat transfer conduction, and the Fick's law of diffusion 2.22 or 2.23 in its one-dimensional form;

$$\vec{J} = -D_\phi \nabla \phi \tag{2.22}$$

$$J_x = -D_\phi \frac{\partial \phi}{\partial x} \tag{2.23}$$

where $\vec{J}$ is the "diffusion flux" ($\frac{mol}{m^2 \cdot s}$), D_ϕ is the diffusion coefficient or diffusivity ($\frac{m^2}{s}$), ϕ is the concentration of the particles ($\frac{mol}{m^3}$), $\nabla \phi$ and $\frac{\partial \phi}{\partial x}$ represent the concentration gradients, in three dimension or along x respectively, with x the position along the direction of diffusion (for the one dimension case).

Similarly to the Nusselt number which gives the ratio of convective and conductive heat transfer, the Sherwood number is a non-dimensional parameter defined as Eq. 2.24. The Schmidt number (Eq. 2.25) gives the ratio of momentum diffusivity (viscocity) and mass diffusivity, which is the mass transfer version of the Prandtl number.

$$Sh = \frac{\text{Mass transfer rate}}{\text{Diffusion rate}} = \frac{KL}{D_\phi} \tag{2.24}$$

where K is the mass transfer coefficient (ms^{-1}), L is the characteristic length (m) and D_ϕ is the mass diffusivity ($m^2 s^{-1}$).

$$Sc = \frac{\text{Viscous diffusion rate}}{\text{Mass diffusion rate}} = \frac{\nu}{D_\phi} \tag{2.25}$$

Another parameter is sometimes considered when analogies between heat and mass transfer are studied; the friction factors. This analogy, namely the Chilton and Colburn J-factor analogy [31], can be written as follows;

$$J_H = \frac{Nu}{Re \cdot Pr^{1/3}} \tag{2.26}$$

$$J_M = \frac{Sh}{Re \cdot Sc^{1/3}} \tag{2.27}$$

where J_H and J_M are the Colburn-Chilton j-factors for heat and mass transfer respectively. The analogy states that $J_H = J_M = \frac{f}{2}$, with f the friction factor, in the case of a fully developed turbulent flow, for $Re \geq 10000$ and $0.7 \leq Pr \leq 160$.

The analogy between a heat exchanger and a biological organism takes its source here. The similarity is noticeable; advection of heat or particles is driven by the fluid motion, and conduction along with diffusion behave similarly; a flux is created by a gradient as illustrated in Table 2.1.

Table 2.1: Parallel between heat and mass transfer.

	Heat transfer	**Mass transfer**
Studied object	Heat	Mass
Convection transfer coefficient	Convection heat transfer coefficient h	Mass transfer coefficient K
Conduction (or diffusion) constants	Thermal conductivity k or diffusivity α	Mass diffusivity D_ϕ
Ratio of convection and conduction	Nusselt number $Nu = \dfrac{hL}{k}$	Sherwood number $Sh = \dfrac{KL}{D_\phi}$
Ratio of viscosity and diffusion	Prandtl number $Pr = \dfrac{\nu}{\alpha} = \dfrac{c_p\mu}{k}$	Schmidt number $Sc = \dfrac{\mu\rho}{D_\phi}$
Conduction flux	Heat flux $\vec{q}$	Mass flux $\vec{J}$
Gradient	Temperature T	Mass concentration ϕ
Equation of conduction	Fourier's law $\vec{q} = -k\nabla T$	Fick's law $\vec{J} = -D_\phi \nabla\phi$
Chilton and Colburn J-factor	$J_H = \dfrac{Nu}{Re \cdot Pr^{1/3}}$	$J_M = \dfrac{Sh}{Re \cdot Sc^{1/3}}$

2.3 Summary of the chapter

A theoretical background has been presented in this chapter as it was necessary to recall the notions and mechanisms involved in the phenomena to be studied. The equations driving the heat and mass transfer have been described, as well as the analogies between heat and mass transfer processes.

As this thesis focuses more on the heat transfer aspect, a review of the work that has been done in this specific area is presented in Sections 3.1 and 3.2. This literature review aims at presenting the studies that, starting from the equations and notions presented in Chapter 2, have been improved up to these days.

Section 3.3.3 presents the history of genetic algorithms in an attempt to show how the principles of this evolutionary numerical technique has developed and how it is suited to the present objectives.

Chapter 3

Literature Review: Convective heat and mass transfer and genetic algorithms

This chapter can be divided into two main parts.

(i) A literature survey of the work done in the area of thermal convection around a single cylinder and an array of cylinders. Many studies in the area of heat transfer have focused on this particular geometry as it is commonly found in engineering applications as illustrated in Fig. 3.1. The heat transfer from cylinders placed in a medium at rest or in a free stream, has been investigated experimentally and numerically for years ([42]- [122]). Several empirical correlations have been derived and provide engineers with good hints on how to design heat exchangers effectively.

(ii) The history of genetic algorithms as this optimization technique has been chosen as the procedure to search for optimal designs of two-dimensional heat sinks in cross-flow. This second part aims at presenting the evolution of GAs and aims at showing their potential for finding optimal solutions to complex problems.

As introduced in section 2.1.1, the physics of heat transfer is greatly affected by the type of flow, or more specifically, by whether forced, natural, or both types of convection have to be taken into account. Figure 3.2 recalls the main forces involved in forced and natural convection for the cylinder case, which is the geometry that has been studied the most.

In the case of a cylinder, the main parameter is its diameter D used in the

Figure 3.1: Pin fin heat sink

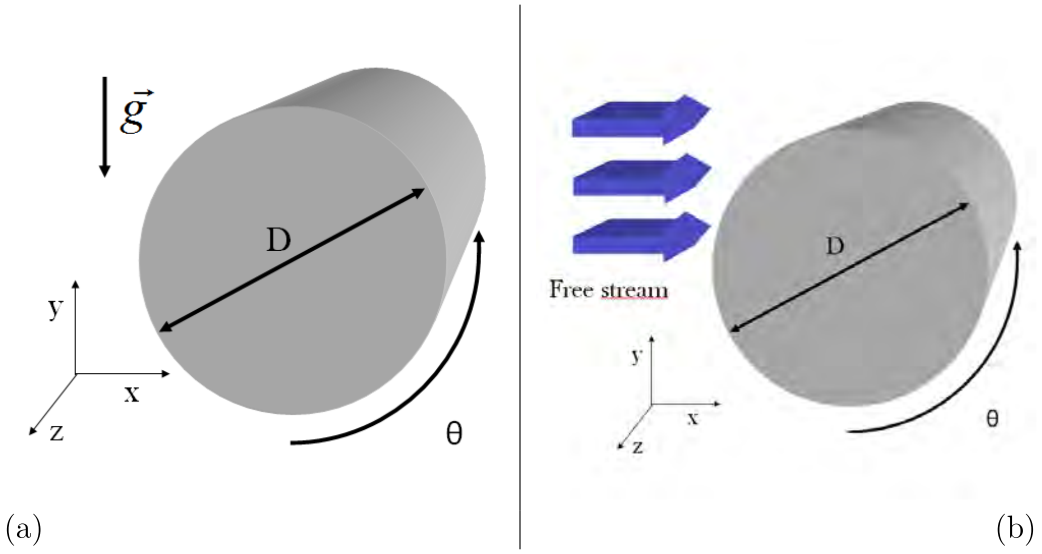

Figure 3.2: Schematic of (a) Natural convection and (b) Forced convection for a cylinder.

computation of the Reynolds number and the Grashof number, characterizing the flow in the case of forced or natural convection respectively. As it is described in the previous sections, studies of heat transfer from cylinders initially focused on time-averaged mean quantities. When the "mean value" is employed, it refers to the average over the cylinder surface; $Nu_m = \frac{1}{2\pi}\frac{1}{L}\int_0^{2\pi}\int_0^{L}\overline{Nu(\theta,z)}d\theta dz$ where θ is the angular coordinate and z is the coordinate along the cylinder's length L.

The studies conducted on forced convection are presented in Section 3.1. Section

3.2 reviews the work done on natural convection, and finally, studies on complex geometries, like arrays of cylinders, and the optimization of their design are reviewed in Section 3.3.1.

3.1 Forced convection heat transfer

This section presents the development that has been made in the field of forced convection, which has been studied experimentally as well as numerically for many years now. Indeed, the situation where a heat transfer device is placed in a high velocity stream of fluid is very common in engineering; almost every cooling device installed on engines producing heat, from a computer up to a nuclear power plant, includes forced convection processes.

3.1.1 Heat transfer in boundary layers

In the case of forced convection, scientists have first studied the problem of heat transfer through a boundary layer, which is a phenomenon occurring at the surface of an object placed in a free stream. Because of the predominance of free stream convection over buoyancy induced convection, the Richardson number is very low ($Ri < 0.1$) and the heat transfer characteristics of the fluid mainly depends on the Reynolds number and the Prandtl number rather than the Rayleigh number.

There are two important pioneers in the analytical prediction of heat transfer through boundary layers. Pohlhausen provided, in 1921, solutions to the boundary layer equations which aim at estimating the heat and mass transfer rate within a laminar boundary layer, in the case of negligible mass transfer [32]. Eckert, who worked on the more general case which considers heat and mass transfer, also provided solutions to the b-equations [33]. The formulation of the similar b-equations is extensively described by Spalding et al. [34], [35], [36] and a brief summary of the history of the analytical work done on this matter is presented;

The continuity, momentum and energy equations are considered in their general form (Eq. 2.9, 2.10 and 2.11 respectively) and rewritten, taking several assumptions into account;

- Natural convection is neglected, that is to say, the buoyancy forces are neglected.
- Steady flow and incompressible fluid.
- Two-dimensional laminar boundary layer.

- Low Mach number.

With all these assumptions, the Navier-Stokes equations reduce to Eq. 3.1, 3.2 and 3.3. Finally these assumptions are also applied to the similar equations, as described in [34] and [36], as shown in Eq. 3.4 and 3.5. These two similar equations are derived for flows in which $\partial u_\infty/\partial x$ is proportional to u_∞^n with n a constant (u_∞ being the upstream flow velocity outside the boundary layer).

Continuity:

$$\frac{\partial u}{\partial x}+\frac{\partial v}{\partial y}=0 \tag{3.1}$$

Momentum:

$$u\frac{\partial u}{\partial x}+v\frac{\partial u}{\partial y}=u_\infty\frac{\partial u_\infty}{\partial x}+\nu\frac{\partial^2 u}{\partial y^2} \tag{3.2}$$

Energy:

$$u\frac{\partial T}{\partial x}+v\frac{\partial T}{\partial y}=\frac{k}{c_p\rho}\frac{\partial^2 T}{\partial y^2} \tag{3.3}$$

where ν is the fluid kinematic viscosity, k its thermal conductivity and c_p its specific heat.

$$f'''+ff''+\beta(1-f'^2)=0 \tag{3.4}$$

and

$$\theta''+Prf\theta' \tag{3.5}$$

where f is the dimensionless stream function so that $\frac{u}{u_\infty}=\frac{\partial f}{\partial y}$ and $\frac{v}{v_\infty}=-\frac{\partial f}{\partial x}$, $\theta=(T-T_S)/(T_\infty-T_S)$ is the dimensionless temperature difference, $\beta=1/(1-n/2)$ is related to the mainstream acceleration and Pr is the Prandtl number.

In 1950, Lighthill suggested solutions to the heat transfer in a laminar boundary layer problem [37] in the following form;

$$\frac{\delta_i^2}{\nu}\frac{u_\infty}{x}=F\left(\frac{x}{u_\infty}\frac{\partial u_\infty}{\partial x}\right) \tag{3.6}$$

and

$$\frac{\Delta_i^2}{\nu}\frac{u_\infty}{x} = F\left(\frac{x}{u_\infty}\frac{\partial u_\infty}{\partial x}, Pr\right) \tag{3.7}$$

where δ_i represents the thickness of the velocity boundary layer ($i \in [1, 2, 4]$ 1 for the displacement, 2 for the momentum and 4 for the shear thickness), Δ_i is "a" thickness of the thermal boundary layer as of δ_i for the velocity boundary layer and $F(...)$ means "some function of...".

Tifford modified slightly Lighthill's solution in order to improve the accuracy of the solutions by using an additional term [38];

$$\left(\frac{u_\infty}{\delta_4}\right)_{effective} = (0.98Pr^{-0.02})^{1.5} \times \left[\left(\frac{u_\infty}{\delta_4}\right)_{actual} - \frac{4}{3}Pr^{-0.25}\frac{\delta_2}{\nu}u_\infty\frac{\partial u_\infty}{\partial x}\right] \tag{3.8}$$

where the suffixes "effective" and "actual" indicate how u_∞/δ_4 should be modified to improve Lighthill's solutions.

In relation to the analytical work that has been done on the heat transfer inside a boundary layer, experimental studies on the forced convection heat transfer have been conducted in the case of channel flows. Sieder and Tate (1936) [39] suggested the following empirical correlations, Eq. 3.9 and 3.10, for the averaged overall heat transfer coefficient along an isolated plate or between two surfaces of length L in the laminar case, at $Re \leq 3 \times 10^5$ and in the turbument case, at $Re \geq 3 \times 10^5$ respectively:

$$h = 0.664\frac{k}{L}Re^{1/2} \cdot Pr^{1/3} \tag{3.9}$$

$$h = 0.036\frac{k}{L}Re^{0.8} \cdot Pr^{1/3} \tag{3.10}$$

where k is the fluid thermal conductivity, L the characteristic dimension of the surface, Re the Reynolds number based on the length L and Pr the Prandtl number.

Similar correlations are found for a flow in tubes or pipes; Sieder and Tate provided Eq. 3.11, for laminar flow ($Re \leq 2100$) [39] and the Dittus-Boelter equation with viscosity correction 3.13 is available for turbulent flow ($Re \geq 10,000$) [40]. In 1943, Hausen suggested the correlation 3.12 which is valid in the transition regime ($2100 \leq Re \leq 10,000$) [41].

$$\frac{hd_e}{k} = 1.86\left(Re \cdot Pr\frac{d_e}{L}\right)^{1/3}\left(\frac{\mu}{\mu_w}\right)^{0.14} \tag{3.11}$$

$$\frac{hd_e}{k} = 0.116(Re - 125)Pr^{1/3}\left[1 + \left(\frac{d_e}{L}\right)^{2/3}\right]\left(\frac{\mu}{\mu_w}\right)^{0.14} \tag{3.12}$$

$$\frac{hd_e}{k} = 0.023Re^{0.8} \cdot Pr^{1/3}\left(\frac{\mu}{\mu_w}\right)^{0.14} \tag{3.13}$$

where d_e is the equivalent diameter, μ is the dynamic viscosity of the fluid and μ_w is the viscosity at the wall temperature.

3.1.2 Time-averaged overall heat transfer from a cylinder

Forced convection has been studied in its simplest form, as described in the previous section, with the analytical prediction of the very basics of the phenomenon: heat transfer through a boundary layer. Experiments on the heat transfer in a channel flow, which is the closest situation to the theoretical boundary layer, have been conducted as it is shown in the previous section.

Scientists have also worked on the understanding of heat transfer, and more precisely here, forced convection of bodies placed in a cross flow. The heat is not transferred from a body to a fluid it contains, but from a body surrounded by a fluid in cross flow as shown in Fig. 3.3. One of the pioneer in the area is certainly Davis who conducted, in 1924, experimental studies on forced convection heat transfer from cylinders using different oils in order to account for a wide range of fluid viscosity [42]. Davis gathered data for a Reynolds number ranging from 0.1 to 200, and in 1932, Ulsomer [43] correlated the data using an equation in the form;

$$Nu = C \cdot Pr^m \cdot Re^n \tag{3.14}$$

where c, m and n are constants taking the following values; $m = 0.31$, $C = 0.91$ and $n = 0.385$ for $0.1 \leq Re \leq 50$ and $m = 0.31$, $C = 0.6$ and $n = 0.5$ for $50 \leq Re \leq 10^4$ [43].

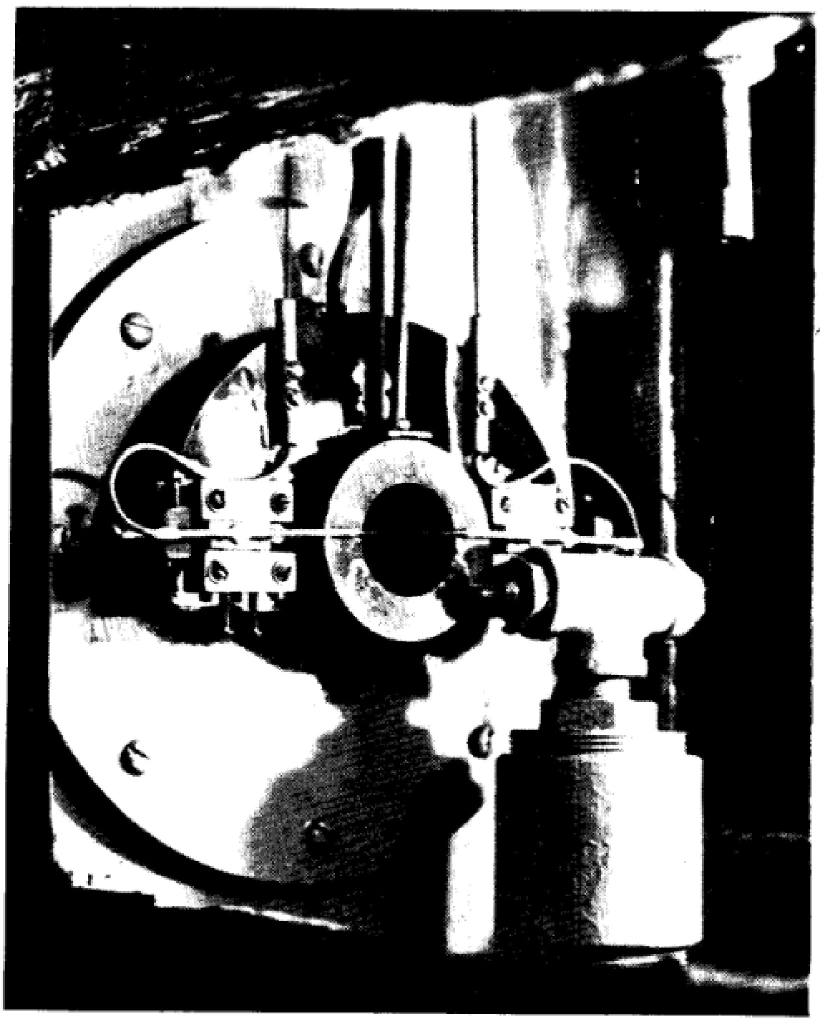

Figure 3.3: Heated wire in water stream, experimental setup, [44].

In 1946, Kramers [45] suggested another form for the empirical correlation consisting in Eq. 3.14 but containing an additional term as follows;

$$Nu = C' \cdot Pr^{m'} + C \cdot Pr^{m} \cdot Re^{n} \tag{3.15}$$

Where the values of the constants C', m', C, m and n are 0.42, 0.2, 0.57, 0.33 and 0.5 respectively.

In 1954, the results obtained previously from Davis [42] and other scientists such as Piret et al. [44], who investigated forced convection from cylinders in water, and which was correlated with Eq. 3.14, correlate well with Eq. 3.15 by McAdams [46], which gave rise to the explicit correlation;

$$Nu = \left[0.35 + 0.56 Re^{0.52}\right] Pr^{0.3} \tag{3.16}$$

In the numerical field, Schuh (1953) [47] and Merk (1959) [48] offered improvements of the analytical similarity solutions. Merk even assumed that these solutions were valid in general and not only as similar solutions.

A new idea emerged in the late fifties, that the heat transfer can be split into two terms; one representing the heat transfer through the laminar boundary layer on the front or upstream portion of the cylinder, and the second representing heat transfer from the back of the cylinder, where separation and turbulence occur as suggested by Douglas and Churchill [49], Hegge Zijnen [50] and Richardson [51]. This led to the following form of correlation;

$$Nu = a \cdot Re^{0.5} + b \cdot Re^{n} \tag{3.17}$$

Where a and b are not constants but rather proportional to Pr^{m}, and n depends on the author, varying from 0.67 for Richardson [51] to 1 for Douglas and Churchill [49].

This correlation has been validated by Perkins and Leppert [52] in 1962; they reported an adequate correlation of their data with correlation 3.17 for a Reynolds number ranging from 40 to 10^5, and Prandtl number varying from 1 to 300 with numerical constants as in the following;

$$(Nu)_a = \left(\frac{\mu_a}{\mu_s}\right)^{0.25} \left[0.53(Re)_a^{0.50} + 0.0019(Re)_a\right] (Pr)_a^{0.40} \tag{3.18}$$

$$(Nu)_a = \left(\frac{\mu_a}{\mu_s}\right)^{0.25} \left[0.30(Re)_a^{0.50} + 0.10(Re)_a^{0.67}\right] (Pr)_a^{0.40} \tag{3.19}$$

where μ is the viscosity of the fluid and the subscripts a and s refer to conditions at ambient temperature and at the cylinder surface temperature respectively.

Spalding and Pun [53] published a paper in 1961 reviewing all the different methods of calculation for the analytical prediction of heat transfer inside the boundary layer, comparing results from the previously mentioned authors who worked on the subject, as well as Squire [54], Stine and Wanlass [55] and Frössling [56] who solved the partial differential equations 3.1, 3.2 and 3.3 with the use of series. The importance of the upstream flow's turbulence intensity on the heat transfer has been described in 1961 by Kestin et al. [57].

In 1965, Fand reported a good agreement between his experimental results on forced convection from a cylinder to water in crossflow with McAdams's correlation, Eq. 3.16 [58]. In 1977, Churchill and Bernstein [59] proposed a universal empirical correlation valid for circular cylinders in cross flow that covers the entire range of Reynolds number and a wide range of Prandtl number, such as $RePr > 0.2$ in the following form;

$$\overline{Nu} = 0.3 + \frac{0.62Re^{0.5}Pr^{1/3}}{\left[1 + (0.4/Pr)^{2/3}\right]^{1/4}} \left[1 + \left(\frac{Re}{282000}\right)^{5/8}\right]^{4/5} \tag{3.20}$$

3.1.3 Local and unsteady heat transfer from a cylinder

More in-depth studies have been conducted on the local forced convection heat transfer from a cylinder, as well as on the unsteady heat transfer. One solution of the local heat transfer, built on experimental results from Schmidt and Wenner [60], theoretical calculations from Frössling [56] and results from Eckert [33], of these two-dimensional boundary layer heat transfer problems, is described by Kestin et al. [57] in 1961 and takes the following form;

$$\frac{U}{U_\infty} = 3.631\left(\frac{x}{D}\right) - 3.275\left(\frac{x}{D}\right)^3 - 0.168\left(\frac{x}{D}\right)^5 \tag{3.21}$$

$$\frac{Nu}{Re^{0.5}} = 0.9449 - 0.7693\left(\frac{x}{D}\right)^2 - 0.3009\left(\frac{x}{D}\right)^4 \tag{3.22}$$

where $x = R\phi$, ϕ being the angular coordinate around the cylinder and R the cylinder radius. D is the cylinder diameter and U_∞ is the free stream velocity. The Prandtl number for which these solutions are valid is $Pr = 0.7$.

In 1963, Perkins and Lepert [61] published their results on the normalized local Nusselt number and compared them with analytical predictions from Lighthill [37], Seban [62] and Eckert [33]. A good agreement is found on the local heat transfer characteristics as shown in Fig. 3.4;

Unsteady numerical studies have been conducted since the late seventies with the works from Apelt and Ledwich [63] and Karniadakis [64]. Karniadakis studied, in 1988, the forced convection heat transfer from a cylinder in cross flow for Reynolds numbers up to 200 by direct numerical simulation (DNS). The numerical results are obtained using a spectral element numerical method. Periodic oscillations of the velocity field, temperature and drag coefficients are reported by Karniadakis as shown in Fig 3.5 and a good agreement with available experimental data is found [64].

Cheng et al. studied the so-called lock-on effect on convective heat transfer from a transversely oscillating circular cylinder for two values of the Prandtl number corresponding to air and water [65] (1997). For the case of a non-oscillating cylinder, they reported good agreement with available data from relevant studies.

In 2000, Mahfouz and Badr [66] investigated the effect of rotational oscillations of a cylinder on the forced convection heat transfer from the cylinder in air. They reported periodic variations in Nusselt number depending on the Reynolds number for $Re = 80, 100$ and 200. Lange et al. [67] and Baranyi [68] also numer-

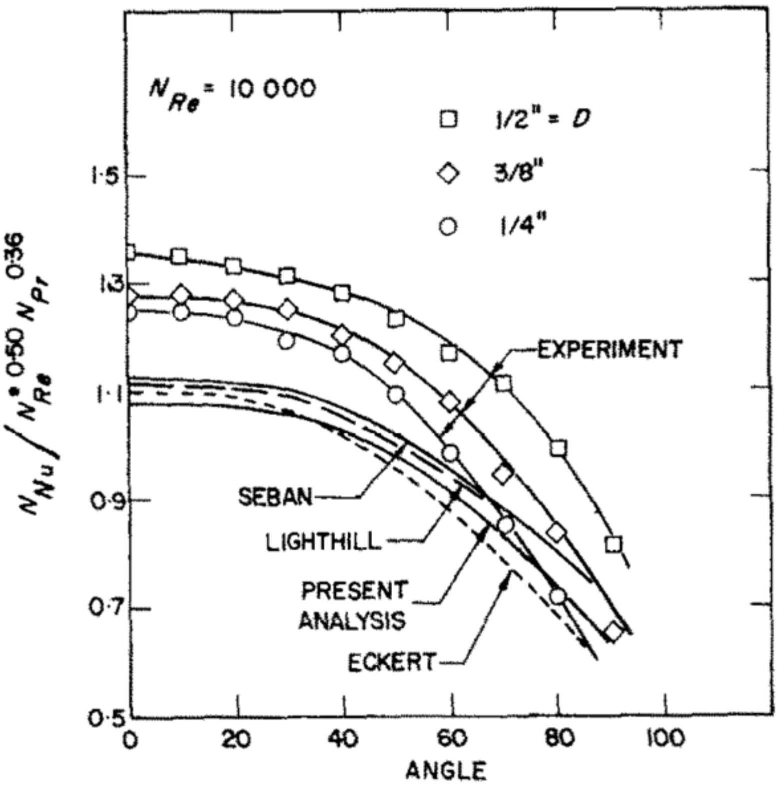

Figure 3.4: Local Nusselt number from [61]

ically studied the heat transfer from a heated cylinder to air. Bhinder et al. [69] conducted a numerical study on the unsteady forced convection heat transfer from a semi-circular cylinder to air at incidence and reported strong dependency of the Nusselt number on the incidence angle. Similarly, studies on forced convection heat transfer from various body shapes have been reported ([70], [71]). However, a few papers numerically investigated unsteady forced convection to water.

The study of unsteadiness for forced convection heat transfer problems has been a little extended to power-law fluids (a generalized Newtonian fluid for which the shear stress and the velocity gradient perpendicular to the plane of shear follow a power-law relationship; $\tau = K \left(\frac{\partial u}{\partial y} \right)^n$) . Indeed, the study of vortex shedding, transition to unsteadiness and the effects of these phenomena on the heat transfer has been conducted by Chhabra et al. [72] and [73] for a range of Reynolds number $40 \leq Re \leq 140$ and Prandtl number $1 \leq Pr \leq 100$. Figure 3.6 shows the transition to unsteadiness achieved by increasing the Reynolds number which confirms

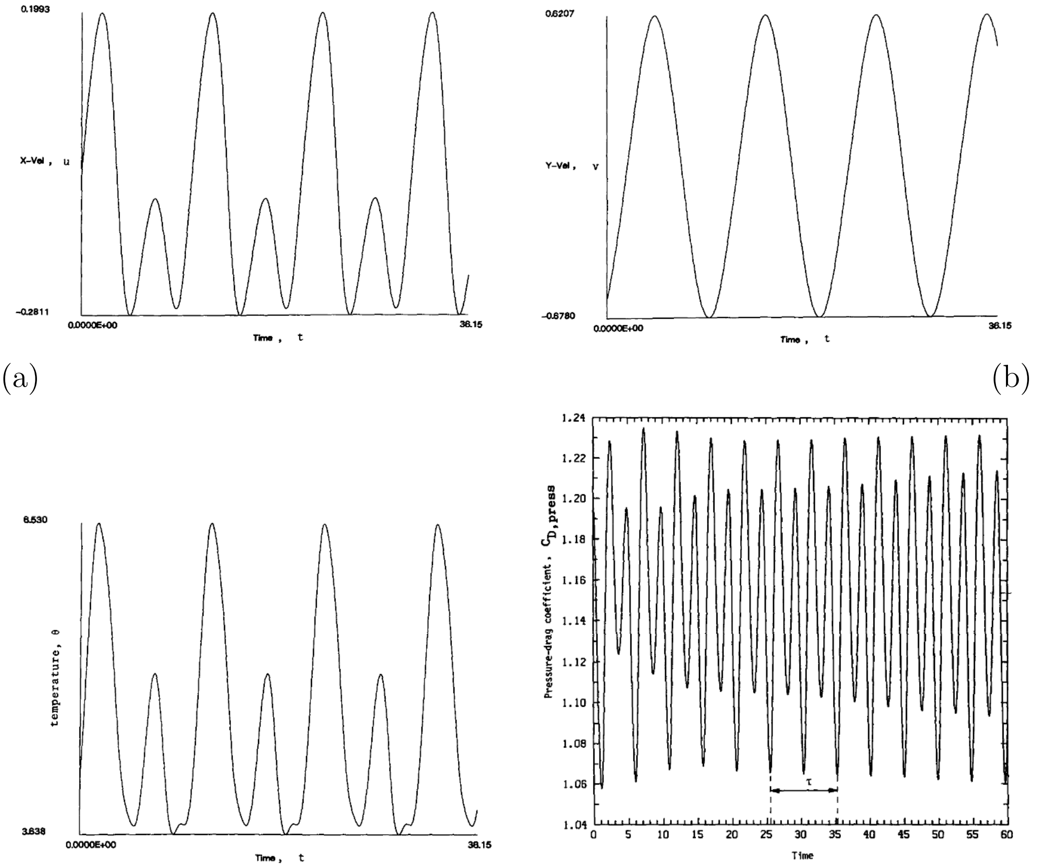

(a) (b)

(c) (d)

Figure 3.5: Numerical investigations by Karniadakis [64]. (a) horizontal velocity, (b) vertical velocity and (c) temperature for $Re = 150$ and $Pr = 0.7$ at a point located $0.92D$ from the rear stagnation point and $0.068D$ from the centreline. (d) pressure-drag coefficient of the cylinder at $Re = 200$.

that the heat transfer characteristics of the cylinder can fluctuate over time, in a situation of forced convection.

3.2 Natural convection heat transfer

When considering natural convection, our understanding is less complete than forced convection, as natural convection is often neglected for high velocity flows which are encountered more often in the engineering field.

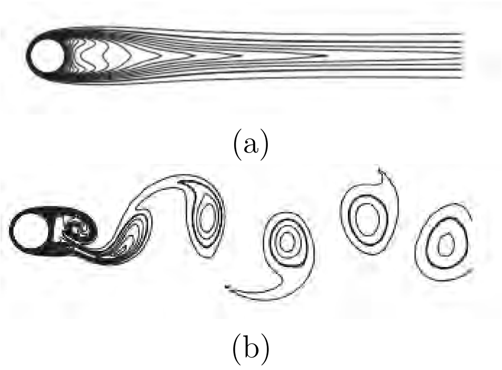

Figure 3.6: Numerical investigations by Chhabra et al. [73]. Isotherms at (a) $Re = 40$, (b) $Re = 100$. $Pr = 10$, $n = 0.4$.

3.2.1 Natural convection from a point or a line heat source

Even though natural convection has been less intensively studied compared to forced convection, the beginning of its analytical study dates back to the mid twenties. The mathematical problem is to predict how heat will transfer from a point or a line source to the surrounding fluid. A brief summary of the history of the studies conducted in this area is presented.

A natural convection plume arising from a point and from a horizontal line heat source has first been described by Zeldovich [74] in Russia in 1937. He employed the similarity methods used by Tollmien [75] to solve for the turbulent flow velocity for the two-dimensional and axi-symmetric jet, and the similarity methods used by Schlichting [76] to solve for the laminar flow velocity. Zeldovich included buoyancy and a similarity form of temperature distribution to his model.

In 1941, Schmidt [77] studied the natural convection in a turbulent plume above a line and point source of heat.

A concise analysis of the natural convection in a boundary layer flow above a plane and axially symmetric sources were presented by Schuh in 1948 [78]. The boundary conditions he used were presented, and by assuming the form of the similarity variable, as originally proposed by Prandtl, and using a numerical integration scheme which corrects velocity and temperature values, initialized at the centerline in order to satisfy conditions at infinity, the coupled differential equations were solved.

In 1951, Yih reported a study of natural convection from a point source [79] and, in 1952, he presented a closed form solution for the temperature and the velocity distribution for the laminar natural convection above a line source of heat for Prandtl numbers 2/3 and 7/3 [80].

3.2.2 Time-averaged overall natural convection heat transfer from a cylinder

Experimental studies of the free convection heat transfer from cylinders started in the late forties with the work of Eckert and Soehngen, who measured the temperature variations using a Zehnder-Mach Interferometer [81]. They already reported that in the case of two vertically aligned cylinders, the lower cylinder's buoyant plume could either have a positive or a negative effect on the upper cylinder's heat transfer capacity, depending on the spacing between the two cylinders. The heat transfer rate was found to decrease with decreasing cylinder spacing [81]. The first empirical correlations for the natural convection problem were calculated by Merk and Prins in 1953 and Lefevre in 1956 for horizontal cylinders (Eq. 3.23, [82]) and vertical cylinders (Eq. 3.24, [83]) respectively;

$$Nu_m = C \cdot Ra^{1/4} \tag{3.23}$$

Where Nu_m is the Nusselt number averaged over a horizontal cylinder area and C depends on the Prandtl number; $C = 0.436, 0.456, 0.520, 0.523$ for $Pr = 0.7, 1, 10, 100$ respectively [82].

$$Nu_m = \frac{4}{3}\left[\frac{7Gr \cdot Pr^2}{5(20+21Pr)}\right]^{1/4} + \frac{4(272+315Pr)L}{35(64+63Pr)D} \tag{3.24}$$

Where Nu_m is the Nusselt number averaged over a vertical cylinder area.

From the analytical study of the free convection from point and line heat sources, the investigations have complexified towards analytical analysis of infinite and finite cylinders. An analytic study of natural convection heat transfer is published by Mahony [84] in 1956. This paper deals with heat transfer from spheres and cylinders, at small Grashof numbers, and focuses on the regions in which conduction or convection are dominant. It is shown that convection is negligible near the body's surface and becomes as important as conduction at a distance from the body of the order of Gr^{-n}, where n varies from 1/3 to 1/2 depending on the shape of the body. In 1961, Lee and Emmons theoretically and experimentally investigated the turbulent natural convection above a line of fire [85]. Theoretically, the governing equations are solved by quadrature for a finite width source, with the use of boundary layer assumptions, as well as assumptions for the lateral entrainment of air, and similar Gaussian profiles for the velocity and the temperature at all heights.

The most complete work that has been done on the subject is, to date, the numerical analysis of Fujii [86]. In this paper, published in 1963, Fujii solved the two-dimensional flow configuration assuming boundary layer behavior, in closed form for a Prandtl number of 2, and for the axisymmetric case for $Pr = 1$ and 2. Numerical integration was also used to solve the differential equations for $Pr = 0.01$, 0.7 and 10.

More recently, in 1967, Brand and Lahey analytically studied the laminar free vertical jet with buoyancy [87]. Although a vertical jet would have a mass flow and a vertical component of the velocity at the origin, no additional parameter was introduced so that the formulation of the problem, along with the boundary condition, is identical to Fujii's work. An additional closed-form solution is presented for a Prandtl number of 5/9 and their numerical solution includes velocity and temperature profiles for $Pr = 0.72$, 5 and 10.

Empirical correlations are also available for isothermal vertical plates (Eq. 3.25, from Oosthuizen, 1999 [88]) and horizontal plates (Eq. 3.27, from Gebhart and Pera, 1970 [89]).

$$Nu_m = \frac{4}{3}\Phi(Pr)Gr^{1/4} \tag{3.25}$$

Where Nu_m is the Nusselt number averaged over the surface and $\Phi(Pr)$ is defined by Oosthuizen and Naylor [88] as;

$$\Phi(Pr) = \left(\frac{0.316Pr^{5/4}}{2.44 + 4.88Pr^{1/2} + 4.59Pr}\right)^{1/4} \tag{3.26}$$

$$Nu_x = 0.394Gr_x^{1/5} \cdot Pr^{1/4} \tag{3.27}$$

Where Nu_x is the local Nusselt number on a horizontal isothermal surface.

In 1972, a paper from Marsters [90] presents results from an experimental study of heat transfer from an array of horizontal cylinders where the complexity of the interaction between numerous cylinders, which cannot be "predicted by simple superposition of single cylinder behavior", is highlighted and an enhancement in the overall heat transfer is already observed. For small spacing between the cylinders which compose the array, the cylinders affected by a thermal plume rising from a cylinder below them have their individual Nusselt number decreased up to 50 percent, but for wider spacing, positive enhancement is observed with an increase of the individual tubes' Nusselt number up to 30 percent [90].

Morgan mostly studied the single cylinder case and presents his experimental results in his paper in 1975 [91]. He describes several empirical correlations for a single horizontal and vertical cylinder, in natural and forced convection configurations, and presents the values of the constant appearing in the empirical correlation from many different investigators.

Results from Stafford and Egan [92] also show that an increase can be obtained, and that an optimum design (i.e., optimal spacing in the case of a simple geometry such as a pair of cylinders) can be achieved in the laminar flow regime, for $10^4 \leq Ra \leq 10^5$. A centre-to-centre distance, $S = 4D$ was found to be the optimum.

In the numerical field, natural convection heat transfer problems have been conducted and provide a consistent body of data for time-averaged results of heat transfer from one or several horizontal or vertical cylinders.

Dai et al. numerically investigated natural convection around a pair of horizontal cylinders, a cold one and a hot one, in an adiabatic cylindrical enclosure in 2015 [93]. They focused on finding the position in terms of the inclination angle θ from the upward direction between the two cylinders, which maximizes the overall heat transfer from the hot tube to the cold tube. The minimum effective heat transfer coefficient between the tubes is found when the hot tube is placed directly above the cold one. This is indeed not difficult to imagine as the thermal plume rising from the hot tube is moving upward and away from the cold tube. The hot fluid has to travel around the boundary of the cylindrical enclosure in order to reach the cold tube; the heat transfer is not optimal. The opposite configuration is naturally coming into mind when looking for the maximum heat transfer coefficient. Dai et al. indeed report an optimum position which is when the cold tube is placed directly above the hot one. However, interestingly, the optimum position is found to be when the cold cylinder is placed above the hot one at an inclination angle $\theta = 60°$ for a Rayleigh number $Ra \leq 1400$ [93].

In 2014, Stafford and Egan also investigated numerically the phenomenon of natural convection from a pair of horizontal cylinders aligned vertically and horizontally, in the laminar flow regime, for a Rayleigh number range $10^4 \leq Ra \leq 10^5$ [92] as shown in Fig. 3.7. A very precise optimal spacing was found for the horizontal alignment case, but in the vertically aligned scenario, the pair of cylinders have multiple constructal configurations and the enhancement of the upper cylinder heat transfer is observed when the combined effects of the lower cylinder thermal plume impose a beneficial buoyancy-assisted flow. They finally predict two constructal configurations for the vertically aligned cylinders pair; one with no spacing $S/D = 0$, where the cylinders form a single tall body, and another with a spacing $S = 3.5D$ which maintains individual performance as well as maximizes the global array performance [92].

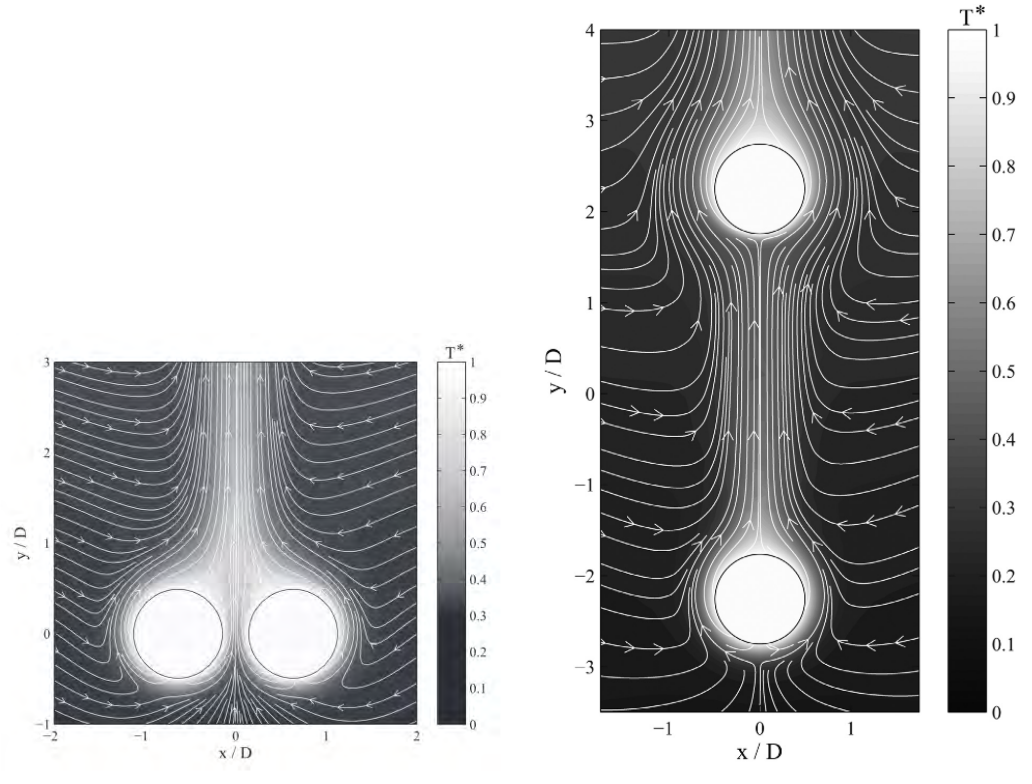

(a) (b)

Figure 3.7: Heatlines and isotherms for cylinders optimally positioned from Stafford and Egan [92], $Ra_D = 10^4$. (a) horizontal alignement, $S = 0.28D$ and (b) vertical alignement, $S = 3.5D$.

An increase of the averaged Nusselt number is reported in other numerical studies. This increase has been observed, either depending on the distance to the free surface for a single immersed cylinder [94], or on the spacing between two vertically aligned cylinders [95]. Park et al. investigated the natural convection from two heated vertically aligned horizontal cylinder in a cold enclosure. They report smaller values of the time-averaged overall Nusselt number of the upper cylinder for Rayleigh numbers from 10^3 to 10^5 but a strong increase is observed for $Ra = 10^6$. They conclude on the strong dependency on the spacing between the two cylinders and the Rayleigh number to the heat transfer potential of the cylinders [95].

Shyam et al. investigated numerically the natural convection from a pair of vertically aligned horizontal cylinders in power-law fluids for a Prandtl number $0.72 \leq Pr \leq 100$, a Grashof number $10 \leq Gr \leq 10^4$, a power-law index $0.3 \leq n \leq 1.5$ and a centre-to-centre spacing $2 \leq S/D \leq 20$. They discuss the effect of the fluid characteristic (shear-thinning and shear-thickening fluid behavior for $n \leq 1$ and $1 \leq n$ respectively) and its impact on the heat transfer potential of the cylinders as well as the effects of the Prandtl number, Grashof number and spacing. Despite the fact that shear-thinning seems to be beneficial to heat transfer whereas shear-thickening has a negative impact on the heat transfer, their results show very similar behavior than studies base on Newtonian fluids. The lower cylinder is not affected much by the presence of a cylinder placed above, and its heat transfer is comparable to that of a single cylinder. However, when two cylinders are vertically aligned, the upper cylinder is greatly affected and Shyam et al. report that there is a variation of the Nusselt number of the oreder of 70% to 130% compared to the Nusselt number of a single cylinder [96].

However not many studies have described the effect of the thermal plume oscillations on the transient local Nusselt number and flow velocity.

3.2.3 Local and unsteady heat transfer from a cylinder

Some publications have discussed the unsteady behavior of the thermal plume rising from a single cylinder.

An experiment of natural convection from a single horizontal cylinder has been conducted by Pera & Gebhart in 1972 [97]. They used solid particles illuminated with a laser beam and a high speed camera in order to capture the fluid motion. The experiment revealed the formation of a plume, which is formed as the boundary layers developing on each side of the cylinder join each other at the top of the cylinder as shown in Fig. 3.8. For Grashof numbers up to 0.5×10^{10} the resulting plume is laminar and steady as shown in Fig. 3.8a and 3.8b where the observed rising plume is straight. However the results from Pera & Gebhart show that at a Grashof number of 1×10^{10} an unsteady wake is created above the cylinder with irregular flow separation and reversal as shown in Fig. 3.8c and 3.8d [97]. These results have been related to the incoming edge effects of the tank containing the cylinder and surrounding water. Similar results and conclusion are obtained by Schorr & Gebhart [98] in 1970 and compared to theoretical results from analytic study [89].

In 1980, laminar natural convection from a horizontal isothermal cylinder has been studied by Kuehn and Goldstein with an interesting approach; a balance between natural convection from a line heat source which is the extreme limit when the Rayleigh number tends to zero, and laminar boundary layer flow (extreme limit for a Rayleigh number which tends to infinity) has to be found in order to solve the flow [99]. A good agreement is found between the results from experiments and results of the time-averaged local Nusselt number over the cylinder surface. These results are often referred to in many paper.

Noto also reported a swaying motion of the thermal plume and published a paper of his experimental study in 1989, aiming at predicting the swaying frequency of such plumes [100]

Unsteady simulations of a two-dimensional buoyancy induced flows from a horizontal line heat source confined in a rectangular vessel has been conducted by Desrayaud and Lauriat in 1993 [101]. The side walls are set to adiabatic while the top and bottom walls are maintained at a constant temperature. A direct simulation is performed and enables to capture the transition to unsteadiness and the swaying motion of the plume that appears for certain values of immersion depth. For these immersion depths, a periodic regime characterized by a swaying frequency is observed and discussed.

in 1999, Kitamura et al. investigated the formation of a turbulent plume in the case of natural convection from a single horizontal cylinder. Their study suggests than above a critical Rayleigh number $Ra_{critical} = 2.1 \times 10^9$, the laminar boundary layers developing along each side of the cylinder eventually separates and transition towards a turbulent boundary layer before they merge at the top of the cylinder. They finally report an increase of the local Nusselt number in the regions of transitional and established turbulence compared to the laminar regions [102]. Figure 3.9 shows the visualized flow field around cylinders for a wide range of investigated Rayleigh number.

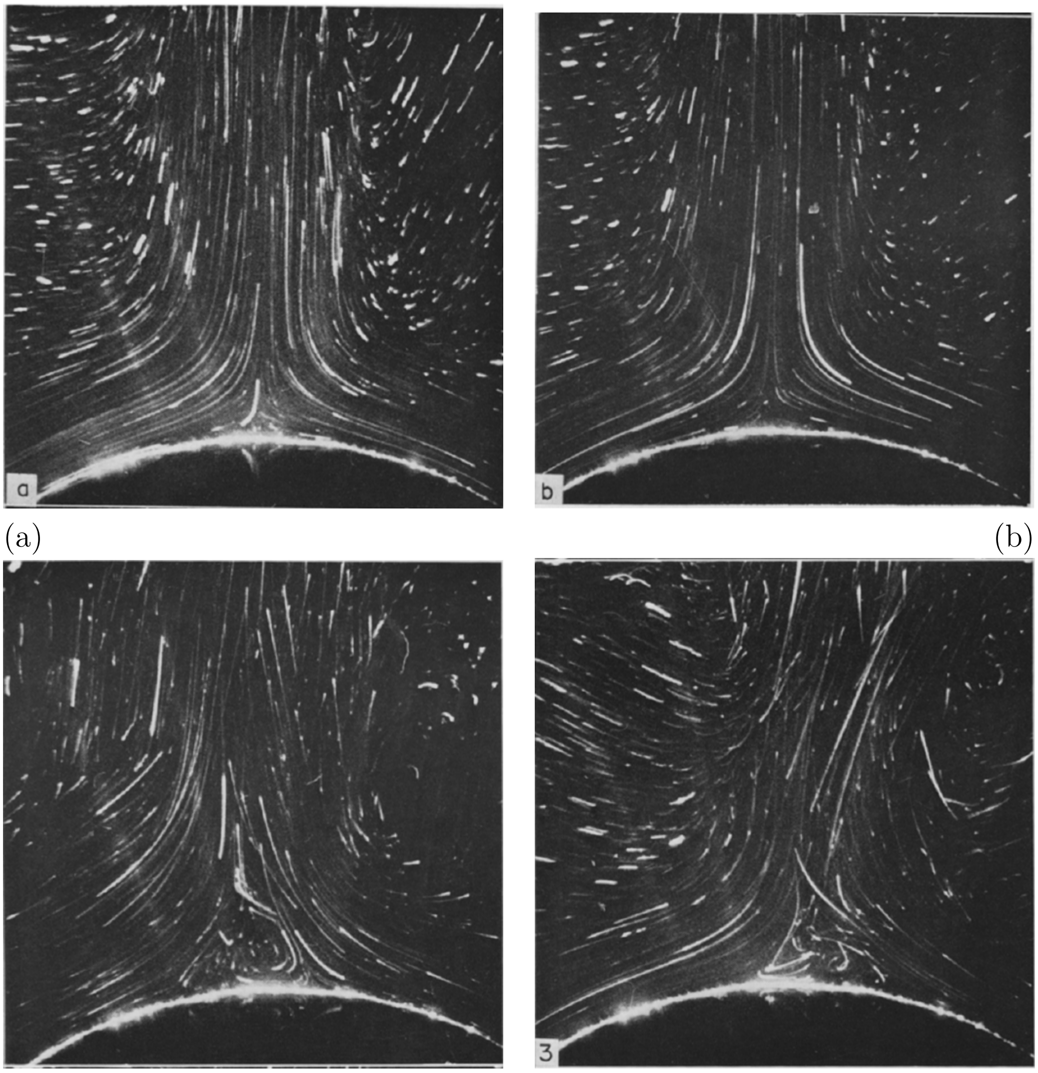

(a) (b)

(c) (d)

Figure 3.8: Visualization of the flow above a heated horizontal cylinder in water from Pera & Gebhart [97]. (a) and (b); steady natural convection at $Gr = 0.25 \times 10^{10}$ and $Gr = 0.5 \times 10^{10}$ respectively, (c) and (d); starting transient natural convection.

Recent experimental studies (2008) revealed a range of cylinder spacing and Rayleigh numbers where beneficial interaction occurs as Eckert ans Soehngen predicted sixty years ago [81]. Indeed it is shown in [103, 104], that for a separation distance of two diameters between the cylinders, the heat transfer of the

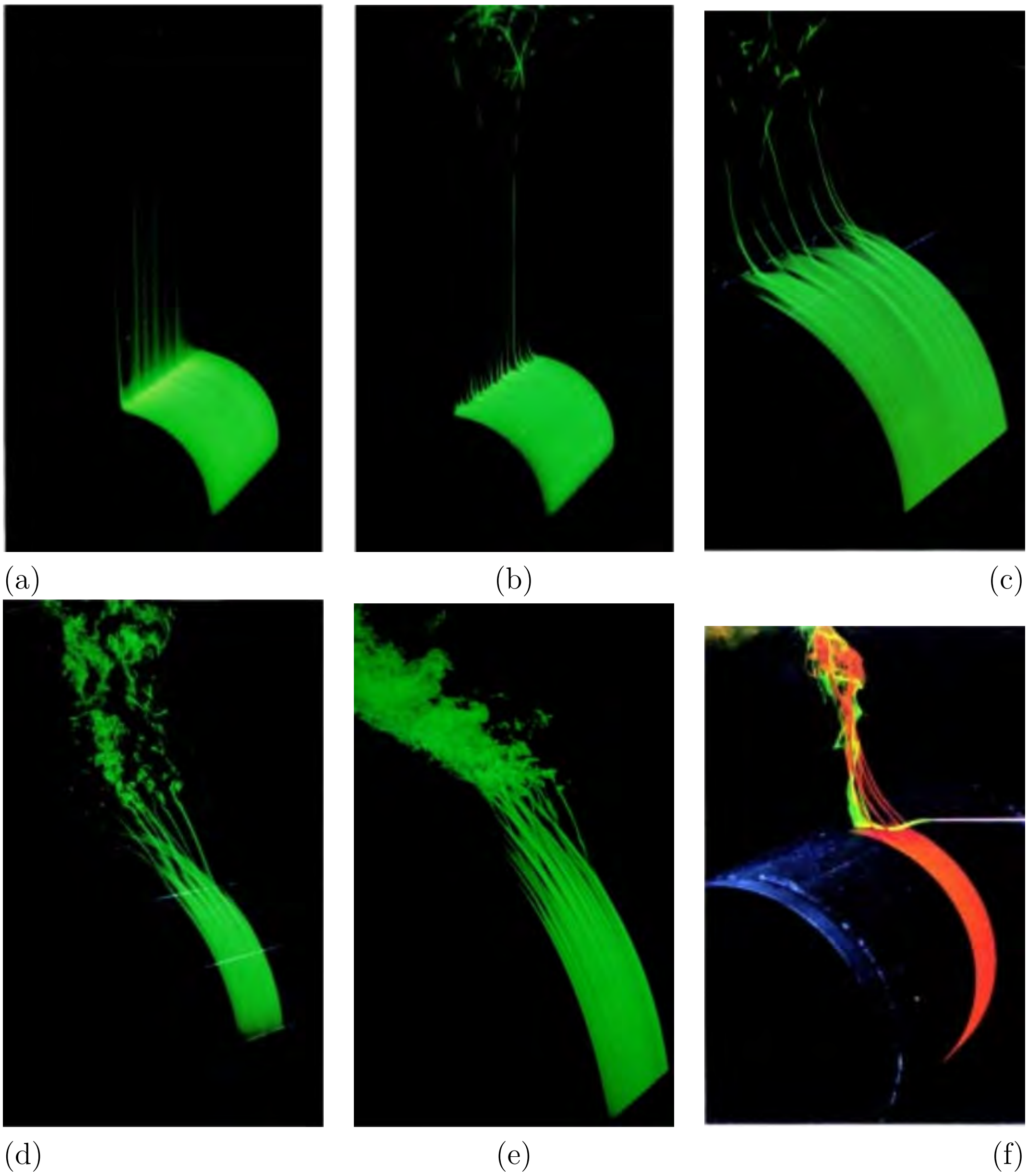

Figure 3.9: Visualized flow fields from Kitamura et al. [102]. (a) $D = 95\ mm$, $Ra_D = 1.29 \times 10^9$, (b) $D = 95\ mm$, $Ra_D = 4.7 \times 10^9$, (c) $D = 300\ mm$, $Ra_D = 2.12 \times 10^{11}$, (d) $D = 500\ mm$, $Ra_D = 5.87 \times 10^{12}$, (e) $D = 800\ mm$, $Ra_D = 3.56 \times 10^{13}$ and (f) $D = 216\ mm$, $Ra_D = 1.98 \times 10^{11}$

upper cylinder is negatively affected for the majority of the cylinder's circumference but a strong enhancement is observed in the local heat transfer near the bottom ($0° \leq \theta \leq 30°$) of the upper cylinder. With a separation distance of $3D$, the enhancement near the bottom is less significant but extend much more around the cylinder ($0° \leq \theta \leq 60°$) and does not significantly drop below that of a single cylinder for $\theta \geq 60°$. Based on experimental measurements of local time-varying Nusselt number, spectral analysis suggested that when the plume from the lower cylinder oscillates out of phase with the plume from the upper cylinder, the mixing around the upper cylinder is enhanced, which in turn reduces the thickness of the thermal boundary layer and finally increases the heat transfer rate.

In 2011, Persoons et al. [105] described an experimental study of the coupling between fluid flow and natural convection heat transfer for a pair of vertically aligned cylinders. The transient behavior of the thermal plume has been characterized for Rayleigh numbers ranging from 1.7×10^6 to 5.5×10^6, which corresponds to the studied range of Eckert and Soehngen [81]. Persoons et al. [105] confirmed a range of cylinder spacing and Rayleigh number where heat transfer from the upper cylinder is enhanced or diminished by the plume interaction. For all the investigated Rayleigh numbers, an overall enhancement with a spacing of $S = 4D$ is noted with its maximum $\delta Nu = (Nu - Nu_0)/Nu_0 \times 100\% = 9.2\%$ for $Ra = 3.6 \times 10^6$. An enhancement of 10.2% is observed for $S = 3D$ and $Ra = 5.3 \times 10^6$, and finally a negative effect on the heat transfer rate for $S = 2D$ and $Ra = 1.8 \times 10^6$ where $\delta Nu = -5.1\%$.

The investigations initiated by Persoons et al. [105] have been pursued and complemented by Quentin et al. (2015) [106] with good agreement in terms of heat transfer and velocity results. This numerical study highlights a tendency to heat transfer enhancement up to 11% in the range $3 \leq S/D \leq 4$ and $4.7 \times 10^6 \leq Ra \leq 5.3 \times 10^6$. Moreover, an attempt at describing and discussing the two main periodic processes involved in the natural convection heat transfer from two vertically aligned horizontal cylinders, is presented [106].

Positive enhancement has also been reported by Grafsronningen and Jensen in 2012 and 2013 [107, 108]. They investigated the change in heat transfer of the upper of a pair of cylinders for Rayleigh numbers ranging from 1.82×10^7 to 2.55×10^8 and spacing $1.5D \leq S \leq 5D$ [107] and for a configuration of three vertically aligned cylinders for Rayleigh numbers $Ra = 1.96 \times 10^7$ and $Ra = 5.35 \times 10^7$ and spacing between the lowermost and middle cylinders and between the middle and upper cylinders from $S = 2D$ to $5D$ [108]. They found an increase in the average Nusselt number of all the cylinders which are not the lowermost, for all the cases.

Park et al. [95] investigated the problem numerically in 2014, and reported asymmetric time-dependent distribution of the isotherms and streamlines about the vertical centerline at $x = 0$ as shown in Fig. 3.10, and periodic oscillations at a Rayleigh number of $Ra = 10^6$ for a centre-to-centre spacing $S = 2.5D$. This swaying motion is correlated with a significant increase of the upper cylinder time-averaged Nusselt number compared to the single cylinder case [95], which seems to warrant a more detailed study of these oscillations. This transition to unsteadiness is also reported by Park et al. in 2013 [109]; the flow and thermal fields eventually reach a steady state for $10^3 \leq Ra \leq 10^6$ but become unsteady for a Rayleigh number above 10^6 and for a spacing between the two cylinder $0 < S/D \leq 0.5$. When the Rayleigh number increases and the effect of convection becomes dominant, the upwelling thermal plume from the cylinders and the downwelling plume from the top wall of the enclosure move back and forth in the right and left directions and create the unsteady periodic oscillations.

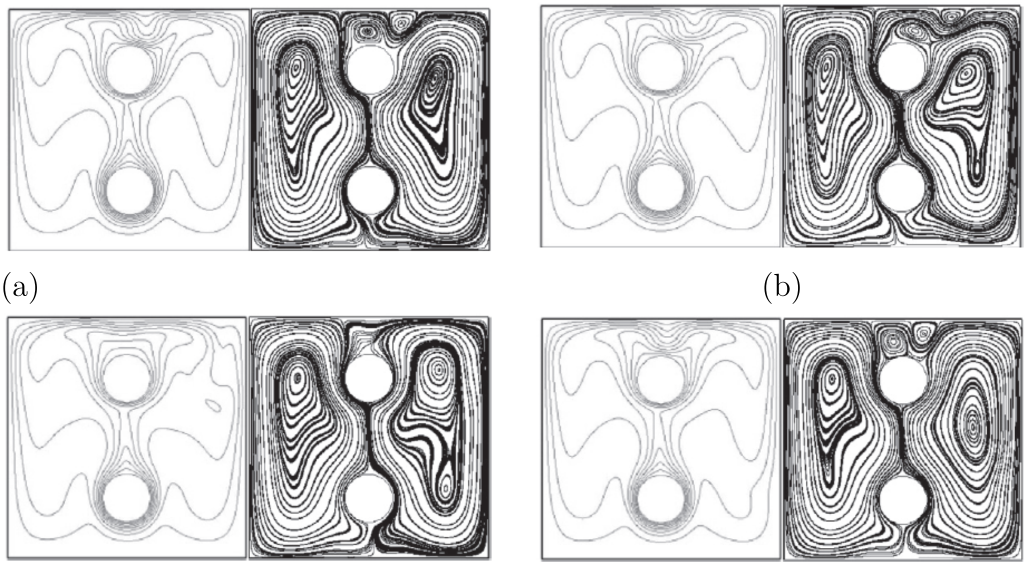

(a) (b)

(c) (d)

Figure 3.10: Instantaneous isotherms and streamlines at selected time instances at $Ra = 10^6$. Data from Park et al. [95]

The oscillatory behavior of the thermal plume rising from a single cylinder has been described by several other papers. Fiscaletti et al. [110] showed experimentally that for the case of a single cylinder, the plume begins to oscillate above a critical Rayleigh number value $Ra_{critical} = 5.88 \times 10^4$. Figure 3.11 shows the oscillating pattern of the velocity field obtained from PIV measurements conducted by Fiscaletti et al. in 2013. The mechanisms leading to plume oscillation and the development of vortices in the cylinder wake have been investigated by Kuehner et al. from 2012 to 2015 [111, 112]. Their conclusion is that the plume flow feeds back into the boundary layer after interacting with the upper free water surface through penetrative convection in the approach flow. A feedback mechanism is formed, which creates the swaying motion. This behaviour doesn't depend on horizontal confinement but rather in vertical confinement. Indeed, Kuehenr et al. found that the swaying motion appears for relatively small submersion depths ($H/D \leq 6$) where penetrative convection reaches the bottom surface of the cylinder, perturbs the boundary layer, and thus creates this oscillating motion.

3.3 Optimization methods and their application for optimizing complex heat transfer geometries

This section is dedicated to the review of studies on optimization techniques in general and more precisely, on optimization methods that could be applied to search for optimal geometries for maximizing the heat transfer from a body.

3.3.1 Complex geometries and early design optimization

Several studies have been conducted on the optimal spacing between the bodies of an array of such bodies, that maximizes the overall thermal conductance of the array.

The first studies reporting an optimal spacing for heat transfer problems dates back to 1984 with the publications of Bar-Cohen & Rohsenow [113] as well as Bejan [114]. Both papers focus on the natural convection heat transfer from vertical parallel plates and present equations for the optimal spacing between the plates which maximizes heat dissipation from the vertical plate array for different boundary conditions (isothermal, isoflux, insulated walls, etc...).

These studies compare experimental and numerical results and present an attempt at analytically predicting this optimal spacing based on the Asymptotic Analysis described in Section 1.1. Other authors studied the optimal spacing for free convection heat transfer from vertical parallel plates such as Kim et

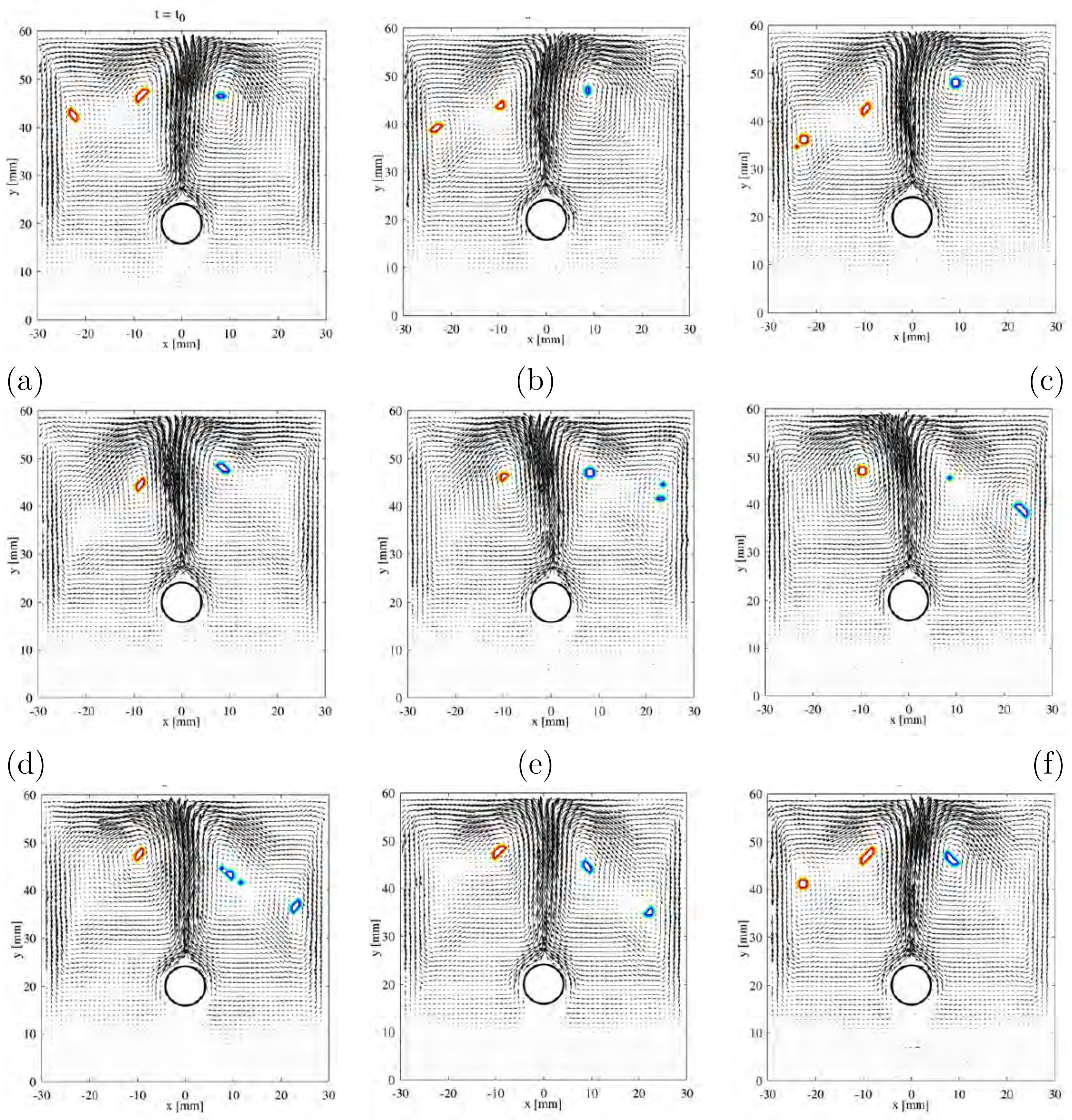

(a) (b) (c)

(d) (e) (f)

(g) (h) (i)

Figure 3.11: PIV measurements from Fiscaletti et al. [110]; instantaneous velocity field from an arbitrary time t_0 for a duration corresponding to one period of the plume oscillation T, $Ra = 1.03 \times 10^5$. (a) $t = t_0$, (b) $t = t_0 + T/8$, (c) $t = t_0 + T/4$, (d) $t = t_0 + 3T/8$, (e) $t = t_0 + T/2$, (f) $t = t_0 + 5T/8$, (g) $t = t_0 + 3T/4$, (h) $t = t_0 + 7T/8$ and (i) $t = t_0 + T$. The vortex cores are indicated in blue and red for clockwise and anti-clockwise rotation, respectively.

al. [115, 116].

The first studies on optimal spacing for packages that are cooled by forced convection appear in 1988 with the work of Nakayama et al. [117] who studied the forced convection heat transfer from arrays of finned geometries that is to say from parallel plates. They were quickly followed by Knight et al. [118] who published a paper in 1991, reporting optimal spacing results from an analytical study of forced convection from finned heat sinks, and an experimental verification published in 1992 [119]. Matsushima et al. [120] and Bejan et al. also report results for optimal spacing between parallel plates [23] and plate fins [121] in forced convection.

In the past twenty years, this field of study has been extended; different types of geometry are investigated, such as arrays of cylinders. Numerical and experimental studies on the forced convection heat transfer from an array of cylinder in cross-flow conducted by Stanescu et al. [13] report good agreements with asymptotic analysis in terms of optimal spacing as shown in Fig. 3.12. More complicated types of flows are also studied with the example of an optimization study in the case of mixed convection from parallel plates, published by Sun et al. in 2012 [122]. They report the existence of an optimal spacing in the case of mixed convection, in agreement with asymptotic analysis yet smaller than the solution for forced convection. They also report a noticeable increase in heat transfer from natural to mixed convection for a relatively small pressure drop addition at the outlet (for $\Delta p \approx 1\ Pa$ the heat flux is increased by a factor of three) at this particular optimal spacing.

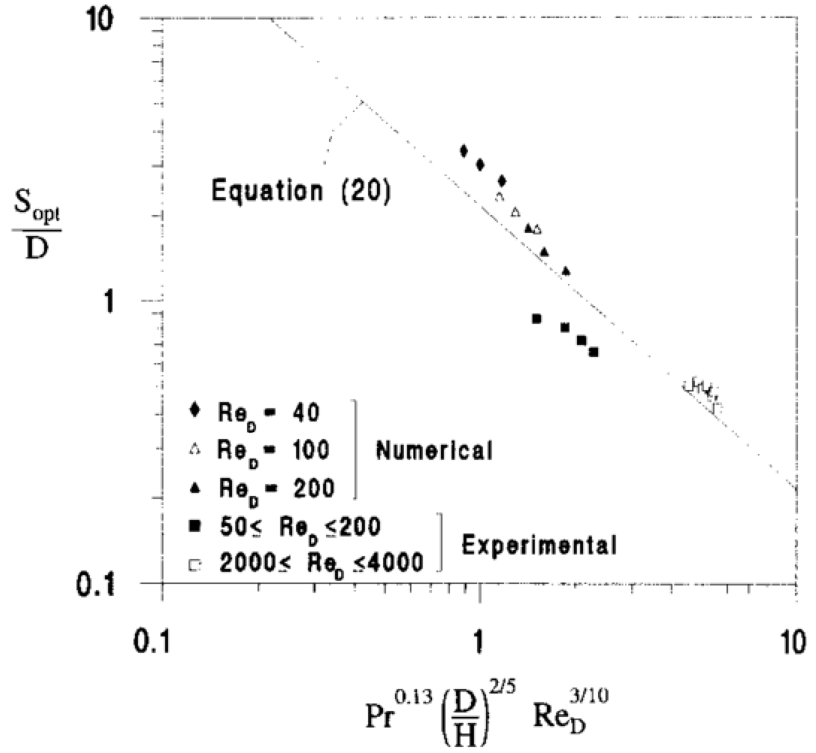

Figure 3.12: The optimal cylinder-to-cylinder spacing for maximum overall thermal conductance: experimental, numerical and scaling results. From Stanescu et al. [13]

3.3.2 A selective review on optimization methods

A review on some available optimization methods is presented in this section. Most of the optimization methods gathered here are taken from the very informative textbook of Nocedal and Wright [123].

3.3.2.1 Direct methods for linear, quadratic and linear-fractional programming

Direct methods aim at solving an optimization problem exactly, in a finite amount of steps.

Linear Programming (LP) is a class of direct optimization methods that achieve the best solution to a mathematical problem represented by a linear objective function and for which the space of all possible solutions, called the polytope, is defined by linear constraints on the problem's parameters. Such polytopes are represented in Fig. 3.13 and 3.14. The history of linear programming is extensively reviewed by Dantzig in [124]. The pioneers of LP are, according to Dantzig, Kantorovich and Koopmans for their work in the early 40's. They received the Nobel prize of economics in 1975 for their work on the subject [125]. After the Second World War, Dantzig developed by himself a general linear programming formulation and finally invented the Simplex algorithm, a general linear programming problems solver [123, 124]. Basically the Simplex algorithm starts with a random solution that can be represented by a matrix in which rows describe the objective function and the constraints. These solutions can also be illustrated by a random vertex on the polytope as shown in Fig. 3.13 and 3.14. Iteratively, pivot operations on the matrix that represents the problem are performed, which corresponds to moving the current solution to an adjacent vertex, until a better solution cannot be found anymore. At this point the optimal solution is known [123].

Later on, linear programming optimization was extended to quadratic problems and problems for which the objective function is a ratio of two polynomials, namely the linear-fractional programming. These types of problems can be solved using different methods, among which, some extensions of the simplex algorithm [123].

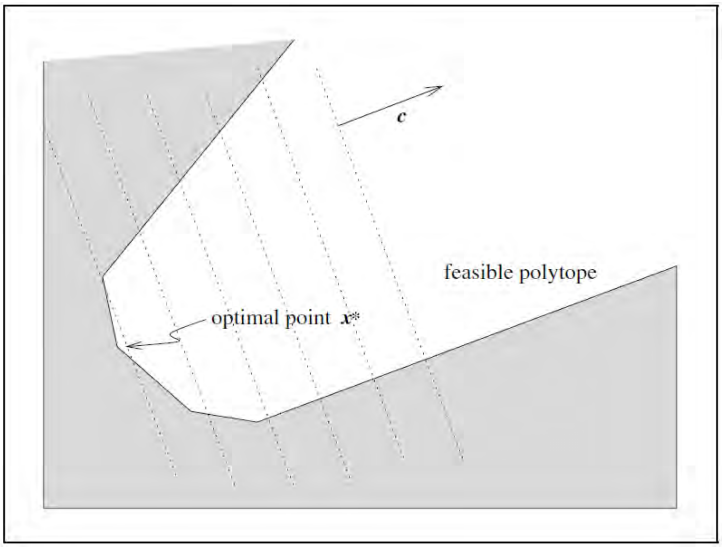

Figure 3.13: A two-dimensional linear program polytope (solutions space) with the optimal solution $x*$, the objective gradient c and iso-values of the solution represented by dotted lines [123]

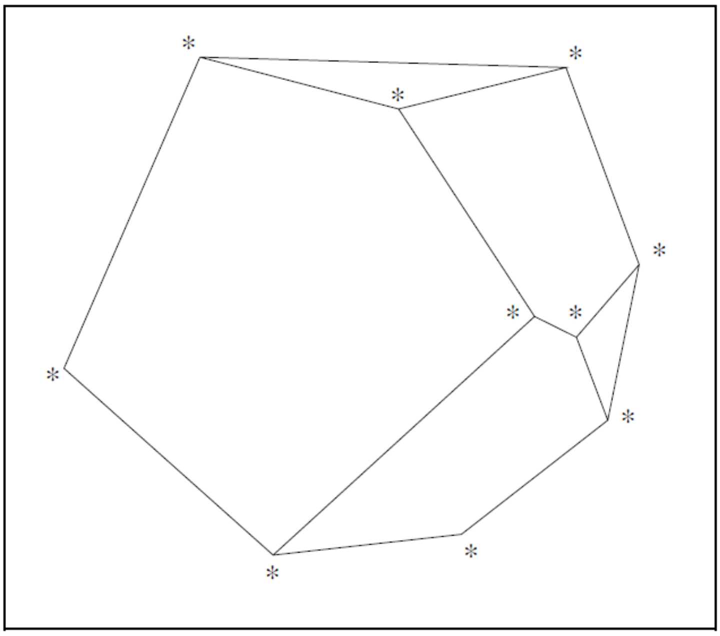

Figure 3.14: Representation of vertices of a three-dimensional polytope [123]

3.3.2.2 Iterative methods

For nonlinear equations (except the quadratic and linear-fractional problems), direct methods are not able to produce an optimal solution and for linear equations with a tremendous number of parameters the expensive computational cost makes the use of direct methods impossible.

Another type of methods are iterative search which are optimization techniques that travel iteratively inside the space of all possible solutions in order to minimize (or maximize) an objective function. There are two main types of traveling strategies [123]. Although they both use a quadratic model of the objective function to generate steps, they perform it in different ways as shown in Fig. 3.15:

• **Line search methods** generate a search direction, and then focus their efforts on finding a suitable step length α along this direction in order to minimize the objective function.

• **Trust region methods** define a region around the current iterate within which they trust the model to be an adequate representation of the objective function, and then choose the step to minimize the model in this region.

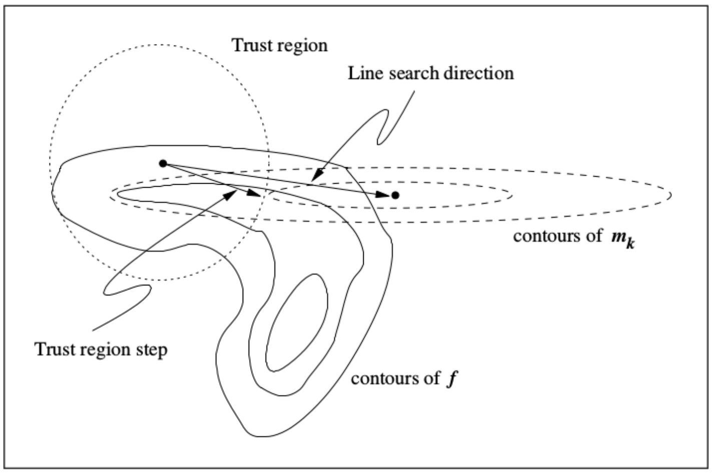

Figure 3.15: Trust region and line search methods. f is the true objective function, whereas m_k is the quadratic model of f at iteration k. Both trust region and line search methods use m_k to define their next step [123].

Several iterative methods that use either line search or trust region iterative strategies have been developed. Some of the most famous are recalled here.

a) Coordinate descent method

The coordinate descent method is a search line method that minimizes the multivariable objective function $F(x_1, x_2, ...x_n)$ by minimizing F along one direction at a time, that is to say, according to one variable x_i at a time as illustrated on Fig. .

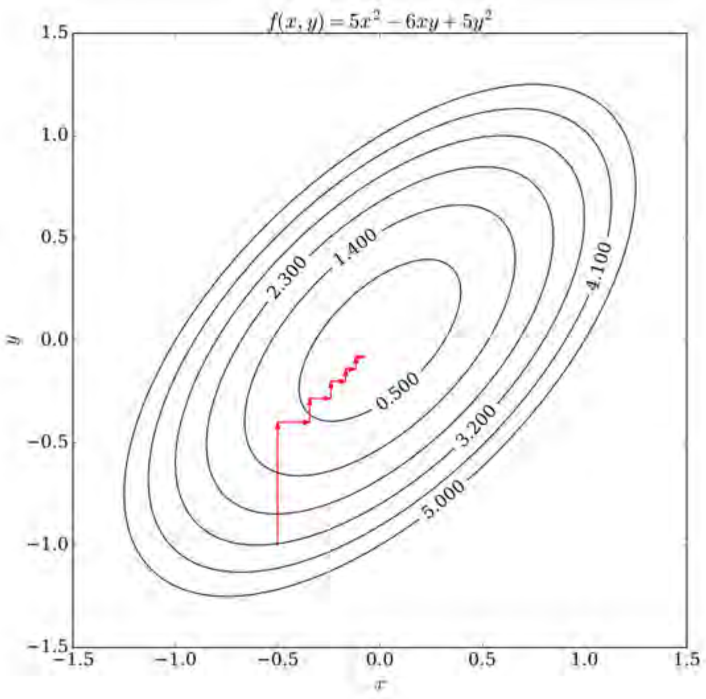

Figure 3.16: Successive steps of the coordinate descent method for minimizing a two-dimensional objective function

b) Newton and quasi-Newton's methods

The Newton's method is an example of trust region method that aims at finding the roots of the gradient of the objective function model m_k, which correspond to locations of extrema. This method uses finite differences to evaluate the objective function's Hessian $\nabla^2 f$ - supposedly trusted inside the trust region - at each step. This method is very efficient when computing the exact Hessians, that is to say for problems where the objective function is mathematically defined and twice differentiable [123].

In quasi-Newton methods the Hessian matrix does not need to be computed. The Hessian is updated by analyzing successive gradient vectors instead. The first quasi-Newton method was developed in the mid 1950s, when W.C. Davidon, a physicist working at Argonne National Laboratory, was using the coordinate descent method to perform a long optimization. As computers were not very stable at that time, the computer system would always crash before the calculation was finished and Davidon decided to find a way of accelerating the iteration [123].

c) Gradient descent method

Another well-known line search method is the gradient descent method where the direction of the iterative step is defined by the gradient of the objective function's model. Similarly to the Newton's method, the objective function, or its model, and its gradient, must be well defined as a function of the problem's parameters.

d) Limitations of the iterative methods

These methods require to define a model of the objective function with a certain level of trust and have trouble dealing with non-smooth objective functions. They are efficient to find a local optimum but fail to provide the global optimum of a problem that present several local optima [123].

One way to deal with this problem is to perform these local optimizations starting from several different initial solutions, increasing drastically the total computational time to find the global optimum. Moreover, the user must define a strategy to ensure that the different initial solutions are chosen so that the global optimum is likely to be found. A good knowledge of the problem that is being optimized is required.

3.3.2.3 Heuristic methods

Heuristic methods, often simply called "heuristics", are optimization methods that aim at finding satisfactory optimal solutions rather than exact optimal solutions. Some of them are briefly described in the next paragraphs.

a) Hill climbers with random restart

Hill climbing is a famous optimization method in which a multivariable objective function $F(\mathbf{x}) = F(x_1, x_2, ...x_n)$ is maximized (or minimized) by iteratively changing one variable x_i to x_i' and comparing the new solution $F(x_1, x_2, ...x_i', ...x_n)$ to the previous one $F(\mathbf{x})$ (they differ from gradient descent methods, which adjust all of the values in $\mathbf{x}$ at each iteration according to the gradient of the hill). If an improvement is found, the new solution is kept and the hill climber "moves" to that new vertex of the search space, progressively climbing the hill that represents the increase of the objective function. This is repeated until no change in the solution is found, which corresponds to the discovery of a local optimum. The change of variable can be determined using different strategies. The simplest strategies consist in choosing the nearest vertex or compare all the neighbours.

In an improved version of hill climbing, this hill ascension is inserted in a loop that performs the ascension for a number of different initial guesses, determined randomly. This enables to search for a global optimum rather than only refining a local area of the search space.

b) An evolutionary algorithm: the stochastic hill climber

A brief description of the basics of evolutionary computation is presented in Section 1.2.4. A particular example of such algorithms is the "stochastic hill climbing". Instead of comparing the solution at iteration k, $F_k(\mathbf{x})$, to the neighbours and moving to the better solution, a variable is randomly chosen and randomly modified and the new solution is evaluated and computed. This stochastic approach proved to be efficient for very wide search spaces for which a neighbour-to-neighbour ascension is too expensive in terms of computational cost.

c) Genetic algorithms

The history and principles of genetic algorithms are more extensively presented in Section 3.3.3.

3.3.3 History of Genetic Algorithms

This Section is dedicated to the study of genetic algorithms (GAs) and their potential for cooling devices improvement.

In 1950, Alan Turing, who is considered the father of computers by many, published "Computing Machinery and Intelligence" in which the learning process of a machine is investigated and eventually parallels the principles of evolution [126]. Turing states; "It is probably wise to include a random element in a learning machine. A random element is rather useful when we are searching for a solution of some problem." before reminding that "It should be noticed that it is used in the analogous process of evolution." [126]

The concept of evolutionary computation was born in the late 50's and early 60's. The subject was mostly investigated by biologists and geneticists such as N. A. Barricelli, A. Fraser and Burnell [127]. In the late 60's and early 70's, Ingo Rechenberg and Hans-Paul Schwefel were able to solve engineering problems using evolution strategies [128, 129] and artificial evolution became recognized as an optimization process. However, the process was more similar to hill-climbers than genetic algorithms. In this technique, a single parent candidate [1] was mutated to one offspring and the better between the two was kept as the parent for the future mutation. There was no population, nor cross-overs.

Since the early 70's, genetic algorithms as we use them nowadays and their power to generate robust solutions have been more deeply studied and described.

---

[1] The vocabulary used in this Chapter can be confusing as it originally comes from the genetic field but has spread to many different scientific areas. Multiple synonyms of "candidates" are used among the genetic computation community such as "individuals", "phenotypes", "chromosomes". They all represent the same object, which is a set of parameters (sometimes called genes) that define one of the possible solutions to the problem. The "parent" individuals are mated and mutated from one generation to the next, to create new "offspring" or "child" individuals.

Holland explicitly suggests crossovers and other recombination operators among a population of candidates [130].

From this point on, the principle of genetic algorithms that we use today was defined as described in Section 3.3.4.

Holland then identifies and defines the schema - a subset of candidates sharing some common attributes - as the unit of selection [130]. If we consider an optimization problem in the search space of all 8-bit strings, any 8-bit string can be represented by "$* * * * * * **$", where "$*$" can either be a "1" or a "0". A schema H is defined as a sub-ensemble of the ensemble containing all the 8-bit strings. For example; $H_1 =$"$11 * * * * * *$" or $H_2 =$"$*0 * 0 * 011$"; the schema H_1 (resp. H_2) represents all the 8-bit strings with a "1" at the first and second positions (resp. with a "0" at positions 2, 4 and 6 and a "1" at positions 7 and 8). The defining length $\delta(H)$ of a schema H is the distance between the fixed bits that are located the furthest apart. The order $o(H)$ of a schema H is the number of fixed bits. In our example, $\delta(H_1) = 1$, $o(H_1) = 2$, $\delta(H_2) = 6$ and $o(H_2) = 5$.

In 1975, Holland specifies a bound on the expected growth of these schemata in his famous paper, "Adaptation in natural and artificial systems"; the Holland's schema theorem, which is sometimes called the fundamental theorem of genetic algorithms [131]. This theorem says that short, low-order schemata (low-order subsets or families of candidates, later called Building Blocks) with above-average fitness increase exponentially with successive generations. This was expressed as an equation;

$$E(m(H, t + 1)) \geq \frac{m(H, t)f(H)}{a_t}(1 - p) \tag{3.28}$$

where E is the expected value, $m(H, t)$ is the number of candidates belonging to the schema H at generation t, $f(H)$ is the observed average fitness of schema H and a_t is the average fitness of the entire candidates pool at generation t. p is the probability of disruption of the schema h by crossover or mutation and can be expressed as;

$$p = \frac{\delta(H)}{l - 1}p_c + o(H)p_m \tag{3.29}$$

where $o(H)$ is the order of the schema H, $\delta(H)$ its defining length, l is the length of the code and p_m and p_c are the probability of mutation and crossover respectively.

This theorem describes GAs as powerful tools to look for solutions to complex optimization problems. An important notion first introduced by Holland [131] is the building block (BB), that is to say, a low-order sub-family (schema) of chromosomes (candidates) showing a high fitness compared to the average. According to Eq. 3.28, if a BB is randomly discovered as cross-overs and mutations happen, then the number of chromosomes that belong to this BB is going to increase. Since the growing number of chromosomes inside a BB already present a relatively high fitness compared to the average chromosome of the entire pool, cross-overs and mutations among the BB increase the chance to generate an even higher fitness individual. However, one has to understand that this theorem is limited in the sense that it is true for an infinitely large population.

The same year, De Jong publishes his PhD thesis [132] in which the potential of GAs is confirmed, by showing that they can perform well on a variety of test functions, including noisy, discontinuous, and multimodal search landscapes.

Since the late 70's, genetic algorithms have been applied to a wide range of subjects, from abstract mathematical problems to engineering practical issues [17]. And nowadays, with the increase of computational power, evolutionary algorithms have touched any field one can think of, from trading market, aerospace engineering, microchip design, biochemistry, assembly lines planning, etc.

With this growing interest for GAs, many researchers started investigating how to make the best use of these algorithms. As it has been shown, GAs rely on an initial population, probability to have mutations and cross-overs. These are key parameters that have an impact on the solution provided by the GA, and therefore, a GA user has to understand them in order for the algorithm to be tuned effectively.

That is the issue J. J. Grefenstette addressed in 1986 when he used genetic algorithms to find the optimal parameters of genetic algorithms for a particular test function [133]. He tried to find the optimal values of six parameters; population size n, crossover rate c, mutation rate m, renewal rate r, scaling window w and whether ellitism is considered or not s. Up to now, the "standard" genetic algorithm was based on De Jong's work who reported "rule of thumb" settings for GAs, that can be seen as settings that perform ok for a wide range of optimization problems and from where to start investigating the optimal GA settings [132]. These general settings presented the following parameters: GA_J(n,c,m,r,w,s) = $Ga(50, 0.6, 0.001, 1.0, noscaling, elitist)$. After Grefenstette, the best genetic algorithm with respect to his test function was $GA_G = GA(30, 0.95, 0.01, 1.0, 1, elitist)$.

Population sizing has been one of the important topics to consider in evolutionary computation [19], because according to many researchers, a "small" population size could guide the algorithm towards a poor solution [134,135], and a "large" population size could make the algorithm spend more computational time in finding a solution [136, 137]. A trade-off needs to be found by feeding the algorithm with "just enough" chromosomes (candidates) in order to find "good" solutions. This trade-off is perfectly illustrated on Fig. 3.17 (from [136])

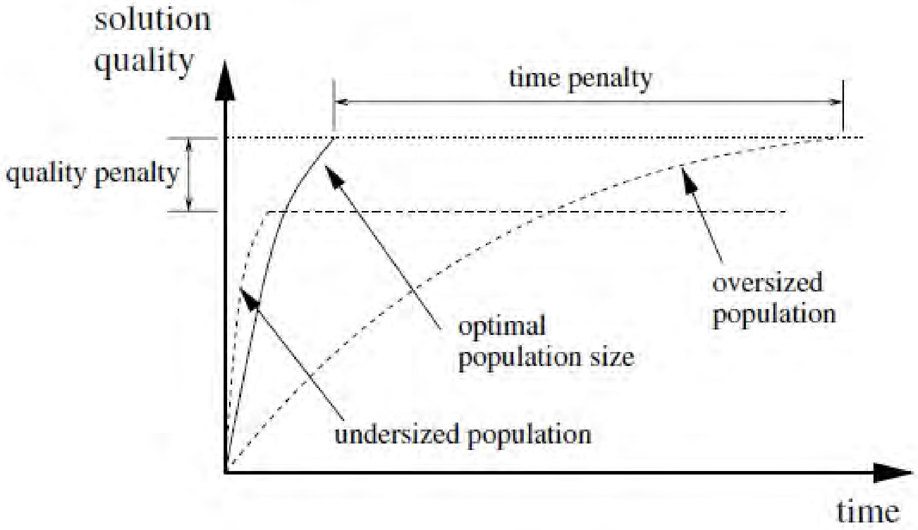

Figure 3.17: Population sizing in genetic algorithms [136]. Too small and the user pays a quality penalty. Too large and the user pays a time penalty.

This difficulty of choosing the right population size was analyzed theoretically in 1989 by Goldberg [18]. His analysis leads to the conclusion that the optimal population size increases exponentially with the problem complexity and is rather large even for moderate chromosome lengths. He put this pessimistic prediction into perspective by stating; "Too few empirical studies have been performed to know whether the theory provides quantitatively accurate predictions" [18].

Alander later ironically noticed in 1992 that "the most commonly used method (to find the optimal population size) according to GA literature has been to set population size equal to the usually well working value of 50" [19]. Or as Goldberg said "choose as large a population as you can" [18].

Later on, Goldberg et al. [21] studied this problem considering that building blocks (BBs) must be carefully supplied to GAs in order to obtain good results. Other studies [134, 138] agree that the optimal population size is in direct relation to the difficulty, or complexity of the problem. The more difficult, complex, a problem is, the bigger the initial population should be. Pelikan et al. [134] performed another study of population sizing using the Bayesian Optimization Algorithm (BOA). The principle is to randomly generate an initial population and a Bayesian network is fitted on the selected best individuals of this first generation. Iteratively, the population at generation $t+1$ is composed of the best candidates of generation t plus some new candidates, created according to the Bayesian network.

Another study by Harik and Lobo [139] concludes that the optimal population size is proportional to the number of building blocks in the problem. This also means that if not enough BBs are supplied in the initial population, the algorithm may not find a correct solution. They also addressed the problem of sizing the population using self-adaption. Two principal approaches can be used; (1) a pre-running self-adaption, in which case the population size remains the same in each generation [139], or (2) a progressive self-adaption where the population size can change from one generation to another [140].

Among all the studies that have been done about the effects of the GA parameters tuning on the algorithm's accuracy and effectiveness, the most common method (especially for population sizing) is recognized to be the empirical method [141]. The algorithm is tested with several different sets of parameters and the configuration that gives the most accurate and repetitive results is the one reported.

Genetic algorithms have been used for some time to deal with optimization problems involving computational fluid dynamics. In 2000, Poloni et al. utilized a combination of a genetic algorithm, a neural network and a gradient based optimization technique to optimize the design of a sailing yacht fin keel [142]. Genetic algorithms can be applied to the optimization of the design of a various type of systems, such as compressor rotor [143], or freight trucks [144] involved in aerodynamic optimization problems. More interestingly for the present research, GAs have been used for the optimization of heat transfer devices: the design optimization of heat exchangers of various sizes [145–147].

3.3.4 Fundamentals of genetic algorithms

If the solution of a complex problem implying objectives to be fulfilled while under constraints is searched, such a solution (or optimal candidate) is nothing more than a candidate whose characteristics best fit the problem. Then if a group of several candidates with good results is found, the solution (or the best fitted candidate to the problem) can be built from a combination of characteristics from the successful group.

This evolutionary computation technique can be split into four main stages as shown in Fig. 3.18. A general description of each stage is given below.

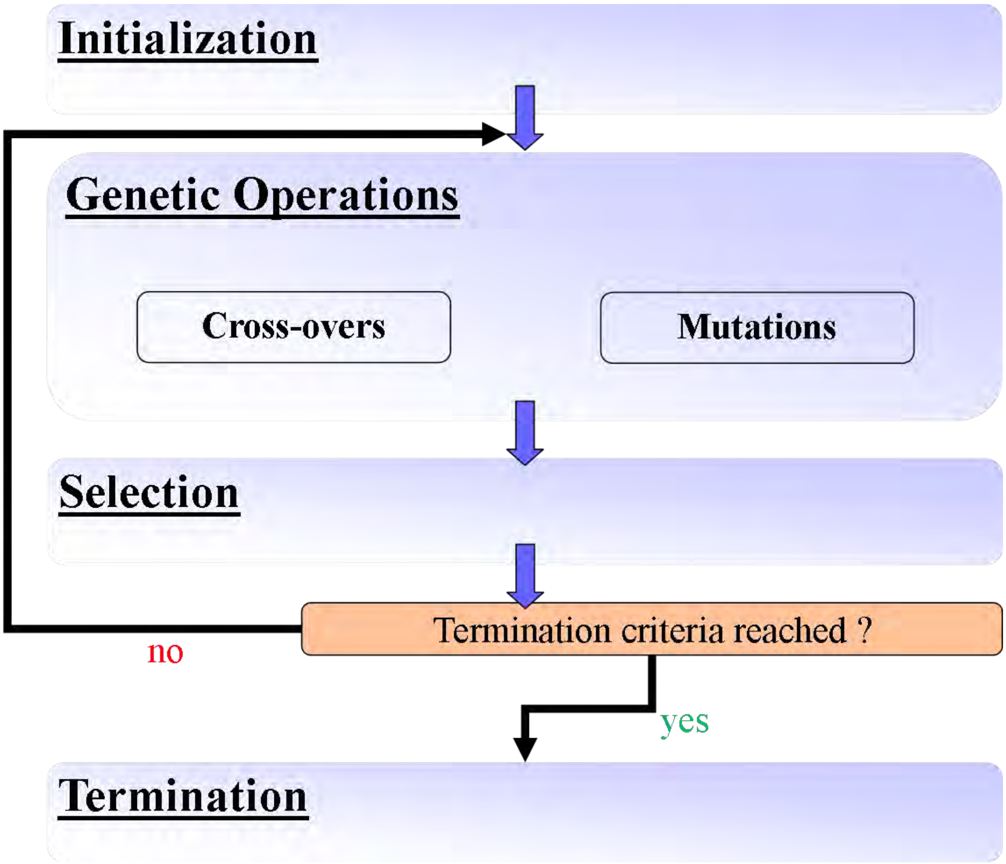

Figure 3.18: Genetic algorithms general chart.

3.3.4.1 Genetic algorithm 1^{st} stage: Initialization

To begin with, a set of candidates is chosen to be the first generation. When searching for a global extremum within an optimization problem, the first set of candidates has to cover the largest part of the solution space in order not to miss any local extremum which could be a global one. Many methods of first selection are available.

3.3.4.2 Genetic algorithm 2^{nd} stage: Genetic operations

The next stage is to breed a new generation of individuals. Diversity is the key to evolution so that the more diversified candidates there are, the more likely one is to find the fittest. At this point, there is a probability that candidates selected from the previous generation (or from the initial population) are:
(i) Cross-overed (or recombined): Two "parent" candidates are selected randomly among the breeding group in order to create two "child" or "offspring" candidates to be included in the next generation. The process is repeated with other random "parent" candidates.
(ii) Mutated: random "parent" individuals see one or several of their characteristics (also called genes) changed randomly.

These two genetic operators are repeated until the desired size is reached for the new generation population and ensure that new potentially better candidates appear among the diversity of the pool.

3.3.4.3 Genetic algorithm 3^{rd} stage: Selection

Then the candidates are compared using the so-called "fitness" function that assigns each candidate a weight (or rank), illustrating how well they fit the problem. The aim of this comparison is to find the best performers among the candidates' pool. A proportion of the whole population is then selected to breed the next generation, where fitter candidates are basically more likely to be selected. The fitness function is the core of the genetic algorithm. It dictates what makes a candidate "good" or "bad". For "simple" problems, the fitness function can be expressed as a "simple" mathematical equation, but for complex problems (non-linear, noisy, etc.), the expression of the fitness function is often impossible to determine and the weight of each individual has to be computed with the use of an estimation, a model, a simulation etc.

3.3.4.4 Genetic algorithm 4^{th} stage: Termination

This generational process is repeated until a termination condition has been reached. Common terminating conditions are:

- A solution is found that satisfies minimum criteria
- Fixed number of generations reached
- Allocated budget (computation time/money) reached
- The highest ranking solution's fitness is reaching or has reached a plateau such that successive iterations no longer produce better results

3.3.5 The strengths and weaknesses of genetic algorithms and implications for this thesis

In this section, a non-exhaustive list of the GAs pros and cons is presented. These characteristics aim at supporting the choice of genetic algorithm as the optimization method.

3.3.5.1 Strengths of the genetic algorithm

- The first and most important point is that genetic algorithms are parallel. Most other algorithms are serial and can only explore the search space of a problem in one direction at a time, and if the solution they discover is only a local optimum, there is nothing to do but abandon all work previously completed and start over. However, since GAs have a population of multiple candidates, they can explore the search space in multiple directions at once. If one path turns out to be a dead end, they can easily abandon it and keep on searching along more promising directions, giving them a greater chance, each run, of finding the optimal solution.

Moreover, the advantage of parallelism goes beyond this: the evaluation of the fitness of one candidate of the search space gives information about all the schemata containing this candidate. Let us consider the search landscape of all the 8-bit strings (used as an example in Section 3.3.3) that can be represented by "$* * * * * * **$", where "$*$" can either be a "1" or a "0". The string "00110101" is a member of this space. But it is also a member of the schema (or sub-space) "$0 * * * * * **$", the schema "$*011 * * * *$", the schema "$*0 * 1 * 10*$" and so on. By evaluating the fitness of this particular string, a genetic algorithm would be sampling each of these many schemata to which it belongs. Over many of such evaluations, it would build up an increasingly accurate value for the average fitness of each of these schemata, each of which having many members. Therefore, a GA that explicitly evaluates a small number of individuals is implicitly evaluating a much larger group of individuals. This is the "central advantage" of GAs over other optimization methods [15–18].

• Due to the parallelism that allows them to implicitly evaluate many schemata at once, genetic algorithms are particularly well-suited to solving problems where the space of all potential solutions is truly huge, that is to say, too large to search the whole search space in a reasonable amount of time. In a linear problem, the fitness of each component is independent, so any improvement to any one part will result in an improvement of the system as a whole. However, in real-world problems, nonlinearity is the norm, where changing one component may have unexpected effects on the entire system, and where multiple changes that are individually detrimental may lead to much greater improvements in fitness when combined. Non-linearity results in an exponential increase of the number of required evaluations: the space of 1,000-digit binary strings can be exhaustively searched by evaluating only 2,000 possibilities if the problem is linear, whereas if it is nonlinear, an exhaustive search would require evaluating 2^{1000} possibilities!

Fortunately, the implicit parallelism of a GA allows it to overcome this huge number of possibilities, successfully finding optimal or very good results in a short period of time after directly sampling only small regions of the vast search landscape [148]. For example, a genetic algorithm developed jointly by engineers from General Electric and Rensselaer Polytechnic Institute produced a high-performance jet engine turbine design that was three times better than a human-designed configuration and 50% better than a configuration designed by an expert system by successfully navigating a solution space containing more than 10387 possibilities. Conventional methods for designing such turbines are a central part of engineering projects that can take up to five years and cost over $2 billion; the genetic algorithm discovered this solution after two days on a typical engineering desktop workstation [15].

• "A classic problem for all systems that adapt and learn", states Holland in 1992 [15] is the known dilemma of *exploration vs. exploitation.* Once a solution above average is found, should the optimization methods focus on this local area and make the best use of it or search for others? Evolutionary algorithms have proven to be effective at escaping local optima and discovering the global optimum in problems for which the search landscape is complex, noisy and discontinuous [15, 19–21]. Cross-over is the key element for this. In other methods such as hill-climbers and gradient methods, each candidate is "on its own", exploring the search space in its immediate vicinity without reference to what other individuals may have discovered. However, cross-overing enables a transfer of information from one candidate to an other, notably a transfer of information between successful, above average, candidates. As a result, it could potentially produce an offspring that has the strengths of both parents and the weaknesses of neither [149, 150].

• Another advantage of parallelism is that genetic algorithms can efficiently manipulate many parameters simultaneously [148].

• Finally, GAs know nothing about the problems they are meant to solve and although it could be seen as a disadvantage, it is rather a strength: Instead of using previously known information to guide the optimization, they make random changes and use the candidates' fitness to determine which candidates should be kept. No need for the user to provide any information concerning the shape, or characteristics of the search space. It allows GAs to start an optimization objectively, with an "open mind". This potentially allows the discovery of solutions that were completely unexpected, that might even never have occured to human designer or user guided-optimization methods [17, 18, 149, 150].

3.3.5.2 Limitations of the genetic algorithm

• In Nature, the representation method of the candidates undergoing evolution is the genetic code. It is inherently robust and, with very few exceptions, any sequence of DNA is translated into a protein. Unlike in Nature, one of the main disadvantage of genetic algorithms is that the optimization problem has to be defined, represented by parameters. The difficulty is that any candidate is defined as a set of these parameters and the representation method must be able to tolerate random changes as the candidates will mutate and will be cross-overed during the procedure.

• One of the main problems is how to write the fitness function(s). These fitness functions must be defined so that higher fitness is reachable and actually does correspond to a better solution. This problem is even more important in the case of multiple objectives optimization. The fitness function used in Nature is rather straightforward: the organisms that manage to survive and reproduce are fit, those who fail are unfit.

- As it has been shown in Section 3.3.3, the GA tuning parameters such as initial population size, cross-overs and mutation rates, selection pressure, etc... have a drastic impact on how the GA performs and should be chosen with care. Living organisms do face similar difficulties, and evolution has dealt with them. It is true that if a population size falls too low, mutation rates are too high, or the selection pressure is too strong (such a situation might be caused by drastic environmental change), then the species may go extinct.

- One type of problems that genetic algorithms have difficulty dealing with are problems with "deceptive" fitness functions [16]. Deceptive fitness functions are functions where the locations of improved fitness give misleading information about the global optimum. For example, we can consider the space of 8-bit strings "$********$" and define the fitness function to be proportional to the number of 1's in the string (so that "00010001" is fitter than "00000001" for example) except for "11111111" and "00000000" that are defined to be the lowest and highest fitness respectively. It should be noticed that this kind of optimization problems are also difficult to solve for other optimization methods.

- Finally, one well-known problem that can occur with a GA is the premature convergence. If an individual that is more fit than most of its competitors emerges early in the process, it may reproduce so quickly and abundantly that it drives down the population's diversity too soon, which leads to an early convergence towards a local optimum [16, 148]. This phenomenon does occur in Nature and is known as a genetic drift.

Table 3.1 presents a selection of different studies that have been done utilizing genetic algorithm for various types of optimization problems and whether these studies investigate how GAs operate.

3.4 Summary of the chapter and implications for the goals of this thesis

First, a review of the work that has been done in the field of heat transfer, especially forced and natural convection from cylinders, has been presented in the first

Table 3.1: Optimization literature review: Presentation of different investigations dealing with optimization problems.

Paper	*Study using genetic algorithms*	*Mathematical test functions*	*Computational fluid dynamics*	*Heat transfer*	*Population size investigation*
Nakayama et al. (1988) [117]	–	–	–	✓	–
Bejan et al. (1992) [23]	–	–	–	✓	–
Dejong et al. (1975) [132]	✓	✓	–	–	–
Alander et al. (1992) [19]	✓	✓	–	–	✓
Weilin et al. (2006) [143]	✓	–	✓	–	–
Poloni et al. (2000) [142]	✓	–	✓	–	–
Hilbert et al. (2006) [145]	✓	–	✓	✓	–
Xie et al. (2008) [147]	✓	–	✓	✓	–
Goals of present study	✓	(compared with)	✓	✓	✓

sections of this chapter. Experimental, analytical and numerical approaches have been used to investigate the heat transfer from a point, a line and a cylindrical heat source and as it has been shown in this chapter, similarities appeared in the results from the different investigators. Indeed, the phenomenon of heat transfer can become fully unsteady for high Reynolds number flows in the case of forced convection and for high Rayleigh number flows in the case of natural convection. The heat transfer from finite surfaces such as a cylinder strongly depends on the location on the surface. And finally, the enhancement (positive or negative) of the heat transfer from a body when it is placed near another body is observed by many scientists.

Further in-depth studies of the heat transfer from complex geometries or arrays of cylinders certainly have to account for the local and unsteady aspects of the phenomenon. But there is no doubt in the potential of heat and mass transfer enhancement for confined geometries as it has been highlighted in the literature review.

Secondly, an overview of the development of genetic algorithms has been presented in Section 3.3.3, from the early basic idea to the formalization and study of the parameters that define them. The basic principles of GAs were presented and the main advantages and weaknesses GAs present have been listed in Sections 3.3.4 and 3.3.5 respectively. They show why genetic algorithms are strong candidates for optimizing heat transfer structures.

Indeed, the non-linearity of the Navier-Stokes equations, and more generally, of the phenomena involved in fluid mechanics and heat and mass transfer processes, are preventing researchers from using classical optimization methods when the problem cannot be linearized or at least simplified enough. Moreover, the optimization of the design of a complex geometry would suppose a large number of parameters - think of parametrizing a full coral - and therefore, the parallelism of genetic algorithms become, if not necessary, very convenient for the reasons listed in Section 3.3.5. Additionally, the research of an optimal design for complex geometries is not trivial and can even lead to unexpected results. The fact that GAs do not require any guidance is a strong advantage in the present case.

In terms of limitations, the problem of defining a good fitness function does not hold in the present case since only one objective is to be fulfilled: the maximization of the heat transfer. Premature convergence could be an issue and will have to be dealt with care undoubtedly. The main issue that every genetic algorithms user has to face is to determine the right GA parameters: the population size, the mutations and cross-overs probability, the selection pressure and so on... This last problem is definitely a key issue that has to be addressed.

As genetic algorithms present strong advantages regarding the type of optimization problem investigated in this thesis, a coupled study on heat transfer from confined geometries and the understanding of the use of genetic algorithms to search for optimal designs of heat transfer structures is undertaken. The objectives introduced in Section 1.3 can be more precisely stated:

- The first objective is to develop a numerical methodology to model convective heat transfer from complex geometries, which is (i) experimentally validated, (ii) capable of modeling transient phenomena, and (iii) computationally efficient enough to be used as fitness evaluation in a genetic algorithm procedure.

- The second objective is to derive and study a design optimization methodology based on genetic algorithms for maximizing the heat transfer from a confined geometry: a two-dimensional heat sink in a stream whose flow characteristics are inspired from deep sea coral environment.

The effects of the population size used during the genetic algorithm process must be investigated for this heat transfer optimization problem as it has never been done before, as illustrated in Table 3.1.

Chapter 4

Numerical methodology and implementation

This chapter aims at describing the methodology used to derive the numerical CFD model that is utilized to evaluate the heat transfer from complex geometries in convective heat transfer situations in the first instance, and secondly, the methodology used to develop an optimization procedure implementing the CFD model previously mentioned in order to optimize the geometry of a complex body for maximizing its overall heat transfer.

4.1 Overview of the modelling approach in this thesis

The objective of this work is to develop a complete numerical optimization procedure to determine the optimal design of heat transfer structures. Both CFD simulations dedicated to accurate heat transfer evaluations, and shape optimization for maximizing the overall heat transfer aspects must be performed with care as they are working together in order to fulfill the objective. The methodology of the complete modelling approach, as shown in Fig. 4.1, is decomposed into (i) the development and validation of the CFD model presented in Section 4.3 and (ii) the development and validation of the optimization procedure described in Section 6.

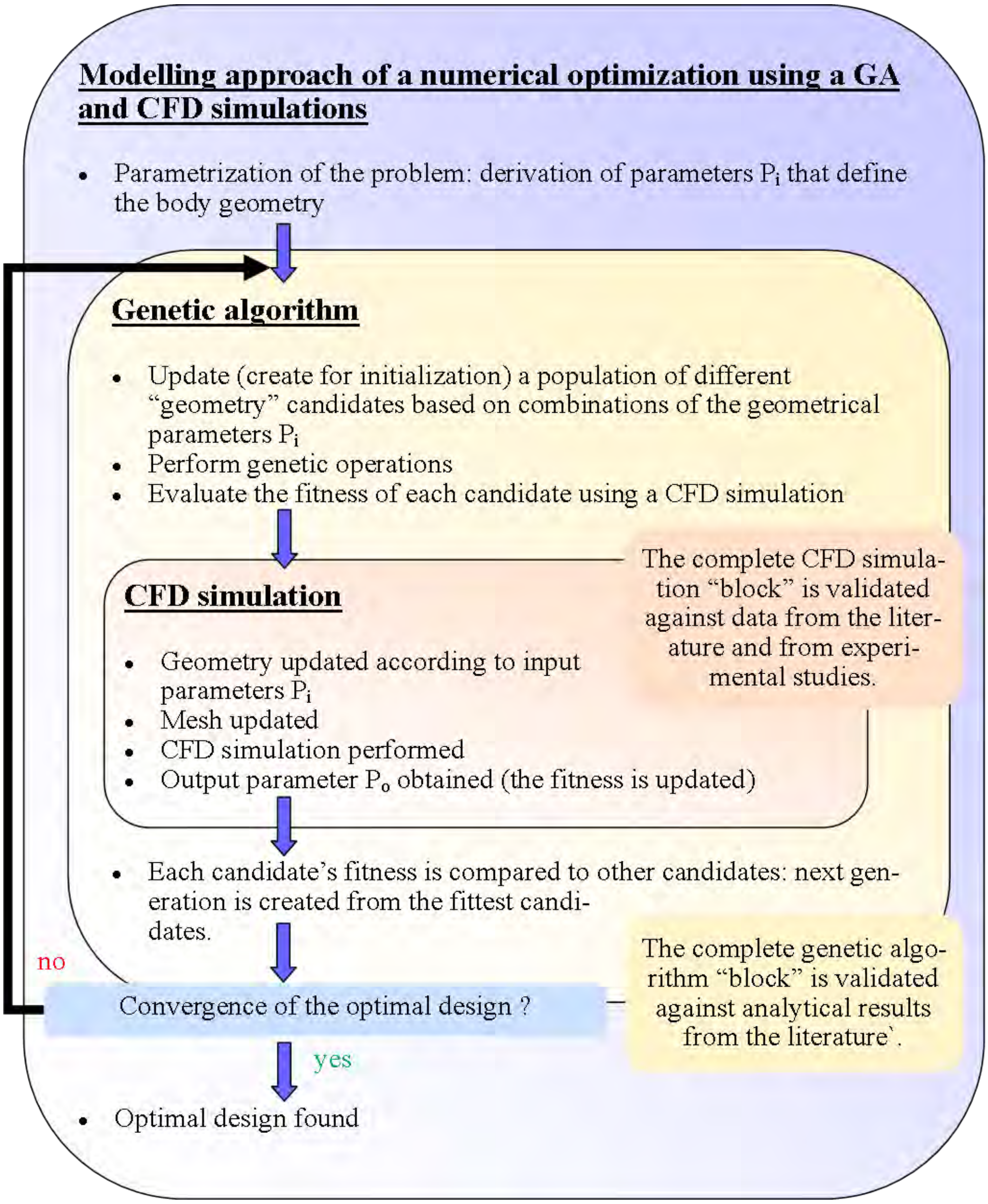

Figure 4.1: Overall modelling approach of the development of a numerical optimization procedure using a genetic algorithm and a CFD model.

4.2 Geometries under investigation

As already mentioned, the numerical optimization procedure aims at determining the optimal design of a complex body that maximizes the overall heat transfer. The results from the literature review that are described in Chapter 3, show that our understanding of heat transfer phenomena is mainly based on studies involving rather simple geometries like line heat sources, cylinders, flat plates, etc...

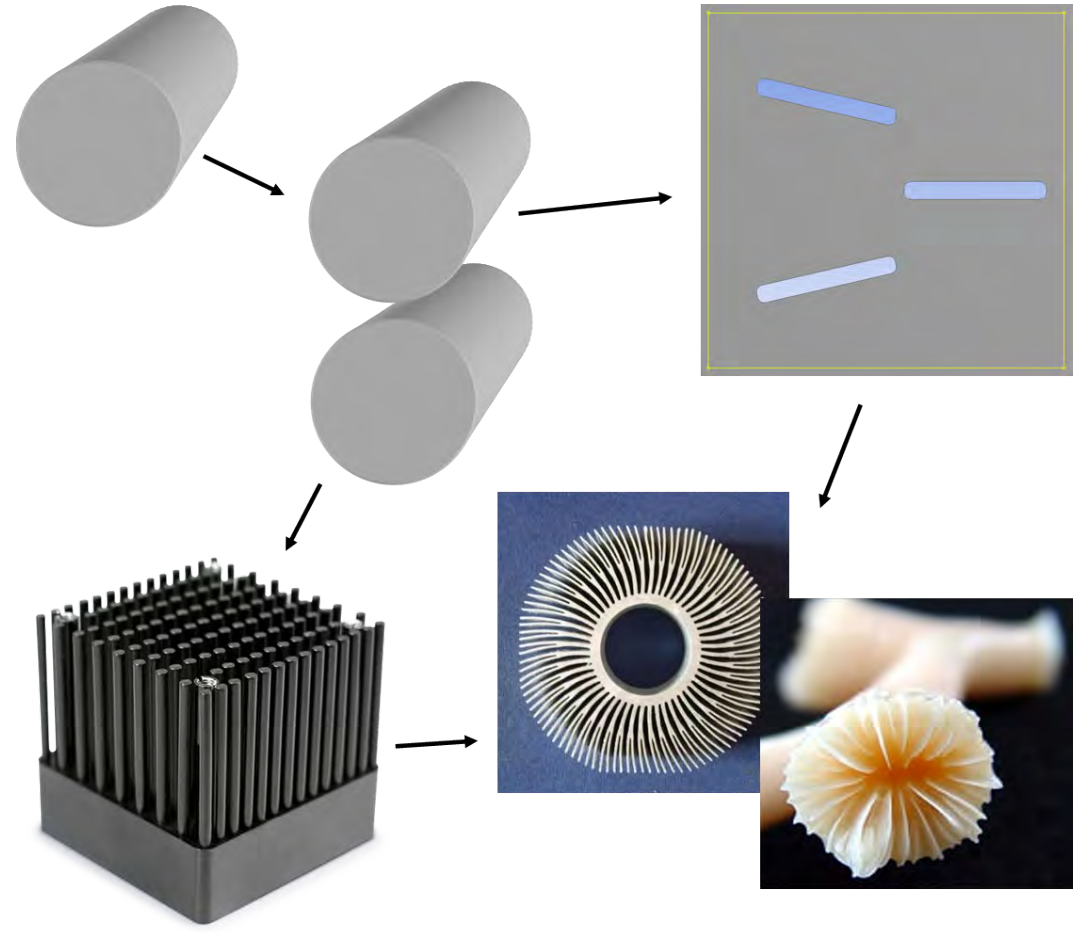

Figure 4.2: Increasing complexity of heat/mass transfer structures, references: [1]

More and more studies are dealing with situations where convective heat transfer from bodies of increasingly complex geometries occurs. In order to move towards the optimization of a design of high complexity, similar to what is found in

---

[1] `http://www.marinebio.net/marinescience/04benthon/index.htm`, `http://www.qats.com/eShop.aspx?q=Custom20Pin20Fin`

Nature and more specifically in this case: corals, one has to increase the problem's complexity progressively. One of the most important results the literature review highlighted, is the fact that the overall heat transfer from several simple bodies (like cylinders for example) could be enhanced when spaced from each others by a particular distance. The study of the interaction between two bodies is the first step towards the study of highly complex bodies as illustrated in Fig. 4.2.

In order to improve our understanding and modelling of heat transfer from complex structures and be capable of optimizing such structures, the studies of (i) the interactions between two two-dimensional heated cylinders and (ii) the interactions between two-dimensional heated elongated fins with rounded corners, have been undertaken and the methodology adopted for these two studies are presented in Sections 4.3 and 4.4. The validation and results of these studies are presented and discussed in Chapters 5 and 6.3.

4.3 Modelling steady and transient heat convection problems

In order to develop an accurate numerical model, one way is to verify it by comparison with experimental results. That is why the numerical methodology is described, in this section, through the case of the interaction between two vertically aligned horizontal cylinders. This particular configuration was investigated experimentally by Persoons et al. in 2011 [105] and experimental results are available for comparison and verification of the numerical model as presented in Section 5.2.

The numerical model has been developed using ANSYS Fluent 14.0 and aims at providing an estimation of the enhancement or diminishment of the natural convection heat transfer from a pair of horizontal cylinders. Both a (steady) Reynolds-Averaged Navier-Stokes (RANS) and Unsteady RANS (URANS) approach are used on a two-dimensional numerical domain.

The derivation of the RANS equations starts from the Reynolds decomposition which splits any quantity into a mean and a fluctuating part by using the so called Reynolds average:

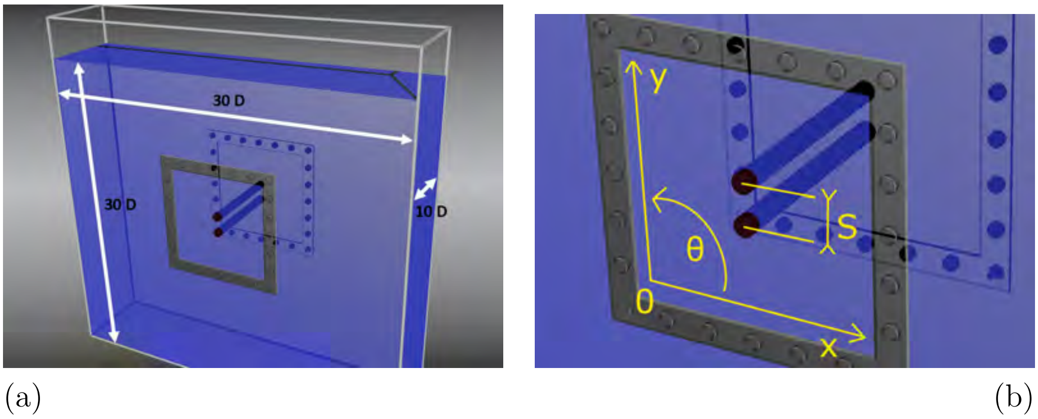

Figure 4.3: (a) Diagram of the natural convection test facility, and (b) close-up view of the cylinder pair, from Persoons et al. [105].

$$F = \overline{f} \tag{4.1}$$

$$f' = f - F \tag{4.2}$$

where $\overline{f}$ denotes the Reynolds average of any quantity $f(x, y, z, t)$, function of space and time. It is extremely important to recall that the Reynolds average is an ensemble average of as shown in Eq. 4.3;

$$\overline{f(x,y,z,t)} = \lim_{N\to\infty}\left(\frac{1}{N}\sum_{n=1}^{N} f_n(x,y,z,t)\right) \tag{4.3}$$

where n represents an event, or an experiment. The experiment is repeated a large number of times and an average over all the experiments is performed.
This ensemble average can be expressed differently (sometimes wrongly) depending on the characteristics of the flow;

Statistical stationarity: the quantity is statistically independent of time. In that case the ensemble average is equivalent to a temporal average;

$$\overline{f(x,y,z)} = \lim_{T\to\infty}\left(\frac{1}{T}\int_0^T f(x,y,z,t)dt\right) \tag{4.4}$$

Statistical homogeneity: the quantity is statistically independent of the location in one (or several) direction. In that case the ensemble average is equivalent to a spatial average;

$$\overline{f(y,z,t)} = \lim_{L\to\infty}\left(\frac{1}{L}\int_0^L f(x,y,z,t)dx\right) \tag{4.5}$$

Statistical periodicity: the quantity is statistically periodic (or pseudo-periodic) of period τ. In that case the ensemble average is equivalent to a phase average;

$$\overline{f(x,y,z,t)} = \lim_{N\to\infty}\left(\frac{1}{N+1}\int_{n=0}^{N} f(x,y,z,t+n\tau)\right) \tag{4.6}$$

Let us consider the Navier-Stokes equations for a Newtonian, incompressible fluid (Eq. 2.14 - 2.16). The introduction of the Reynolds decomposition leads to the Reynolds averaged Navier-Stokes equations shown in Eq. 4.7 - 4.9;

Continuity:

$$\frac{\partial U_i}{\partial x_i} = 0 \tag{4.7}$$

Momentum:

$$\frac{\partial U_i}{\partial t} + U_j\frac{\partial U_i}{\partial x_j} = -\frac{1}{\rho_0}\frac{\partial P}{\partial x_i} + g_i(1-\beta\Delta T) + \nu\frac{\partial^2 U_i}{\partial x_j^2} - \frac{\partial \overline{u_i'u_j'}}{\partial x_j} \tag{4.8}$$

Temperature:

$$\frac{\partial \bar{T}}{\partial t} + U_i\frac{\partial \bar{T}}{\partial x_i} = \alpha\frac{\partial^2 \bar{T}}{\partial x_i^2} + \frac{2\mu}{\rho c_p}\overline{S_{ij}S_{ij}} - \frac{\partial \overline{u_i'T'}}{\partial x_i} \tag{4.9}$$

where c_p is the specific heat per unit mass, β is the thermal expansion coefficient, g_i is the gravitational acceleration vector and $\overline{u_i'u_j'}$ is called the Reynolds stress tensor. There are 5 equations for 14 unknowns: P, U, V, W, $\bar{T}$, $\overline{u'^2}$,$\overline{v'^2}$, $\overline{w'^2}$, $\overline{u'v'}$, $\overline{u'w'}$, $\overline{v'w'}$, $\overline{u'T'}$, $\overline{v'T'}$ and $\overline{w'T'}$. Now it is necessary to close the system in order to solve it.

The first approach would be to derive transport equations for the Reynolds stress tensor $\overline{u_i'u_j'}$ to have enough equations to close the system. However this process leads to the creation of higher moments term as $\overline{u_i'u_j'u_k'}$ and the system remains open. At some point, one has to model the highest moments in the system, using lower moments.

The eddy-viscosity modeling consists in modeling the second moments $\overline{u_i'u_j'}$ and $\overline{u_i'T'}$ using first moments; this is a first order model. The simplest form for eddy-viscosity models are based on the Boussinesq relation;

$$-\rho\overline{u_i'u_j'} = -\frac{2}{3}\delta_{ij} + 2\mu_t S_{ij} \tag{4.10}$$

where μ_t is the so called eddy viscosity.

It is important to notice that the time derivative $\frac{\partial U_i}{\partial t}$ is kept in the RANS equations. However in practice, this term often disappears. Indeed, the Reynolds average is implemented in most CFD codes as a time average, under the assumption of statistical stationary, which leads to solutions independent in time. This is the case in Fluent. For periodic and pseudo-periodic phenomena, the flow is statistically stationary but not steady. Nevertheless, this problem can be coped with by considering that the phenomenon is truly periodic and the periodic (or pseudo-periodic) and turbulent parts respectively characterized by a time-scale t_p and t_t are separated by a time averaging (as Eq. 4.6) over a time t_u so that $t_t \ll t_u \ll t_p$. This is called Unsteady-RANS or URANS. The decomposition gives $u = \tilde{u} + u''$ where $\tilde{u} = \frac{1}{t_u}\int_{-t_u/2}^{t_u/2} u(x,y,z,t+\tau)d\tau$. Figure 4.4 illustrates the difference between RANS and URANS;

The two-dimensional (2D) approach was used in order to save computational time; a single simulation with the 2D mesh, desired time-step and duration takes about 10 hours on a quad-core desktop workstation. Moreover, the experimental facility [105] used for the validation of the numerical model has been designed to approximate infinite cylinders placed in an infinite medium, which mathematically corresponds to a two-dimensional problem. It will be shown later in Fig. 5.23, in the last section of this paper, that a good agreement is found between the present numerical unsteady results for the velocity flow field and 2D PIV measurements carried out in the mid-plane of the test facility by Persoons et al. [105].

The analysis is based on a second order finite volume spatial discretization method for the momentum equation, the PISO velocity-pressure coupling technique (derived from the SIMPLE algorithm [151, 152]) and second order implicit time discretization.

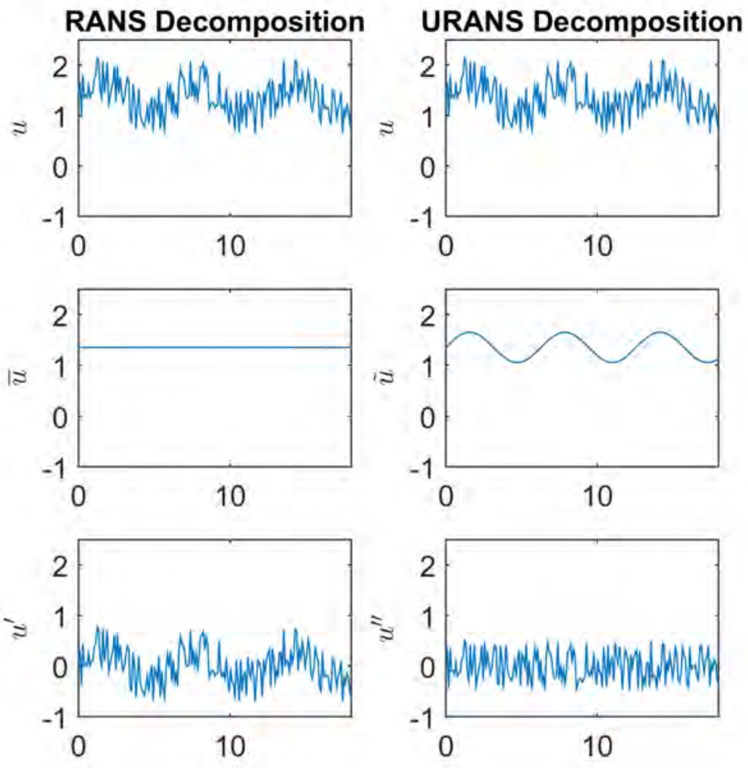

Figure 4.4: The RANS and URANS decompositions

The PISO method, developed by Issa [152], is based on the splitting of operations in the solution of the discretized momentum and pressure equation. At each time step, the fields obtained are close approximations of the exact solution, after convergence inside the operation-splittings loop. Figure 4.5 shows a schematic of the PISO algorithm. As can be seen in Figure 4.5, each time step can be decomposed in three main phases:

In order to compute the velocity field at the time step t^{n+1}, the momentum equation (Eq. 2.10) is first solved using the pressure field at the previous time step $p^n = p(t^n)$, hence called "Momentum Predictor". One can note that since the previous time-step's pressure gradients ∇p^n are used, the prediction of the new velocity field $\tilde{u}^{n+1} = \tilde{u}(t^{n+1})$ is quite rough and this estimation has to be refined (the tilde stands for estimation).

The second phase, called "Pressure Solution", consists in solving the pressure equation using the previously estimated velocity field $\tilde{u}^{n+1}$ in order to compute the pressure correction $p^{n+1,*}$ (where * stands for correction). One can derive the Poisson Equation for the pressure correction by computing the divergence of the momentum equation for the incompressible case (or compressible but at low Mach number), or from the continuity equation by linking the pressure to the density with the state equation for compressible high speed flows (see [153]).

Finally, the velocity field can be updated by computing $u^{n+1,*}$ (through the momentum equation) using the new estimation of the pressure field $p^{n+1,*}$ and the resulting pressure gradients. This is the "Explicit velocity correction".
The two last procedures are repeated until the velocity field satisfies both the continuity and momentum equations.

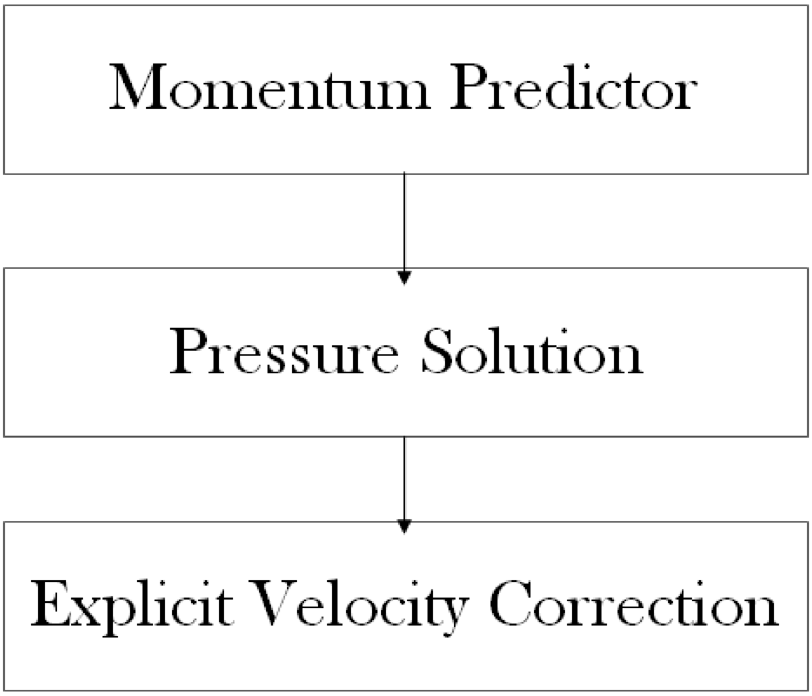

Figure 4.5: Flowchart of the PISO algorithm

The eddy viscosity is obtained using the Shear Stress Transport (SST) $k-\omega$ model with a low-Reynolds model approach to avoid the use of wall functions [151, 154]. This model behaves like a classical $k-\omega$ model in the inner parts of the boundary layer, down to the wall through the viscous sub-layer, and it switches to a $k-\epsilon$ model behaviour in the free-stream regions. This particular two-equations turbulence model has been chosen because of its accuracy both near the wall as well as far from walls. Indeed, many wall treatments expressed as blending function, have been proposed and the one from Menter takes advantage of the fact that the solution to the specific dissipation rate ω equation is known for both viscous and log layer unlike the dissipation rate ϵ used in $k-\epsilon$ models, as shown in Eq. 4.11 and 4.12 [154].

$$\omega_{viscous} = \frac{6\nu}{\beta y^2} \tag{4.11}$$

$$\omega_{log} = \frac{u_\tau}{C_\mu^{1/4}\kappa y} \tag{4.12}$$

where y is the cell centroid distance from the wall. A blending can then be used as follows;

$$\omega = \sqrt{\omega_{viscous}^2 + \omega_{log}^2} \tag{4.13}$$

Low values of y, meaning that the considered cell is close to the wall, implies the dominance of the term in $1/y^2$ and thus, viscous value for ω while the term $1/y$ is dominant (compared to $1/y^2$) for large values of y and the log behaviour of ω is recovered far from the wall. Blending for the friction velocity is also proposed by Menter [154].

However the $k-\omega$ model presents a well known issue; a high sensitivity to the inlet free-stream turbulence properties [151, 155]. In order to cope with this problem, the model switches to the more robust $k-\epsilon$ behaviour in these regions as shown in Eq. 4.14;

$$\nu_t = \frac{\rho a_1 k}{max\left\{a_1\omega, \Omega F_2\right\}} \tag{4.14}$$

where a_1 is a constant, Ω is the vorticity magnitude and F_2 is defined as;

$$F_2 = tanh\left[\left(max\left\{\frac{2\sqrt{k}}{\beta^*\omega y}, \frac{500\nu}{y^2\omega}\right\}\right)^2\right] \tag{4.15}$$

It can be seen that when $a1\omega SF_2$ the turbulent viscosity is $\nu_t = k/\omega$ which is precisely the turbulent kinematic viscosity of a standard $k-\omega$ model. It is allowed to switch to $\nu_t = a_1 k/(SF_2)$ when the standard $k-\omega$ model is unstable.

Under-relaxation factors α are implemented in Fluent in order to damp numerical oscillations. As shown in Eq. 4.16, the smaller the under-relaxation factor, the stronger the damping.

$$\phi_{new} = \phi_{old} + \alpha(\phi_{calculated} - \phi_{old}) \tag{4.16}$$

where ϕ is any variable submitted to under-relaxation.

However, although the damping prevents numerical oscillations, it can also prevent the solver to catch physical, real small oscillations. This is why the under-relaxation factors have been increased from 0.3 to 0.8 for the pressure and from 0.7 to 1 (i.e., no relaxation) for the momentum equation, which increases the sensitivity of the solver to physical oscillations, in an effort to better capture the experimentally observed variations in velocity and temperature. Since a low-Reynolds model is used, a two-dimensional mesh with 8,600 grid cells is designed to ensure the size of the first cells at the cylinder wall does not exceed $y^+ = 1$.

The inner part of the mesh around the cylinders is discretized using quadrilateral cells while the outer part of the numerical domain is discretized with triangular cells as shown in Fig. 4.7. The most common issues associated with the shape of the cells are (i) the error in the computation of the diffusion term caused by the non-orthogonality, or skewness, of the cells and (ii) the error term due to the central-differences; indeed, central-differences are used to estimate the flux term through the face (a line in 2D) connecting two adjacent cells but if the cells are too skewed or have a high aspect ratio, the mid-point between their centroid (where the central-difference is calculated) does not coincide with the centre of the face connecting the cells. It is worth noting that these errors are not only encountered in triangular shaped cells, but also for quadrilateral cells (in 2D). The perfect shape for an orthogonal (i.e., zero skewness) grid would be equilateral triangles and rectangles for the triangular mesh and the quadrilateral mesh respectively. The skewness and aspect ratio of the cells (triangles as well as quadrilaterals) are minimized in order to avoid any non-orthogonality related issues;

- The orthogonality of the triangular cells (as well as for the quadrilateral cells) has been maximized with a minimum of 0.72 and an average of 0.97.
- The aspect ratio has been minimized with a maximum of 2.4 and an average of 1.29.

- A cross-diffusion term is used to compensate error (i) in Fluent [151]

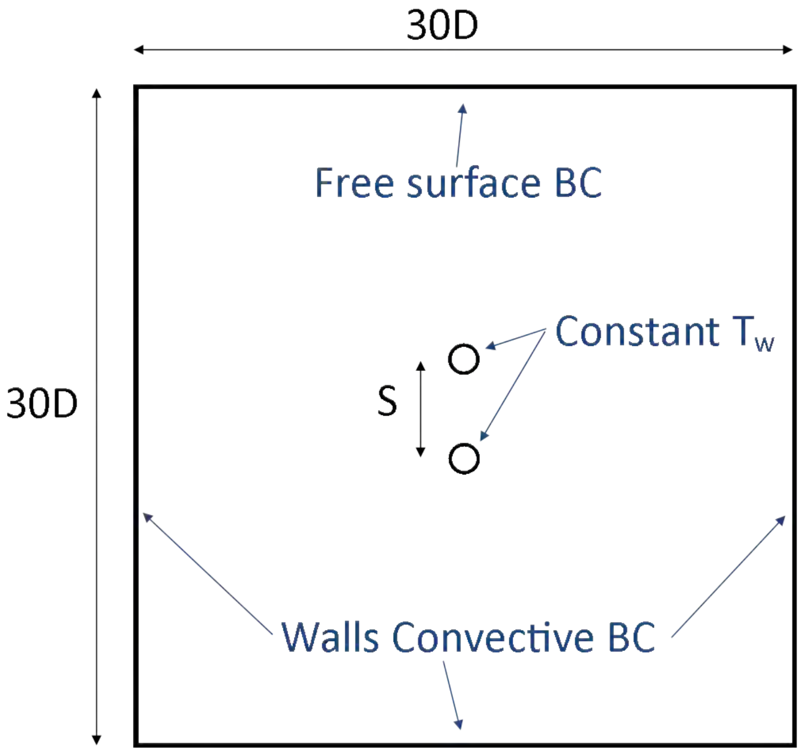

Figure 4.6: Two cylinders numerical domain and boundary conditions

The fluid density is described by the Boussinesq approximation (2.21) which is used in the computation of the buoyancy force term ρg in the momentum equation [151].

The thermal boundary conditions on the bottom and side walls of the tank are defined as convective boundary conditions, representing the small amount of heat loss through the walls of the tank in the experimental test facility [105]. An overall heat transfer coefficient U is computed as;

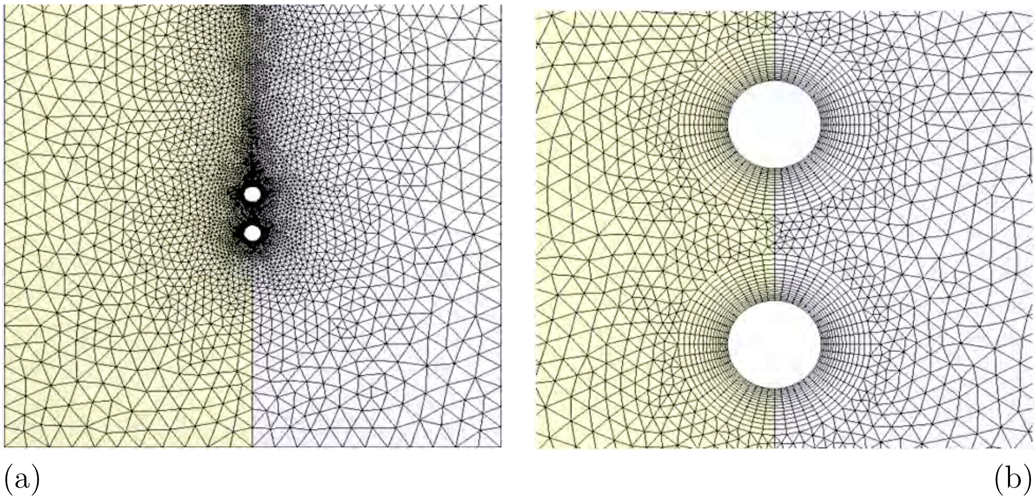

Figure 4.7: (a) Overview of the entire two-dimensional numerical domain meshed, and (b) close-up view of the pair of cylinders showing the transition from structured mesh around the cylinders to unstructured mesh in the surrounding region.

$$\frac{1}{U} = \frac{1}{h_{water}} + \frac{t_{wall}}{\kappa_{wall}} + \frac{1}{h_{air}} \tag{4.17}$$

where t_{wall} and κ_{wall} are the thickness and thermal conductivity of the tank walls, respectively. h_{water} and h_{air} are the estimated average heat transfer coefficients on the inside (water) and outside (air) of the tank, estimated using established empirical correlations [156]. The top side of the numerical domain is defined as free slip surface to represent the free water surface in the experimental test facility [105].

The mesh size and the time step refinement have been studied for a single cylinder, to ensure that the solution is independent of both mesh size and time step, as shown in Fig. 4.8. The characteristic mesh size is represented by Δr in Fig. 4.8 b, which corresponds to the radial thickness of the first layer of structured cells adjacent to the cylinder surface (see Fig. 4.7 b). For the URANS simulations, a time-step of $\Delta t = 50\ ms$ has been used. A grid size of $\Delta r = 0.5\ mm$ was taken for both steady and URANS simulations. Numerical time-averaged Nusselt number results (presented in Section 5.2.1) are evaluated from steady RANS simulation, whereas time-resolved data (presented in Section 5.3.2) are obtained from URANS simulations. The consistency of the RANS results with the average over time of the URANS results has been verified for the single cylinder case.

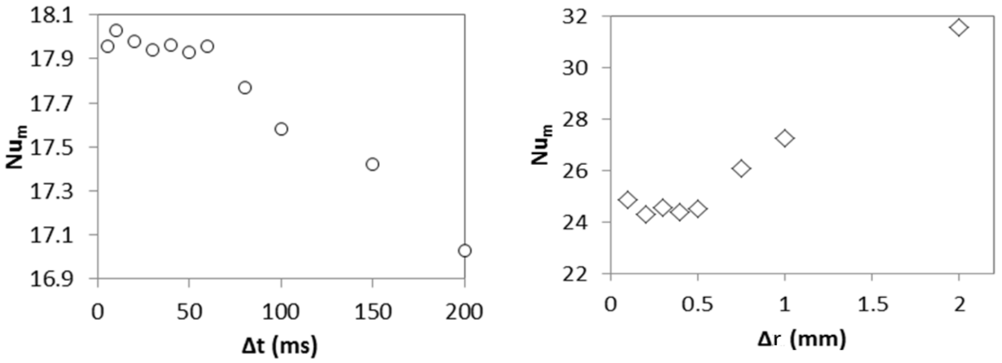

(a) (b)

Figure 4.8: Sensitivity study of the solution to (a) the time step and (b) mesh spacing, for a single cylinder at $Ra = 1.70 \times 10^6$.

The best suited turbulence model is found to be the Shear Stress Transport (SST) $k - \omega$ model, as presented at the beginning of this section. This particular model was chosen because it is recommended by several authors for this type of simulation [151,155].

4.4 Implementation of shape optimization using genetic algorithms

In this section, the implementation of a shape optimization procedure involving a genetic algorithm as illustrated in Fig. 4.1, is detailed. Moreover, the particularities of the genetic algorithm used in the present work are highlighted, namely, the MOGA algorithm (for Multi-Objectives Genetic Algorithm) implemented in ANSYS Workbench. The ANSYS MOGA is a hybrid variant of the NSGA-II [157], an improved version of the Non-dominated Sorting Genetic Algorithm (NSGA) initially proposed by Srinivas and Deb [158].

4.4.1 Shape optimization approach with genetic algorithms and CFD simulations

In this section, the general approach of a shape optimization of structures submitted to convective heat transfer utilizing a genetic algorithm is presented.

a) Definition of a fitness function

As genetic algorithms operate by means of evaluating fitness function, the definition of such fitness function is of primary importance. In the present case, the overall heat transfer rate from a body placed in a fluid is to be maximized: $max(q')$. Therefore, the fitness function has to account for this objective. Because only one objective is considered, the fitness of one design candidate is set to be its overall time-averaged heat transfer rate to the surrounding fluid; that is to say $f(c_i) = q'(p_1, p_2, ...p_n)$ where f is the fitness value and c_i is a candidate geometry defined by the parameters $p_1, p_2, ...p_n$. Therefore, the candidates presenting the higher fitness values fulfill the objective $max[q'(p_1, p_2, ...p_n)]$. This fitness value is obtained from a CFD simulation whose model has been described in Section 4.3.

b) Parametrization of the problem

Many different shapes' fitness must be evaluated throughout the GA process, and these different geometries are to be mutated and cross-overed in order for the concept of "survival of the fittest" to apply. Therefore, each design must be encoded, or represented, to allow these mutations and cross-overs: the parametrization. The problem must be parametrized, similarly to any organism's characteristics which are encoded in its DNA. In the present case, the geometry of the convective heat transfer structure must be defined by a finite amount of parameters, like lengths, angles, curves, etc. For example, in the case of two vertically aligned horizontal cylinders, any given configuration is defined by knowing the cylinders diameter D (forced to be the same) and the centre-to-centre distance S. Each design candidate is then represented by a unique concatenation of values of these parameters. In our example, this concatenation gives the vector, or chromosome, $[D, S]$ and $[0.1, 0.3]$ is the unique geometrical configuration consisting of two cylinders of diameter 10cm spaced by 30cm, centre-to-centre. The genetic operations that apply on these representations are extensively described in Section 4.4.2.

c) Search space dimension and constraints

At this point, the fitness function is defined and the shape of the structure is represented by a finite number n of independent parameters, that is to say, is represented by a chromosome of finite length. The space of all possible solutions, that is to say, all possible geometrical configurations defined by a combination of the n parameters, is a space of dimension n, a n-D search space. In order for the optimization procedure to come up with a solution in a finite amount of time, boundaries on the search space must be set. Closing the search space corresponds to forcing constraints on the parameters that define the candidate. In the present case of shape optimization, this corresponds to geometrical constraints on the heat transfer structure (minimum/maximum size, located inside a fixed area, etc...). These constraints are specific to the problem and will be detailed when needed.

4.4.2 The genetic algorithm workflow in ANSYS MOGA

In this section, the functional principles of GAs are presented and detailed for the MOGA method.

As already presented, in Section 3.3.4, the algorithm can be decomposed into four main stages that are shwon in Fig. 3.18 and precised in Fig. 4.9;

4.4.2.1 Genetic algorithm: Step 1. Initialization

A method for generating the individuals of the initial population is used. It has been recognized that the initial population has to show diversity. For a very large number of initial candidates, a random distribution over the search space is the best option to increase diversity. However, in order to ensure a diverse repartition of the first generation individuals, even for small population size, GAs may use more sophisticated algorithms to initialize the population. ANSYS MOGA initialization procedure is based on the Shifted Hammersley Sampling method. It is a quasi-random number generator which has very low discrepancy that is also used for quasi-Monte Carlo simulations. A low-discrepancy sequence is defined as a sequence of points that approximates the equidistribution in a multi-dimensional cube in an optimal way. In other words, the design space is populated almost

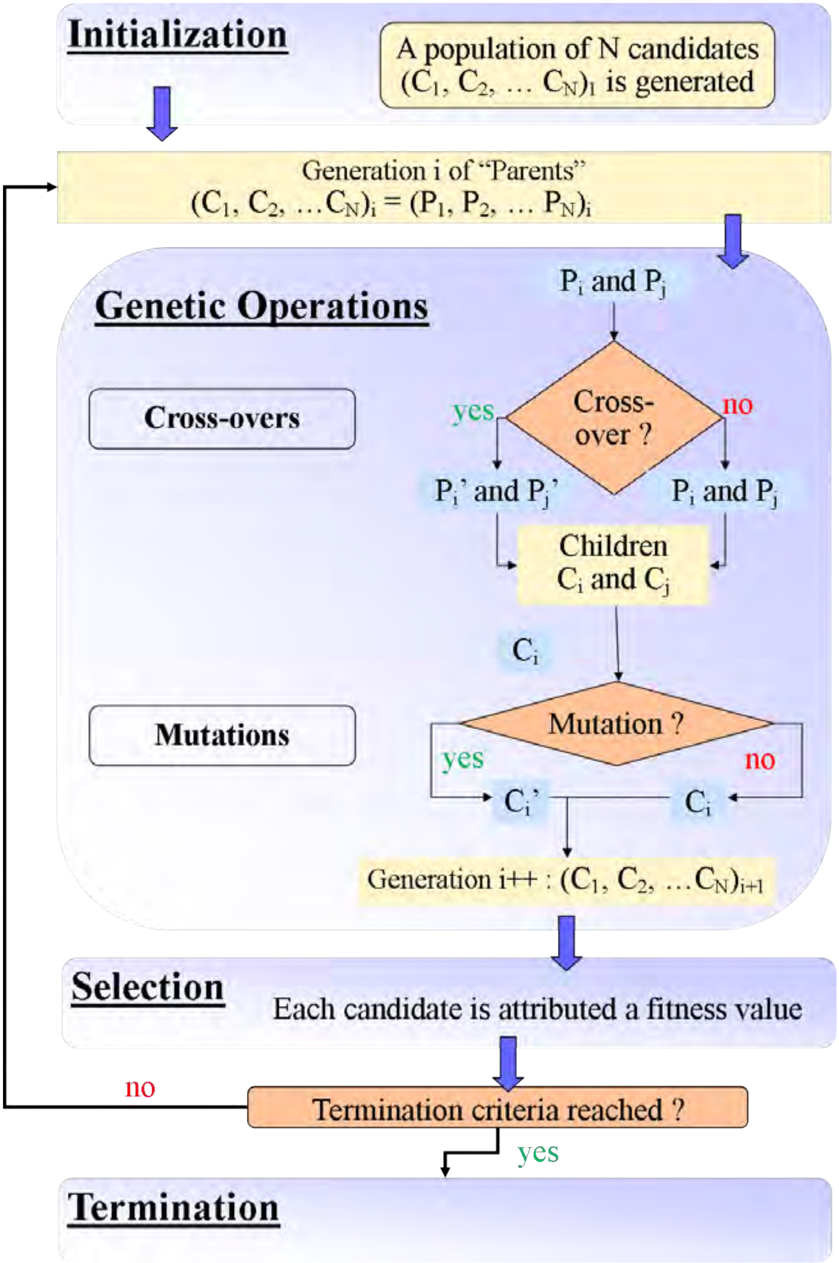

Figure 4.9: A general description of the main stages of a genetic algorithm.

uniformly by these sequences and, due to the inherent properties of Monte Carlo sampling, dimensionality is not a problem (i.e., the number of points does not increase exponentially with an increase in the number of input parameters) [151].

It should be noted that unlike the classical GA, the MOGA proposes two independent controls for (i) the initial population size and (ii) the size of the population that is selected to form the next generation, presently called the "evolving population" [151]. These two controls have been kept equal in all the optimizations performed in this work in order to avoid misleading interpretations of the results that could be due to an evolving population too small even though the initial population was large enough. Further studies on the effect of different combinations of these two controls would help towards a more profound understanding of how GAs must be tuned.

4.4.2.2 Genetic algorithm: Step 2. Genetic operations

Genetic operators are used at this stage in order to create the next generation: cross-overs and mutations.

a) Discrete chromosomes

Originally, genetic algorithms were developed in the framework of discrete, chromosome-like manipulations. Basically, each discrete parameter is represented by a binary chain. If a parameter can take up to two different values, a 1-bit chain is used, if a parameter can take up to eight different values, a 3-bits chain is used; a n-bits chain will represent a parameter with 2^n values.

Then the concatenation (in the same order) of all the chains that represent the different parameters, forms the chromosome that represents the individual. These chromosomes can be cross-overed and mutated following different methods;

a).1 Discrete chromosomes: Type 1. Cross-over

Two parent chromosomes have a probability p_c (defined by the GA user) to be cross-overed following three different types of cross-over operator;

- One point cross-over

A cross-over point is randomly chosen within the chromosome length and the two parent chromosomes interchange all the bits after (or before) this point, creating two new offspring as shown in Fig. 4.10.

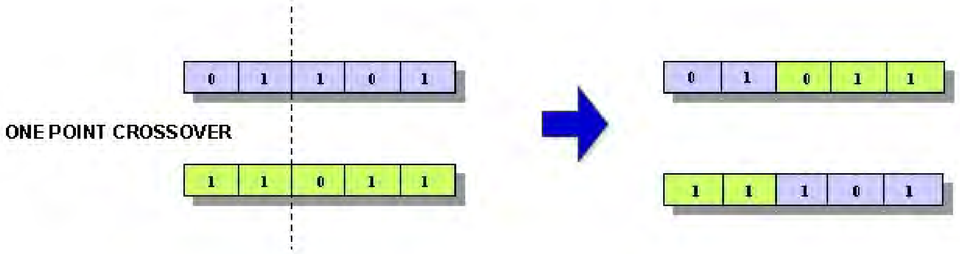

Figure 4.10: One point cross-over example with two 5-bits parent chromosomes forming two new offspring.

- Two points cross-over

A two-point cross-over operator randomly selects two cross-over points within the chromosome length and the two parent chromosomes interchange all the bits in between these points, creating two new offspring as shown in Fig. 4.11.

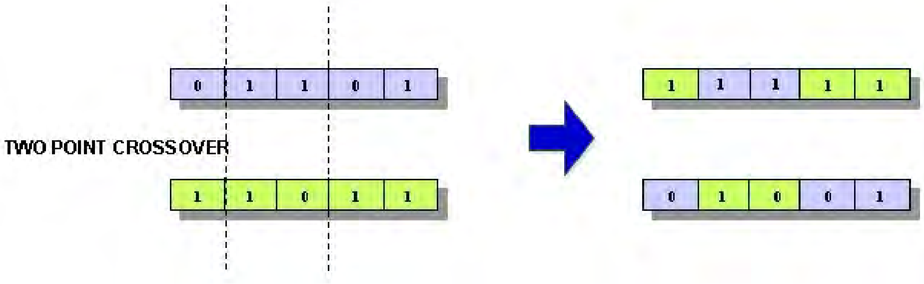

Figure 4.11: Two points cross-over example with two 5-bits parent chromosomes forming two new offspring.

- Uniform cross-over

In the case of a uniform cross-over, the (uniform) cross-over operator decides which parent chromosome will contribute to each of the gene values in the first offspring chromosome. Then the exact opposite of the first offspring is created as the second child. This "decision" is defined by a probability; the "mixing ratio". Such a uniform cross-over operation is shown in Fig. 4.12.

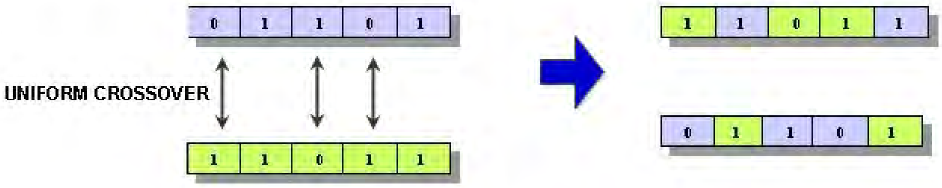

Figure 4.12: Uniform cross-over example with two 5-bits parent chromosomes forming two new offspring.

As explained earlier, building blocks are the basis upon which high fitness chromosomes can be found [131]. The one and two points cross-over operators perform parent chromosomes mixing at a segment level as they interchange a complete consecutive set of genes within the parent chromosomes. On the other hand, the uniform cross-over operator is a gene level mixing tool that can potentially destroy building blocks. One might think that this last type of cross-over is disadvantageous but for some problems, the additional flexibility of gene level mixing outweighs the disadvantage of destroying BBs [151].

a).2 Discrete chromosomes: Type 2. Mutation

For discrete chromosomes, when mutation occurs, it alters one or more gene values from its initial state. Typically, the mutation operator has a 50% chance to invert each gene; if it is a "0", it becomes a "1" and if it is a "1" it becomes a "0". The probability that a mutation occurs p_m is controlled by the GA user.

b) Continuous parameters

If parameters are now encoded using floating genes instead of a concatenation of binary chains, a continuous version of cross-over and mutation can be used;

b).1 Continuous parameters: Type 1. Cross-over

For a continuous cross-over, the cross-over operator linearly combines the two parent chromosome vectors to produce two new offspring according to Eq. 4.18;

$$\forall i \in [1:n]\,,\quad \begin{array}{rcl} C_1(i) & = & \mathrm{a}\times P_1(i) + (1-a)\times P_2(i) \\ \mathrm{C}_2(i) & = & \text{(1-a)}\times P_1(i) + a \times P_2(i) \end{array} \tag{4.18}$$

where $C_{1,2}(i)$ (resp. $P_{1,2}(i)$) is the i^{th} floating gene of the n-floating-genes child $C_{1,2}$ (resp. the n-floating-genes parent $P_{1,2}$) and a is a randomly chosen parameter between 0 and 1 [159].

This is how the ANSYS MOGA treats the continuous cross-overs. The probability of two n-floating-genes parent chromosomes to be cross-overed is $p_c = 0.9$ [159].

b).2 Continuous parameters: Type 2. Mutation

For continuous mutation, a polynomial mutation operator is applied, as shown in Eq. 4.19;

$$\forall i \in [1:n]\,,\quad C(i) = P(i) + (P_{max}(i) - P_{min}(i))\delta \tag{4.19}$$

where $C(i)$ and $P(i)$, are the i^{th} floating gene of the child C and parent P respectively. $P_{max}(i)$ and $P_{min}(i)$ are the upper and lower bound of the i^{th} floating gene of P and δ is a small variation calculated from a polynomial distribution [159]. The probability of such mutation to happen is $p_m = 0.01$ [159].

An improvement of these genetic operations has emerged recently and is called elitism [160–163]. The principle of elitism is that instead of populating the next generation exclusively with "children" of the breeding group, the best candidates from the previous generation (the "parent" generation) are also conserved, unaltered. Recent results [161, 162] clearly show that elitism can speed up the performance of the GA significantly, while helping to prevent the loss of good solutions once they have been found.

4.4.2.3 Genetic algorithm: Step 3. Selection

In the case of computational fluid dynamics, each candidate is represented by a set of geometric parameters. For any generation, the fitness of each candidate is evaluated using a CFD simulation of the geometric configuration defined by the candidates' parameters. That means that one must perform as many simulations as candidate's fitness evaluations. Each individual's defining parameters are used to build a geometry and a mesh. A CFD simulation is then performed using the considered mesh and the output quantity(ies) of interest is(are) stored. The fitness is equal to the CFD simulation output value, or to a weighted sum of output values in the case of multiple-objectives optimization. These weight coefficients depend on the importance of one output compared to another: coefficients are higher for more important outputs. The fitness of each candidate is then compared with all other candidates fitness in order to determine the best ones among the current generation.

4.4.2.4 Genetic algorithm: Step 4. Termination

Within the ANSYS MOGA algorithm, the termination criteria can be;

- For multi-objectives optimization; a certain percentage of the population on the Pareto front.
- A fixed number of generations is reached
- Convergence stability is reached defined as;

$$\begin{array}{ccc} \dfrac{\left|\overline{f(t)} - \overline{f(t-1)}\right|}{f_{max} - f_{min}} & < & \dfrac{S}{100} \\ & \text{and} & \\ \dfrac{\left|\sigma(t) - \sigma(t-1)\right|}{f_{max} - f_{min}} & < & \dfrac{S}{100} \end{array} \tag{4.20}$$

where $\overline{f(t)}$ is the mean fitness at generation t, $\sigma(t)$ is the fitness standard deviation at generation t, f_{max} and f_{min} are the maximum and minimum fitness in the first generation respectively, and S is the desired stability percentage.

4.5 Computing resources

As already mentioned many times, a single complete shape optimization procedure involves several CFD simulations. As it will be presented in Section 6, the different investigated optimizations involve a number of CFD simulations ranging from dozens to a thousand. Needless to say that an optimization involving a thousand CFD simulations of a turbulent flow around a complex geometry cannot be performed on a traditional workstation in an acceptable amount of time.

In order to cope with this issue, the optimization have been performed in parallel, on numerous cores provided by the Irish Centre for High-End Computing (ICHEC). The ANSYS files are sent to the "fionn" ICHEC's server and a job is submitted and wait for the number of cores that are requested to be available so that the process can start. There is a total of around eight thousand $\approx$ 2.3 GHz cores available for a peak performance of 147.5 TFlops [164].

The main issue remaining is that only limited amount of licenses are available for ANSYS jobs. Basically 128 "tokens" are available and each time a job is started, it uses a number of tokens that depends on the requested number of nodes (one node corresponds to 24 cores). The first node needs 12 tokens and each additional node requires 8 tokens [165]. These tokens being shared among all ICHEC users that run ANSYS jobs, although a larger number of cores is available compared to a classical 4-cores workstation, the computing resource is strongly limited.

Moreover, a job must be submitted with a time limit, namely the "walltime". If this limit is reached, the job is killed in order to avoid errors such as infinite loop. The maximum walltime is 144 hours [166].

As a result of (i) the limitation of the number of nodes because of the ANSYS licenseing issue, and (ii) the limitation of the walltime, all the simulations performed and discussed in the present work have been run on the fionn server using two nodes, that is to say 48 cores, with a walltime limit set at the maximum 144 hours. The queue time between the job submission and the actual start of the optimization varies from a couple of minutes to a couple of days as it depends on the number of people using ANSYS licenses (tokens) at the moment the job is submitted. As a result, there is a limit in the complexity of the shape optimization that can be performed on this system, even though the improvement from a typical 4-cores workstation is more than noticeable as shown in Table 4.1.

4.6 Summary of the chapter

The methodology approach to derive a CFD model to simulate the flow around a complex structure and accurately evaluate the convective heat transfer from this structure to the fluid, is developed in Section 4.3 for a benchmark case of two ver-

Table 4.1: Comparison of computing resources between a typical workstation and the fionn system from ICHEC.

system	**Workstation**	**Fionn ICHEC**
CPU	Intel Core i3-2120	Intel Xeon E5-2695
CPU clock	3.30 GHz	2.40 GHz
Number of cores	4	48
FLOPS	52.8 GFlops	921.6 GFlops
Limitations	Can not use the computer for something else if full power dedicated to the optimization	Walltime limit of 144 hours, queuing time

tically aligned, isothermally heated, horizontal, two-dimensional cylinders. The choice of this particular case is twofold: (i) starting from rather simple but interacting geometries is the first step towards the study of heat transfer from more complex structures and (ii) experimental data is available for validation of the numerical model for both steady and transient situations as presented in Section 5.2.

Section 4.4 presents the approach undertaken in order to derive a shape optimization procedure that involves a genetic algorithm and CFD simulations using the model described in Section 4.3. This shape optimization process has been utilized to discover optimal designs for different geometrical and flow configurations in the limit of the available computing resources. The first case studies the optimal spacing between parallel plates and compare the numerical results obtained from the shape optimization process described in Section 4.4 with analytical results from the literature [23, 24]. The second case presented in Chapter 6 investigates the optimal design of a heat sink composed of three and five fins as an additional step towards more complicated geometries that are encountered in Nature.

Chapter 5

Numerical results: Transient heat transfer from a pair of cylinders

This chapter presents the results from the numerical study investigating the problem of heat transfer from two heated two-dimensional cylinders. The numerical methodology developed to deal with this problem has been presented in Section 4.3. The methodology is now verified against experimental data in Section 5.2 and new results obtained using this CFD method are presented and discussed in the Section 5.3.

5.1 Background and motivation

The study of the natural convection from a pair of vertically aligned, isothermally heated, horizontal two-dimensional cylinders is investigated in order to obtain numerical results comparable to experimental data available from Persoons et al. [105]. Their experimental study focuses on how the Rayleigh number and the centre-to-centre distance S separating the two cylinders as shown in Fig. 4.3 can affect the heat transfer characteristics of the top cylinder. The present numerical work aims at replicating the exact configuration presented and studied by Persoons et al. [105] so that the comparison for verification that is presented in this Section is relevant. As both steady and transient results are reported by Persoons et al., the comparison will validate the capability of the numerical model developed in Section 4.3, to model and capture transient phenomena that could help providing a further understanding of the convective heat transfer mechanisms.

The objectives of this benchmark study are;

• to verify the numerical model presented in Section 4.3, based on previous experimental data [105]

And because Persoons et al. [105] could only provide hypotheses and partial explanations for the observed phenomena based on the limited amount of experimental data available, the numerical results - after validation - were discussed and highlighted a new objective;

• to reveal the nature of the thermal plume oscillations and their influence on the heat transfer effectiveness based on numerical results as presented in Section 5.3

This should yield a more profound insight into the nature of unsteady natural convection from a pair of cylinders, to complement the experimental approach [105].

5.2 Validation of the Ansys Fluent CFD model

This section presents a detailed validation of the CFD model for natural convection heat transfer from one or two isothermally heated horizontal circular cylinders, using empirical data available in the literature as well as from experimental data from Persoons et al. [105]. Validation of the results is obtained by comparison with the experimental results for the ranges of Rayleigh numbers and cylinder spacings that were available from the work of Parsoons et al. [105].

5.2.1 Time-averaged heat transfer from a single cylinder

The time-averaged mean surface heat transfer coefficient results have first been compared for a single cylinder test case to a widely used empirical correlation [82] (in the form of Eq. 3.23) which is valid for a range of Rayleigh numbers ranging from 0.5×10^6 to 6×10^6 as shown in Fig. 5.1. Equation 3.23 is recalled;

$$Nu_m = C \cdot Ra^{1/4} \tag{5.1}$$

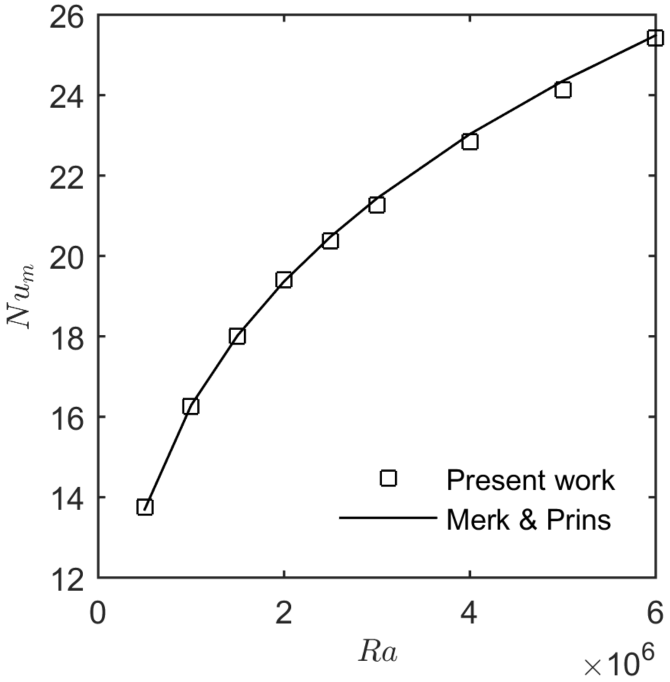

Figure 5.1: Mean time-averaged Nusselt number for a single cylinder. Verification of numerical results by comparison with empirical correlation from Merk & Prins [82] (Eq. 5.1 with $C = 0.515$) $R^2 = 0.9994$. Equation 5.2 is not shown for clarity.

For the same range of Rayleigh number ($0.5 \times 10^6 \leq Ra \leq 6 \times 10^6$), the results of the CFD model with a single cylinder (yet otherwise the same tank dimensions as described in the preceding sections) are in good agreement with the above correlation from Merk & Prins (for $Pr = 7$, $C = 0.515$ in Eq. 5.1). The mean time-averaged Nusselt number results have been least square fitted with the power law correlation;

$$\mathrm{Nu}_m = 0.551 Ra^{0.245} \quad (\mathrm{R}^2 = 0.9991) \tag{5.2}$$

As the main objective of the paper is to study oscillations of the thermal plume arising from the bottom cylinder, a study of the local effects of this plume on the top cylinder is required. Therefore, in addition to only comparing the time-averaged heat transfer, a more detailed validation of the local heat transfer rate around a single cylinder is carried out.

For the single cylinder CFD model results, the time-averaged local Nusselt number has been evaluated at small surface increments every 10° from the bottom ($\theta = 0°$) to the top ($\theta = 180°$) of the cylinder. The results for different values of Rayleigh number have been compared to the results obtained by Kuehn and Goldstein [99] and are shown in Fig. 5.2. The results are normalized by dividing the local Nusslet number by $C \times Ra^{1/4}$ with $C = 0.551$ for the present work's results (value taken from Eq. 5.2) and C taken from Kuehn and Goldstein's study for their results. It can be noted that our CFD results fit the results by Kuehn & Goldstein for the investigated Rayleigh number range ($10^4 \leq Ra \leq 5.3 \times 10^6$) although a small difference is seen for $Ra = 10^4$, especially for $135° \leq \theta \leq 180°$. The coefficient of determination between the present work and Kuehn & Goldstein results are, $R^2 = 0.9154, 0.9545, 0.9896$ for $Ra = 10^4, 10^5, 10^6$, respectively.

5.2.2 Time-averaged heat transfer from a pair of cylinders

The validation of the CFD model with experimental results has also been conducted for natural convection from a pair of isothermally heated horizontal cylinders in water. The two horizontal cylinders are vertically aligned, separated by a centre-to-centre distance S, as shown in Fig. 4.3 and heated at the same temperature T_S. The surface temperature T_S is set to different values corresponding to the targeted Rayleigh numbers (Ra is computed using Eq. 2.7 so in the case of a cylinder, Eq. 5.3 is used). The results for the investigated ranges of Rayleigh numbers Ra and dimensionless spacing S/D are summarised in Table 5.1.

$$Ra = \frac{g\beta(T_s - T_\infty)D^3}{\nu\alpha} \tag{5.3}$$

Where D is the cylinders' diameter, T_s is the temperature of the cylinders and T_∞ is the water bulk temperature.

a) Effects of the Rayleigh number

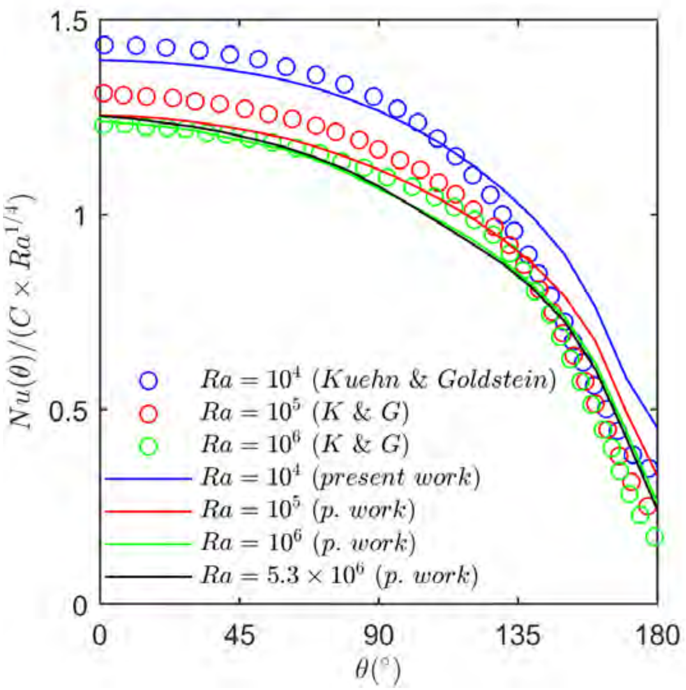

Figure 5.2: Normalised local Nusselt number. CFD results as solid lines (from top to bottom; $Ra = 10^4, 10^5, 10^6, 5.3 \times 10^6$) and Kuehn & Goldstein's results as markers (from top to bottom; $Ra = 10^4, 10^5, 10^6$) [99].

Fig. 5.3 shows the (a) numerical and (b) experimental results for a spacing $S = 2D$. A good qualitative agreement is found, with curves showing similar trends and inflection points, marking three distinct heat transfer regions (I, II, III). The Nusselt number decreases sharply from the bottom of the cylinder for $0^\circ \leq \theta < 40^\circ$ (region I) followed by a more gradual decrease for $40^\circ \leq \theta < 150^\circ$ (region II) and again a sharper decrease towards the top of the cylinder ($150^\circ \leq \theta < 180^\circ$, region III). For each tested Rayleigh number, a monotonic increase of the local Nusselt number with Rayleigh number is observed. The numerical and experimental results exhibit a reasonable quantitative agreement as this region of gradually decreasing Nu (region II) is reached at around $\theta = 40^\circ$ with a similar value of $Nu \approx 20$ in both sets of results for all Rayleigh number.

Fig. 5.4 shows the comparison between numerical and experimental results for the three investigated Rayleigh numbers. Region I shows a good quantitative agreement between numerical and experimental data. Region II shows a reasonable agreement, although the experimental local Nusselt number data exhibit a more pronounced plateau, especially at higher Rayleigh numbers, whereas the numerical data retain a monotonic decreasing trend for increasing angle. Region III (near the top of the cylinder) shows decreasing local Nusselt number values in both numerical and experimental results, yet there remains a discrepancy near $\theta = 180°$. The discrepancy between the experimental and numerical results consistently appears near the top of the cylinder as shown in Fig. 5.4. Although there is no certain reason why we observe this discrepancy, it might be due to the fact that in the case of the experimental measurements, the local Nusselt number near the top of the cylinder is averaged over a broader circumferential span than the numerical surface of integration, due to the finite sensor size. As the local Nusselt number is a minimum at the 180° position, this would contribute towards the experimental results being higher than the numerical results. However, for the purpose of verifying the CFD code, the observed agreement in the trends and locations of these three regions is considered to be satisfactory.

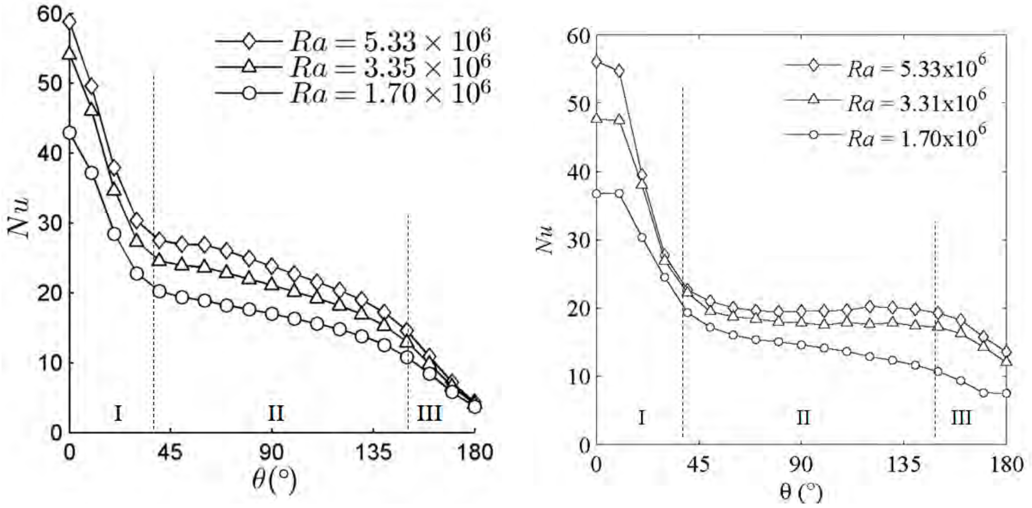

(a) (b)

Figure 5.3: Local Nusselt number along the circumference of the upper cylinder for $S = 2D$. (a) Numerical and (b) experimental results [105].

A numerical simulation has also been conducted for $S = 3D$ and for the same Rayleigh numbers, as shown in Fig. 5.5. In the case of a spacing of $S = 3D$, the relationship between the local Nusselt number and the angular location along the top cylinder's circumference is more progressive. Especially in region II, where the decrease of the local Nusselt number with θ is rather linear than the plateau observed in the case of $S = 2D$. However, the 3 regions along the circumference (I,

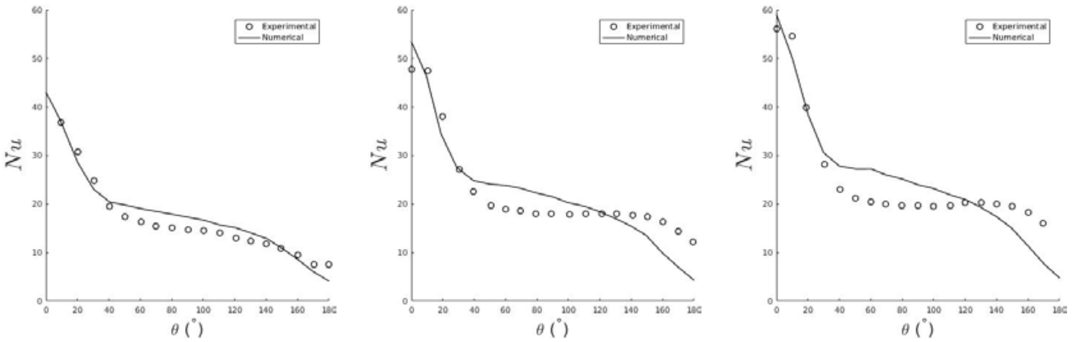

(a) $Ra = 1.7 \times 10^6$, $R^2 = 0.9281$
(b) $Ra = 3.31 \times 10^6$, $R^2 = 0.9023$
(c) $Ra = 5.33 \times 10^6$, $R^2 = 0.8939$

Figure 5.4: Local Nusselt number along the circumference of the upper cylinder for $S = 2D$. Numerical and experimental results comparison and coefficients of determination. [105, 106].

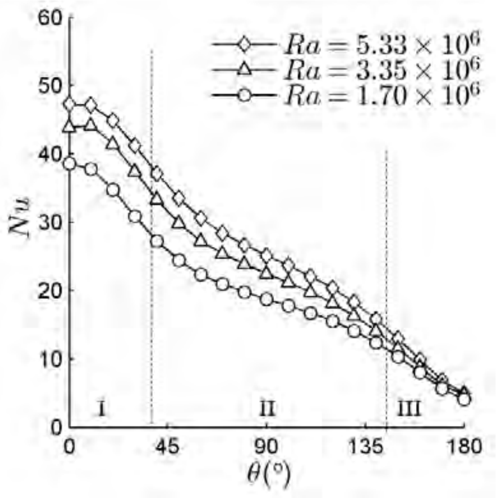

Figure 5.5: Local Nusselt number along the circumference of the upper cylinder for $S = 3D$ (numerical results).

II, III) can still be observed with a concave decrease for $0° \leq \theta \leq 40°$, an inflection of the curve at $\theta = 40°$ and a convex decrease up to $\theta = 150°$, back to a concave decrease up to $\theta = 180°$. From the numerical results shown in Figs. 5.3 and 5.5, it can be concluded that the Rayleigh number mainly influences the averaged Nusselt number. In other words, a change in Rayleigh number does not significantly alter the relative local Nusselt number at a given position θ when normalised by the averaged Nusselt number. A global trend appears in the distribution of the local Nusselt number, which is scaled up or down as a whole with an increase or decrease in Rayleigh number, respectively, as shown in Fig. 5.3 and 5.5. This scaling however only slightly affects the local Nusselt number around 180° (the top of the upper cylinder). The sensitivity of the Nusselt number curve to a change in Rayleigh number is expressed by a similar power law relationship as Eq. 5.2.

b) Effects of cylinder spacing S/D

The effect of the spacing on the distribution of the local Nusselt number has been investigated in more detail for a Rayleigh number $Ra = 5.33 \times 10^6$. Figure 5.6 shows the local time-averaged Nusselt number distributions for (a) the numerical model and (b) experimental measurements for three cylinder spacings and the single cylinder case. Each set of results shows a satisfactory agreement in terms of absolute values and trends with coefficients of determination above 0.8 as shown in Fig. 5.7, with the exception of the region near the top of the cylinder where the experimental data diverges.

Unlike the Rayleigh number, Fig. 5.6 demonstrates that the cylinder spacing S/D has a strong influence on the local Nusselt number distribution. The sharp decrease in local Nusselt number near the bottom of the cylinder is more pronounced for smaller spacings, and tends to a more gradual trend at larger spacing $S/D > 3$. For $S = 2D$, the Nusselt number drops by 54% (from 59 to 27) between $\theta = 0°$ and 40° whereas for $S = 4D$, the Nusselt number drops by only 13% from $\theta = 0°$ to 40°.

The greater the dimensionless spacing S/D, the more closely the Nusselt number distribution agrees with the single cylinder results, as shown in Fig. 5.8. Indeed when the two cylinders are far from each other, the interaction between them is weak and if the distance is great enough, this interaction is expected to become negligible. For the investigated range ($2 \leq S/D \leq 4$), Fig. 5.8 shows that the increase in local heat transfer coefficient near the bottom of the cylinder reduces from a maximum of 90% for $S/D = 2$ to 23% for $S/D = 4$. A reduction in local heat transfer (albeit smaller in magnitude) is observed in the upper half of the cylinder; however the reduction magnitude in this region is less affected by the cylinder spacing.

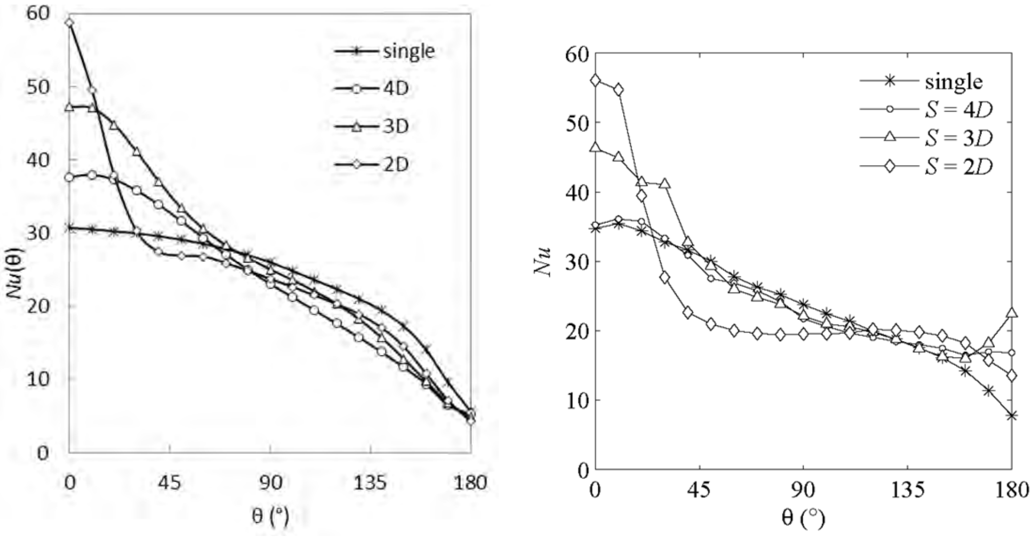

(a) (b)

Figure 5.6: Local time-averaged Nusselt number along the circumference of the upper cylinder for $Ra = 5.33 \times 10^6$. (a) Numerical and (b) experimental results [105].

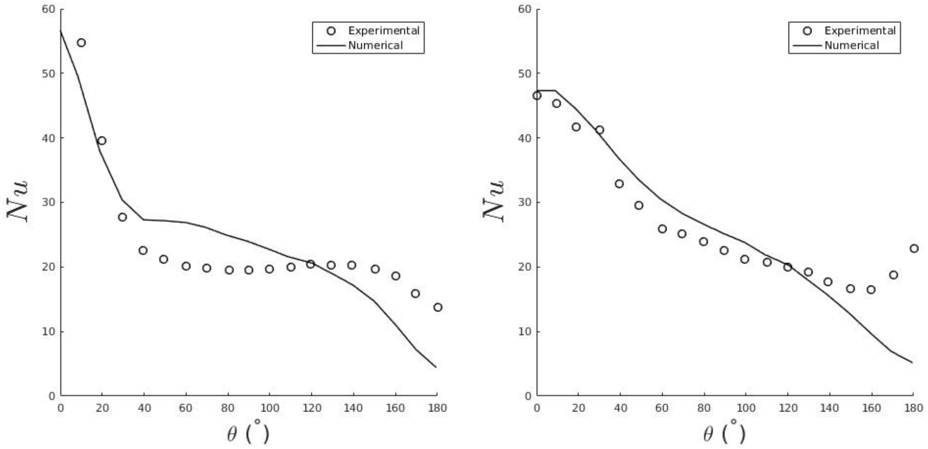

(a) $S = 2D$, $R^2 = 0.8174$ (b) $S = 3D$, $R^2 = 0.8435$

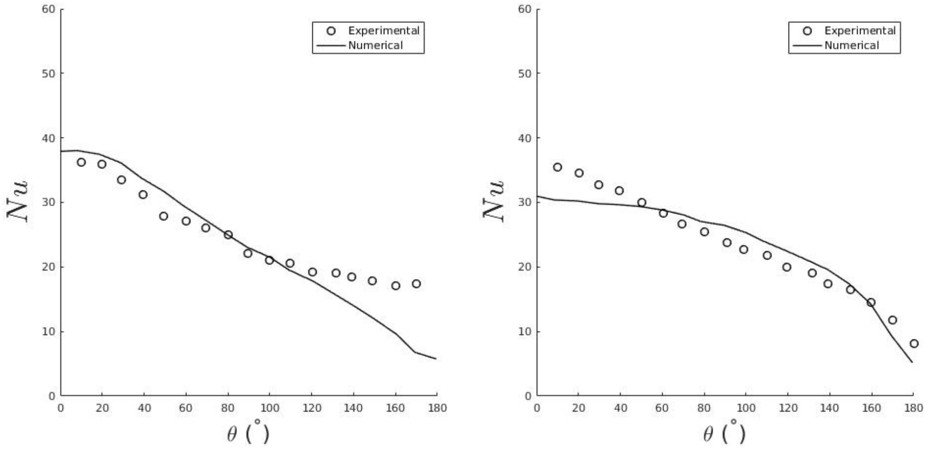

(c) $S = 4D$, $R^2 = 0.8373$ (d) Single cylinder, $R^2 = 0.8967$

Figure 5.7: Local time-averaged Nusselt number along the circumference of the upper cylinder for $Ra = 5.33 \times 10^6$. Numerical and experimental results comparison and coefficients of determination [105, 106].

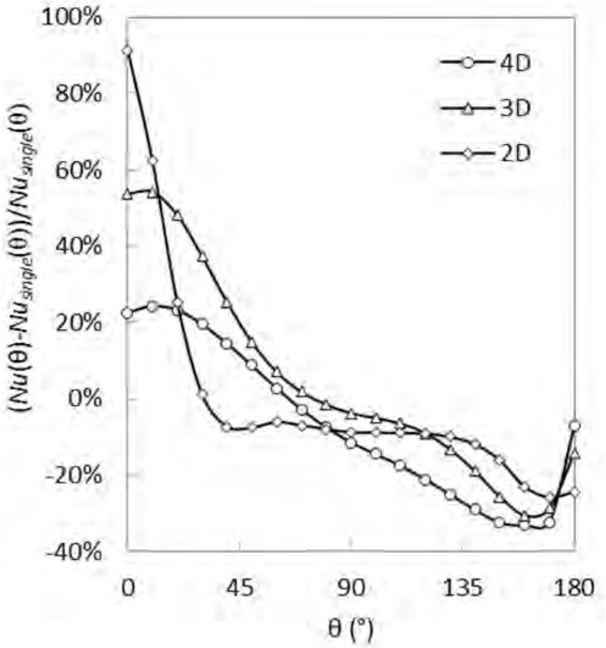

Figure 5.8: Deviation of the local time-averaged Nusselt number from the single cylinder case along the circumference of the upper cylinder for $Ra = 5.33 \times 10^6$.

Figure 5.9 compares the numerical against experimental values for the local Nusselt number for the same three spacings at $Ra = 5.33 \times 10^6$. The highest values of Nusselt number represent the region near the bottom of the upper cylinder. A good agreement can be noted for most values within approximately ±15%, except for the smallest values representing the heat transfer near the top of the cylinder. In this region, the numerical results consistently underpredict the experimental values as explained in section a).

The numerical approach adopted to study the benchmark case of natural convection heat transfer from a pair of vertically aligned horizontal cylinders has been presented in Section 4.3. The numerical results of time-averaged Nusselt number from a single cylinder and from a pair of cylinders have been compared to results found in the literature [82], [99] as well as from experimental results [105]. A reasonable agreement was found, which validates the CFD model for this type of simulation.

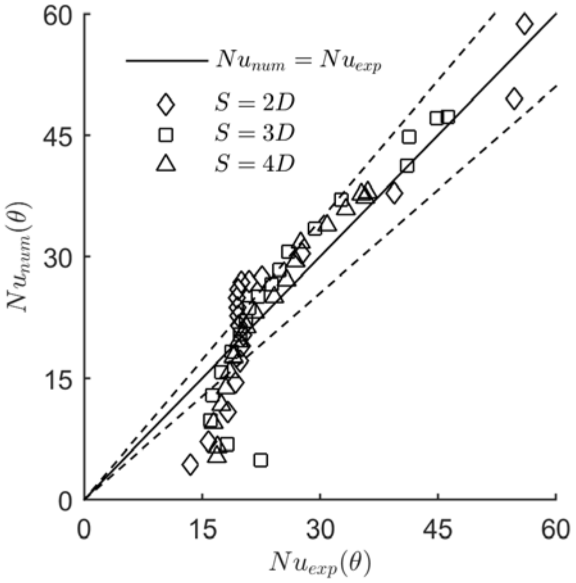

Figure 5.9: Numerical versus experimental local Nusselt number at $\Delta\theta = 10^\circ$ increments along the circumference for $Ra = 5.33 \times 10^6$. ±15% limits indicated with dotted lines.

5.3 Results and discussion: transient natural convection from a pair of cylinders

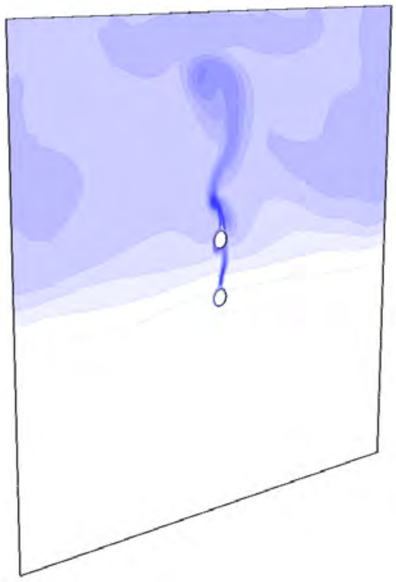

Figure 5.10: Thermal plume arising from a pair of cylinders, temperature contours.

As highlighted previously, the local and unsteady aspects of the heat transfer phenomena are the key to understand how the upper cylinder's capacity to transfer heat can be augmented by simply placing it above another cylinder. Numerical results from the verified CFD model of overall performance as well as unsteady and local heat transfer and velocity field quantities are presented in this chapter. The present chapter ends with a discussion and an attempt at explaining these results.

5.3.1 Mean time-averaged results

Besides using the mean time-averaged numerical results described in Chapter 4.3 in order to verify the CFD model, some of these results are already relevant to the study of heat transfer performance of cooling devices. Indeed, Table 5.1 summarizes the time-averaged mean Nusselt number results as a function of the Rayleigh number and cylinder spacing. The normalized heat transfer enhancement compared to the single cylinder case (at the same Rayleigh number) is represented in Table 5.1 by percentage values of δNu_m, defined as;

Table 5.1: Mean time-averaged Nusselt number Nu_m of a single cylinder and the upper of a pair of vertically aligned cylinders with the values in brackets representing the relative deviation to a single cylinder, $\delta Nu_m \times 100\%$. Experimental results from [105].

Case	$Ra = 1.7 \times 10^6$		$Ra = 3.35 \times 10^6$		$Ra = 5.33 \times 10^6$	
	Num.	Exp.	Num.	Exp.	Num.	Exp.
Single cylinder	$Nu_m = 18.3$	$Nu_m = 16.9$	$Nu_m = 21.6$	$Nu_m = 20.7$	$Nu_m = 23.6$	$Nu_m = 23.8$
$S/D = 4$	$Nu_m = 19.2$ (+5.0%)	$Nu_m = 18.0$ (+6.1%)	$Nu_m = 23.3$ (+7.7%)	$Nu_m = 22.8$ (+9.2%)	$Nu_m = 24.5$ (+4.1%)	$Nu_m = 24.3$ (+2.0%)
$S/D = 3.5$					$Nu_m = 26.2$ (+11.0%)	
$S/D = 3$	$Nu_m = 19.5$ (+6.5%)	$Nu_m = 18.2$ (+7.2%)	$Nu_m = 23.1$ (+6.8%)	$Nu_m = 22.4$ (+7.6%)	$Nu_m = 26.1$ (+10.8%)	$Nu_m = 26.5$ (+10.2%)
$S/D = 2.5$					$Nu_m = 25.6$ (+8.6%)	
$S/D = 2$	$Nu_m = 18.1$ (−0.9%)	$Nu_m = 16.1$ (−5.1%)	$Nu_m = 22.3$ (+3.1%)	$Nu_m = 22.3$ (+7.2%)	$Nu_m = 24.7$ (+4.9%)	$Nu_m = 24.5$ (+3.1%)
$S/D = 1.5$					$Nu_m = 23.7$ (+0.7%)	

$$\delta Nu_m = \frac{Nu_m - Nu_{m,single}}{Nu_{m,single}} \tag{5.4}$$

It is worth noting that, even for the numerical results, the overall heat transfer does not exhibit a monotonic dependence on either the spacing, or the Rayleigh number. Indeed the relative deviation from a single cylinder Nusselt number varies between slightly negative values (e.g., −1.8% for $S = 4D$ and $Ra = 5.33 \times 10^6$) to positive values up to +11% for $S = 3.5D$ at $Ra = 5.33 \times 10^6$.

Figure 5.11 shows a contour plot of the heat transfer enhancement δNu_m (in percentage values) as a function of cylinder spacing and Rayleigh number. Apart from

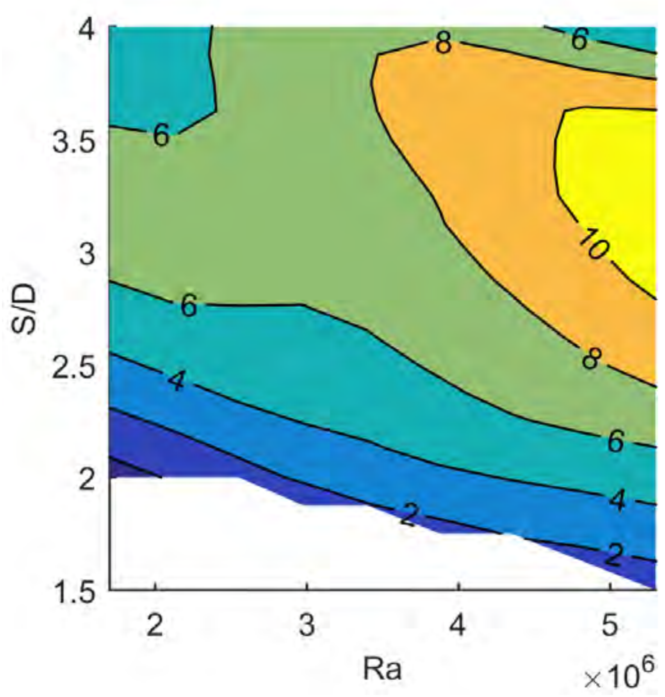

Figure 5.11: Heat transfer enhancement $\delta Nu_m = (Nu_m - Nu_{m,single})/Nu_{m,single}$ ($\times100\%$) as a function of Rayleigh number and cylinder spacing S/D.

the sudden decrease at $S = 4D$ and $Ra = 5.3\times10^6$, the heat transfer enhancement δNu_m tends to increase with increasing Ra and decrease with decreasing S/D. The locus of optimum spacing and Rayleigh number, for the specific configurations investigated, is in the range $2.8D \leq S \leq 3.6D$ and $4.7\times10^6 \leq Ra \leq 5.3\times10^6$. However the objective of this study was not to provide a definitive optimum, and further work would be needed to ascertain that the 10% contour in Fig. 5.11 is in fact a global extremum.

5.3.2 Spectral analysis of local Nusselt number and flow velocity

Results have been presented in the previous section for the local time-averaged Nusselt number and demonstrate the strong dependence of the Nu distribution on the cylinder spacing S/D. Since experimental measurements for the same conditions have previously revealed strong oscillatory flow and heat transfer [105], unsteady (URANS) simulations have been performed for each case in Table 5.1 to further investigate the origin of these oscillations, and their relationship to heat transfer enhancement. As discussed in Section 4.3, a time step of $\Delta t = 50\ ms$ has been used. The simulations ran for 80,000 iterations or a simulated time of 4,000 s. Figure 5.12 presents a sequence of the instantaneous temperature field captured with an interval of 6s.

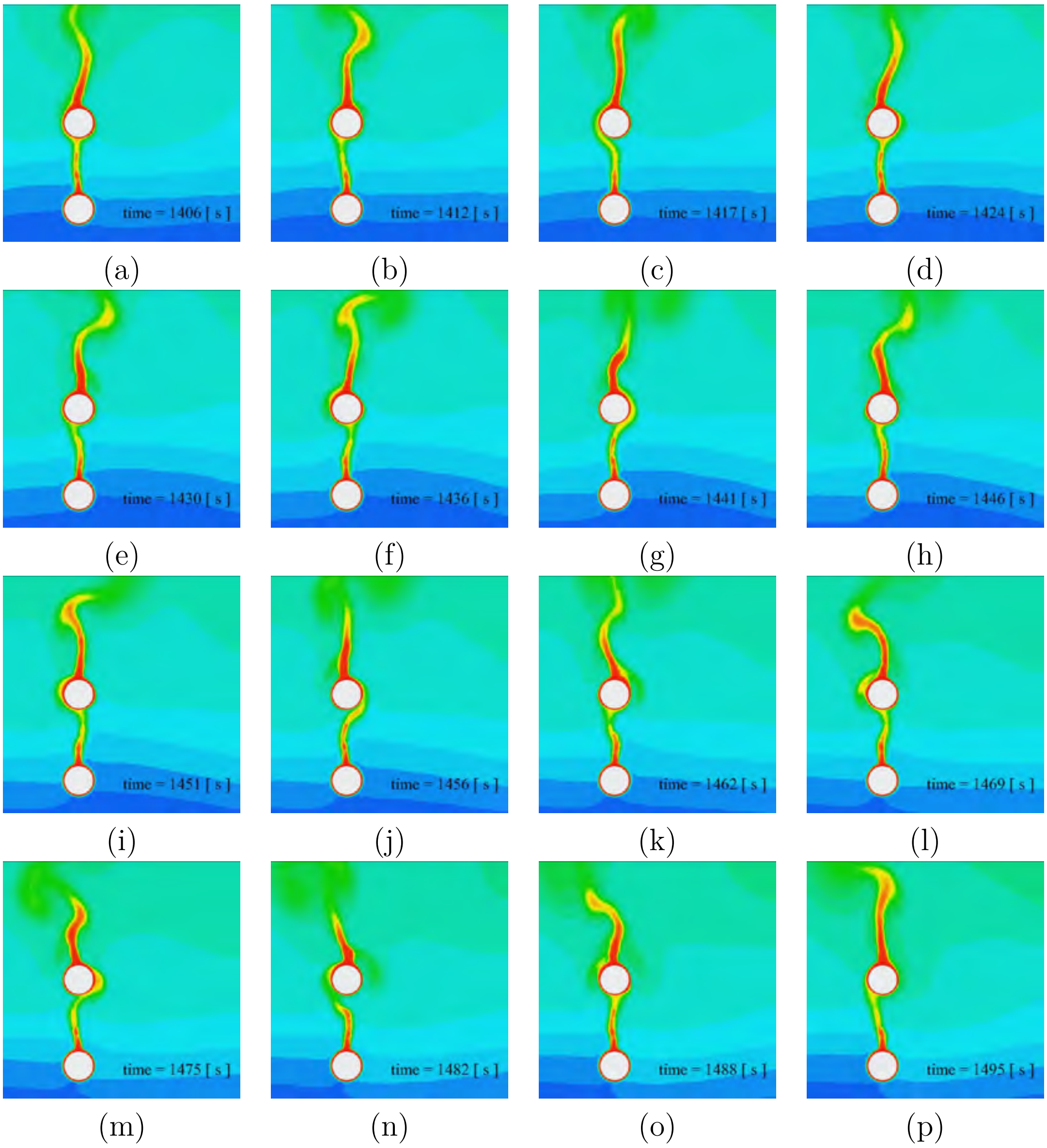

(a) (b) (c) (d)
(e) (f) (g) (h)
(i) (j) (k) (l)
(m) (n) (o) (p)

Figure 5.12: Sequence of the instantaneous temperature distribution, from $t = 1406s$ (a) to $t = 1495s$ (p).

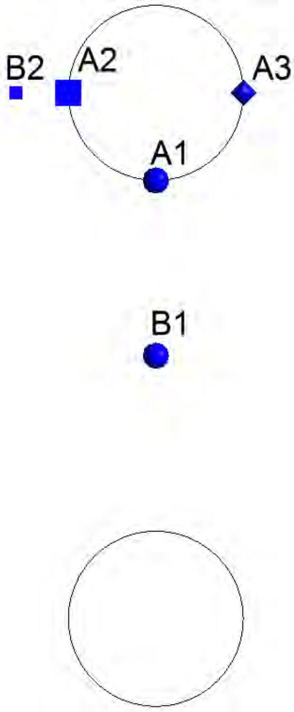

Figure 5.13: Monitored points where solution data is extracted for FFT spectra and coherence analysis (see Figs. 5.14-5.17).

Figure 5.13 identifies a number of points where time-resolved local Nusselt number and fluid velocity data are extracted for further analysis in this section. Points $A1$, $A2$ and $A3$ are defined on the circumference of the upper cylinder at angular locations $\theta = 0°, -90°, 90°$, respectively. Points $B1$ and $B2$ are defined in the flow field with $B1$ midway between the two cylinders. At the location $B1$, the reference plume velocity V_{ref} is averaged along a horizontal line;

$$V_{ref} = \frac{1}{b}\int_{-b/2}^{b/2} \overline{V}(x, y = y_{B1})dx \tag{5.5}$$

where the plume width b is defined as the distance between the locations (along the same horizontal line through $B1$) where the upward time-averaged velocity magnitude drops to 25% of the peak velocity. Point $B2$ is somewhat arbitrarily defined at a radial distance from point $A2$ equal to $b/2$. Figure 5.22 shows that the trajectory of the vortex centres passes close to this point which ensures that any fluctuations of the local velocity vector are captured in the analysis. In other locations adjacent to the side of the upper cylinder, oscillations are observed at the same frequencies yet different magnitudes.

For the sake of brevity, the spectral analysis is only presented in full for a single representative case in the investigated range, $Ra = 3.35 \times 10^6$ and $S = 3D$. Figure 5.14 shows the strong oscillations arising at the bottom of the upper cylinder ($\theta = 0°$, point $A1$) in the local Nusselt number. A supplemental video of the developing flow field from the start of the simulation until $t = 570\ s$ is provided as an electronic appendix A. After the start of the simulation ($t = 0\ s$), the flow initially develops as a stable plume, switching to a quasi-periodic oscillation at $t \approx 250\ s$. Once plume oscillation is established, the flow switches between regimes of almost purely harmonic swaying and more random fluctuations, as previously observed experimentally [105].

Figure 5.15 shows a close-up view of these quasi-periodic oscillations, where the data in Fig. 5.15 a are obtained from the numerical results and in Fig. 5.15 b from experimental measurements at the same conditions [105]. The strong temporal fluctuations in local Nusselt number shown in Figs. 5.14 and 5.15 a, correspond to lateral swaying oscillations of the thermal plume rising from the lower cylinder. Depending on the time-varying position and shape of the plume, the buoyant flow occasionally impinges directly onto the bottom of the upper cylinder causing a sharp rise in instantaneous local Nusselt number, or it is deflected along either side of the cylinder, causing a reduction in local Nu. The fluid temperature and flow velocity magnitude and direction near the bottom of the upper cylinder (point $A1$) also vary strongly.

Upon closer inspection of Fig. 5.14, the plume oscillations seem to switch between two regimes, a quasi-periodic pattern alternated by more random fluctuations. This behaviour agrees with the previous experimental observations [105]. In fact, a remarkable similarity can be seen in the periodic fluctuations in Fig. 5.15 a (numerical results) and Fig. 5.15 b (experimental results [105]). The fact that the numerical model is able to capture both the temporal characteristics and Nu amplitude of the oscillation provides strong validation evidence for the URANS methodology.

Figure 5.15 shows the variations of the Nusselt number at the lowest point of the upper cylinder (point $A1$). The Nusselt number at point $A1$ goes approximately from 25 up to 60 with a time average of $1/T \int\limits_0^T Nu(\theta = 0°, t)dt = Nu_m \approx 43$ as is

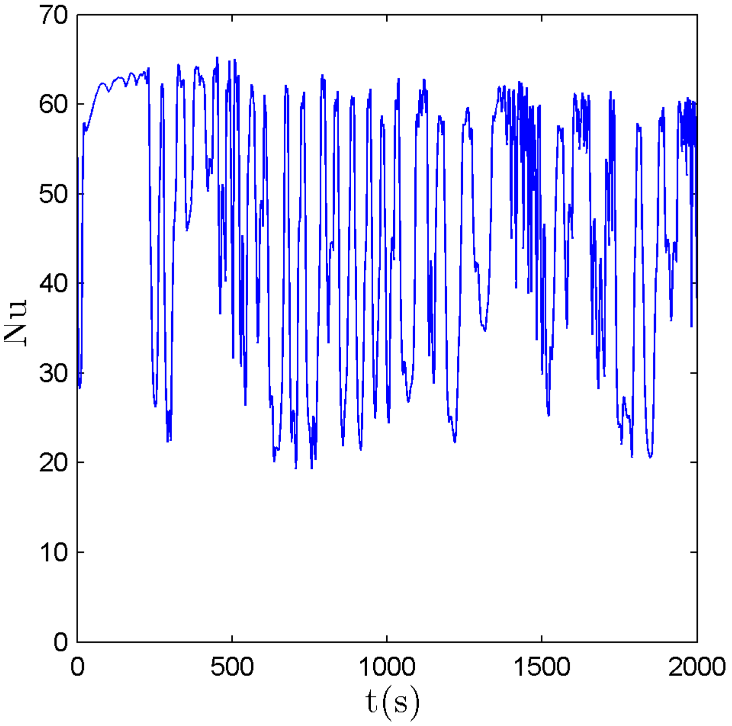

Figure 5.14: Time history of the local Nusselt number at $\theta = 0°$ (point $A1$ in Fig. 5.13) for $Ra = 3.35 \times 10^6$, $S = 3D$. The start-up and initial oscillations from 0 s until 570 s are shown in the supplemental video in appendix A.

shown on Fig. 5.5. Interestingly, the Nusselt number achieved by a single cylinder with the same Rayleigh number is 28 (this value has been calculated from the data shown in Fig. 5.2, with $Pr = 7$ and $C = 0.515$, $Nu = 1.25 \cdot C \cdot Ra^{1/4}$). The deviation of the time-averaged local Nusselt number from that for a single cylinder, at the location $\theta = 0°$, is observed, and is remarkably high with $\delta_{Nu_m(0Â°)} = 53.6$ %, as shown in Fig. 5.8. The increase or decrease of the global heat transfer characteristics of the upper of a pair of cylinders compared to the single cylinder case appears to be directly linked to these oscillations.

For this same dataset ($Ra = 3.35 \times 10^6$ and $S = 3D$), a frequency analysis of the local Nusselt number at points $A1$ and $A2$, and velocity at points $B1$ and $B2$ has been performed.

Figures 5.16a and 5.16b show the Fourier transform of the local Nusselt number at point $A1$ and the vertical velocity at point $B1$, based on a sampling frequency of 2 Hz for a 500 s long signal. For this case, a distinct peak frequency $f_1 = 0.0195$ Hz is found in both Nusselt number and vertical velocity, while a

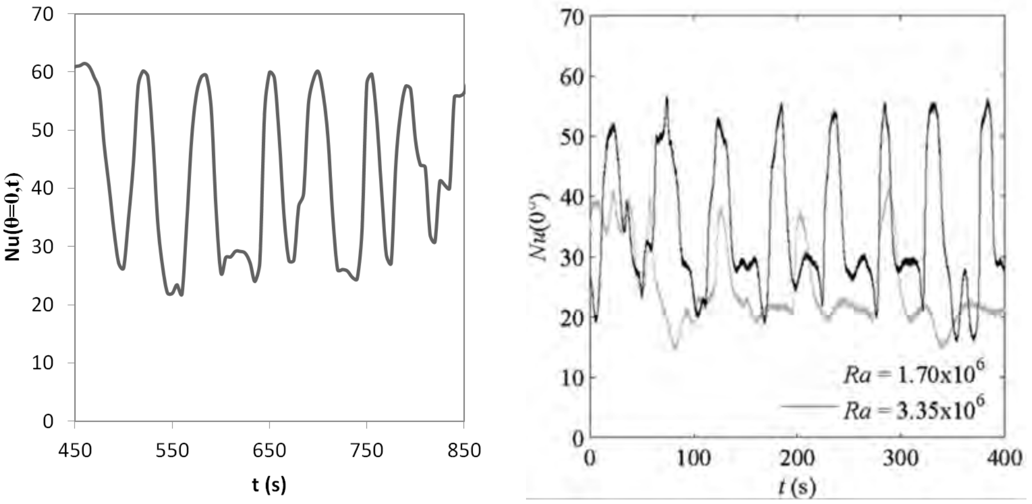

(a) (b)

Figure 5.15: Time-resolved local Nusselt number at $\theta = 0°$ (point $A1$ in Fig. 5.13) for $Ra = 3.35 \times 10^6$, $S = 3D$. (a) Numerical and (b) experimental results [105].

peak frequency $f_2 = 0.00977\ Hz$ is found for the horizontal velocity. It is worth noting that the frequency of the vertical velocity oscillations is twice the frequency of the horizontal velocity oscillations at point B1. Reymond et al. [104] also reported a similar pair of frequencies governing the oscillations; they observed peak frequencies at 0.016 Hz and 0.008 Hz for a spacing of $S = 1.5D$ and $2D$ and a Rayleigh number of 6×10^6. This can be explained by the fact that each time the thermal plume oscillates around the centreline from the left side to the right side, it corresponds to one full period for $V_y(t)$ but only half a period for $V_x(t)$. Figures 5.16c and 5.16d show a peak frequency $f_2 = 0.00977\ Hz$ for the Nusselt number at point $A2$ and both velocity components at point $B2$.

Figure 5.17a shows the magnitude and phase angle of the coherence spectrum $C_{A1,B1}$ between the Nusselt number at point $A1$ and the velocity components at point $B1$. Similarly, Fig. 5.17b shows the coherence spectrum $C_{A2,B2}$ between the Nusselt number at point $A2$ and the velocity components at point $B2$.

Figures 5.16a and 5.16b show a sharp peak frequency at $f_1 = 0.0195\ Hz$ while 5.17a shows a broad range of high coherence at low frequencies up to approximately 0.03 Hz with a peak at $f_3 = 0.0234\ Hz$. This suggests that the oscillations at points $A1$ and $B1$ follow a coherent periodic pattern with a base frequency f_3. In the low frequency range up to 0.03 Hz, Fig. 5.17a shows a strong correlation

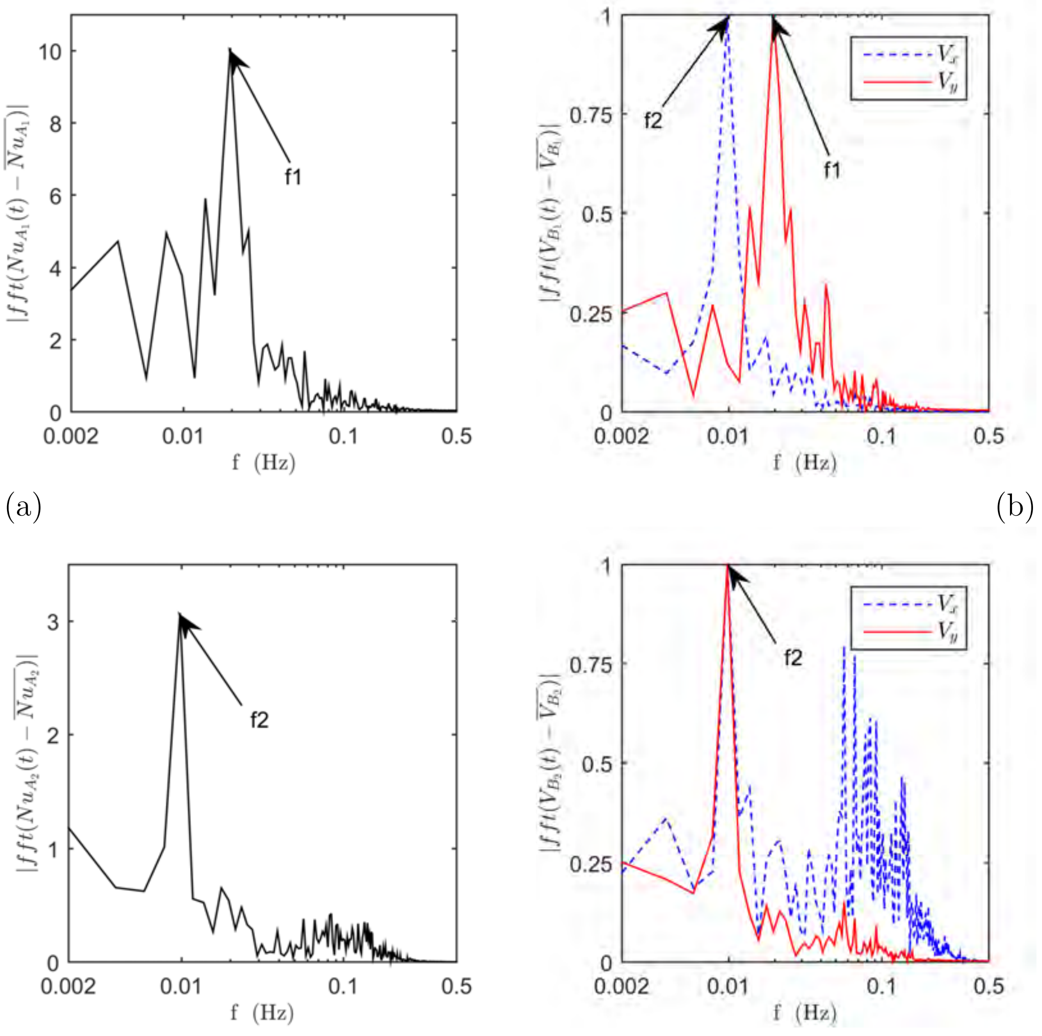

(a) (b)

(c) (d)

Figure 5.16: FFT amplitude spectrum for (a) local Nusselt number at point $A1$ ($\theta = 0°$), (b) (normalized FFTs) velocity components V_x and V_y at point $B1$, (c) local Nusselt number at point $A2$ ($\theta = -90°$) and (d) (normalized FFTs) velocity components V_x and V_y at point $B2$ (see Fig. 5.13) ($Ra = 3.35 \times 10^6$, $S = 3D$).

between the Nusselt number at $A1$ and the vertical velocity at $B1$, even though both locations are separated by a distance $\Delta y_{A1B1} = (S - D)/2 = D$. The correlation between Nusselt number at $A1$ and the horizontal velocity at $B1$ is small throughout the entire frequency range.

Figure 5.17a shows that the coherence phase angle near the peak frequency

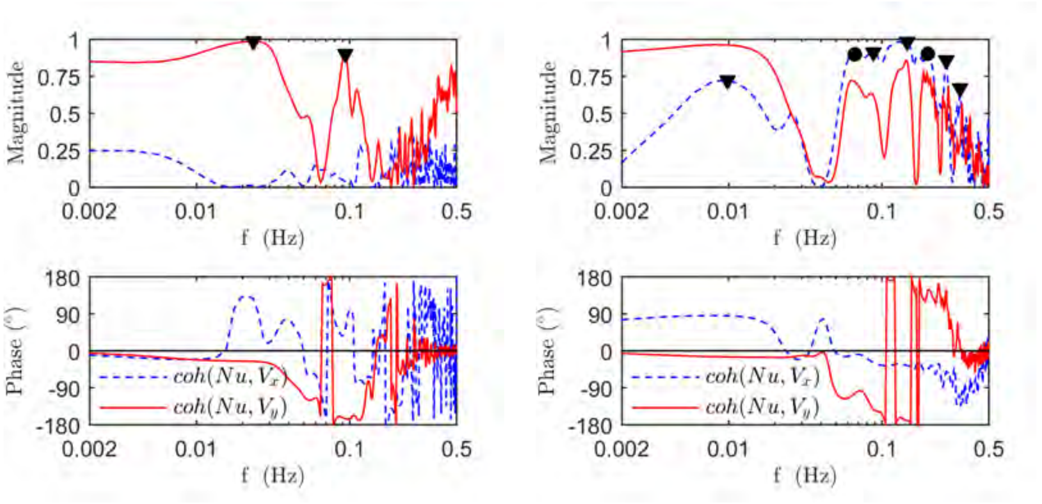

(a) (b)

Figure 5.17: Magnitude and phase angle of the coherence spectrum (a) between local Nusselt number at $A1$ and velocity components V_x and V_y at $B1$, (b) between local Nusselt number at $A2$ and velocity components V_x and V_y at $B2$ ($Ra = 3.35 \times 10^6$, $S = 3D$).

f_1 is slightly negative ($\Phi_1 \approx -25°$), which indicates that the Nusselt number at $A1$ lags the vertical velocity at $B1$ by $(\Phi_1/360)/f_1 \approx 3.6\ s$. Considering the distance between locations $A1$ and $B1$ (see Fig. 5.13), one can assume than this lag is mainly due to the time it takes the rising fluid inside the thermal plume to be advected from point $B1$ to the stagnation zone near point $A1$. For comparison, based on the value of the reference velocity V_{ref} and distance between points $A1$ and $B1$, the estimated bulk advection time would be $\Delta t = \Delta y_{A1B1}/V_{ref} = 8.8\ s$. However, this can be considered an overestimation since the reference plume velocity is averaged over the full plume width, and the peak velocity in the centre of the plume is about double this average, which means that the time lags are indeed comparable. This advection time lag has been verified for other points in the flow field, and therefore this seems a reasonable explanation for the observed phase lag in Fig. 5.17a.

Interestingly, Fig. 5.17b shows different peak frequencies (marked by triangles and circles) in the coherence spectrum between the Nusselt number on the side of the cylinder (at $A2$) and the velocity components adjacent to that location (at $B2$, a distance $b/2$ from $A2$). Compared to the coherence with the flow below the cylinder (Fig. 5.17a), the coherence between the Nusselt number and the horizontal velocity V_x is much more pronounced alongside the cylinder (Fig. 5.17b).

A peak frequency is observed at $f_2 = 0.00977\ Hz$ (leftmost triangular marker in Fig. 5.17b) which confirms the FFT results shown in Fig. 5.16c and 5.16d. Alongside the cylinder the Nusselt number and both velocity components follow a periodic pattern at the frequency $f_2 = 0.00977\ Hz$. Four distinct peaks at higher frequencies are assumed to be harmonics of this frequency f_2; these are marked by triangles in Fig. 5.17b ($0.08789\ Hz = 9f_2$, $0.1465\ Hz = 15f_2$, $0.2637\ Hz = 27f_2$ and $0.3223\ Hz = 33f_2$.

However, two other peaks can be discerned at $f_4 = 0.06641\ Hz$ and its harmonic at $0.1992\ Hz = 3f_4$. The peak frequency f_4 which can also be observed in the Fourier transform of the horizontal velocity fluctuations, indicates that another periodic pattern is present in the variations of the Nusselt number at point $A2$ and the velocity at point $B2$, especially its horizontal components V_x. This high frequency suggests that rapid variations (the period of these oscillations is $1/f_4 \approx 15\ s$) in the instantaneous heat transfer occur in parallel to the slow fluctuations due to the swaying of the plume (the period is $1/f_2 \approx 100\ s$). The phase angle at this frequency is found to be $\phi_4 = -11.5°$ which indicates that the Nusselt number at point $A2$ lags the horizontal velocity at point $B2$ by $(-11.5/360)/0.06641 \approx 0.5\ s$.

The relationship between flow velocity and Nusselt number on the side of the cylinder can lead to a better understanding of how the buoyant plume dynamics affect the heat transfer characteristics of the upper cylinder. An interpretation of these two periodic phenomena (one characterised by f_1 and f_2 and the other one by f_4) is given in the following section.

In order to better characterise the oscillatory nature of this flow for the entire range of Rayleigh number and cylinder spacing, these three peak frequencies f_1, f_2 and f_4 are represented by dimensionless Strouhal numbers $Sr_1 = 0.171$,$Sr_2 = 0.086$ and $Sr_4 = 0.58$ where

$$Sr = \frac{fD}{V_{ref}} \tag{5.6}$$

Unsteady RANS simulations have been carried out for all test conditions in Table 5.1. The results are analyzed in a similar way as described above for the arbitrarily selected dataset ($Ra = 3.35 \times 10^6$, $S = 3D$), and are summarized in Table 5.2.

Based on the data in Table 5.2, two empirical power law correlations are least squares fitted to the reference plume velocity and the secondary peak Strouhal number, representing the peak oscillation frequency along the side of the cylinder. The reference plume velocity increases monotonically with both Rayleigh number and cylinder spacing, towards a maximum velocity for the single cylinder case (represented by $S/D = \infty$ in Table 5.2). However, the single cylinder case was not taken into account in least square fitting the correlation:

$$V_{ref} = 8.77 \times 10^{-6} Ra^{0.33} \left(\frac{S}{D}\right)^{0.85} \tag{5.7}$$

This correlation shows an RMS deviation of 2.7% and a coefficient of determination $R^2 = 0.98$. The Strouhal number at the side of the cylinder (Sr_2) does not exhibit a strictly monotonic behaviour, yet as a first approximation, Sr_2 decreases for both increasing Rayleigh number and cylinder spacing. For the single cylinder cases, the results for the time history of the Nusselt number at $\theta = 0°$ (corresponding to point $A1$) did not exhibit significant oscillation, and thus no values are obtained for those cases, which agrees with the results of Grafsronningen and Jensen [107].

$$Sr_2 = 219 Ra^{-0.47} \left(\frac{S}{D}\right)^{-1.05} \tag{5.8}$$

This correlation shows an RMS deviation of 24.6% and a coefficient of determination $R^2 = 0.75$. The primary Strouhal number (Sr_1) representing the peak oscillation frequency in the region directly below the cylinder exhibits a maximum of $Sr_1 \approx 0.17$ for the intermediate condition of $Ra = 3.35 \times 10^6$ and $S = 3D$, and therefore does not collapse well to a power law correlation such as Eqs. 5.7 and 5.8. As noted by Persoons et al. [105], the Strouhal number values are comparable in magnitude to those found for vortex shedding behind a cylinder in forced cross-flow with an approach velocity of V_{ref} ($Sr = 0.19 \pm 0.01$) [167]. The following section will examine the unsteady flow fields in the thermal plume in more detail, with particular emphasis on the relationship between vortices and heat transfer enhancement.

5.3.3 Discussion: Effect of vortices in the oscillating plume on the local heat transfer coefficient

Figure 5.18 shows instantaneous velocity magnitude distributions and streamlines around the upper cylinder. Similar results have been obtained from experiment and are shown in Fig. 11 of Persoons et al.'s paper [105]. The colour scale

Table 5.2: Summary of frequency analysis based on URANS results. The dimensionless frequencies Sr_1 and Sr_2 represent peak coherence between Nusselt number and velocity between points $A1$ and $B1$ (Sr_1), and between points $A2$ and $B2$ (Sr_2). Heat transfer enhancement is related to the equivalent single cylinder case at the same Rayleigh number.

Rayleigh number	Cylinder spacing	Reference velocity	Plume width	Peak Strouhal number		Heat transfer enhancement
Ra	S/D	V_{ref}	b/D	Sr_1	Sr_2	δNu_m
5.33×10^6	∞ (single)	6.2 mm/s	0.53	–	–	–
	4	5.3 mm/s	0.57	0.094	0.033	+4.1%
	3.5	4.2 mm/s	0.47	0.086	0.049	+11.0%
	3	4.1 mm/s	0.50	0.094	0.058	+10.8%
	2.5	3.5 mm/s	0.40	0.101	0.051	+8.6%
	2	2.8/ mm/s	0.43	0.104	0.083	+4.9%
	1.5	2.2 mm/s	0.20	0.145	0.079	+0.8%
3.35×10^6	∞ (single)	5.5 mm/s	0.60	–	–	–
	4	4.4 mm/s	0.77	0.092	0.054	+7.7%
	3	3.4 mm/s	0.53	0.171	0.026	+6.8%
	2	2.4 mm/s	0.43	0.122	0.085	+3.1%
1.70×10^6	∞ (single)	4.0 mm/s	0.62	–	–	–
	4	3.5 mm/s	0.73	0.093	0.042	+5.0%
	3	2.7 mm/s	0.53	0.150	0.075	+6.5%
	2	1.9 mm/s	0.47	0.137	0.167	−0.8%

represents velocity magnitude from 0 to 18 mm/s. Based on the behaviour shown in Fig. 5.18 and on the spectral analysis described in section 5.3.2, the hypothesis has been developed that the fluctuations of the Nusselt number in various points on the cylinder circumference are affected by the combination of (i) the overall swaying of the plume and (ii) smaller scale vortices that periodically form alongside the plume at inflection points. On alternating sides of the cylinder, vortices can be seen to appear, advect, and merge with larger scale recirculating flows surrounding the plume and stretching into the rest of the domain.

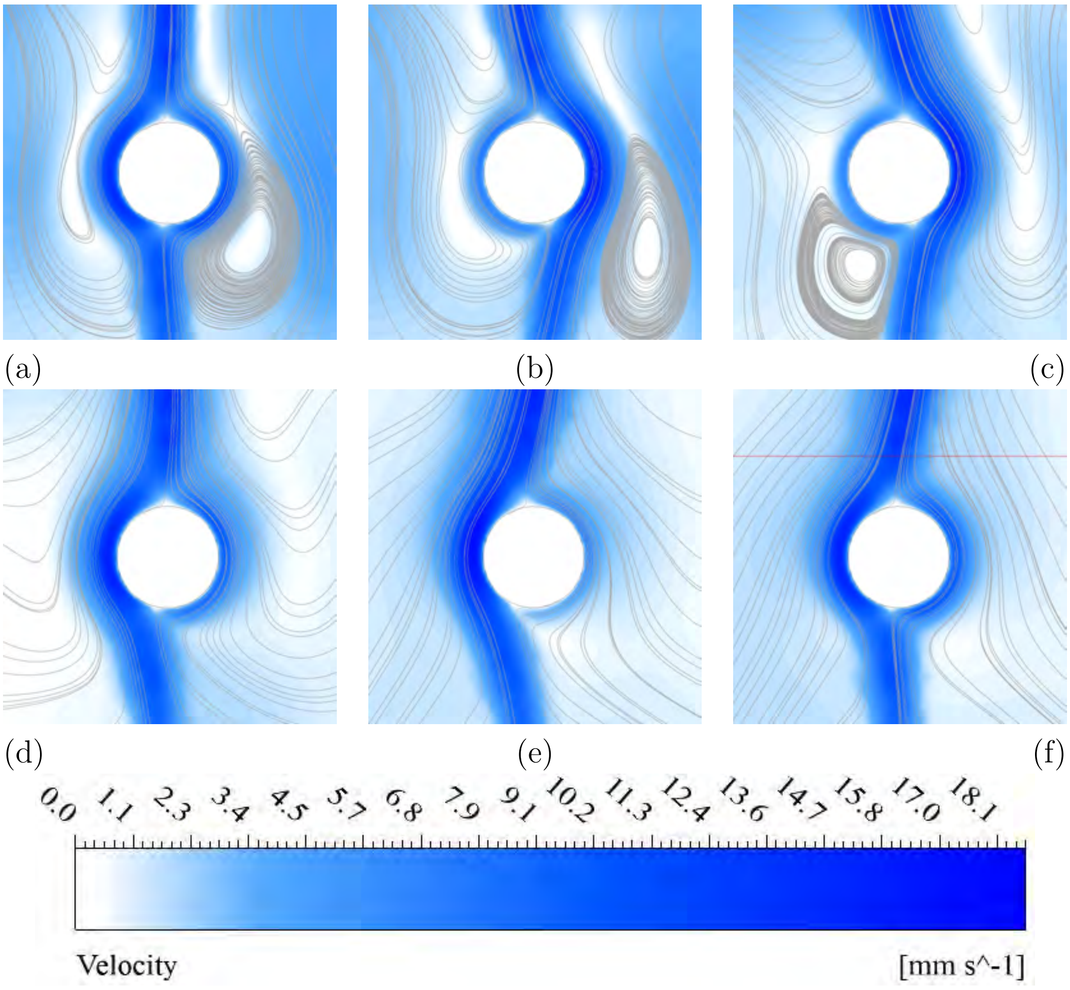

Figure 5.18: Instantaneous streamline and velocity magnitude plot at (a) $t = 280\ s$, (b) 300 s, (c) 320 s, (d) 340 s, (e) 360 s, (f) 380 s, showing one plume oscillation period ($Ra = 3.35 \times 10^6$, $S = 3D$).

Figure 5.18 shows that a vortex is appearing alternately on each side of the upper cylinder, prior to the plume motion at an approximate angular position of $\theta = \pm 40^\circ$ as shown in Fig. 5.18a (where the sign depends on whether the vortex forms on the left or on the right hand side of the cylinder). Consequent to the creation of the vortex, the plume is deflected toward the side where the vortex has developed. The plume remains attached to the side of the cylinder. The vortex is seen to travel around the cylinder with its centre at an approximate distance of b, the plume width, from the cylinder surface, as shown in Fig. 5.18b.

As the vortex propagates (from $\theta = 40^\circ$ to $\theta = 120^\circ$ on the right hand side and similarly on the left hand side of the cylinder), it is stretched vertically, following the plume direction, until it eventually dissipates. When this vortex has almost disappeared at approximately $\theta = \pm 120^\circ$, another vortex forms at the opposite side of the cylinder at a position $\theta \mp 40^\circ$ as shown in Fig. 5.18c. It is worth noting that when this new vortex forms (Fig. 5.18c), the thermal plume arising from the lower cylinder is still attached to the cylinder on the opposite side, i.e. on the side where the previous vortex had been created. Once the new vortex appears, the plume sways towards its side of the cylinder (as seen in Figs. 5.18d and 5.18e) and the pattern is repeated.

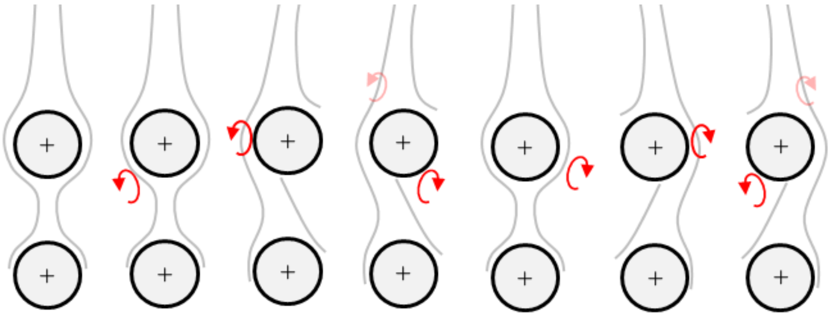

Figure 5.19: Schematics of the stages of (i) plume swaying corresponding to low frequency oscillations of the velocity in between the two cylinders and the local Nusselt number at point $A1$ (ii) vortex formation linked to high frequency fluctuations of the velocity and the local Nusselt number observed at the side of the upper cylinder.

Figure 5.19 shows a schematic diagram which illustrates our interpretation of this pattern. In Fig. 5.19, the thin grey lines represent the outline of the plume as it sways through one full cycle. The curved red arrow represents the two vortices that form on alternating sides of the upper cylinder. In the diagram, the first one forms at $\theta = -40°$ and propagates until it dissipates at $\theta = -120°$, at which time the second vortex forms at $\theta = +40°$. The second vortex then propagates upwards until it dissipates at $\theta = +120°$ and the cycle repeats itself.

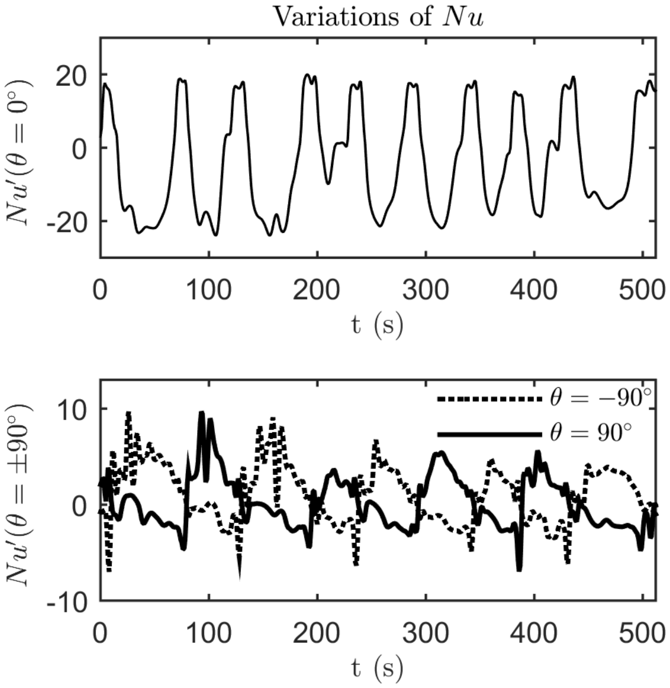

Figure 5.20: Nusselt number variations around a zero mean ($Nu' = Nu - \overline{Nu}$) at (a) point $A1$ ($\theta = 0°$), (b) $A2$ ($\theta = -90°$) and $A3$ ($\theta = +90°$) ($Ra = 3.35 \times 10^6$, $S = 3D$).

Firstly, the plume swaying explains why the dominant frequency of the *Nusselt number* oscillation at points $A2$ and $A3$ on the side of the cylinder (represented by Sr_2) is half the peak oscillation frequency at point $A1$ (represented by Sr_1), at least for most conditions listed in Table 5.2. Indeed, Fig. 5.20 shows the *Nusselt number* variations about the mean value, $Nu' = Nu - \overline{Nu}$, at points $A1$ ($\theta = 0°$), $A2$ ($\theta = -90°$) and $A3$ ($\theta = +90°$). The oscillations of Nu' at points $A2$ and $A3$ are similar in waveform but are 180° out of phase, or shifted by half a period. At each trough of $Nu'(0°)$ in Fig. 5.20a, a peak in the *Nusselt number* is alternately reached in Fig. 5.20b for $Nu'(\pm 90°)$ which explains the factor of two between the peak frequencies Sr_1 and Sr_2.

Secondly, the higher frequency oscillations represented by Sr_4 can be explained by the effect of vortices on local instantaneous heat transfer enhancement and can be illustrated by taking a closer look at the time evolution of the local Nusselt number at point $A2$ and the adjacent transverse (horizontal) velocity V_x at point $B2$. As explained in the previous section, the coherence spectrum revealed a strong dependency between these two signals at a peak frequency of $f_4 = 0.06641\ Hz$ between the Nusselt number and the V_x velocity fluctuations, which could not be explained merely by bulk advection.

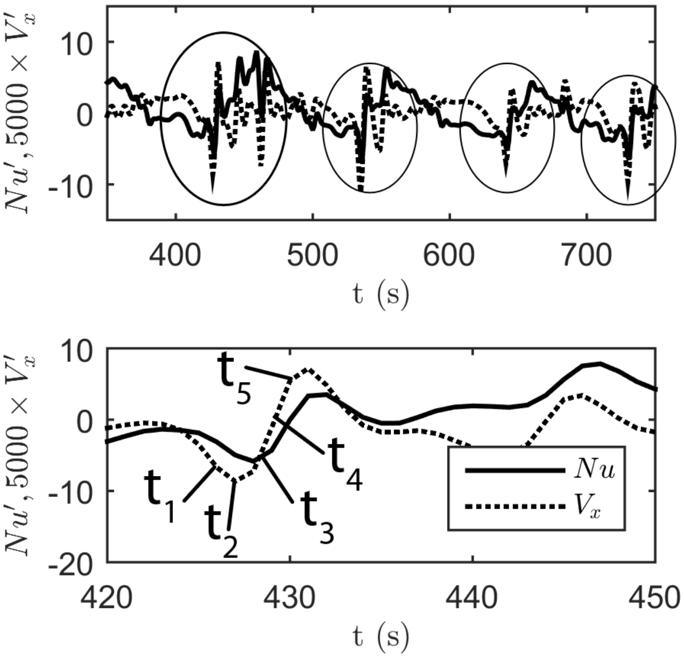

Figure 5.21: Fluctuations of the *Nusselt number* at point $A2$ and the transverse velocity (arbitrarily scaled) at point $B2$ ($Ra = 3.35 \times 10^6$, $S = 3D$). Five indicated events in (b) correspond to the flow fields shown in Fig. 5.22.

Figure 5.21 shows both signals (with subtracted mean and arbitrarily scaled) for (a) a time duration of 400 s, and (b) a close-up view of 30 s corresponding to the leftmost encircled interval on Fig. 5.21a. The two signals are quite similar which confirms the high coherence between them (see Fig. 5.17b). The four encircled events in Figure 5.21a exhibit a repeating pattern with a period corresponding to Sr_2 (here, a frequency $f_2 \approx 0.0097\ Hz$ or period $1/f_2 \approx 100\ s$).

As explained above, this long period represents the plume swaying and alternating between both sides of the cylinder. However, upon closer inspection each encircled event also contains higher frequency oscillations. Figure 5.21b shows these oscillations corresponding to the frequency $f_4 = 0.06641\ Hz$ identified in the coherence spectrum between the Nusselt number at point $A2$ and the velocity at point $B2$ (Fig. 5.17b) and the Fourier transform of the velocity at point $B2$ (Fig. 5.16d). This â˜highâ$^{\text{TM}}$ frequency oscillation is characterised by a period of approximately $1/f_4 \approx 15$ s. In terms of Strouhal number, $Sr_4 = f_4 D/V_r ef \approx 0.58$. A broadly comparable peak frequency was also found experimentally by Persoons et al. [105] ($Sr = 0.46 \pm 0.02$) and Grafsronningen and Jensen [107] ($1/f \approx 7\ s$, $S/D = 2$, $Ra = 5.2 \times 10^7$ corresponding to a Strouhal number $Sr = 0.73$). As shown in Fig. 5.21b, the Nusselt number (solid line) lags the velocity V_x (dotted line) by approximately 0.5 s which confirms the results from the coherence phase lag.

Figure 5.22 and 5.23 show the instantaneous flow fields from the present numerical results and experimental PIV results from Persoons et al. [105] respectively, at the five time instants identified during one of the high-frequency oscillations in Fig. 5.21b. The numerical results show a good agreement with the experiment in terms of vortex size, plume width and velocity magnitude. However a difference is noticeable as the vortex centre reaches the position $\theta = -120°$ in Fig. 5.22e whereas the vortex centre seems to be located at the position $\theta = -90°$ in Fig. 5.23e. The vortex captured numerically is moving faster than what is seen in the experimental results even though the local Nusselt number at point $A2$ is oscillating at the same frequency $f_4 = 0.0664\ Hz$. At $t = t_1$ the plume is still impinging on the bottom of the cylinder although it is already starting to sway towards the left hand side of the cylinder. The swaying is difficult to see in Fig. 5.22 and 5.23 because of the different time scales involved, with a period of $1/f_2 \approx 100\ s$ for plume swaying compared to $1/f_4 \approx 15\ s$ for this high frequency oscillation.

Considering the data shown in Fig. 5.21b, the horizontal velocity fluctuations at point $B2$ are first negative (times t_1, t_2 and t_3), pass by zero at time t_4 and then reach a positive peak at time t_5. This shows that the vortex is rotating in an anticlockwise direction on the left hand side of the cylinder. At $t = t_1$ the anticlockwise vortex shown in Fig. 5.22 is visible with a centre at an angular position $\theta = -40°$. Point $B2$ is at the leading edge of the vortex, with local flow directed away from the cylinder, or negative horizontal velocity fluctuations. This corresponds to a decrease from 0 to -10 approximately in the variations of the local Nusselt number at point $A2$ according to the data shown in Fig. 5.21b.

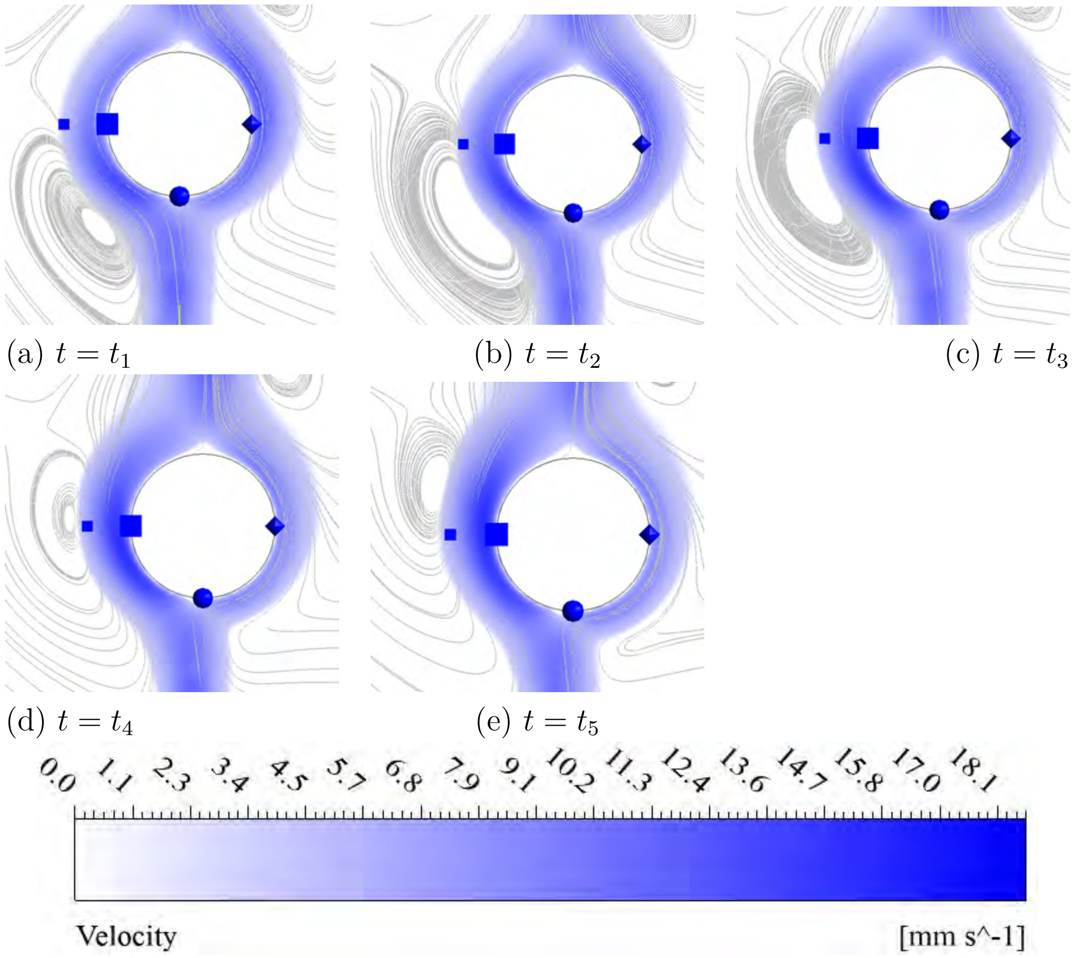
(a) $t = t_1$

(b) $t = t_2$

(c) $t = t_3$

(d) $t = t_4$

(e) $t = t_5$

Figure 5.22: Instantaneous streamline and velocity magnitude corresponding to five events indicated in Fig. 5.21: (a) $t_1 = 426\ s$, (b) $t_2 = 427\ s$, (c) $t_3 = 428\ s$, (d) $t_4 = 429\ s$, (e) $t_5 = 430\ s$. $Ra = 3.35 \times 10^6$, $S = 3D$, with points $A1$, $A2$, $B2$ and $A3$.

Over the next four seconds (t_1 through t_5), the vortex travels from an angular position $\theta = -40°$ to $\theta = -120°$. During that time, the local transverse velocity in $B2$ goes from a negative extremum at $t = t_2$ (i.e., flow pulling away from point $A2$) to a positive extremum at $t = t_5$ (i.e., flow impinging onto point $A2$). This leads to an increase from -10 to $+10$ in the variations of the local Nusselt number at point $A2$.

The URANS simulation enabled us to identify how the variations in transverse velocity at point $B2$ correlate with the variations of Nusselt number at point $A2$. However, the time-averaged local Nusselt number at point $A2$ is 24.1 as is

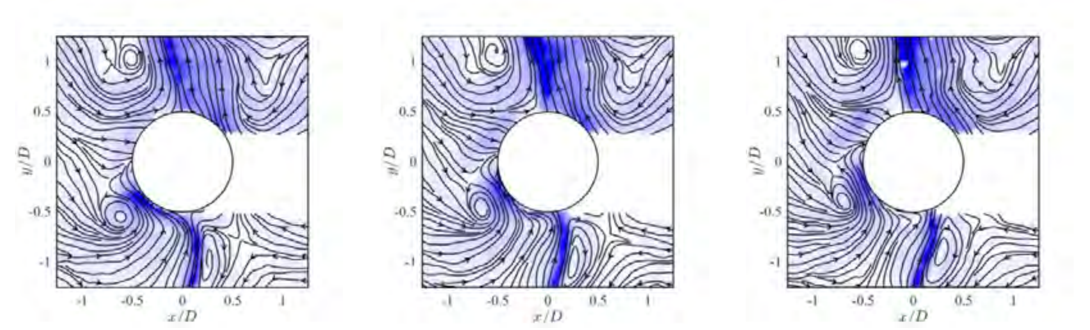

(a) $t = t_1$ (b) $t = t_2$ (c) $t = t_3$

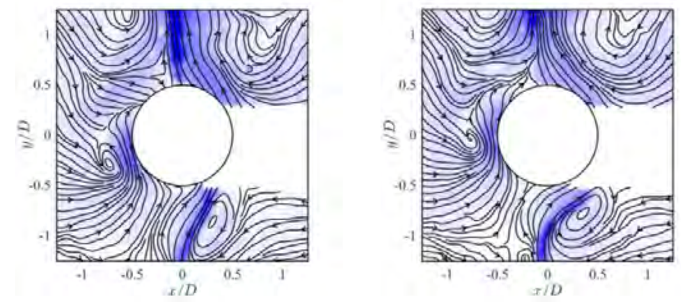

(d) $t = t_4$ (e) $t = t_5$

Figure 5.23: Instantaneous streamline and velocity magnitude (experimental data) corresponding to five events indicated in Fig. 5.21: (a) $t_1 s$, (b) $t_2 = t_1 + 1s$, (c) $t_3 = t_1 + 2s$, (d) $t_4 = t_1 + 3s$, (e) $t_5 = t_1 + 4s$, from PIV data set also presented in Persoons et al. [105].

shown in Fig. 5.5 whereas the time-averaged local Nusselt number of a single cylinder is 23.5 at that same location with the same Rayleigh number, according to the data presented in Fig. 5.2. The difference between the time-averaged local Nusselt number at this location ($\theta = -90°$) and the single cylinder case is only $\delta_{Nu_m(-90°)} = 2.5\%$. The change in local Nusselt number at point $A2$ due to the presence of another cylinder seems not to contribute as much to the global enhancement of the heat transfer potential of the upper cylinder as does the change in local Nusselt number at point $A1$.

5.4 Summary of the chapter

The results from the numerical model developed in Section 4.3 has been compared to experimental data obtained from Persoons et al. [105]. A good agreement is found between the numerical and experimental results, for both the single cylinder and the pair of cylinders cases.

A number of steady RANS simulations were carried out for a range of Rayleigh numbers ($1.7 \times 10^6 \leq Ra \leq 5.3 \times 10^6$) and centre-to-centre cylinder spacing ($1.5 \leq S/D \leq 4$). The overall time-averaged heat transfer rate is found to be affected by both the Rayleigh number and the cylinder spacing, in a similar way to that observed experimentally [105]. Mean heat transfer enhancement results are presented in Fig. 5.11 and Table 5.1, showing a locus of optimum spacing (to achieve maximum enhancement) in the range $3D \leq S \leq 4D$ and $4.7 \times 10^6 \leq Ra \leq 5.3 \times 10^6$, with more pronounced enhancement for increasing Rayleigh number. A maximum enhancement of $\delta Nu \approx +11\%$ was observed for $Ra = 5.33 \times 10^6$ and $S = 3.5D$.

For all conditions described in Table 5.1, an unsteady RANS simulation was also carried out. After an initial non-oscillating start-up, regimes of quasi-periodic plume oscillations alternating with seemingly random fluctuations were observed in the numerical results and two regimes characterized by two different frequencies were identified. Having observed remarkably similar unsteadiness in the previous experiments [105], this agreement further confirmed the validity of the numerical methodology. Fourier transforms and coherence spectra were calculated for local Nusselt number and flow velocity signals, extracted from different points in the domain. A strong periodicity and coherence between heat transfer and flow velocity was observed. Trends were analysed in the peak oscillation frequencies (expressed as dimensionless Strouhal numbers) for the entire investigated range of Ra and S/D.

The unsteady results were analysed in further detail, yielding interpretations for the two main time scales in this flow, resulting from (i) slow large scale swaying of the buoyant plume with a period of approximately 100 s and (ii) faster dynamics of vortices forming adjacent to the plume with a corresponding time scale of approximately 15 s., and their effect on local instantaneous heat transfer enhancement has been discussed. Based on the present study, the low frequency (i.e., large time scale) fluctuations correspond to the swaying of the thermal plume rising from the lower cylinder. This phenomenon affects the overall heat transfer of the upper cylinder to a greater extent than the high frequency fluctuations associated with the formation and propagation of vortices at the side of the upper cylinder.

Overall, the availability of detailed time-resolved flow and heat transfer data from the URANS simulations has provided insight into this flow beyond the practical limitations of experimental measurements [105]. However, the experimental data was indispensable to validate the numerical model. Therefore, only by combining the strengths of both approaches was this study (in combination with the previous work [105]) able to provide explanations for the intricate dynamics of this natural convection configuration. The details of this numerical work, the comparison with experimental data and the discussion of the results, have been published by Pelletier et al. [106].

Chapter 6

Numerical results: Shape optimization using genetic algorithms

This Chapter is dedicated to the study of design optimization, by the use of genetic algorithms, and its potential for cooling devices improvement. The numerical shape optimization procedure introduced in Section 4.4 is validated against analytical results from the literature [23,24] in Section 6.2. Section 6.3 presents the results from the numerical shape optimization study of two-dimensional elongated fins in forced convection that has been performed using the shape optimization model derived in Section 4.4.

6.1 Background and motivation

In order to study the possibility of heat transfer enhancement by optimizing the shape of the structure subjected to heat transfer, the understanding of the numerical shape optimization procedure that is used is necessary. Therefore, the performance of the shape optimization method developed in Section 4.4 must be validated against trusted data. Secondly, with the idea of moving towards heat/mass transfer structures of high complexity, the study of the shape optimization of a heat sink composed of three, and later on, five fins is presented in Section 6.3. This study corresponds to another step as illustrated in Fig. 4.2.

It is important to recall that, because of the increasing complexity of the problem due to the non-linear coupling through the advection term in the heat equation of the Navier-Stokes equations and the heat transfer phenomena in general, and finally because the objective of discovering a global optimal shape that maximizes the overall heat transfer from a complex structure without any information about the fitness landscape of the problem (smoothness, number of local optima, etc...), the approach of Darwinist evolution has been chosen, by the means of a genetic algorithm.

The objectives of the studies presented in Chapter 6 are

- to validate the numerical shape optimization procedure presented in Section 4.4, based on analytical studies [23, 24] as presented in Section 6.2

- to study how genetic algorithms operate when combined with CFD simulations, and how the GA tuning parameters affect the determination of the optimal solution as presented in Section 6.3.3

- to study the flow and interactions captured for the simulated optimal shape solution in order to understand why this particular design is the fittest as presented in Section 6.3.4

6.2 Validation of the ANSYS MOGA optimization tool

This section presents the case and results of an ANSYS MOGA optimization that has been compared to the analytical solution to this optimization problem. The objective is to determine the optimal spacing for maximum heat transfer from a stack of parallel heated infinite plates, arranged in a fixed two-dimensional volume, that are cooled by forced convection.

6.2.1 Analytical analysis

In order to determine the spacing that maximizes the overall heat transferred from the plates to the coolant fluid analytically, one can use the asymptotic analysis, or order of magnitude analysis as explained in the introduction. This approach is precisely described by Bejan et al. [23, 24] for both laminar and turbulent cases and a summary of the development of the analysis is presented here.

Let us consider the geometry of Fig. 6.1. A set of parallel plates of length L and thickness t, each of them heated at the uniform temperature T_w, are confined in a volume $H \times L$ and spaced by the distance D. An incoming flow, parallel to the plates, with a free stream at temperature T_∞ is created by imposing a pressure head ΔP across the volume $H \times L$. To determine the optimal spacing D between the plates is the same as determining the optimal number of plates n inside the volume of thickness H

$$n \approx \frac{H}{D+t} \tag{6.1}$$

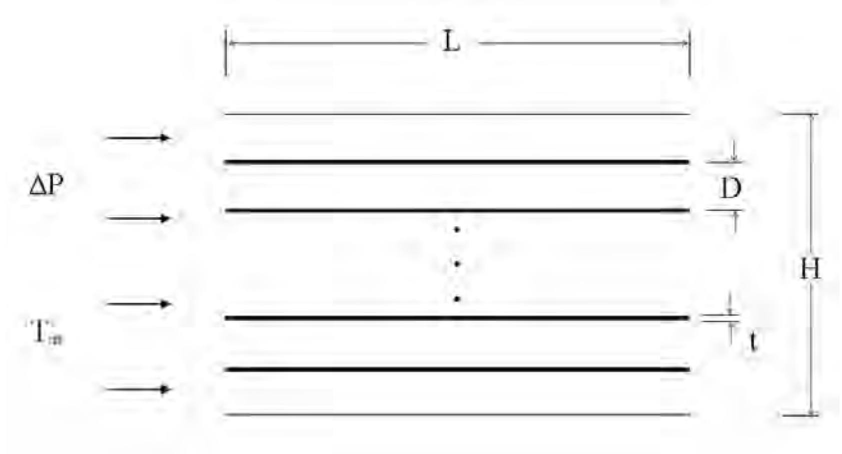

Figure 6.1: Stack of parallel plates cooled by forced convection [23]

Intuitively, if the plates are far apart, there is a small number of plates inside the fixed volume so the total heat transferred to the coolant fluid is low. On the other hand if the number of plates inside the channel is increased up to the point where the plates touch each other, the fluid is prevented from flowing and the overall heat transfer drops. So there is a situation in between these two extreme situations, where the overall heat transfer is maximum.

6.2.1.1 Laminar forced convection

A laminar forced convection and $t \ll D$ are assumed so that Eq. 6.1 becomes

$$n \approx \frac{H}{D} \tag{6.2}$$

a) Small D limit.

If the limit $D \to 0$ is considered, the developing length of the thermal boundary layers x^* in each channel formed by two consecutive plates is really small compared to the plate's length L; $x^* \ll L$. Therefore the fluid outlet temperature is T_w and the average fluid velocity of this plane Poiseuille flow is given by Eq. 6.3

$$U = \frac{D^2}{12\mu}\frac{\Delta P}{L} \tag{6.3}$$

The total mass flow rate through the entire stack per unit of depth $\dot{m}'$is then

$$\dot{m}' = \rho U H = \rho H \frac{D^2}{12\mu}\frac{\Delta P}{L} \tag{6.4}$$

where ρ is the fluid density.

The total heat transfer rate from the entire stack to the fluid is

$$q_a' \approx \dot{m}' c_p (T_w - T_\infty) = \rho H \frac{D^2}{12\mu}\frac{\Delta P}{L} c_p (T_w - T_\infty) \tag{6.5}$$

In conclusion, in the limit $D \to 0$, the total heat transfer rate decreases as D^2 as illustrated qualitatively in Fig. 6.2.

b) Large D limit.

In the opposite case, where $D \to \infty$, the boundary layers developing on each surface are distinct, that is to say: each channel looks like the entrance of a parallel-plate duct. The overall force balance on the whole volume $H \times V$ requires

$$\Delta P \cdot H = 2n\overline{\tau_w}L \tag{6.6}$$

where n is the number of channels and $\overline{\tau_w}$ is the L-averaged wall shear stress

$$\overline{\tau_w} = Cf_L \cdot \frac{1}{2}\rho U_\infty^2 = 1.328 Re_L^{-1/2}\frac{1}{2}\rho U_\infty^2 \tag{6.7}$$

using the empirical correlation $Cf_x = \frac{0.664}{\sqrt{Re_x}}$ for the laminar boundary layer.

Combining Eq. 6.6 and 6.7 yields

$$U_\infty = \left(\frac{1}{1.328}\frac{\Delta P \cdot H}{nL^{1/2}\rho\nu^{1/2}}\right)^{2/3} \tag{6.8}$$

The total heat transfer rate from one surface (per unit of depth) q_1' is derived from the overall Nusselt number

$$\overline{Nu_L} = \frac{\overline{h}L}{k} = \frac{\overline{q_1'}}{T_w - T_\infty}\frac{L}{k} = 0.664 Pr^{1/3} Re_L^{1/2} \tag{6.9}$$

where $\overline{q_1'}$ is the L-averaged heat flux per unit of depth.

The total heat transfer rate from the entire stack of n channels, that is to say $2n$ surfaces is

$$q_b' = 2nq_1' = 2nL\overline{q_1'} = 2nk(T_w - T_\infty)0.664 Pr^{1/3} Re_L^{1/2} \tag{6.10}$$

Using Eq. 6.2 and 6.8 for the expressions of n and U_∞, the total heat transfer rate becomes

$$q_b' = 1.208k(T_w - T_\infty)H\frac{Pr^{1/3}L^{1/3}\Delta P^{1/3}}{\rho^{1/3}\nu^{2/3}D^{2/3}} \tag{6.11}$$

The second conclusion is that the heat transfer rate from the entire stack decreases with $D^{-2/3}$ when $D \to \infty$ as shown qualitatively on Fig. 6.2.

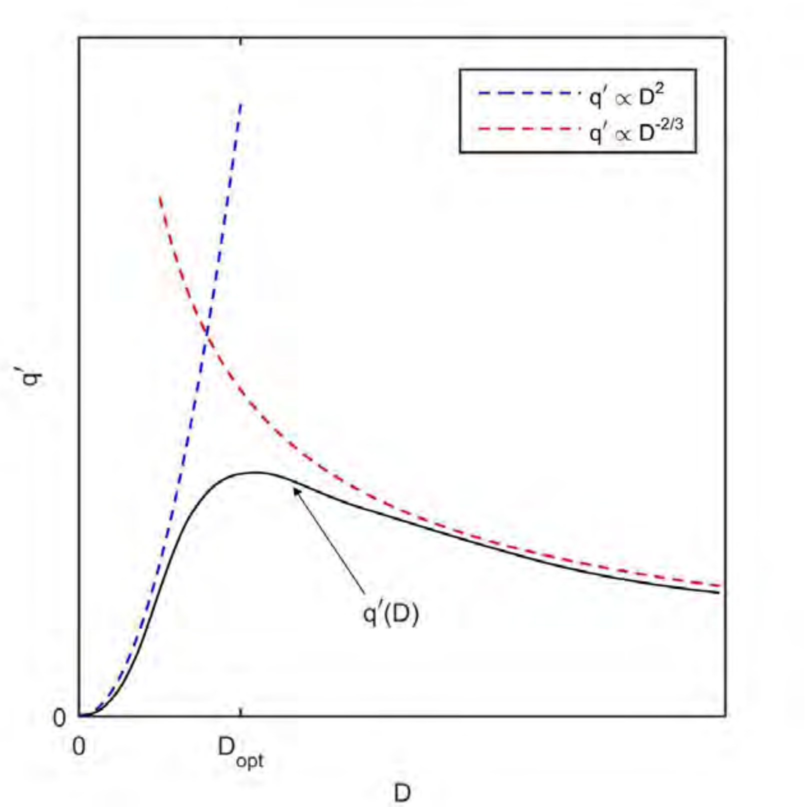

Figure 6.2: Determining the optimal spacing by intersecting the asymptotes 6.5 and 6.11.

Figure 6.2 suggests that the unknown curve $q'(D)$ reaches a maximum for a value D_{opt} that is of the same order as the D value obtained by intersecting the two asymptotes:

$$\frac{D_{opt}}{L} \approx 2.73\left(\frac{\mu\alpha}{\Delta P \cdot L^2}\right) \tag{6.12}$$

where μ and α are the viscocity and thermal diffusivity of the coolant fluid [23].

6.2.1.2 Turbulent forced convection

Bejan et al. performed a similar analysis to determine the optimal board-to-board spacing between parallel plates cooled by turbulent forced convection [24]. The configuration is the same as for the laminar case except for the board thickness that is not necessarily negligible compared to the board-to-board spacing so that $t \ll D$ doesn't hold anymore and Eq. 6.1 is not simplified so that $n \approx H/(D+t)$.

a) Small D limit.

When $D \to 0$, the board-to-board spacing is small enough so that a fully developed turbulent flow goes through each channel defined by two consecutive half-plates and the outlet temperature is the the same as the board temperature. The total heat removed from the entire stack is then

$$q'_a \approx \dot{m}' c_p (T_w - T_\infty) \tag{6.13}$$

where $\dot{m}' = n\rho U D$ is the mass flow rate, with U the average velocity through each channel in the case of a fully developed turbulent flow:

$$U = \left(\frac{D\Delta P}{\rho L f} \right)^{1/2} \tag{6.14}$$

where f is the friction factor.

The $D \to 0$ asymptote of the total heat transfer rate from the entire stack is then

$$q'_a = \frac{H c_p (T_w - T_\infty)}{1 + \frac{t}{D}} \left(\frac{\rho D \Delta P}{L f} \right)^{1/2} \tag{6.15}$$

b) Large D limit.

In the opposite extreme, a boundary layer develops on each board while the fluid at the core of each channel flows at the velocity U_∞ and is at the coolant temperature T_∞. By assuming that the force experienced by each board is dominated by skin friction, a force balance on the whole control volume $H \times L$ gives

$$H\Delta P = 2n\overline{\tau}L \tag{6.16}$$

where $\overline{\tau}$ is the L-averaged wall shear-stress. Combining Eq. 6.16 and the definition of the skin friction coefficient $C_f = \frac{\overline{\tau}}{\frac{1}{2}\rho U_\infty^2}$ yields

$$U_\infty = \left(\frac{H\Delta P}{n\rho L C_f}\right)^{1/2} \tag{6.17}$$

The total heat transfer rate from one plate q'_1, that is to say through one boundary layer, is

$$q'_1 = \overline{q'_1} \cdot L = St \cdot L\rho c_p U_\infty (T_w - T_\infty) \tag{6.18}$$

where $\overline{q'_1}$ is the L-averaged heat flux and St is the Stanton number

$$St = \frac{1}{2} C_f Pr^{-2/3} \tag{6.19}$$

Eq. 6.19 is derived using the Colburn analogy between momentum and heat transfer in the boundary layer flow.

Finally, recombining Eq. 6.18 and Eq. 6.17 and noticing that the total heat transfer rate from the entire stack equals the heat transfer rate from one board, multiplied by the number of boards $2n$ where n is the number of channels, leads to the $D \to \infty$ asymptote of $q'(D)$

$$q_b' = 2nq_1' = Hc_p(T_w - T_\infty)Pr^{-2/3}\left(\frac{\rho L C_f \Delta P}{t+D}\right)^{1/2} \tag{6.20}$$

In conclusion, in the turbulent case, the heat transfer rate from the entire stack increases with D when D is small and decreases with D when D is large. This means that there is a D value for which the heat transfer rate from the $2n$ boards is maximized. By intersecting the two asymptotes corresponding to Eq. 6.15 and 6.20, Bejan et al. conclude with a prediction of the optimal spacing D_{opt} as a function of the pressure difference ΔP, the Prandtl number Pr and the plate slenderness t/L, as shown in Fig. 6.3 [24].

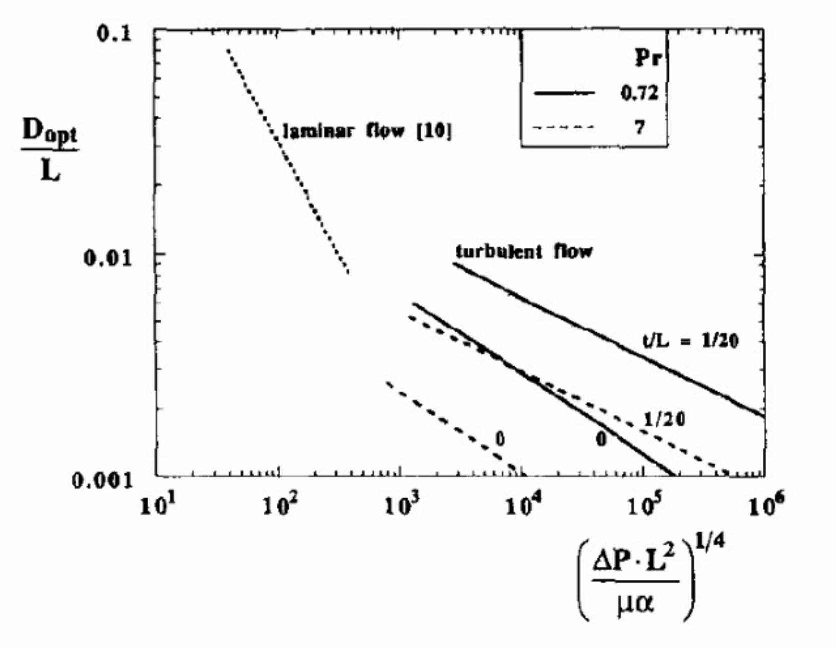

Figure 6.3: The optimal spacing as a function of ΔP, Pr and t/L. From [24]

6.2.2 Parallel plate spacing optimization using a genetic algorithm

In order to assess the efficacy of a genetic algorithm coupled with CFD simulations, the MOGA algorithm implemented in ANSYS has been used to search for an optimal solution to the optimization problem discussed in the previous section and compare its results with the analytical results described above.

6.2.2.1 Parametrization of the problem

The first stage is to design and parametrize a CFD simulation that can represent the problem previously described. The situation is rather simple here: one of the channels defined by two consecutive half-plates of length L and thickness $t/2$ is considered as shown in Fig. 6.4. They are separated by a distance D and are heated at the same temperature $T_w = 323\ K$. An outlet pressure boundary condition with $P_{out} = P_0 = 101325\ Pa$ and an inlet pressure BC with $P_{in} = P_0 + \Delta P$ and $T_\infty = 293\ K$ are imposed. The total heat transfer rate from the two half-plates q'_1 is defined as the output and is used to attribute a fitness to each geometrical configuration. The CFD model used for this optimization in the case of turbulent forced flow, is the same as the one developed and presented in Chapter 4.3.

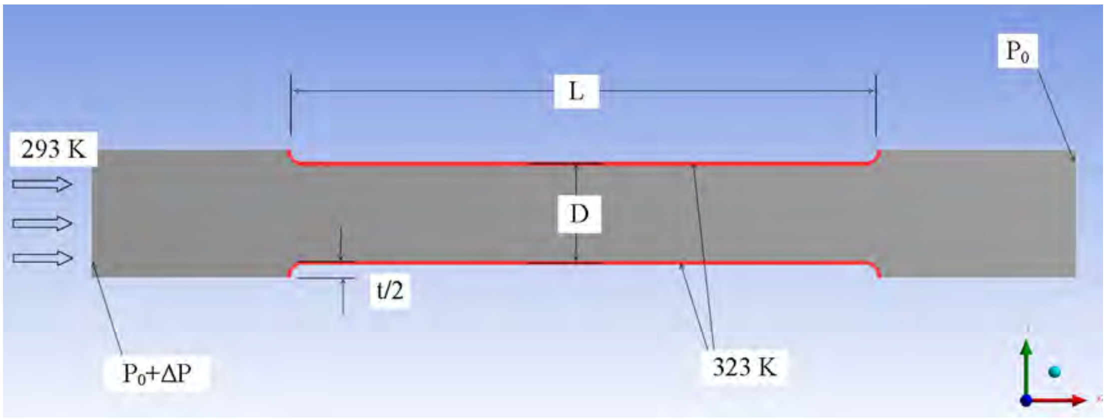

Figure 6.4: Geometry and boundary conditions of the parallel plates cooled by forced convection.

Four different combinations of the parameters t/L, ΔP and turbulence models are investigated as presented in Table 6.1

Table 6.1: Investigated configurations for the optimization of the parallel plates forced convection

optimization $n°$	t/L	ΔP (Pa)	Turbulence model
1	$\ll 1$	0.5	Laminar
2	$\ll 1$	5	Laminar
3	1/20	10k	kw-SST
3	1/20	25k	kw-SST

6.2.2.2 Optimization settings

In order to search for the optimal spacing D between the parallel plates contained in a fixed volume $H \times L$, the objective of the optimization is set to maximizing the total heat transfer rate from the entire stack q', that is to say the heat transfer rate from one channel q'_1 multiplied by the number of channels $n \approx H/(D+t)$ that fits the volume $H \times L$:

$$q' = q'_1 \times n = q'_1 \times \frac{H}{D+t} \tag{6.21}$$

where H is arbitrarily set to 200 mm in these simulations.

The MOGA algorithm is used with an initial population size of 50 individuals, a cross-over and mutation probability of $p_c = 0.9$ and $p_m = 0.01$ respectively and a target stability percentage $S = 2\%$ for the termination.

6.2.2.3 Results from MOGA

The results obtained from the four optimization processes are described and compared using non-dimensional values for the board-to-board spacing $\frac{D}{L}$ and the pressure drop $\left(\frac{\Delta P \cdot L^2}{\mu\alpha}\right)^{1/4}$ or a combination of these numbers

$$\delta = \frac{2D}{L}\left(\frac{\Delta P \cdot L^2}{\mu\alpha}\right)^{1/4} \tag{6.22}$$

where $2D = D_h$ is the hydraulic diameter. The non-dimensional heat transfer rate is also used and is defined as

$$q'_{norm} = \frac{q'}{(\rho \Delta P/Pr)^{1/2} \cdot H c_p (T_w - T_\infty)} \tag{6.23}$$

Using these non dimensional numbers, the two asymptotes for the heat transfer rate removed from the entire stack in the limits $D \to 0$ and $D \to \infty$ simplify; basically for the laminar forced convection, Eq. 6.5 and 6.11 respectively become

$$q'_{a,norm} = \frac{1}{12} \left(\frac{\delta}{2} \right)^2 \tag{6.24}$$

$$q'_{b,norm} = 1.208 \left(\frac{\delta}{2} \right)^{-2/3} \tag{6.25}$$

Results of the total non-dimensional heat transfer rate q'_{norm} obtained for some of the individuals evaluated through the advancement of optimization $n°1$ (see Table 6.1) as a function of the board-to-board spacing are shown in Fig. 6.5. They are compared to the results of Bejan et al. [23]. As it is shown on Fig. 6.5, the total heat transfer rate from the entire stack of parallel plates is underestimated in the present simulations compared to the theoretical value calculated by Bejan et al. [23]. This could be due to the fact that Bejan et al. assumed $t \ll L$ so that the total force experienced by the the plates (used in their force balance evaluation) is only due to friction. However more interestingly, the location, on the x-axis, of the optimal board-to-board spacing that maximizes the overall heat transfer rate q'_{norm} from the present work's optimization agrees well with the analytical results from [23]. Moreover, as shown by the two curves $q'_{a,norm}$ and $q'_{b,norm}$ on Fig. 6.5, the asymptotic behavior of the heat transfer rate evaluated numerically as a function of the board-to-board spacing agrees with the order-of-magnitude study described in the previous section. Both analytical and numerical optimization studies conclude with the optimal spacing

$$\frac{\delta_{opt}}{2} = \frac{D_{opt}}{L} \left(\frac{\Delta P \cdot L^2}{\mu \alpha} \right)^{1/4} \approx 3.033 \tag{6.26}$$

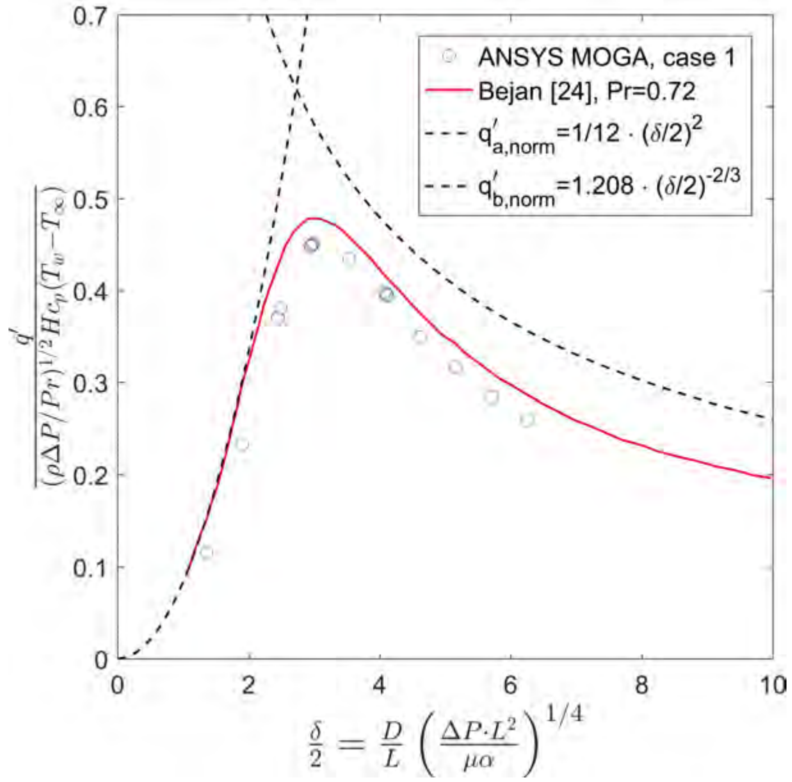

Figure 6.5: The optimal board-to-board spacing for maximum heat transfer.

The results obtained from the four investigated cases presented in Table 6.1 are plotted against the imposed pressure drop and compared to the analytical results from Bejan et al. [24] in Fig. 6.6. The results for board-to-board optimal spacing D_{opt}/L from the present MOGA investigations define two distinct regimes (laminar and turbulent) that are in good agreement with the analytical study.

This study shows that there is an optimal board-to-board spacing D_{opt} that maximizes the total heat transfer rate from a stack of parallel plates inside a fixed volume $H \times L$ in the case of forced convection generated by a pressure drop ΔP. This optimal spacing has been determined both analytically using an asymptotic analysis [23,24], and numerically using the ANSYS MOGA genetic algorithm. The results from the two methods are in good agreement and this comparison is used as a validation of the numerical optimization approach. It is important to notice that the validity of the MOGA approach stands for both laminar and turbulent cases. However, although GAs can show a strong potential, as it is the case in this study, the user must be aware that the good agreement found between the analytical and

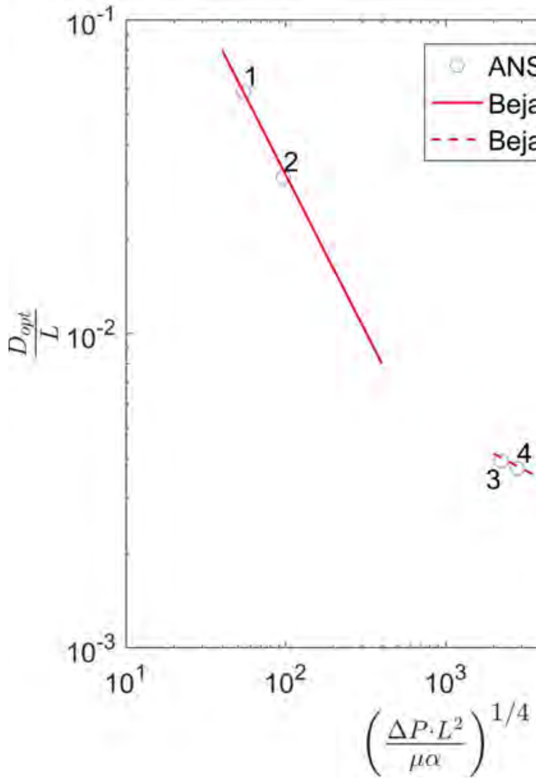

Figure 6.6: Comparison between present work MOGA results and analytical results [24] with $Pr = 7$ and $t/L = 1/20$

numerical optimizations may depend on the parameters that have been chosen for the ANSYS MOGA (initial population size, cross-over and mutation rates,...) and must then be careful on how to tune genetic algorithms in future studies.

6.3 Results and discussion: optimization of a generic plate-fin heat sink in cross-flow

6.3.1 Description of the simulation

The CFD model coupled with the ANSYS MOGA genetic algorithm validated in the previous section can now be used for maximizing the heat transfer from two-dimensional fins in cross flow. This section is dedicated to the study of the optimization of a new problem, more specifically, on how the results obtained from the MOGA can be trusted, and what are the effects of the GA's initial population size on the results. A discussion on the MOGA results is also developed.

The problem posed here is to optimize the design of a heat sink placed in a stream of coolant fluid. A $H \times L = 40$ mm × 40 mm heat sink is composed of three, and later on, five 16 mm × 2 mm fins with rounded corners with a radius of curvature $r = 0.8\ mm$. The $H \times L$ fixed volume is placed in a 500 mm × 200 mm channel as shown in Fig. 6.7. An inlet pressure $P_{in} = P_{atm} + \Delta P$ with $\Delta P = 10\ Pa$ and an outlet pressure $P_{out} = P_{atm}$ are used as boundary conditions. The fins are heated at the constant temperature of $T_w = 323\ K$ and the fluid enters the channel at temperature $T_\infty = 293\ K$. Water is chosen as the coolant fluid and each candidate's fitness evaluation is performed using a RANS simulation that outputs the total heat flux from the fins to the fluid q'. The k-w SST turbulence model is used for the reasons described in Chapter 4.3. The mesh is designed in order for the k-w SST model to be used down to the viscous sublayer inside the boundary layers that will develop along the fins. Accordingly, at the fins/water interface, the first cell height value is chosen to be $\Delta y = 1 \times 10^{-2}\ mm$. The mesh generated for a random geometry is shown in Fig. 6.8.

One fin is placed along the axis of symmetry in the direction of the flow and one (or two) other fin(s) is (are) placed at each side of the middle fin. The fins are defined by a number from 1 to 5 from the top left corner towards the middle fin following the anti-clockwise direction as shown in Fig. 6.9. Three parameters are used in order to define the position and orientation of each of these fins; x_i, y_i and θ_i where x_i is the coordinate of the centre of the fin i from the left side of the $H \times L$ fixed volume along the direction of the flow, y_i is the coordinate from the bottom side of the $H \times L$ fixed volume along the direction perpendicular to

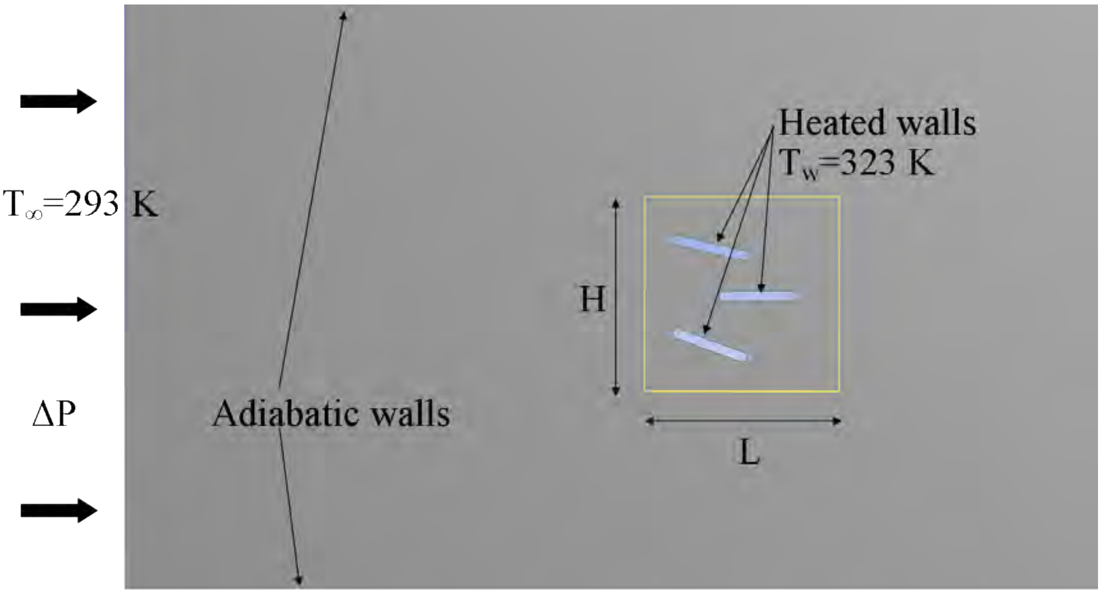

Figure 6.7: Geometry and boundary conditions for the three fins in cross flow simulation

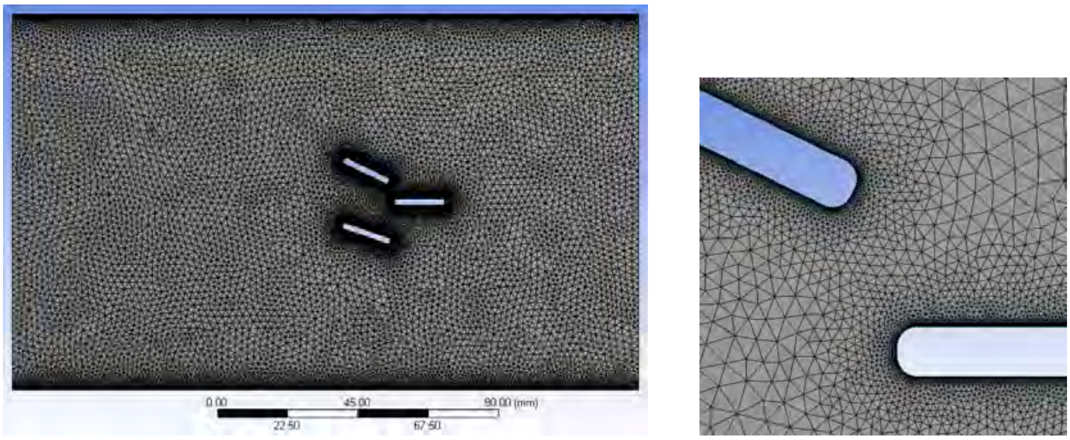

(a) Total numerical domain

(b) Close-up view

Figure 6.8: Three fins configuration meshed for a random geometry.

the flow and θ_i is the angle of the fin's axis with the x-direction, as shown in Fig. 6.10.

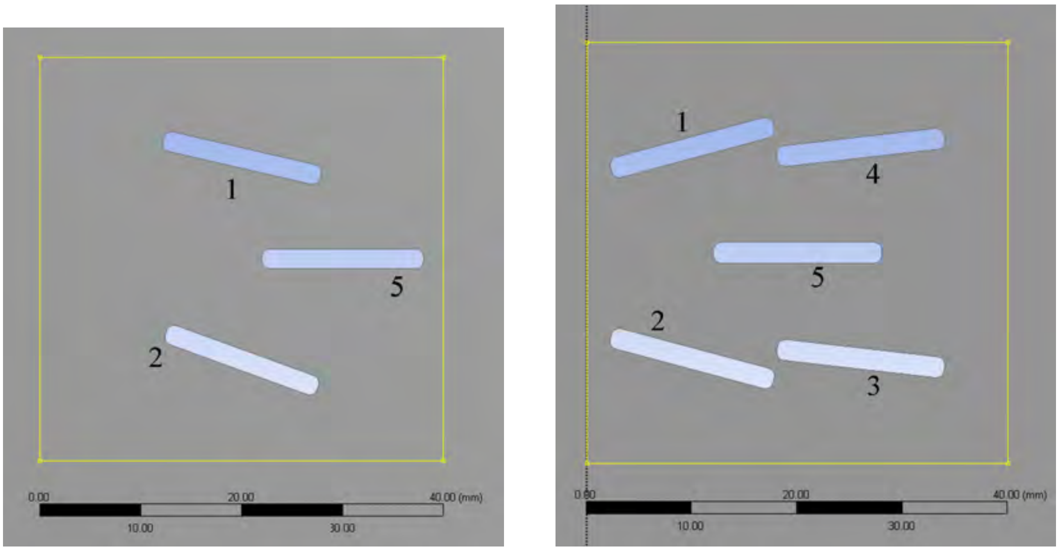

(a) Three fins

(b) Five fins

Figure 6.9: Fins disposition inside the fixed volume 40 mm × 40 mm.

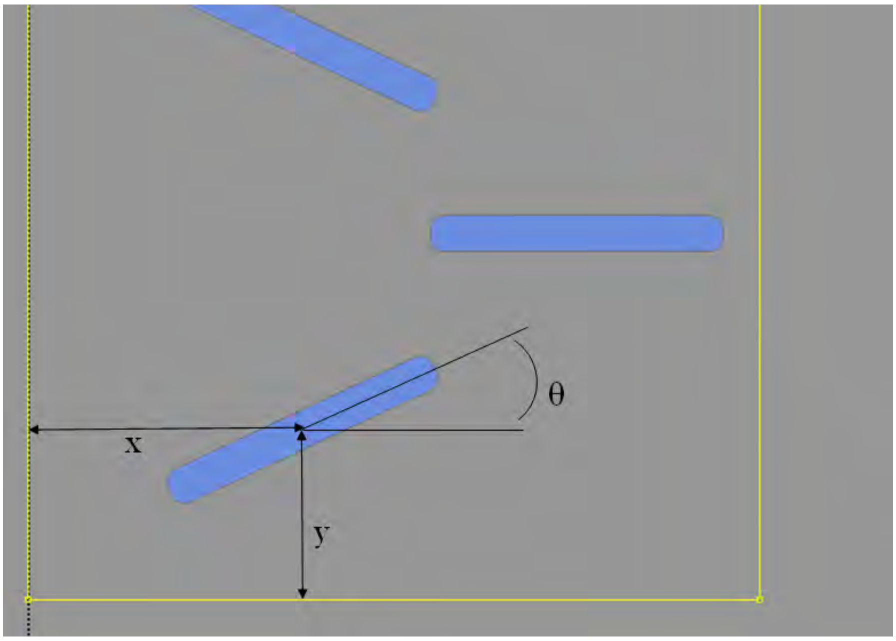

Figure 6.10: Design parameters

6.3.2 Definition of the shape optimization procedure

The optimization process begins with the choice of; (A) objectives to be fulfilled, (B) parametrization of the design (the parameters will correspond to the characteristics defining each candidate) and (C) constraints as introduced in Section 4.4.1.

6.3.2.1 Objectives

The design aims at being optimized in order to fulfill desired objectives. In this case, the objective is to maximize the total heat transfer rate from the fins to the fluid.

The optimization process aims at finding a configuration which could enhance the cooling, by increasing the heat transfer rate from forced convection, while keeping constant the pressure drop across the heat sink. The fitness function of each design candidate is equal to the overall heat transfer rate from the fins q'.

6.3.2.2 Parametrization

The parameters defining the different "design candidates" must cover the space of all possible solutions. In this case, the design is defined by the location and orientation of the fins. The middle fin can be translated along the x-axis and the other fins can be moved and rotated inside the $H \times L = 40$ mm $\times$ 40 mm fixed area. Therefore, thirteen (respectively seven) parameters would be required to describe all the possible combinations of position and orientation of each of the five (respectively three) fins, namely: x_5 and x_i, y_i and θ_i for $i \in [1, 4]$ (respectively for $i \in [1, 2]$). Any combination of these parameters defines the characteristics of a candidate and will be conserved unaltered, cross-overed, mutated or simply forgotten in the evolutionary process. This means that the search space is a thirteen-dimensional space in the case of five fins that are independently located and oriented. However, in order to understand how GAs, and more specifically the ANSYS MOGA, works, several optimizations have been performed over search landscapes of lower dimensions (that is to say fewer independent parameters) for the three fins case, as summarized in Table 6.2.

Table 6.2 shows different optimization setups with increasing dimension of the search-space. Parameters can be fixed to a precise value, defined as a function of other parameters, or take a value in a given interval (obviously the search space has to be closed since an infinite number of evaluations would be required

Table 6.2: Increasing search-space dimension - optimization of three fins in cross flow.

space dimension	x_1 (mm)	y_1 (mm)	θ_1	x_2 (mm)	y_2 (mm)	θ_2	x_5 (mm)
1	13.28	10	$\boldsymbol{[-\frac{\pi}{2},\frac{\pi}{2}]}$	x_1	$H-y_1$	$-\theta_1$	30
1	13.28	$\mathbf{[20,40]}$	10°	x_1	$H-y_1$	$-\theta_1$	30
2	$\mathbf{[0,40]}$	10	$\boldsymbol{[-\frac{\pi}{2},\frac{\pi}{2}]}$	x_1	$H-y_1$	$-\theta_1$	30
3	$\mathbf{[0,40]}$	$\mathbf{[20,40]}$	$\boldsymbol{[-\frac{\pi}{4},\frac{\pi}{4}]}$	x_1	$H-y_1$	$-\theta_1$	30
4	$\mathbf{[0,40]}$	$\mathbf{[20,40]}$	$\boldsymbol{[-\frac{\pi}{4},\frac{\pi}{4}]}$	x_1	$H-y_1$	$\boldsymbol{[-\frac{\pi}{4},\frac{\pi}{4}]}$	30
5*	$\mathbf{[0,40]}$	$\mathbf{[20,40]}$	$\boldsymbol{[-\frac{\pi}{4},\frac{\pi}{4}]}$	x_1	$H-y_1$	$\boldsymbol{[-\frac{\pi}{4},\frac{\pi}{4}]}$	$\mathbf{[0,40]}$

otherwise). The bolded intervals are independent parameters over which the evolutionary search is to be made. The last line refers to an optimization similar to the previous line (of dimension four) but the horizontal position of fin 5 is not fixed anymore. All the configurations described by the combinations of the 5 parameters could have been obtained considering a 4-D search space involving the relative horizontal position of the fins, namely $x_1 - x_5$. However, this optimization is performed over a 5D search-space in order to investigate a search space of higher dimension.

Figure 6.11 shows five random geometry configurations generated in different search spaces: Figure 6.11 a,b,c,d and e show a random geometry designed in the search-space of dimension 1,2,3,4 and 4*, respectively, presented in Table 6.2. The independent parameters are indicated in the captions.

For the five fins case, an optimization has been performed with an imposed symmetry about a fixed middle fin. This corresponds to the following setup: $x_1 = x_2 \in [0mm, 20mm]$, $y_1 = y_2 \in [20mm, 40mm]$, $\theta_1 = -\theta_2 \in [-\pi/2, \pi/2]$, $x_4 = x_3 \in [20mm, 40mm]$, $y_4 = y_3 \in [20mm, 40mm]$, $\theta_4 = -\theta_3 \in [-\pi/2, \pi/2]$, $x_5 = y_5 = 20\ mm$ and $\theta_5 = 0$.

6.3.2.3 Constraints

In order for the geometries and meshes to be generated without errors, constraints on the parameters are necessary. Indeed, (i) two fins cannot overlap and (ii), up to now x_i and y_i - that is to say the center of the fins - are restricted to the $H \times L$ volume, whereas the objective is to ensure that each fin in itself is entirely

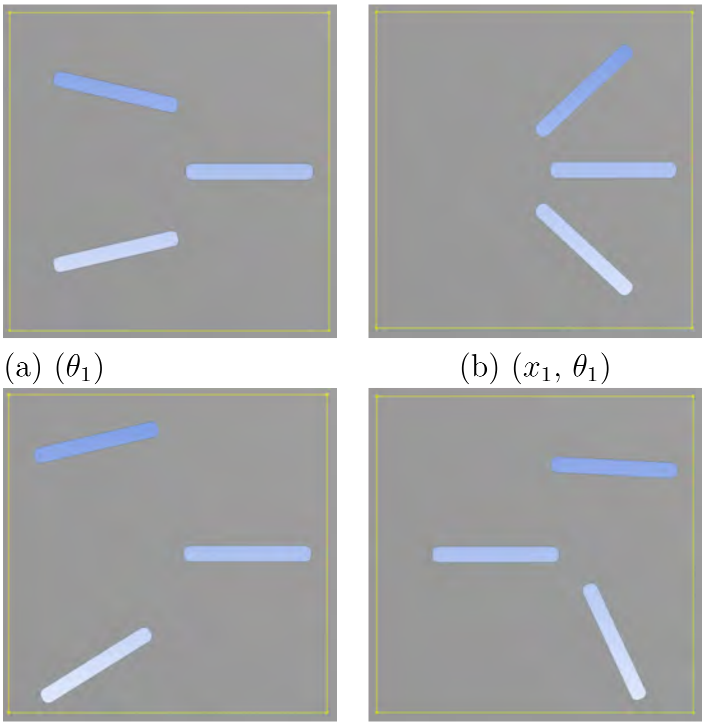

(a) (θ_1) (b) (x_1, θ_1) (c) (x_1, y_1, θ_1)

(d) $(x_1, y_1, \theta_1, \theta_2)$ (e) $(x_1, y_1, \theta_1, \theta_2, x_5)$

Figure 6.11: Random geometries represented by vectors from 1D to 5D search-landscapes.

bounded to the volume. The parameters defined in the previous paragraph are therefore submitted to the following constraints;

- The minimum distance between two fins is 0.5 mm.
- The fins have to be located inside the 40 mm × 40 mm box, strictly.

For three fins, these constraints are mathematically written as follows (in mm);

- $x_i + 7.2 \times cos(\theta_i) + 0.2 \times sin(\theta_i) + r \leq 40$, for $i = 1, 2$
- $x_i - 7.2 \times cos(\theta_i) - 0.2 \times sin(\theta_i) + r \geq 0$, for $i = 1, 2$
- $y_1 + 7.2 \times sin(\theta_1) + 0.2 \times cos(\theta_1) + r \leq 40$
- $y_1 - 7.2 \times sin(\theta_1) - 0.2 \times cos(\theta_1) - r \geq 21.5$
- $y_2 + 7.2 \times sin(\theta_2) + 0.2 \times cos(\theta_2) + r \leq 18.5$
- $y_2 - 7.2 \times sin(\theta_2) - 0.2 \times cos(\theta_2) - r \geq 0$

For the five fins case, the entire search space defined by all the possible positions for fins 1 and 4 in the top half volume (resp. fins 2 and 3 in the bottom half) can be similarly described if the location of the centre of fin 1 (resp. fin 2) is imposed inside the top left square (resp. bottom left), and the fin 4's centre (resp. fin 3) inside the top right square (resp. bottom right) as shown in Fig. 6.12

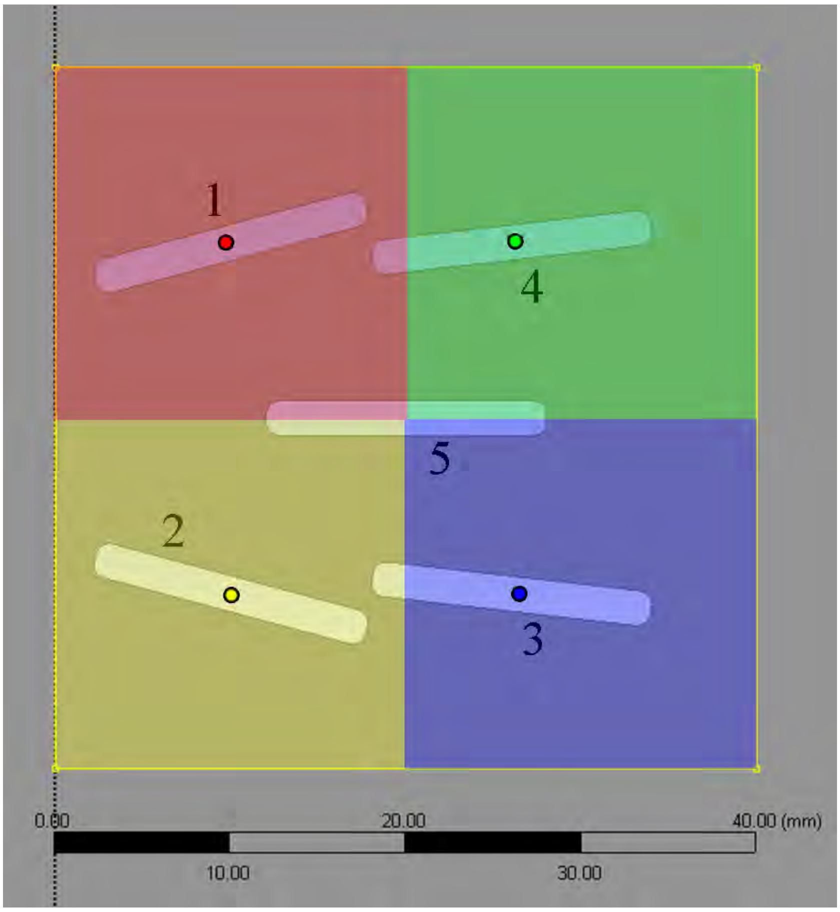

Figure 6.12: $H \times L$ volume divided into four squares, each fin's centre is restricted to a square.

The constraints then become:

- $x_i - 7.2 \times cos(\theta_i) - 0.2 \times sin(\theta_i) - r \geq 0$, for $i = 1, 2$
- $x_i \leq 20$, for $i = 1, 2$
- $x_i \geq 20$, for $i = 3, 4$
- $x_i + 7.2 \times cos(\theta_i) + 0.2 \times sin(\theta_i) + r \leq 20$, for $i = 3, 4$
- $y_i + 7.2 \times sin(\theta_i) + 0.2 \times cos(\theta_i) + r \leq 40$, for $i = 1, 4$
- $y_i - 7.2 \times sin(\theta_i) - 0.2 \times cos(\theta_i) - r \geq 21.5$, for $i = 1, 4$

- $y_i + 7.2 \times sin(\theta_i) + 0.2 \times cos(\theta_i) + r \leq 18.5$, for $i = 2, 3$
- $y_i - 7.2 \times sin(\theta_i) - 0.2 \times cos(\theta_i) - r \geq 0$, for $i = 2, 3$

Besides, when considering fins 1 and 4 (resp. fins 2 and 3), an additional non-overlap constraint is required. Indeed, when the centre of the fins located at the same side of fin 5 are close to each other, the orientation of the fins can only take certain values. This constraint can be divided into three different cases:

- If the distance between the centres of each fin $D = \sqrt{(x_i - x_j)^2 + (y_i - y_j)^2}$ (where $(i, j) = (1, 4)$ or $(2, 3)$) is greater than a fin's length $L_f = 16\ mm$, then the fins have no chance to overlap and no further constraint is needed.

- If $L_f/2 + W_f/2 < D \leq L_f$ where $W_f = 2\ mm$ is the fin's width, the situation illustrated in Fig. 6.13 is encountered.

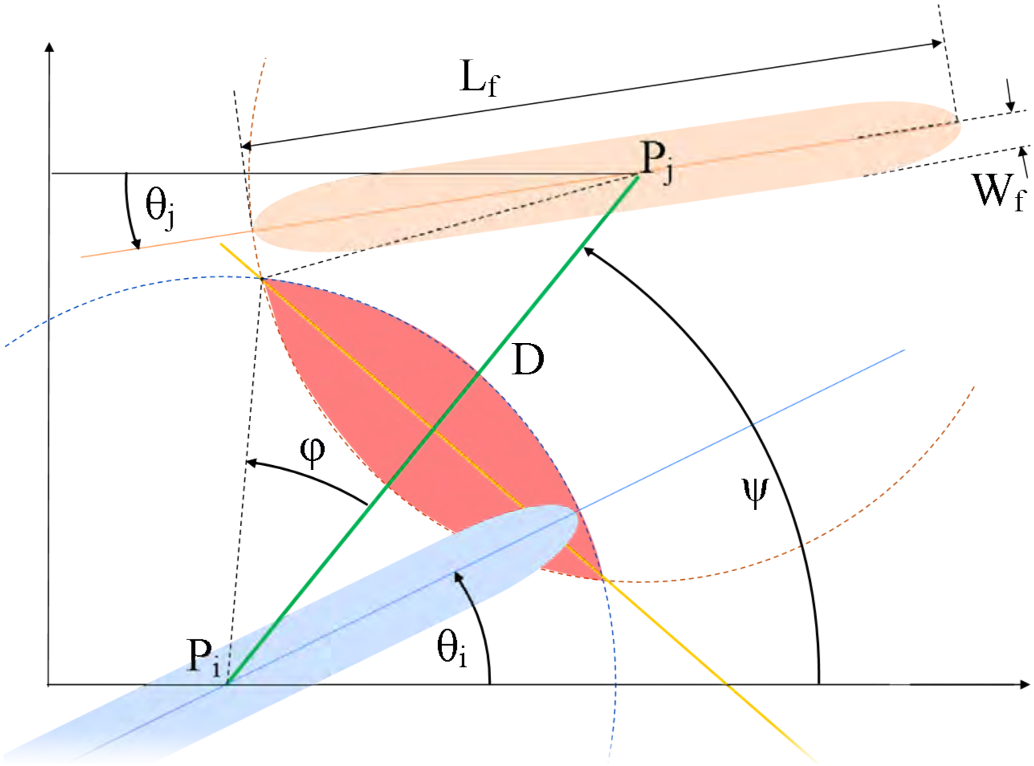

Figure 6.13: Schematic of the geometrical configuration of two close fins and the overlap area in red.

When the distance between the centers of the two fins is in the range $[L_f/2 +$

$W_f/2\ ;\ L_f]$, an overlap region appears as illustrated in red in Fig. 6.13. ϕ is the semi-angle formed by the overlap cone and ψ is the angle between the direction of the centre-to-centre (P_i, P_j) straight line and the x-axis.

(i) In such case, if fin i is oriented so that it doesn't enter the overlap region, the fins won't overlap. This happens for $|\psi - \theta_i| > |\phi|$ or, since all the angles are in the interval $[0;\pi]$, for $cos|\psi - \theta_i| < cos|\phi| = D/L_f$.

(ii) If fin i enters the overlap area, another constraint is required on fin j. The orientation of fin j corresponding to the symmetrical position of fin i about the yellow line in Fig. 6.13 is the worst case scenario where the two fins overlap completely. This configuration is encountered when $\theta_j = \psi + (\psi - \theta_i) = 2\psi - \theta_i$ In order not to have an overlap, fin j must be oriented away from this worst configuration which can mathematically be defined as the following constraint:

$$\begin{array}{ll} \text{if } \dfrac{L_f}{2} + \dfrac{W_f}{2} + \delta < D \leq L_f + \delta \text{ and } cos|\psi - \theta_i| > \dfrac{D}{L_f} \text{ then} & |2\psi - \theta_i - \theta_j| > \phi \\ \text{or} & cos|2\psi - \theta_i - \theta_j| < \dfrac{D}{L_f} \end{array} \tag{6.27}$$

where δ is a safety parameter.

- Finally if $D < L_f/2$ the fins are forced not to enter the overlap area at all which leads to two additional constraints:

$$\begin{array}{ll} \text{if } D < \dfrac{L_f}{2} + \delta \text{ then} & |\psi - \theta_i| > \phi \\ \text{or} & cos|\psi - \theta_i| < \dfrac{D}{L_f} \end{array} \tag{6.28}$$

and

$$\text{if } D < \frac{L_f}{2} + \delta \text{ then} \quad cos|\psi - \theta_j| < \frac{D}{L_f} \tag{6.29}$$

Let us summarize all the constraints and conditions on these constraints that ensure that no error will occur during the course of the optimization procedure. If $Bool(a > b)$ is the boolean function that equals 1 if true (if $a > b$) and 0 if false (if $a < b$), constraints 6.27, 6.28 and 6.29 respectively become

$$Bool\left(\frac{L_f}{2} + \frac{W_f}{2} + \delta < D \leq L_f + \delta\right) \times Bool\left(cos|\psi - \theta_i| > \frac{D}{L_f}\right) \times \left(cos|2\psi - \theta_i - \theta_j| - \frac{D}{L_f}\right) \leq 0 \tag{6.30}$$

$$Bool\left(D < \frac{L_f}{2} + \delta\right) \times \left(cos|\psi - \theta_i| - \frac{D}{L_f}\right) \leq 0 \tag{6.31}$$

$$Bool\left(D < \frac{L_f}{2} + \delta\right) \times \left(cos|\psi - \theta_j| - \frac{D}{L_f}\right) \leq 0 \tag{6.32}$$

With these constraints imposed to the ANSYS MOGA, the creation and meshing of all the geometries that are to be evaluated through the successive generations can be done without the errors that would otherwise have stopped the optimization progress.

6.3.2.4 Genetic algorithm parameters

As it has been highlighted in Section 3.3, the parameters controlling the behavior of the GA must be tuned, or must be chosen with care. In any case, they should be stated, as the results most probably depend on them. In the future optimizations, the MOGA algorithm has been used with a cross-over and mutation probability of $p_c = 0.9$ and $p_m = 0.01$ respectively, and a target stability percentage $S = 2\%$ for the termination. The initial population size is an object of investigation and varying values have been investigated, from 10 to 100 individuals. The "evolving population" size is always set to be equal to the initial population size so that a n-individuals population is initially generated and at each generation, the best n candidates among the children and parents from the previous generation, are selected.

6.3.3 Results from the ANSYS MOGA optimization

In this section, results obtained from the different optimization cases listed in Table 6.2 are presented. More specifically, the effect of the initial population size on the results and the total computing time required to find the optimal design, is investigated. No attention is paid to the flow field in this section, only the optimization tuning is investigated (the study of the velocity, temperature and pressure fields is developed in Section 6.3.4 for specific geometries of interest). Table 6.3 shows all the performed optimizations.

Table 6.3: Set of optimizations investigated, with different initial population sizes and number of parameters.

case #	# of fins	search space dimension	initial population sizes investigated
1	3	1 (θ_1)	10, 20, 30, 40, 50
2	3	1 (y_1)	10, 20, 30, 40, 50
3	3	3 (θ_1, x_1, y_1)	20, 25, 30, 35, 40, 50, 60, 80
4	3	4 (θ_1, x_1, y_1, θ_2)	15, 20, 25, 30, 35, 40, 50, 60, 80, 100
5	3	5* (θ_1, x_1, y_1, θ_2, x_5)	40, 50, 60, 80
6	5	6 (θ_1, x_1, y_1, θ_4, x_4, y_4)	50

At the start of each new optimization, the initial population is randomly generated which means that the initial population generated at the start of two optimization runs are different, even if the parameters defining the optimization are exactly the same. This, plus the inherent randomness of mutations and cross-overs, means that two optimizations will produce different results, that is to say, different optimal solutions. It is important to understand that this holds for two optimizations that present the exact same parameters (initial population size, mutation and cross-over rates, selection pressure, etc...).

The way to deal with this issue is to run many of these simulations to gather statistical data on the obtained results. Indeed, a set of many of the same optimization giving different results, but with a low standard deviation, provides good information on how close the computed mean optimal solution is to the theoretical one.

Unfortunately, a complete optimization process is time consuming, especially in the present case where a CFD simulation has to be performed for each design fitness evaluation. In the present work, the results that are presented and discussed are preliminary and must be analyzed with care.

6.3.3.1 Three fins shape optimization: 1-D search space

The first two shape optimizations performed for the case of three fins in cross flow is made over a one-dimensional search space: the first optimization investigates θ_1, while in the second, only y_1 is investigated, corresponding to cases #1 and #2 in Table 6.3. In both cases, the symmetry along the middle fin is imposed and we are looking for the optimal angle of attack θ_1 in case #1, or the optimal vertical position y_1 in case #2, when all the other parameters are locked. The optimizations have been performed with a population size ranging from 10 to 50 individuals as shown in Table 6.3.

As it is shown in Fig. 6.14, the total heat transfer rate from the three fins is increased up to approximately $q'_{opt} = 6.8\ W$ with the angle $\theta_{1,opt} \approx 19°$.

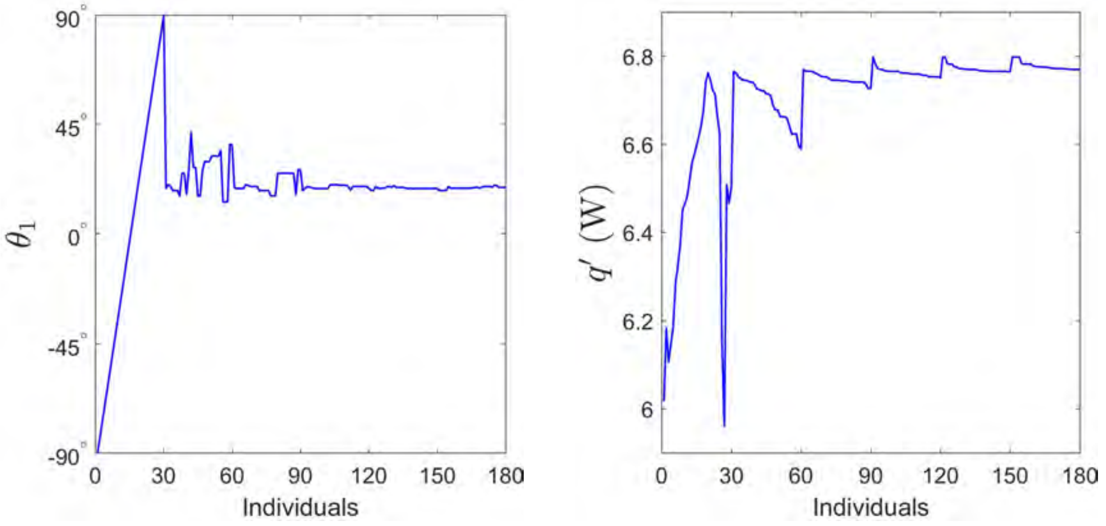

(a) Angle convergence

(b) Heat transfer rate convergence

Figure 6.14: Convergence of (a) the optimal angle θ_1 and (b) the overall heat transfer rate

Figure 6.14 shows an example of the values of the angle θ_1 and the overall heat transfer rate q' of all the individuals that have been evaluated through an optimization procedure over the 1-D search space of the θ_1 values. In the particular case shown in Fig. 6.14, the initial population size is set to 30. Each generation corresponds to 30 candidates, meaning that every 30 simulations, a new population is created by selecting the best individuals of the previous set of 30 simulations. This is observed on Fig. 6.14(a) and 6.14(b) as both values of θ_1 and q' are refined every 30 individuals' fitness evaluation.

It can already be observed in Fig. 6.14(b), that the evaluation of the overall heat transfer rate q' ranges from approximately 6 W up to 6.8 W. By only modifying the angle of attack of the fins, the total heat transfer rate can increase by more than 10% from the worst to the best case scenario. An optimization over a one-dimensional search space can already provide useful results.

Table 6.4 (resp. 6.5) presents the results obtained for the optimal angle $\theta_{1,opt}$ (resp. optimal vertical position $y_{1,opt}$) and the corresponding total heat transfer rate q'_{opt}, for all the different initial population sizes investigated for cases #1 and #2 from Table 6.3.

Table 6.4: Converged parameter $\theta_{1,opt}$ and objective q'_{opt} and total computational time for the investigated initial population sizes, case #1.

Initial pop. size	$\theta_{1,opt}$ (°)	$q'_{opt}(W)$	computational time (min)
10	24.5	6.76	36
20	19.7	6.82	101
30	19	6.79	184
40	19.5	6.83	345
50	19.1	6.86	469

Table 6.5: Converged parameter $y_{1,opt}$ and objective q'_{opt} and total computational time for the investigated initial population sizes, case #2.

Initial pop. size	$y_{1,opt}$ (°)	$q'_{opt}(W)$	computational time (min)
10	36.17	6.81	84
20	35.33	6.83	179
30	35.27	6.83	247
40	35.29	6.83	454
50	35.26	6.83	543

Interestingly, the solution provided by the genetic algorithm depends on the initial population size, for both the optimal parameter ($\theta_{1,opt}$ or $y_{1,opt}$) and the total heat transfer rate q'_{opt}, as shown in Tables 6.4 and 6.5. It should be noticed that, as already stated earlier, due to the huge amount of computational time required for the convergence of these shape optimization procedure, it has not been possible to perform many of the same simulations in order to obtain statistical results. However, it can already been observed that the dependency is not monotonic, and for a population size higher than 20, the solution provided by the GA does not depend on the population size anymore. This behavior is more easily observed on Fig. 6.15 that illustrates the data presented in Tables 6.4 and 6.5.

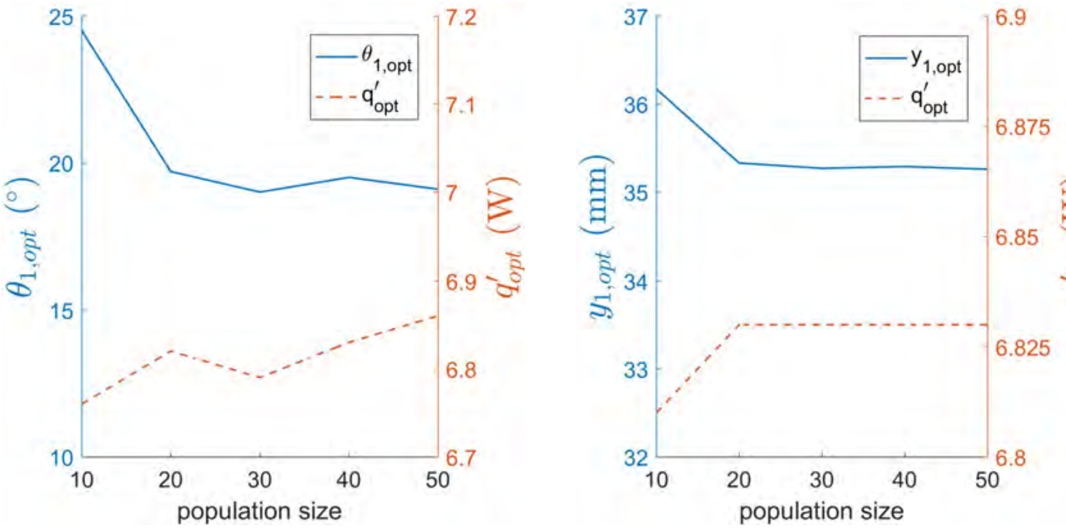

(a) Case #1, varying θ_1 (b) Case #2, varying y_1

Figure 6.15: Results for (a) the optimal angle $\theta_{1,opt}$, (b) the optimal vertical position $y_{1,opt}$, and total heat transfer rate q'_{opt} as a function of the population size for shape optimizations over a 1-D search space, cases #1 and #2 from Table 6.3)

As it could have been expected at first sight, with larger population sizes, the results are more accurate, repeatable and therefore present a higher level of confidence. However this increase of reliability has a price: the computational cost. Indeed Tables 6.4 and 6.5 also present the total computing time required for each shape optimization to converge to the imposed convergence stability percentage $S = 2\%$, on 48 cores. These results are plotted in Fig. 6.16 for case #1 and #2. A linear progression is fitted to the data using a least square method.

Figure 6.16 illustrates an expected result: the total computing time required for the optimization to converge increases with the population size. A linear fit has

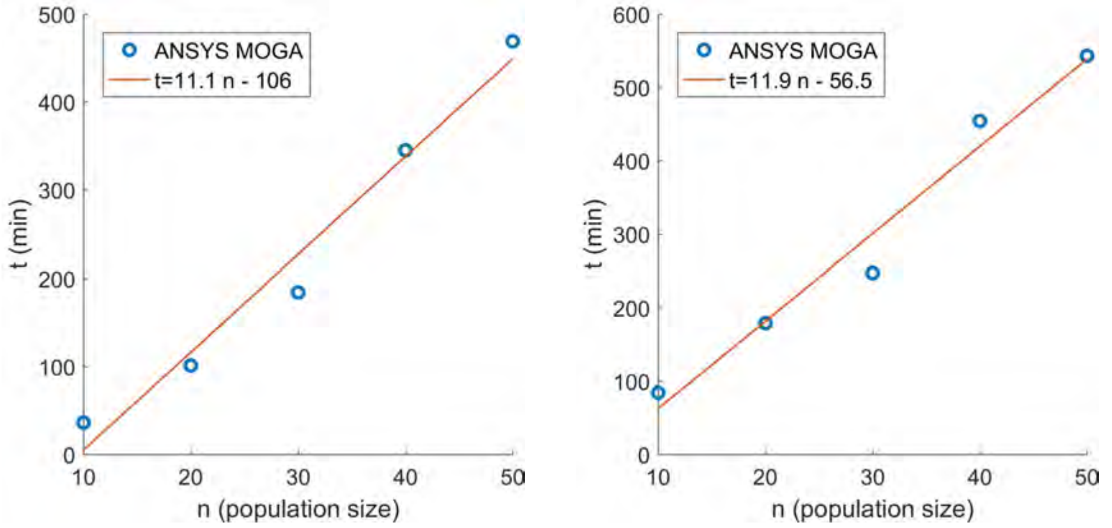

(a) Case #1, varying θ_1 (b) Case #2, varying y_1

Figure 6.16: Optimization's computing time t as a function of the population size n for (a) case #1 and (b) case #2 - parallel computing on 48 cores.

been performed on each data set, as shown in Eq. 6.33 and 6.34. One important result shown in Fig. 6.16 is that, even though optimizations over 1-D search space dimension involving other parameters than θ_1 or y_1 have not been performed, it appears that the relation between the population size and the computing time depends on the number of parameters (search space dimension) rather than on the parameter itself. Indeed the fitted linear curves, and especially the slopes, plotted in Fig. 6.16(a) and 6.16(b) are very close.

$$t = 11.1 \times n - 106 \qquad (R^2 = 0.973) \tag{6.33}$$

$$t = 11.9 \times n - 56.5 \qquad (R^2 = 0.969) \tag{6.34}$$

The linear fitting could seem strange because the data plotted in Fig. 6.16(a) and 6.16(b) appears not to follow a linear progression at first sight. However a linear relationship between the computing time and the population size has been reported by other authors [19] and this linear fit will become much clearer when the results for the shape optimization over higher dimension search space will be presented, especially the results for the 4-D search space presented in Section 6.3.3.3.

The results obtained from the MOGA differ slightly from a linear progression and this could be due to multiple reasons. One of them is certainly the lack of time or computing power available, that stand as an obstacle to the constitution of a relevant statistical set of data. Therefore, some of the results presented in Tables 6.4 and 6.5 and in Fig. 6.16 could be misleading results that deviate from the average result.

The objective of any GA user is to find the right balance between confidence and execution time. In this particular case, with a small 1-D search space, an optimization with a population of 20 individuals appears to provide an optimal angle $\theta_{1,opt}$ and an optimal vertical position $y_{1,opt}$ close to the result obtained with a much larger population size. Moreover, this conclusion does not depend on the parameter itself, but only on the number of parameters. According to these results, the "optimal" population size that balances confidence and computing time in the case of the present optimizations #1 and #2, over a 1-D search space, is 20.

6.3.3.2 Three fins shape optimization: 3-D search space

Shape optimizations have been performed over a three-dimensional search space: the optimal combination of three parameters, namely θ_1, x_1 and y_1, is investigated. This corresponds to the case #3 in Table 6.3 in which the symmetry about the middle fin is still imposed on the top and bottom fins.

Table 6.6 presents the results obtained for the optimal angle $\theta_{1,opt}$ optimal horizontal position $x_{1,opt}$ and optimal vertical position $y_{1,opt}$, and the corresponding total heat transfer rate q'_{opt}, for all the different initial population sizes investigated for the case #3 from Table 6.3.

The first noticeable result presented in Table 6.6 is that the discovered optimal overall heat transfer rate q'_{opt} has increased from 6.8 W (case #1) to 7.23 W (case #3) by allowing an optimization over a 3-D search space rather than over one dimension only. This result is not surprising since the optimal angle and position are searched for, rather than the angle for a fixed position, nevertheless, the increase is quite significant. Indeed the total heat transfer rate from the three fins optimized in case #3 is increased by approximately 7% as compared to the optimal solution of case #1.

The second result that should be looked at is the difference in the optimal

Table 6.6: Converged parameters $\theta_{1,opt}$, $x_{1,opt}$ and $y_{1,opt}$ and objective q'_{opt} and total computational time for the investigated initial population sizes, case #3.

Initial pop. size	$\theta_{1,opt}$ (°)	$x_{1,opt}$ (mm)	$y_{1,opt}$ (mm)	$q'_{opt}(W)$	computational time (min)
20	24.6	17.8	33.7	7	165
25	22.7	31.9	30.6	7.2	267
30	24.9	31	32	7.2	451
35	23.8	32.2	33.3	7.23	484
40	23	32.2	31.7	7.23	622
50	23.6	32.3	31.1	7.23	1047
60	22.8	30.8	31.7	7.2	818
80	23.7	32.4	30.7	7.23	1053

solution for the angle θ_1 between case #1 and #3. In case #1, the optimal angle is $\theta_{1,opt1} \approx 19°$ whereas in case #3, $\theta_{1,opt2} \approx 23°$. This result could be an example of the effect of non-linearity: a slight modification of a particular parameter in one direction could have a positive a effect on the fitness function when all the other parameters are fixed, but this same change could have a negative impact when conjugated with changes of other parameters. This is the reason why the GA user must define and parametrize the problem with care. In order to investigate the effect of each parameter on the overall heat transfer rate from the fins, all the evaluations of q' performed through the successive generations of the optimization with a population of 80 individuals are interpolated, resulting in a mapping of the 3-D fitness function $q'(\theta_1, x_1, y_1)$. The projections of this interpolation on the 2-D sub-spaces are shown in Fig. 6.17.

The first noticeable observation in Fig. 6.17 is that the results do not cover the entire search space ($\theta_1 \in [-45°, 45°]$, $x_1 \in [0mm, 40mm]$, $y_1 \in [20mm, 40mm]$). This phenomenon is due to the constraints that force the fins to remain inside the fixed volume $H \times L$.

Some parameters have a more important impact on the overall heat transfer rate q' than others. In this particular case #3, Fig. 6.17(b) and 6.17(c) show that y_1 has a small effect on the results compared to θ_1 and x_1. Indeed, if an iso-θ_1 (resp. iso-x_1) line is drawn on the data shown in Fig. 6.17(b) (resp. 6.17(c)), it can be noticed that the q' value changes only slightly along this line. In contrast, Fig. 6.17(a) and 6.17(b) show that θ_1 is a high-impact parameter and similarly, Fig. 6.17(c) shows that x_1 has more impact on the total heat transfer rate compared to

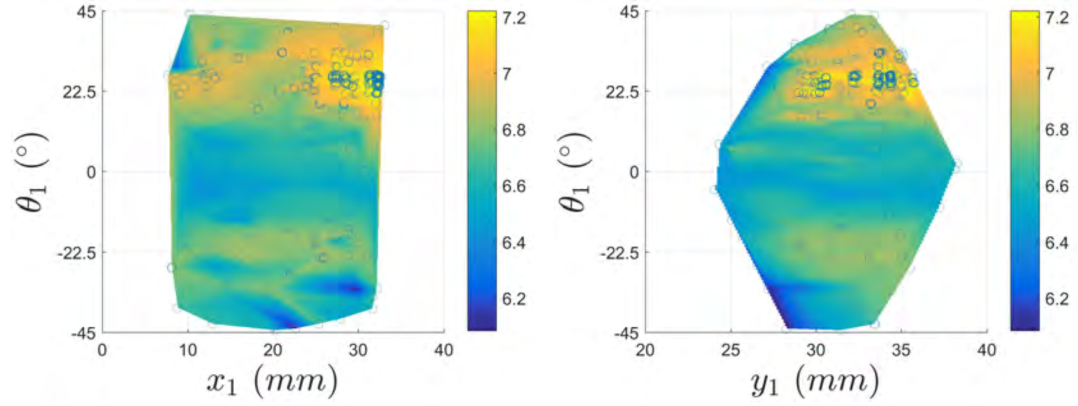

(a) Projection on the (θ_1, x_1) 2-D sub-space (b) Projection on the (θ_1, y_1) 2-D sub-space

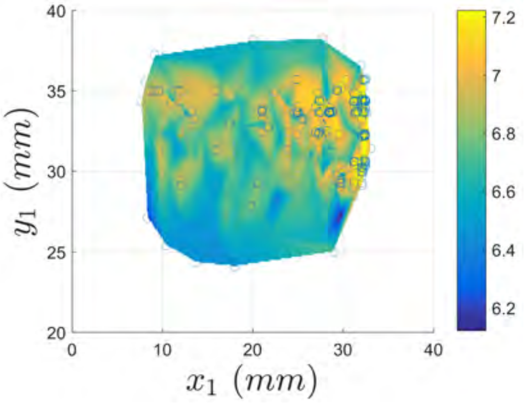

(c) Projection on the (x_1, y_1) 2-D sub-space

Figure 6.17: Overall heat transfer rate q' results interpolated and projected on different two-dimensional sub-spaces of the search space, case #3. The circle markers correspond to raw evaluations.

y_1. From Fig. 6.17(a), it seems that θ_1 is globally the most impactful parameter among the three.

Table 6.6 also presents the computing time required to complete all the case #3 shape optimizations on 48 cores, as a function of the population size. These results are shown in Fig. 6.18 and a linear progression is fitted to the data using a least square method.

To begin with, the most noticeable element seen in Fig. 6.18 is the result obtain with a population size of 50 individuals. The point (50,1047) plotted in Fig. 6.18

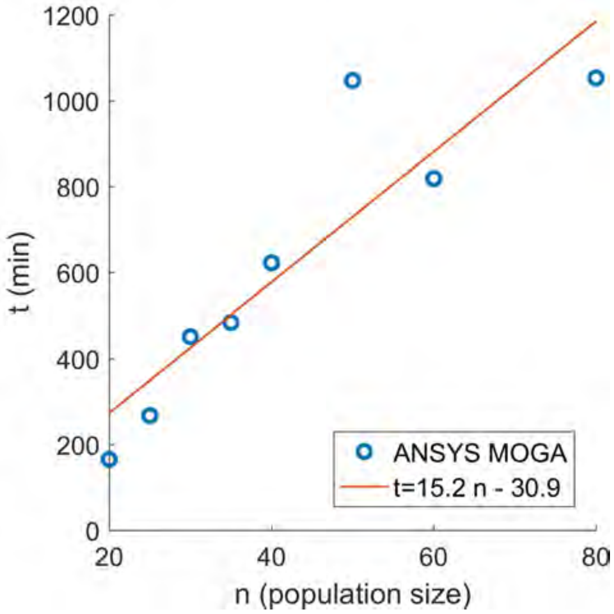

Figure 6.18: Optimization's computing time t as a function of the population size n for case #3 - parallel computing on 48 cores.

deviates strongly from the linear fit. The reason of this deviation is believed to come from the random characteristic of genetic algorithms that can, in some cases, end up with a solution that is different from the average solution. This is a perfect example that explains why the solutions from GAs should be studied statistically by running several optimization procedures with the exact same parameters. Unfortunately, this statistical approach could not be achieved in this work due to computing resource limitations. Indeed, a statistical study on the case #3 optimization with a population of 80 individuals demands a huge computational effort as a single complete optimization procedure takes approximately 1000 min, that is to say, 16h 40m according to Table 6.6 (this result does not take the queuing time into account).

Secondly, an important observation that can be made when looking at Fig. 6.18, is the increase of the linear fitting curve's slope, compared to cases #1 and #2 that are plotted in Fig. 6.16. The slope of the relationship between population size and computing time increased from approximately 11 for a 1-D search space to 15 for a 3-D search space. The relation between the slope of the $t(n)$ curve and n is investigated and discussed more precisely in Section 6.3.3.4.

6.3.3.3 Three fins shape optimization: 4-D search space

The next set of shape optimizations corresponds to case #4 in Table 6.3. The optimization is performed by searching for the optimal combination of four parameters: θ_1, x_1, y_1 and θ_2. The symmetry about the middle fin is no longer imposed to the geometry because θ_1 and θ_2 can vary regardless.

The results obtained for the optimal angles $\theta_{1,opt}$ and $\theta_{2,opt}$, optimal horizontal position $x_{1,opt}$ and optimal vertical position $y_{1,opt}$, and the corresponding total heat transfer rate q'_{opt}, are presented in Table 6.7, for all the different initial population sizes investigated for the case #4 from Table 6.3.

Table 6.7: Converged parameters $\theta_{1,opt}$, $x_{1,opt}$, $y_{1,opt}$ and $\theta_{2,opt}$ and objective q'_{opt} and total computational time for the investigated initial population sizes, case #4.

Initial pop. size	$\theta_{1,opt}$ (°)	$x_{1,opt}$ (mm)	$y_{1,opt}$ (mm)	$\theta_{2,opt}$ (°)	q'_{opt} (W)	computational time (min)
15	-41.9	20.7	33.9	-35.6	6.9	141
20	24.8	31.4	33.7	-32.8	7.17	333
25	24.7	31.4	33.5	-23.4	7.21	484
30	35.5	31.6	33.3	-23.1	7.16	508
35	23.4	31.9	33.6	-24.5	7.22	662
40	23.1	31.5	34.1	-24.9	7.21	1245
50	24.1	30.6	33.9	-25.8	7.2	1202
60	23.1	31.9	32.9	-23.9	7.23	1354
80	24.3	31.9	32.4	-24.6	7.23	1840
100	24.9	31.6	33.1	-26.4	7.23	2015

The first important observation is that, when comparing Tables 6.6 and 6.7, it can be noticed that the overall heat transfer rate obtained for the discovered optimal solution on the 4-D search-space is 7.23 W, and therefore, no improvement is made compared to the previous optimization on the 3-D search space.

One interesting aspect of the investigation of this #4 set of optimizations is the potential asymmetry of the solutions. Indeed, the symmetry of the top and bottom fins about the middle fin is forced in cases #1, #2 and #3, for which $x_2 = x_1$, $y_2 = y_1$ and $\theta_2 = -\theta_1$. But in case #4, θ_1 and θ_2 are independent. However the results obtained and shown in Table 6.7 lead to the conclusion that the optimal configuration is symmetrical, even though symmetry is not forced. Indeed the optimal solution provided by the GA is represented by the following combination: $x_{1,opt} \approx 31.5mm$, $y_{1,opt} \approx 33mm$, $\theta_{1,opt} \approx 24°$ and $\theta_{2,opt} \approx -25°$. Although θ_2 is free to vary regardless of θ_1, the GA ended up with an optimal solution close to the one obtained for the case #3 as seen in Fig. 6.19. Indeed, the projection of the investigated solutions of case #4 for a population of 100 individuals on the two-dimensional sub-spaces (θ_1, x_1), (θ_1, y_1) and (x_1, y_1) are presented in Fig. 6.19, and the main observation is that these results are close to the ones from case #3, presented in Fig. 6.17. More precisely, similarities are observed in the range of overall heat transfer rate resulting from the investigated solutions, the location of the areas of solutions with high heat transfer rates, the monotony of q' as a function of y_1, and so on.

Moreover, Fig. 6.20 shows the projection of the solutions on the (θ_1, θ_2) 2-D sub-space. The results from Fig. 6.20 seem symmetrical about the red dashed line. This line corresponds to symmetrical configurations: the top and bottom fins are symmetrically oriented about the middle fin as $\theta_2 = -\theta_1$ on this line. Additionally, two solutions in Fig. 6.20 symmetrically located about the red dashed line are, in theory, equivalent. Indeed the configuration (with x_1 and y_1 being fixed) where $\theta_1 = \alpha$ and $\theta_2 = \beta$ is, in theory, the exact same configuration as the one with $\theta_2 = -\alpha$ and $\theta_1 = -\beta$. That is why the projection of the solutions on the (θ_1, θ_2) space is symmetrical about the red dashed line as shown in Fig. 6.20.

From this figure, it can be seen that the solution with the highest overall heat transfer rate is located on the line of symmetrical configurations, at the bottom right corner of Fig. 6.20, which is coherent with the result of the GA presented in Table 6.7. However, Fig. 6.20 also shows that asymmetrical solutions can score higher overall heat transfer rates than certain symmetrical solutions. For example, configurations where $25° \leq \theta_1 \leq 35°$ and $5° \leq \theta_2 \leq 30°$ which correspond to the orange area in the top-right corner in Fig. 6.20, or the equivalent configurations across the red dashed line for $-35° \leq \theta_2 \leq -25°$ and $-30° \leq \theta_1 \leq -5°$, all present a total heat transfer rate of 7 W on average. On the other hand, the symmetrical and near-symmetrical configurations close to the parallel case with $-10° \leq \theta_1 \leq 0°$ and $0° \leq \theta_2 \leq 10°$ result in an overall heat transfer rate of approximately 6.6 W. Interestingly, although the best solution is symmetrical, non-symmetrical geometries performed better than the close-to-parallel symmetrical configurations, with a total heat transfer rate increased by about 6 % for these particular sets of configurations.

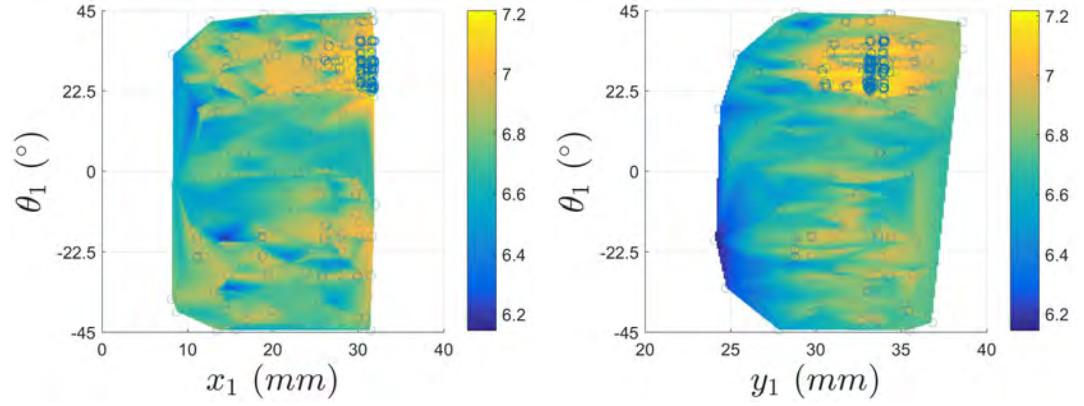

(a) Projection on the (θ_1, x_1) 2-D sub-space (b) Projection on the (θ_1, y_1) 2-D sub-space

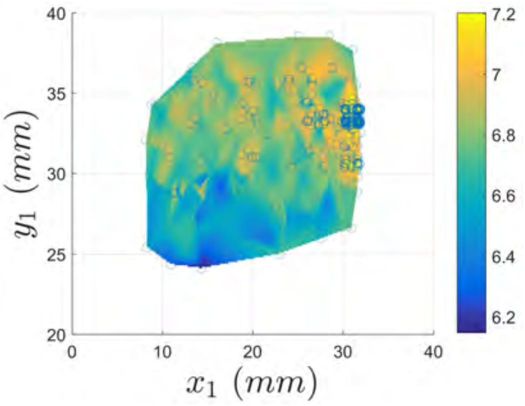

(c) Projection on the (x_1, y_1) 2-D sub-space

Figure 6.19: Overall heat transfer rate q' results interpolated and projected on different two-dimensional sub-spaces of the search space, case #4, population size equal to 100. The circle markers correspond to raw evaluations.

Although the GA provides an optimal solution for case #4 similar to the one from case #3, the computing time required to discover this same optimal solution has increased compared to case #3 along with the slope of the linear relationship of the computing time as a function of the population size, as presented in Table 6.7 and illustrated in Fig. 6.21:

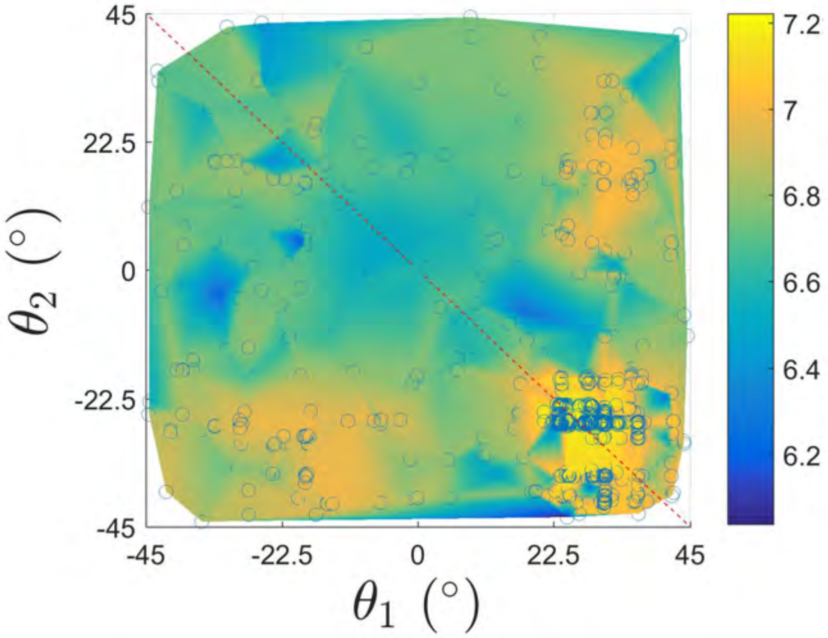

Figure 6.20: Overall heat transfer rate q' results interpolated and projected on the (θ_1, θ_2) 2-D sub-space, case #4, population size equal to 100. The circle markers corresponds to raw evaluations and the dashed red line correspond to symmetrical configurations.

6.3.3.4 Three fins shape optimization: 5-D search space

For this case #5 of shape optimizations presented in Table 6.3, the search-space is five-dimensional, as the solutions are a combination of five parameters: θ_1, x_1, y_1, θ_2 and x_5.

The results obtained for the optimal angles $\theta_{1,opt}$ and $\theta_{2,opt}$, optimal horizontal position $x_{1,opt}$ and $x_{5,opt}$ and optimal vertical position $y_{1,opt}$, and the corresponding total heat transfer rate q'_{opt}, are presented in Table 6.8, for all the different initial population sizes investigated for the case #5 from Table 6.3.

The difference between cases #4 and #5 lies only in the possibility for the horizontal position of the middle fin to vary. It has already been precised that even though only the relative position of the fins matters in theory, adding x_5 as a modifiable parameter does increase the search-space dimension by one. The first interesting result that can be seen in Table 6.8 is that performing the shape optimization over this particular 5-D search-space enabled the discovery of a new

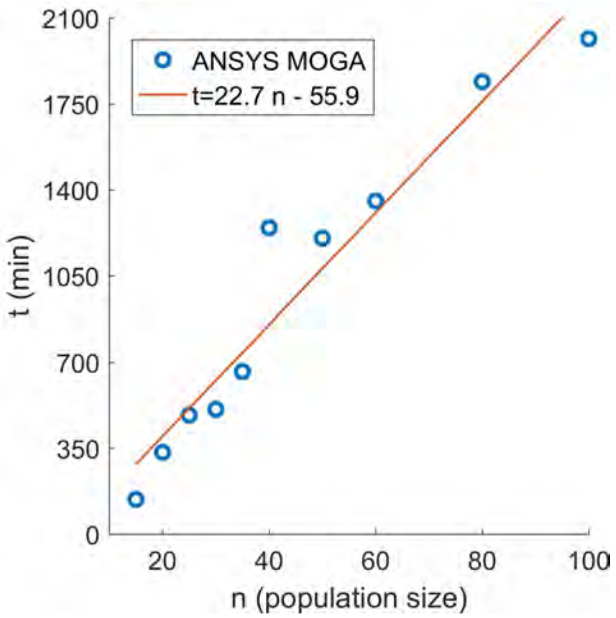

Figure 6.21: Optimization's computing time t as a function of the population size n for case #4 - parallel computing on 48 cores.

Table 6.8: Converged parameters $\theta_{1,opt}$, $x_{1,opt}$, $y_{1,opt}$, $\theta_{2,opt}$ and $x_{5,opt}$ and objective q'_{opt} and total computational time for the investigated initial population sizes, case #5.

Initial pop. size	$\theta_{1,opt}$ (°)	$x_{1,opt}$ (mm)	$y_{1,opt}$ (mm)	$\theta_{2,opt}$ (°)	$x_{5,opt}$ (mm)	q'_{opt} (W)	computational time (min)
40	18.5	16.4	30.6	-21.1	10.4	7.26	770
50	22.1	21.8	33.4	-20.8	13.2	7.25	1102
60	23.5	15.5	32.6	-21.2	9.7	7.269	1221
80	23.2	16.2	32.4	-21.3	10.1	7.268	2103

optimal solution that scores an even higher total heat transfer rate with approximately 7.27 W, compared to the 7.23 W of cases #3 and #4. As the fins are confined in the fixed volume $H \times L$, allowing the middle fin to move horizontally leads to new values of relative positions between the fins, among which, an even fitter one.

The projections of the solutions obtained for the individuals investigated throughout the shape optimization process of case #5 with a population size of 80 does not provide additional information but are presented in Appendix B.

Nevertheless, Table 6.8 provides information about the computing time required to perform the shape optimization over a five-dimensional search-space. These computing time results are illustrated in Fig. 6.22:

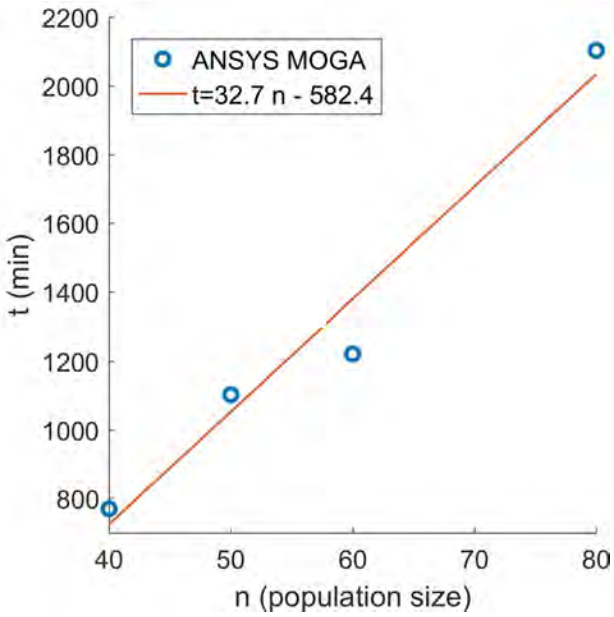

Figure 6.22: Total optimization's computing time as a function of the population size for case #5 - parallel computing on 48 cores.

An increase of both the computing time required to perform the shape optimization for a given population size, and the slope of the relationship between computing time and population size, is also observed for the case #5 as shown in Fig. 6.22. Although the study could not be performed over more search-spaces of different dimensions, an investigation can be done on the effect of the number of parameters (or search-space dimension) on the total computing time required for the GA to discover an optimal solution when coupled with CFD simulations. As it has been shown through the different cases, from case #1 to #5, the relationship between population size and computing time follows a linear behavior and the slope of this linear relationship increases with the search-space dimension. Indeed, Fig. 6.16(a), 6.18, 6.21 and 6.22 are combined together in Fig. 6.23 in order to show the evolution of the slope of $t(n)$ with the search-space dimension.

As it is shown in Fig. 6.23, the relationship between computing time and pop-

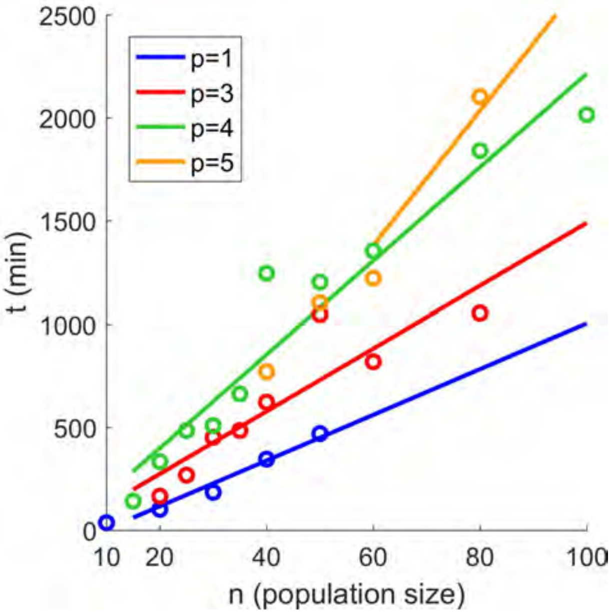

Figure 6.23: Optimization's computing time t as a function of the population size n and the search-space dimension p - parallel computing on 48 cores.

ulation size $t(n)$ is linear for a given search-space dimension p. The $t(n)$ curves present an increasing slope with p and are close to proportional curves, that is to say linear relationships with a y-intercept equal to 0, except for the 5-D search-space ($p = 5$) results. The discrepancy could possibly be due to misleading isolated results compared to the mean results one would have obtained with a statistical study. Nevertheless, the increase of the $t(n)$ slope with p is undeniable. Such linear relationship $t(n)$ and such evolution of the slope of $t(n)$ with the problem's complexity have been reported by Alander [19]. In his paper, Alander uses a test problem that is to find a sub-bitstring of size m of a given bitstring. The fitness function is the hamming distance between the chromosome and the targeted string. The complexity is defined by Alander to be the sub-bitstring's length, that is to say, m. His study is extensively described in [19]. Fig. 6.24 shows the execution time t as a function of the population size n and problem complexity c (with $c = m$).

The results from [19] show a linear relationship between the population size and the processing time for a given problem's complexity c, and show an increase of the $t(n)$ linear relationship's slope with the problem's complexity. In Alander's study, the complexity is well defined, namely: the complexity is the length of the sub-bitstring that must be determined. Therefore, he is able to present results of the

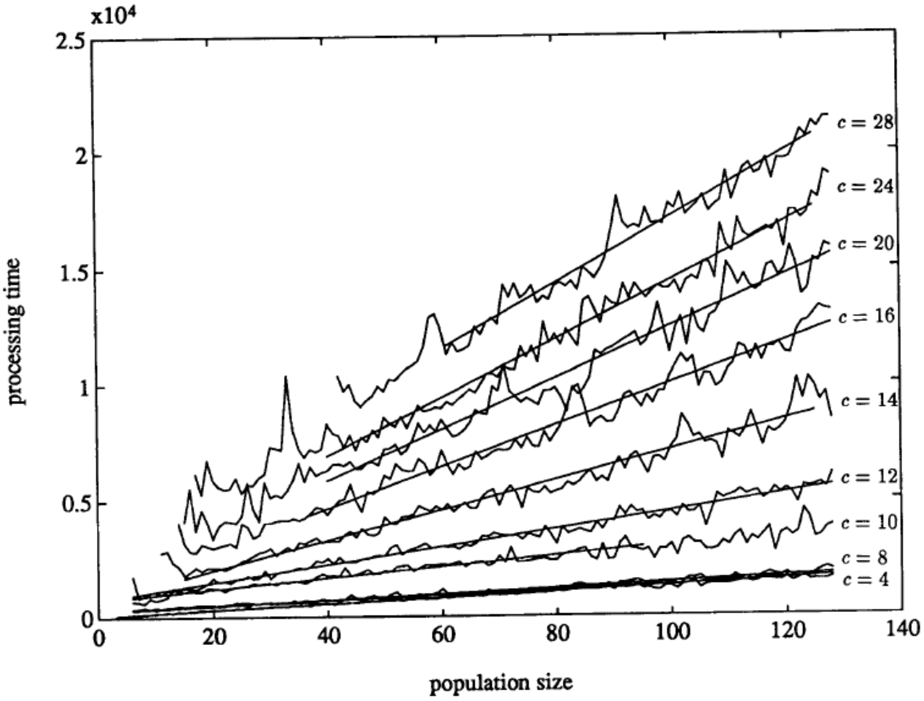

Figure 6.24: Optimization's computing time t as a function of the population size n and the problem's complexity c (time in relative units), [19].

slope of the $t(n)$ curve, k_1, as a function of the complexity c, as shown in Fig. 6.25.

Alander [19] fitted a linear curve to the data he obtained for the $t(n)$ curve's slope k_1 as a function of the complexity c as shown in Fig. 6.25. The relationship between k_1 and c appears to be rather non-linear at low complexity problems and tends towards linearity with increasing complexity.

Unlike Alander's study in which the complexity is well defined, the complexity of the present optimization problem depends on many parameters such as the search-space dimension, the way the fitness function is calculated, that is to say by using a CFD simulation, thus depending on the flow characteristics, and so on.

Figure 6.26 shows the relationship between k_1, the slope of the $t(n)$ curve, and p, the search-space dimension, based on the results from the present shape optimization procedure:

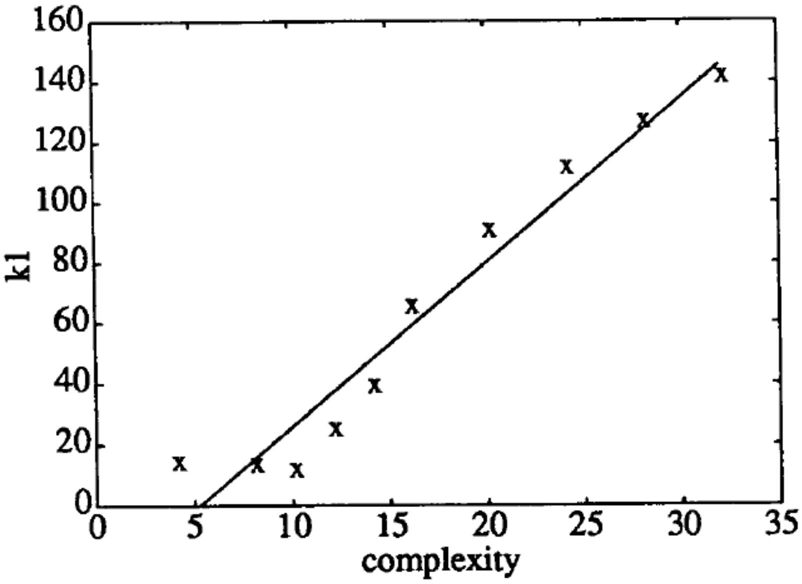

Figure 6.25: Slope of the processing curve k_1 as a function of the complexity c, [19].

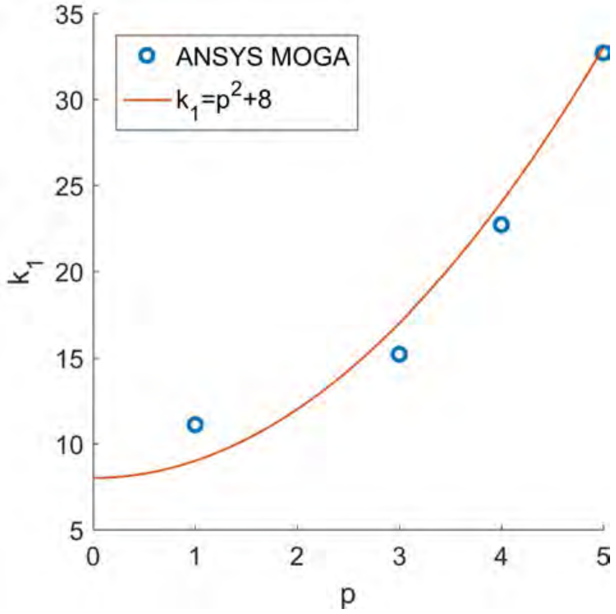

Figure 6.26: Slope of the $t(n)$ curve k_1 as a function of the search-space dimension p, present work.

As shown in Fig. 6.26, the relationship between the search-space dimension p, and the slope of the $t(n)$ linear curve k_1, is fitted with a square function. The slope of the linear relationship between processing time and populations size k_1 increases proportionally to the square of the search-space dimension p. When comparing these results to the results from [19] shown in Fig. 6.25, it can be hypothesized that: (i) either the complexity c of the present problem is proportional to the search-space dimension p and the results presented in Fig. 6.26 correspond to the low end of the complexity values shown in Fig. 6.25, for $7 \leq c \leq 15$ approximately, or (ii), c is proportional to the square-root of p in the present case. In order to compare the results from different studies, a repeatable method for the evaluation of complexity, independent of the problem's type, is required.

Additionally, it has been highlighted that the solution provided by the shape optimization procedure converges to a constant value with the increase of the population size. Therefore, there is, for each search-space dimension, a minimum population size that enables the discovery of the optimal solution that does not depend on the population size anymore. The optimal population, that is to say, the minimum population that achieves the discovery of the population size's independent solution, is estimated from Tables 6.4, 6.6, 6.7 and 6.8, and is plotted against the search-space dimension in Fig. 6.27.

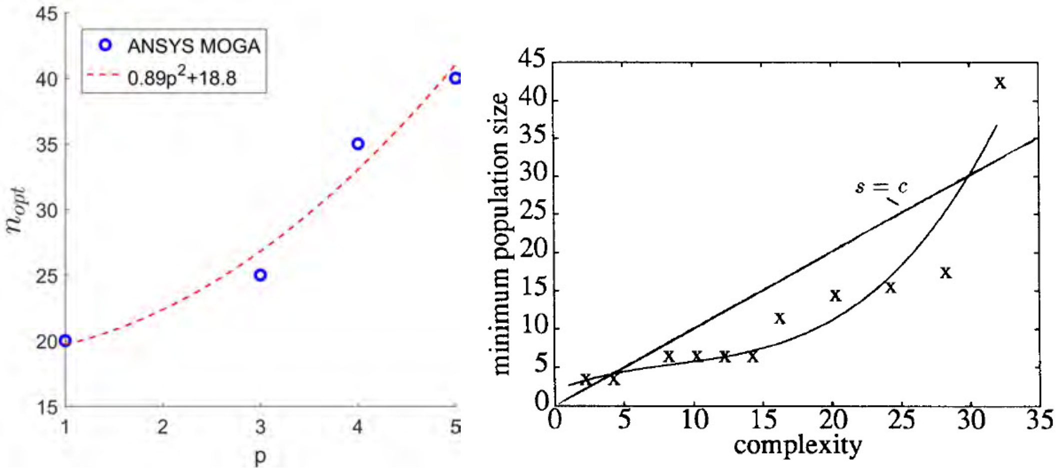

(a) Optimal population size n_{opt} against search-space dimension p

(b) Minimum population size s against problem's complexity c [19]

Figure 6.27: Optimal population size as a function of the search-space dimension (present work) and the complexity (from [19]).

According to the estimation of the optimal population size n_{opt} from the present numerical results, the relationship between n_{opt} and the search-space dimension p is fitted with a second-order polynomial curve, as shown in Fig. 6.27(a), such as n_{opt} appears to increase with the square of p. Alander reports non-linear results regarding the relationship between the minimum population size and the problem's complexity as shown in Fig. 6.27(b) [19]. A good agreement is noticeable regarding the trends in Fig. 6.27(a) and 6.27(b).

However, the small amount of available data in the present work, due to computer resource limitations, in addition to the difficulty to define a complexity parameter that does not depend on the problem's type, is preventing a more relevant comparison between results obtained from the shape optimization procedure combined with CFD simulations and the results reported by Alander [19]. It also should be noted that the present results must be considered with care as they are isolated results, which means that the problem is not studied statistically, as mentioned in Section 6.3.3.2.

6.3.4 Flow study of the optimal solution

All the different shape optimization procedures presented in Sections 6.3.3.1 to 6.3.3.4, that is to say cases #1 to #5, have provided an optimal solution to the problem of the three fins in cross flow. The optimal solution discovered by the ANSYS MOGA is analyzed and compared to another configuration in an attempt to understand the physics that could explain the advantage of this particular geometry that has been found to be optimal.

The optimal configuration is represented by the following vector of parameters: $(\theta_{1,opt} = 23°, x_{1,opt} = 16mm, y_{1,opt} = 32.5mm, \theta_{2,opt} = -21°, x_{5,opt} = 10mm)$ as shown in Table 6.8. This optimal configuration is compared to the geometry $(-23°, 16mm, 32.5mm, 21°, 10mm)$. This geometry correspond to the "convergent" version of the "divergent" optimal configuration as illustrated in Fig. 6.28 where both geometries are presented.

Firstly, the pressure and velocity fields have been compared as shown in Fig. 6.29 and 6.30 respectively.

Figure 6.29 shows the pressure field for both the optimal and convergent geometries. Firstly, it can be observed that the pressure range is similar for both configurations with 101315 $Pa \leq P \leq$ 101335 Pa. Interestingly, because of the

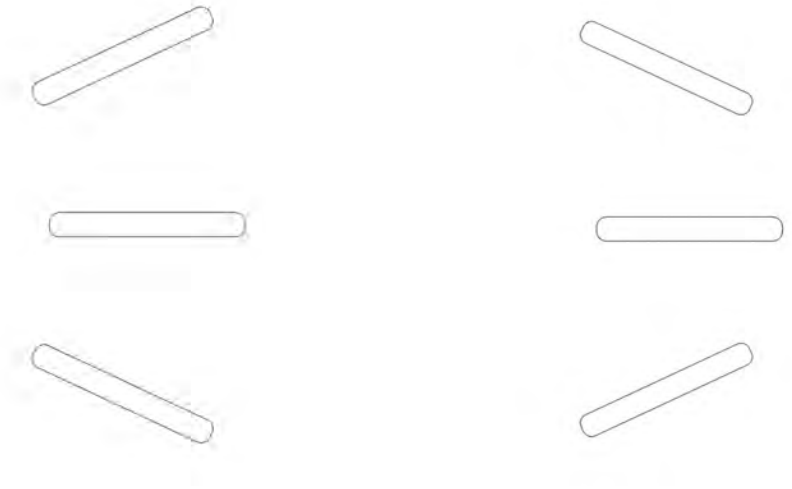

(a) (b)

Figure 6.28: Investigated geometries: the optimal geometry $(23°, 16mm, 32.5mm, -23°, 10mm)$ (a) is compared to another configuration (b) $(-23°, 16mm, 32.5mm, 23°, 10mm)$ in an attempt to understand what makes the optimal configuration optimal.

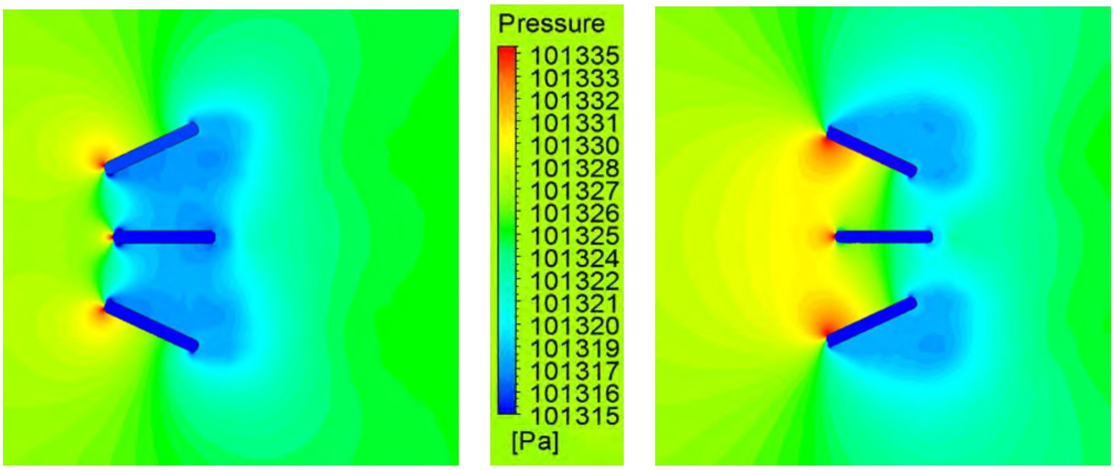

(a) (b)

Figure 6.29: Pressure field for the optimal geometry $(23°, 16mm, 32.5mm, -23°, 10mm)$ (a) and the convergent geometry $(-23°, 16mm, 32.5mm, 23°, 10mm)$ (b)

inclination of the top and bottom fins, low pressure recirculation zones and high pressure zones around the stagnation points create completely different pressure

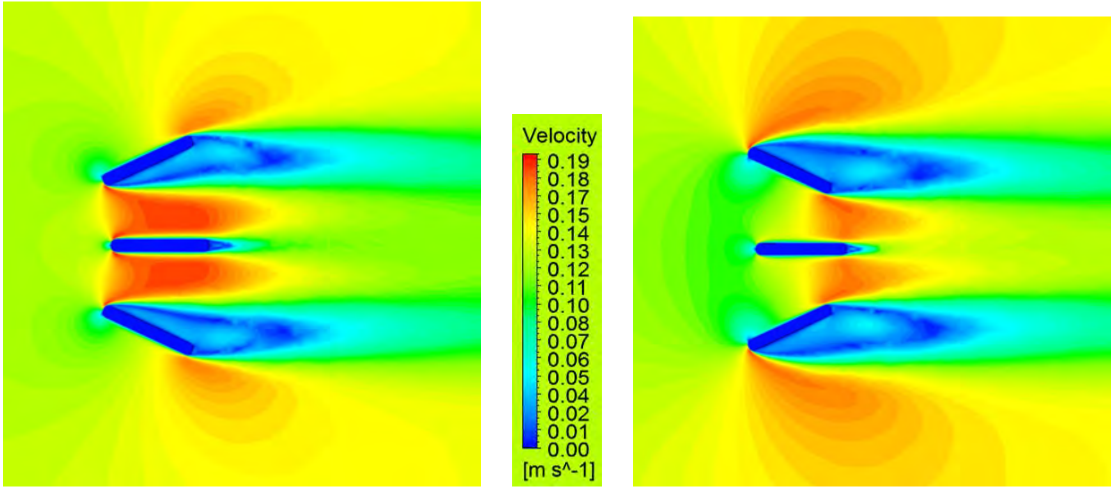

(a) (b)

Figure 6.30: Velocity field for the optimal geometry $(23^{\circ}, 16mm, 32.5mm, -23^{\circ}, 10mm)$ (a) and the convergent geometry $(-23^{\circ}, 16mm, 32.5mm, 23^{\circ}, 10mm)$ (b)

fields between Fig. 6.29(a) and 6.29(b).

In Fig. 6.29(a), the top (resp. bottom) fin's stagnation point is located on the top (resp. bottom) side of the fin, that is to say, the stagnation points on fins 1 and 2 (top and bottom fins) are located at the outter side of the fins, and therefore, high pressure regions (with $P \approx 101.332\ Pa$) appear outside the heat sink. On the other hand, the low pressure recirculation zones created by the inclination of the top and bottom fins are located towards the middle fin as shown in Fig. 6.29(a). As a result, a $P \approx 101.316\ Pa$ low pressure zone appears in between the top and middle fin as well as between the bottom and middle fin, creating a low pressure corridor around the middle fin. This low pressure corridor explains why the velocity around the middle fin is higher in Fig. 6.30(a), with $V \approx 0.18\ m \cdot s^{-1}$, than in Fig. 6.30(b) with $V \approx 0.13\ m \cdot s^{-1}$. Unlike what was expected, the "convergent" situation leads to a decrease of the velocity and an uneven value of the velocity along the middle fin, whereas the optimal "divergent" geometry enables a higher, almost constant, velocity along the entire length of the middle fin.

As shown in Fig. 6.29 and 6.30, the pressure and velocity fields of both cases around the top and bottom fins are very similar qualitatively and quantitatively. The heat transfer rate from the top and bottom fins is expected not to be different between the optimal case and the convergent case. However, because of the pressure distribution and the resulting velocity field around the middle fin, the heat transferred from the middle fin is expected to be higher in the optimal situation.

The temperature field of both the optimal and the convergent case are shown in Fig. 6.31.

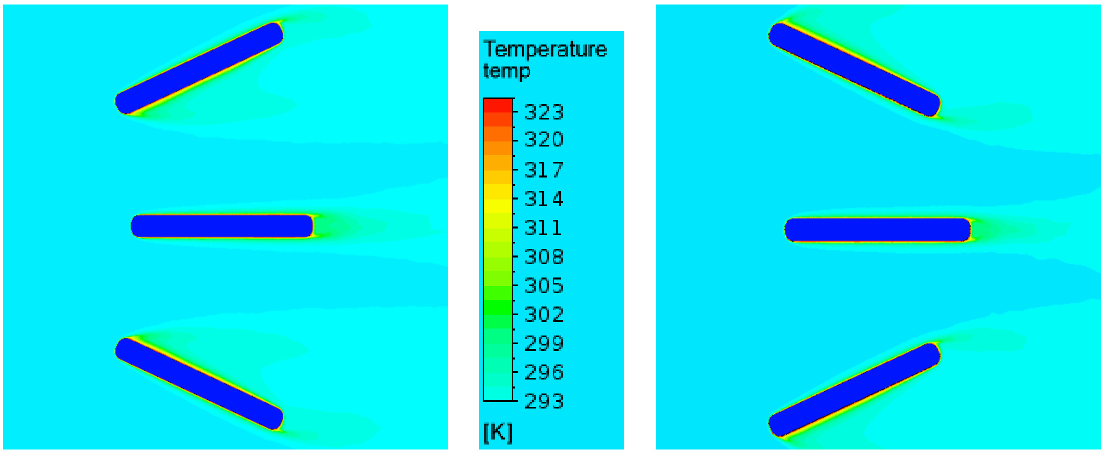

(a) (b)

Figure 6.31: Temperature field for the optimal geometry $(23°, 16mm, 32.5mm, -23°, 10mm)$ (a) and the convergent geometry $(-23°, 16mm, 32.5mm, 23°, 10mm)$ (b)

The difference in the temperature field, and especially the developing thermal boundary layers, between the optimal and the convergent case is not visible at this scale and therefore, a local study is conducted, that focuses on the middle fin.

The temperature is monitored along radial lines placed along the middle fin, corresponding to the blue lines shown in Fig. 6.32.

The distance from the wall δ_{99} at which the local fluid temperature has decreased to reach the temperature of $T_{99} = T_\infty + 0.01 \times (T_w - T_\infty)$ is defined as the "99% thermal boundary layer thickness". This distance is representative of the capacity of the fin to transfer heat to the surrounding fluid in the sense that, the thicker the thermal boundary layer, the higher the distance between near-wall hot fluid, and further colder fluid, that is to say, the higher the thermal resistance. The 99% thermal boundary layer thickness δ_{99} is plotted as at the monitored locations along the middle fin as shown in Fig. 6.33.

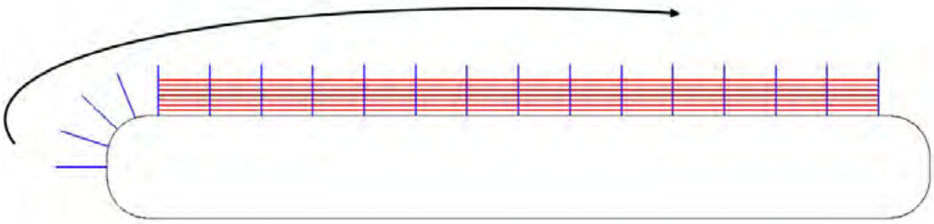

Figure 6.32: Monitoring positions. Nineteen 1 mm long radial lines numbered from 1 to 19 from left to right and seven 14 mm long horizontal lines numbered from 1 to 7 with increasing distance from the wall.

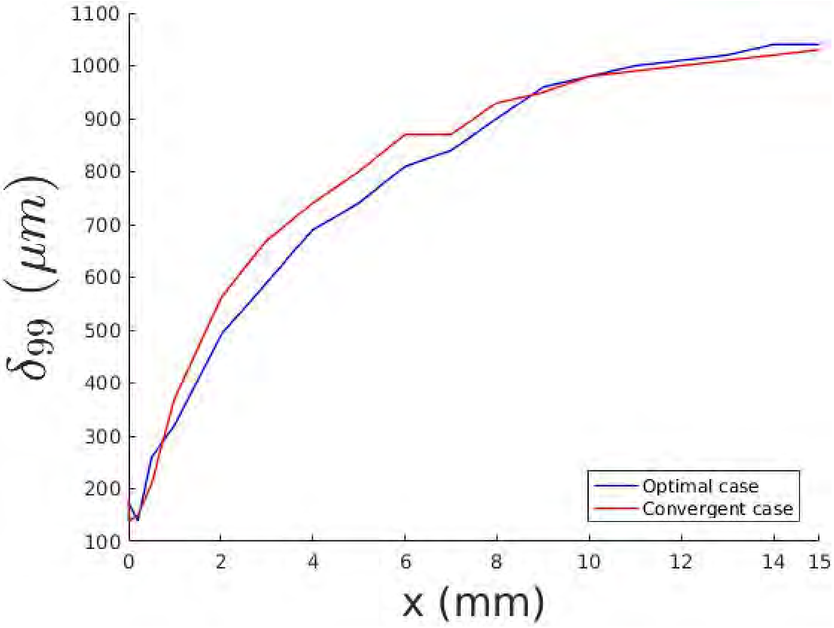

Figure 6.33: Boundary layer thickness along the middle fin.

As shown in Fig. 6.33, the boundary layer developing along the middle fin in the optimal case is thinner than in the convergent case up to $x \approx 9mm$, with a relative difference $\left|\frac{\delta_{99,opt} - \delta_{99,conv}}{\delta_{99,conv}}\right|$ up to 17% at $x = 3mm$, and thicker for $9mm \leq x \leq 15mm$, which involves that the thermal resistance in the first half along the fin is smaller in the optimal case. This would imply a better heat transfer in this region, in the optimal case compared to the convergent case.

In order to pursue the investigation, the study of heat transfer related quantities at the fins surface, is conducted. First of all, the overall Nusselt number $Nu = hL/k$, of each fin are compared, as presented in Table 6.9. The wall heat transfer coefficient h and the fluid's thermal conductivity k are obtained from the simulation, and the length that has been used to compute the Nusselt number is $L = 10\ mm$.

Table 6.9: Comparison of the surface-averaged Nusselt numbers of each fin for the convergent and the optimal cases

Convergent case			Optimal case		
top fin	middle fin	bottom fin	top fin	middle fin	bottom fin
375	436	374	387	458	388

The results shown in Table 6.9 show that in both cases, the overall Nusslet number of the middle fin is higher than the Nusselt number of the top and bottom fins. As the geometries under investigation are almost symmetrical, it is not surprising to have close overall Nusselt numbers for the top and bottom fins. More interestingly, the results shown in Table 6.9 can be observed in the light of the expectations presented in the previous paragraph. Indeed, the overall Nusselt number of the top (resp. bottom) fin in the optimal case, is slightly higher with $Nu = 387$ (resp. 388), than the top (resp. bottom) fin in the convergent case which scores 375 (resp. 374). However, the increase of performance from the convergent to the optimal case is more pronounced on the middle fin with an increase of overall Nusselt number from 436 to 458.

As extensively presented in Sections 3 and 5, the local characteristics of physical quantities related to heat transfer must be taken into account. Figure 6.34 shows the local Nusslet number at the surface of the middle fin for both the optimal and the convergent geometries. The horizontal location x is defined from the leading edge of the middle fin: $x = 0\ mm$ and $x = 0\ mm$ respectively correspond to the leftmost and rightmost point of the fin.

As shown in Fig. 6.34, the local Nusselt number varies significantly along the middle fin in both the optimal and the convergent cases. The higher local Nusselt number is reached, in both cases, near the stagnation point, where the flow

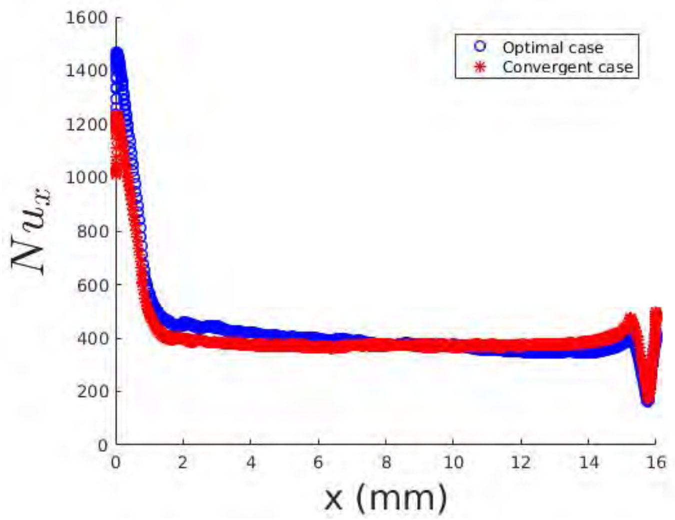

Figure 6.34: Local Nusselt number along the middle fin's surface for both optimal and convergent cases.

impinges the fin. The local Nusselt then decreases rapidly from 0 mm to 2 mm, and remains stable along the fin after the flow passed the fin's rounded corner. Moreover, the local Nusselt number is higher in the optimal case up to $x \approx 8mm$, which correlates well with the observation that the boundary layer thickness is smaller in this region in the optimal case, as shown in Fig. 6.33. The evolution of near-wall components have also been monitored into adjacent wall cells, that is to say in the thermal boundary layer, at the different monitoring locations along the fin shown in Fig. 6.32.

The time-averaged of the streamwise velocity gradient term $\dfrac{\partial u}{\partial x}$ is monitored from the fin's surface up to a distance of 1 mm away from the wall at the nineteen different different locations along the fin's surface shown in Fig. 6.32. The results for both cases are shown in Fig. 6.35.

The legend representing the results obtained from the monitoring lines numbered from 6 to 19, is omitted for clarity, as the results fall down to relatively low values compared to the results at locations 1 to 5 as it can be observed in Fig. 6.35. Results are very similar qualitatively between the convergent and optimal case. Indeed the streamwise velocity gradient increases rapidly as the fluid flows around the rounded corner with a peak at location 3 and decreases as rapidly as it increased, until it reaches a flat low value that stays approximately constant

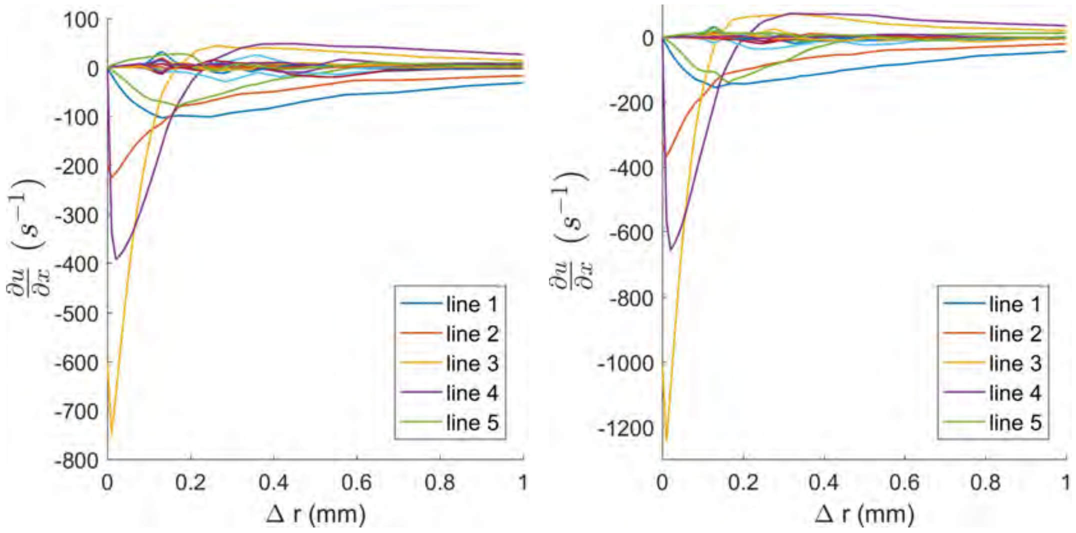

(a) Convergent case

(b) Optimal case

Figure 6.35: Time-averaged streamwise velocity gradient in the near-wall region at different locations along the middle fin. Δr represents the perpendicular distance from the wall.

along the fin. However, the results differ quantitatively with a maximum absolute value for the streamwise velocity gradient 40% higher in the optimal configuration compared to the convergent situation. The difference in value of the streamwise velocity gradient can explain the difference in local Nusselt number values at this location as the streamwise velocity gradient represents the convective acceleration.

The observation of the streamwise velocity gradient and the local Nusselt number is refined on the near wall region after the rounded corner corresponding to $1\ mm \leq x \leq 8\ mm$ in Fig. 6.34. $\dfrac{\partial u}{\partial x}$ is monitored at fixed radial distances from the fin's surface, from 1 mm to 8 mm along the fin after the rounded corner. This corresponds to the seven horizontal lines shown in Fig. 6.32. The streamwise velocity gradient is averaged in the radial direction in order to obtain a local radially-averaged streamwise velocity gradient along the fin, as presented in Fig. 6.36, against the local Nusselt number, for both the convergent and the optimal cases.

As shown in Fig. 6.36, the local Nusselt number and the local streamwise velocity gradient present a reasonable degree of coherence. Indeed, higher values of the streamwise velocity gradient for small $x \leq 2$ in the optimal configuration causes

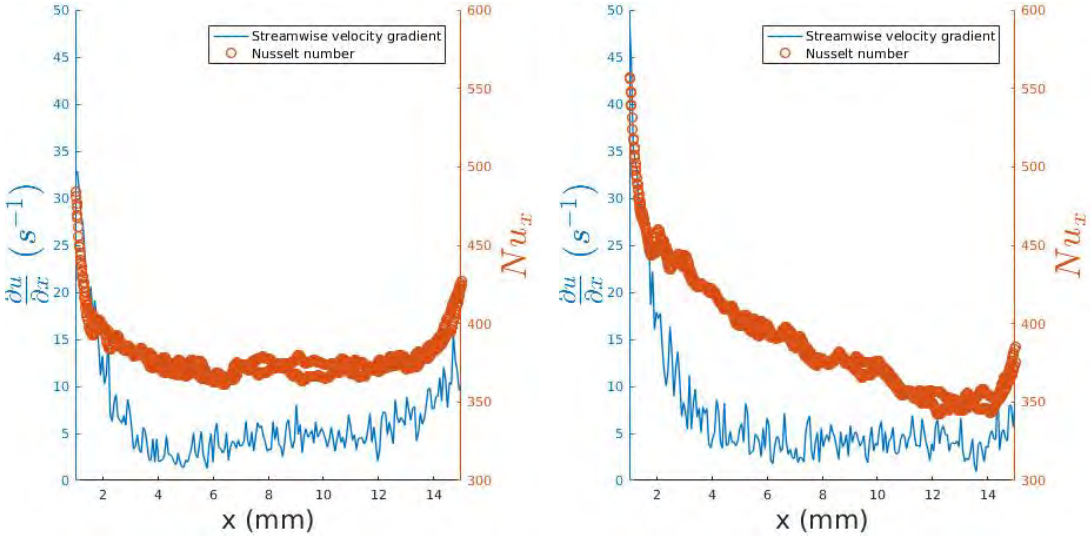

(a) Convergent case

(b) Optimal case

Figure 6.36: Radially-averaged local streamwise velocity gradient in the near-wall region along the middle fin against the local Nusselt number.

a higher local Nusselt number in this region which then decreases progressively as shown in Fig. 6.36(b). On the other hand, the streamwise velocity gradient does not exceed 30 s^{-1} for $x \leq 2$ for the convergent case, which leads to a lower local Nusselt number as shown in Fig. 6.36(a).

Another interesting component to observe in the near-wall region is the turbulent kinetic energy $k = 1/2(\overline{u'}^2 + \overline{v'}^2 + \overline{w'}^2)$ (where $w = 0$ in two-dimension). The turbulent kinetic energy is averaged radially and plotted as a function of the location along the fin and against the local Nusselt number, in Fig. 6.37.

As shown in Fig. 6.37, the coherence between the turbulent kinetic energy and the local Nusselt number is more important than between the streamwise velocity gradient and Nu_x. It is clear that the increase in local Nusselt number for the optimal case, compared to the convergent geometry, is related to an increase of the turbulent kinetic energy in the first half region along the fin, near the wall.

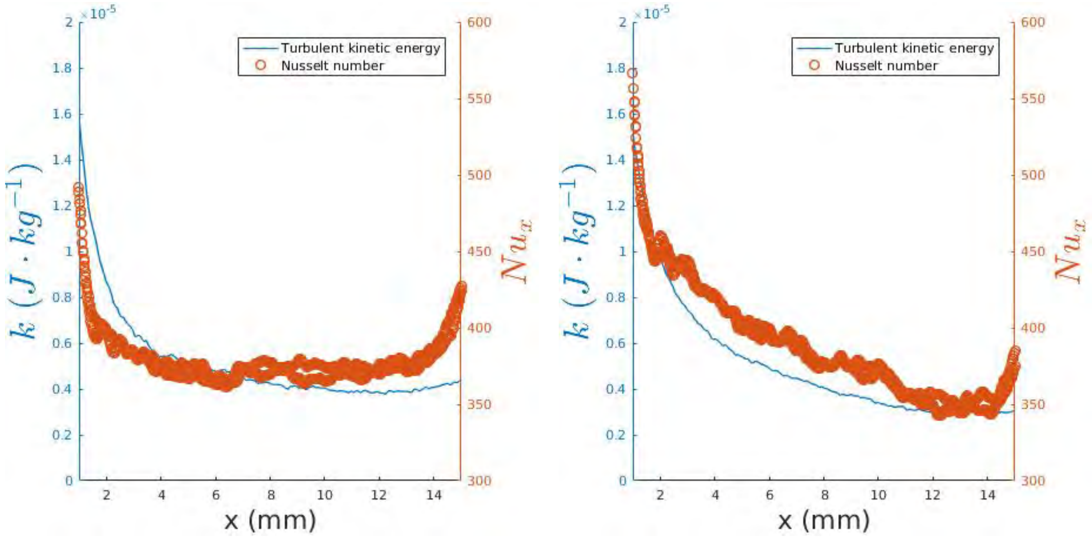

(a) Convergent case

(b) Optimal case

Figure 6.37: Turbulent kinetic energy $k = 1/2(\overline{u'}^2 + \overline{v'}^2)$ in the near-wall region along the middle fin against the local Nusselt number.

6.4 Summary of the chapter

Numerical results of a shape optimization that aims at maximizing the overall heat transfer rate from a heat sink composed of three or five fins, are presented in Chapter 6.

The numerical shape optimization procedure uses a genetic algorithm combined with a numerical CFD model, and is validated against analytical results in Section 6.2. A good agreement is found between the present numerical results and the analytical study.

This shape optimization procedure is then used to search for an optimal geometry that maximizes the heat transfer rate from three fins in cross flow, as presented in Section 6.3. Several different optimizations are performed in order to investigate the behavior of the genetic algorithm when combined with CFD simulations as the fitness function's evaluations. The convergence of the optimal solution discovered by the optimization procedure towards a constant configuration that does not depend on the GA's parameters indicates that the optimization procedure is capable of finding the optimal solution.

Moreover, a new study on the effects of one particular GA's parameter (which is the population size) on the results provided by the GA when used in combination with CFD simulations, and on the total processing time, is undertaken. The results show that the relationship between the population size and the computing time, for a given search-space dimension, is linear. However the slope of this linear curve increases with the dimension of the search-space. These results are in good agreement with results from the literature although they refer to different types of optimization problems and fitness functions. One of the next challenges in the understanding of genetic algorithms, is the definition of the complexity of an optimization problem, regardless of the problem's type.

Finally, the flow field and the local heat transfer from the fins of two different geometrical configurations, one "bad" solution, and the optimal one, are studied and compared. The increase of heat transfer rate in the optimal case, compared to the convergent case, is related to the increase of the local streamwise velocity gradient $\frac{\partial u}{\partial x}$ and turbulent kinetic energy k, especially along the middle fin, that presents a higher increase compared to the side fins. The increase of $\frac{\partial u}{\partial x}$ and k and the decrease of the thermal boundary layer thickness responsible for the higher heat transfer rate in the first half along the fin, could be explained by the increase of the velocity around the middle fin as the optimal geometry leads to the creation of a low pressure corridor that drives and accelerates the fluid.

Chapter 7

Conclusions and further work

7.1 Summary of the findings of this research work

This study is an investigation of the shape optimization of heat transfer structures surrounded by a fluid. A complete shape optimization approach is detailed, from the development of a computational fluid dynamics model that accurately evaluates the heat transfer phenomena in a fluid flow situation, to the development of a shape optimization procedure that resorts to the CFD model. One important aspect of this study is that both the CFD and the shape optimization processes are validated against experimental and analytical data from the literature and from in-house results.

Based on the literature review, most of the studies dealing with the understanding of heat transfer phenomena focused on simple geometries such as cylinders. However, some authors report enhancement of heat transfer characteristics in some cases with several bodies, more complex geometries, which confirms that the heat transfer potential can be improved by a shape modification. Additionally, the unsteady and local aspects of the heat transfer phenomena have been highlighted in the literature review. As a result, the investigation of a shape optimization approach using a CFD model that accurately predicts heat transfer phenomena, is undertaken.

The choice of the optimization method is guided by the literature review, that presents different methods with their advantages, and limitations. Genetic algorithms are recognized as the best approach to deal with heat and mass transfer problems, leading to the development of a shape optimization procedure featuring a CFD model and a genetic algorithm. This optimization process is used to search for the optimal geometry of a three fins heat sink in cross flow. This chapter highlights the main conclusions regarding the objectives stated in Section 1.3, and precised in Section 3.4, and presents possible new trails of investigation regarding the shape optimization of heat and mass transfer structures.

- A CFD numerical model has been developed to solve the flow around two close cylinders in natural convection. Realistic boundary conditions, computational domain, fluid properties and turbulence models have been adjusted based on a real natural convection heat transfer situation as presented in Section 4.3. The results from the numerical model have been compared to experimental data obtained from the real situation [105] and show a good agreement. The availability of detailed time-resolved flow and heat transfer data from the URANS simulations has provided insight into the interacting flow from two cylinders in natural convection, beyond the practical limitations of experimental measurements.

- Consequently, a shape optimization procedure featuring a genetic algorithm has been developed around the CFD model in order to optimize the geometry of complex structures for maximizing the heat transfer. After validation, a new study on how genetic algorithms operate when combined with CFD simulations has been conducted in the case of the shape optimization of a three fins heat sink in cross flow. The results provided by the GA converge towards a constant solution with the increase of the population size which indicates that an optimal solution exists and can be discovered by the GA when combined with the present CFD model. Moreover, a linear relationship between the computing time and the population size which agrees with other studies [19] is found, and a relationship between the search-space dimension and the slope of the linear curve is highlighted.

7.2 Suggestions for further work

A shape optimization procedure using genetic algorithms and CFD simulations to search for optimal geometries that maximize the heat transfer has been developed, validated, and provides promising results regarding the improvement of our understanding of GAs in combination with the developed CFD model, and regarding the improvement of heat transfer structure designs.

The utilization of such shape optimization procedure featuring a GA and CFD simulations can be extended to different problems, particularly to mass transfer problems as mass and heat transfer phenomena are similar. The study of coral growth using such shape optimization tool was initially considered.

Coral growth cannot be explained by pure shape optimization. Indeed, several other phenomena are, at least partially, responsible for the development of corals. The process of accretion for example, is reported by some authors to be one of the main phenomena that drive the coral growth [3]. Another example is the active enhancement of mass transport that corals can perform using small polyps that generate vortices in the boundary layer as reported by Shapiro et al. [5].

However, the enhancement of mass transfer and growth dynamics inside coral colonies can be affected by hydrodynamic phenomena. For example, the increase of the velocities inside the colony, and thus the increase of mass transfer, can be related to the presence of waves, as compared to a steady flow, in which case the velocity outside the colony is much higher than inside [4]. The shape optimization procedure developed in this work can be adapted to investigate the effect of the addition of waves to a steady flow on the optimal shape of heat or mass transfer structures. A CFD model that simulates the five fins heat sink in an oscillating flow has been developed but the model uses a URANS simulation for which the computational cost is much higher compared to a RANS simulation. It is comprehensible that the optimization of the heat sink in an oscillating - wave induced - flow would only be possible with significant computing resources.

The following points list different investigations that could be conducted in order to progress in our understanding of shape optimization and its applications on heat transfer structures improvement as well as on the study of organisms relying on mass transfer such as corals.

- To pursue the investigation of the effects of GA's parameters on the results and computing time, and define the "complexity" of a GA as a characteristic that allows a comparison between optimization problems different in nature. This characteristic could enable the GA user to have some expectations regarding the results, based on other optimization problems.

- To use an adaptive population size genetic algorithm in order to cope with the issue of the determination of the optimal population size. Obviously this method would be a less cost-effective option compared to a fixed population size GA for which the optimal population size has been accurately evaluated. However, this method could appear beneficial considering the difficulty to evaluate the optimal population size of a given optimization problem.

- To perform the shape optimization for cases with an increasing number of fins in order to move towards bio-inspired geometries. Obviously the computing resources are the main limitation in this case. The use of parallel computing and large number of processors is required, and in order to increase the available number of cores, the use of another, open-source, CFD solver, such as OpenFOAM, could be beneficial in order to deal with license restrictions.

- To consider three-dimensional structures. Indeed, the shape optimizations presented in this work have been done on two-dimensional bodies. One challenging improvement (in terms of computing resources mainly) of the present work is to extend the shape optimization procedure to three-dimensional geometries, as another step towards bio-inspired shapes.

- To use this shape optimization procedure in order to understand coral growth dynamics at a colony level by superimposing waves-induced movements to the steady flow. The unsteady simulations required to solve such unsteady flow, that are performed at each fitness evaluation, imply a significant increase of the available computing resources.

7.3 Publications

The results obtained during the course of this PhD project are synthesized in two peer-reviewed journal articles and conference materials as listed below.

- Q. Pelletier, T. Persoons and D.B. Murray, Numerical Study of the Natural Convection Heat Transfer of a Pair of Vertically Aligned Horizontal Cylinders, 1st CADFEM Ireland Users' Meeting ANSYS Regional Conference, Dublin, Ireland (2014)

- Q. Pelletier, D.B. Murray and T. Persoons, Unsteady natural convection heat transfer from a pair of vertically aligned horizontal cylinders, Int. J. Heat Mass Transfer vol. 95 pp. 693-708 (2016)

- Q. Pelletier, D.B. Murray and T. Persoons, Numerical optimization of unsteady natural convection heat transfer from a pair of horizontal cylinders, 7th European Thermal-Sciences Conference, 19-23 June 2016, Krakow, Poland

- Q. Pelletier, T. Persoons and Sajad Alimohammadi. Numerical shape optimization of two-dimensional fins in cross-flow: on the effects of the population size of genetic algorithms for CFD applications. In preparation.

Bibliography

[1] International Energy Agency, Key World Energy Statistics (KWES), (2015)

[2] A. Bejan, Shape and Structure, from Engineering to Nature, Cambridge University Press, (2000)

[3] N. Chindapol, J. A. Kaandorp, C. Cronemberger, T. Mass, A. Genin, Modelling Growth and Form of the Scleractinian Coral Pocillopora verrucosa and the influence of Hydrodynamics, PLOS Computational biology, vol. 9, issue 1 (2013)

[4] S. G. Monismith, Hydrodynamics of Coral Reefs, Annu. Rev. Fluid Mech. 39:37â"55 (2007)

[5] O. H. Shapiroa, V. I. Fernandeza, M. Garrena, J. S. Guastoa, F. P. Debaillon-Vesquea, E. Kramarsky-Winterb, A. Vardib, and R. Stockera. Vortical ciliary flows actively enhance mass transport in reef corals, Proc Natl Acad Sci USA, vol. 111 no. 37 pp. 13391-13396 (2014)

[6] D.S. Lemmons, Perfect form, Princeton Univ. Press, Princeton, NJ, (1997)

[7] A. Bejan, Advanced Engineering Thermodynamics, 2nd ed., Wiley, New York, (1997)

[8] A. Bejan, Street network theory of organization in nature, J. Adv. Transport, Vol. 30, pp. 85-107, (1996)

[9] A. Bejan, G. A. Ledezma, Streets, tree networks, and urban growth: optimal geometry for quick access between a finite-size volume and one point, Physica A, Vol. 255, pp. 211-217, (1998)

[10] A. Bejan, Entropy generation minimization: The new thermodynamics of finite-sized devices and finite-time processes, J. Appl. Phys., Vol. 79 , pp. 1191-1218, (1996)

[11] A. Bejan, General criterion for rating heat-exchanger performance, Int. J. of heat and mass transfer, Vol. 21, pp. 655-58, (1978)

[12] A. Bejan, Second law analysis in heat transfer, Energy, Vol. 5, pp. 721-32, (1980)

[13] G. Stanescu, A.J. Fowler and A. Bejan, The optimal spacing of cylinders in free-stream cross-flow forced convection, Int. J. Heat and Mass Transfer 39, pp 311-317, (1996)

[14] D. A. Nield and A. Bejan, Convection in Porous Media. Springer, New York (1992)

[15] J. H. Holland. Genetic algorithms. Scientific American, p. 66-72 (1992)

[16] M. Mitchell. An Introduction to Genetic Algorithms. MIT Press, (1996)

[17] D. E. Goldberg, Genetic Algorithms in Search Optimization and Machine Learning. Addison-Wesley, Reading (1989)

[18] D. E. Goldberg, Sizing populations for serial and parallel genetic algorithms. Proceedings of the Third Int. Conf. on Genetic Algorithms, pp 70-79 (1989)

[19] J. T. Alander, On Optimal Population Size of Genetics Algorithms. CompEuro '92 . Computer Systems and Software Engineering (1992)

[20] L. Davis. Handbook of Genetic Algorithms. Van Nostrand Reinhold, New York (1991)

[21] D. E. Goldberg, K. Deb, and J. H. Clark. Genetic Algorithms, Noise, and the Sizing of Populations. IlliGAL Report No. 91010 (1991)

[22] J.R. Culham, Y.S. Muzychka, IEEE Trans. Components and Packaging Technologies, Vol. 24, pp. 159-165, (2001)

[23] A. Bejan and E. Sciubba, The optimal spacing of parallel plates cooled by forced convection, Int. J. Heat Mass Transfer 35, 3259-3264 (1992)

[24] A. Bejan, A. M. Morega, The optimal spacing of stack of plates cooled by turbulent forced convection. Int. J. Heat Mass Transfer, Vol. 37, no. 6, pp. 1045-1048, (1994)

[25] A. Stevenson, C. Rocha, Deep Sea Research Part I: Oceanographic Research Papers , Vol. 71, pp. 73-78, (2013)

[26] S. V. Garimella, T. Persoons, J. Weibel, L.-T. Yeh, Technological drivers in data centers and telecom systems: Multiscale thermal, electrical, and energy management, Applied Energy, Vol. 107, pp. 66-80, (2013)

[27] A. Bejan, A. D. Kraus, Heat Transfer Handbook, John Wiley ” Sons Inc., New Jersey, Canada, (2003)

[28] J. Boussinesq, Théorie Analytique de la Chaleur, Vol. 2. Gauthier-Villars, Paris (1903)

[29] A. Oberbeck, Uber die Wärmeleitung der Flüssigkeiten bei Berücksichtigung der Strömungen infloge von Temperatur Differenzen, Ann. Phvs. Chem. 7, 271-292 (1879)

[30] F. Kreith, R. F. Boehm et al., Heat and Mass Transfer, Mechanical Engineering Handbook, Ed. Frank Kreith, Boca Raton: CRC Press LLC, (1999)

[31] T. H. Chilton, A. P. Colburn, Mass Transfer (Absorption) Coefficients Prediction from Data on Heat Transfer and Fluid Friction, Ind. Eng. Chem., 26 (11), pp 1183â“1187 (1934)

[32] E. Pohlhausen, Der Wärme austausch zwischen festen Körpern und Flussigkeiten mit kleine Reibung und kleiner Wärmeleitung. Z. Angew. Math. Mech. 1, 115 (1921)

[33] E. R. G. Eckert, Die Berechnung des Wärmeübergangs in der laminaren Grenzschicht. Forschungsh. Ver. Dtsch. Ing. 416, 1 (1942)

[34] D. B. Spalding, Mass transfer through laminar boundary layers-1. The velocity boundary layer. Int. J. Heat Mass Transfer, 2, 15 (1961)

[35] D. B. Spalding and H. L. Evans, Mass transfer through laminar boundary layers–2. Auxiliary functions for the velocity boundary layer. Int. J. Heat Mass Transfer, 2, 199 (1961)

[36] D. B. Spalding and H. L. Evans, Mass transfer through laminar boundary layers–3. Similar solutions of the b-equation. Int. J. Heat Mass Transfer, 2, 314 (1961)

[37] M. J. Lighthill, Contributions to the theory of heat transfer through a laminar boundary layer. Proc. Roy. Sot. A202, 359-377 (1950)

[38] A. N. Tifford, On the theory of heat transfer through a laminar boundary layer. J. Aero. Sci. 18, 283-284 (1951)

[39] E. N. Sieder and G. E. Tate, Heat Transfer and Pressure Drop of Liquids in Tubes, Ind. Eng. Chem., 28, 1429-1436, (1936)

[40] Incropera, Frank P., DeWitt, David P. Fundamentals of Heat and Mass Transfer (6th ed.). New York: Wiley. p. 514. ISBN 978-0-471-45728-2. (2007)

[41] H. Hausen, Darstellung des Wärmeauberganges in Rohren durch verallgemeinerte Potenzbeziehungen, Z. VDI, 4, 91-98, (1943)

[42] A. H. Davis, Convective cooling of wires in streams of viscous liquids, Phil. Meg. 47, 1057-1092 (1924)

[43] J. Ulsomer, Forsch. Geb. kg. 3, 94 (1932)

[44] E. L. Piret, W. JAMES and M. STACEY, Heat transmission from fine wires to water, Industr. Engng Chem. 39, 1098-11O3 (1947)

[45] H. A. Kramers, Physica 12, 61-80 (1946)

[46] W. H. McAdams, Heat Transmission, Third Ed. McGraw-Hill, New York (1954)

[47] H. Schuh, A new method for calculating laminar heat transfer on cylinders of arbitrary cross-section and on bodies of revolution at constant and variable wall temperature. Kungl Tckniska, Stockholm, Aero. TN 33 (1953)

[48] H. J. Merk, Rapid calculations for boundary layer transfer using wedge solutions and asymptotic expansions. J. Fluid Mech. 5, 460-480 (1959)

[49] W. J. M. Douglas and S. W. Churchill, Recorrelation of data for convective heat transfer between gases and single cylinders with large temperature differences, Chem. Engng Prog. Symp. Series 52, 23-28 (1956)

[50] B. G. Van Der Hegge Zijnen, Modified correlation formulae for the heat transfers by natural and forced convection from horizontal cylinders, Appl. Sci. Res. A 6, 129-140 (1957)

[51] P. D. Richardson, Estimation of the heat transfer from the rear of an immersed body to the region of separated flow, ARL 62-423, ASTIA, AD 290-339 (1962)

[52] H. C. Perkins and G. Leppert, Forced convection heat transfer from a uniformly heated cylinder, J. Heat Transfer 84,257-261 (1962)

[53] D. B. Spalding and W. M. Pun, A review of methods for predicting heat transfer coefficients for laminar uniform-property boundary layer flows, Int. J. Heat Mass Transfer, 5, 239-249 (1962)

[54] H. B. Squire, Heat transfer calculation for aerofoils. Aero. Res. Coun. (London), Rept. and Mem. No. 1986 (1942)

[55] H. A. Stine and K. Wanlass, Theoretical and experimental investigation of aerodynamic heating and isothermal heat transfer parameters on hemispherical noses with laminar boundary layers at supersonic Mach Numbers. NACA Technical Notes 3344 (1954)

[56] N. Frössling, Verdunstung, Wärmeübertragung und Geschwindigkeitsverteilung bei zweidimensionaler und rotationssymmetrischer laminaren Grenzschichtströmung. Lunds. Univ. Arsskr. N.F. Avd. 2, 35 (1940) (English transl. NACA Technical notes 1432)

[57] J. Kestin, P. F. Maeder and H. H. Sogin, The influence of turbulence on the transfer of heat to cylinders near the stagnation point. 2. Angew. Math. Phys. 12, 115-32 (1961)

[58] R. M. Fand, Heat transfer from a cylinder to water in crossflow, Int. J. Heat Mass Transfer 8, 995 (1965)

[59] S.W. Churchill, M. Bernstein, A correlating equation for forced convection from gases and liquids to a circular cylinder in cross flow, ASME Journal of Heat Transfer, 99 300-306 (1977)

[60] E. Schmidt and K. Wenner, Heat Transfer Over the Circumference of a Heated Cylinder in Transverse Flow, Technical memorande, NACA TN 1050, October (1943)

[61] H. C. Perkins Jr. and G. Leppert, Local Heat-Transfer Coefficients on a Uniformly Heated Cylinder, Int. J. Heat Mass Transfer. Vol. 7, pp. 143-158. (1964)

[62] R. A. Seban, The influence of free stream turbulence on the local heat transfer from cylinders, J. Heat Transfer, Trans. ASME, 82, 101-107 (1960)

[63] C.J. Apelt, M.A. Ledwich, Heat transfer in transient and unsteady flows past a circular cylinder in the range $1 < R < 40$, J. Fluid Mech. 95 (4) 761-777 (1979)

[64] G.E. Karniadakis, Numerical simulation of forced convection heat transfer from a cylinder in crossflow, Int. J. Heat Mass Transfer, 31, 107-118 (1988)

[65] C.-H. Cheng, J.-L. Hong, A. Win, Numerical prediction of lock-on effect on convective heat transfer from a transversely oscillating circular cylinder, Int. J. Heat Mass Transfer 40 1825-1834 (1997)

[66] F.M. Mahfouz, H.M. Badr, Forced convection from a rotationally oscillating cylinder placed in a uniform stream, Int. J. Heat Mass Transfer 43 3093-3104 (2000)

[67] C.F. Lange, F. Durst, M. Breuer, Momentum and heat transfer from cylinder in laminar cross-flow at 10?4 6 Re 6 200, Int. J. Heat Mass Transfer 41 3409-3430 (1998)

[68] L. Baranyi, Computation of unsteady momentum and heat transfer from a fixed circular cylinder in laminar flow, J. Comput. Appl. Mech 4 13-25 (2003)

[69] A.P.S. Bhinder, S. Sarkar, A. Dalal, Flow over and forced convection heat transfer around a semi-circular cylinder at incidence, Int. J. Heat Mass Transfer 55 5171-84 (2012)

[70] T. Igarashi, Fluid flow and heat transfer around rectangular cylinders (the case of a width/height ratio of a section of o.33e1.5), International Journal of Heat Mass Transfer 30 893-901 (1987)

[71] M. Ali, O. Zeitoun and A. Nuhait, Forced convection heat transfer over horizontal triangular cylinder in cross flow, Int. J. Heat Mass Transfer 50 106-114 (2011)

[72] V.K. Patnana, R.P. Bharti, R.P. Chhabra, Two-dimensional unsteady flow of power-law fluids over a cylinder, Chem. Eng. Sci. 64 2978-2999 (2009)

[73] V.K. Patnana, R.P. Bharti, R.P. Chhabra, Two-dimensional unsteady forced convection heat transfer in power-law fluids from a cylinder, Int. J. Heat Mass Transfer 53 4152-67 (2010)

[74] Y.B. Zeldovich, Limiting laws of freely rising convection currents, Zh. Eksp. Teor. Fiz. 7(12), 1463-1465 (1937)

[75] W. Tollmien, Berechnung turbulenter Ausbreitungsvorgange, Z. Angew. Math. Mech. 6, 468-478 (1926)

[76] H. Schlichting, Laminare Strahlausbreitung, Z. Annew. Math. Mech. 13. 260-263 (1933)

[77] W. Schmidt, Turbulente Ausbreitung Eines Stromes Erhitzten Luft, II. Z. Angew. Math. Mech. 21, 351-363 (1941)

[78] H. Schuh, Boundary layers of temperature, Section B.6 of W. Tollmienâ™s boundary layers, British Ministry of Supply, German Document Center, Reference 3220T (1948)

[79] C. S. Yih, Free convection due to a point source of heat, Proc. 1st U.S. Natn. Congr. Appl. Mech., pp. 941-947 (1951)

[80] C. S. Yih, Laminar free convection due to a line source of heat, Trans. Am. Geophys. Un. 33(5), 669-672 (1952)

[81] E.R.G. Eckert, E.E. Soehngen, Studies on heat transfer in laminar free convection with the Zehnder-Mach interferometer, AF Technical report, (1948)

[82] H. J. Merk and J. A. Prins, Thermal Convection in Laminar Boundary Layers I, II, and III, Appl. Sci. Res., A4, 11-24, 195-206, 207-221, (1953-54)

[83] E. J. LeFevre and A. Ede, Laminar Free Convection from the Outer Surface of a Vertical Circular Cylinder, Proc. 9th International Congress on Applied Mechanics, Brussels, Vol. 4, pp. 175-183, (1956)

[84] J. J. Mahony, Heat transfer at small Grashof number. Proc. Roy. Soc. 238A, 412423 (1956)

[85] S. I. Lee and H. W. Emmons, A study of natural convection above a line fire, J. Fluid Mech., vol. 11, pp. 353-368 (1961)

[86] T. Fujii, Theory of steady laminar natural convection above a horizontal line heat source and a point heat source, Int. J. Heat Mass Transfer vol. 6, pp. 597-606 (1963)

[87] R. S. Brand and F. J. Lahey, Heated laminar vertical jet, J. Fluid Mech., vol. 29, pp. 305-315 (1967)

[88] P. H. Oosthuizen and D. Naylor, Introduction to Convective Heat Transfer Analysis, McGraw-Hill, New York, (1999)

[89] B. Gebhart, L. Pera and A.W. Schorr, Steady Laminar Natural Convection Plumes above a Horizontal Line Heat Source, Int. J. Heat Mass Transfer, vol. 13, pp. 161-171, (1970)

[90] G.F. Marsters, Arrays of heated horizontal cylinders in natural-convection, Int. J. Heat Mass Transfer, vol. 15, pp. 921-933, (1972)

[91] V.T. Morgan, The overall convective heat transfer from a smooth circular cylinder, Adv. Heat Transfer, vol. 11, pp. 199-264, (1975)

[92] J. Stafford, V. Egan, Configurations for single-scale cylinder pairs in natural convection, International Journal of Thermal Sciences, vol. 84, pp. 62-74 (2014)

[93] C. S. Dai, Meng Li, H. Y. Lei and S. X. Wang, Numerical simulation of natural convection between hot and cold microtubes in a cylinder enclosure, Int. J. Thermal Science, vol. 95, pp. 115-122 (2015)

[94] G. Sebastian, S.R. Shine, Natural convection from horizontal heated cylinder with and without horizontal confinement, Int. J. Heat Mass Transfer, vol. 82 pp. 325-34, (2015)

[95] Y.G. Park, M.Y. Ha, C. Choi, J. Park, Natural convection in a square enclosure with two inner circular cylinders positioned at different vertical locations, Int. J. Heat Mass Transfer, vol. 77 pp. 501-18, (2014)

[96] R. Shyam, C. Sasmal, R.P. Chhabra, Natural convection heat transfer from two vertically aligned circular cylinders in power-law fluids, Int. J. of Heat Mass Transfer, vol. 64 pp. 1127-1152 (2013)

[97] L. Pera, B. Gebhart, Experimental observations of wake formation over cylindrical surfaces in natural convection flows, Int. J. Heat Mass Transfer 15 177-180 (1972)

[98] A.W. Schorr, B. Gebhart, An experimental investigation of natural convection wakes above a line heat source, Int. J. Heat Mass Transfer 13 557-571 (1970)

[99] T.H. Kuehn, R.J. Goldstein, Numerical solution to the Navier-Stokes equations for laminar natural convection about a horizontal isothermal circular cylinder, Int. J. Heat Mass Transfer 23 971-979 (1980)

[100] K. Noto, Swaying motion in thermal plume above a horizontal line heat source, J. Thermophys. 3 428-434 (1989)

[101] G. Desrayaud, G. Lauriat, Unsteady confined buoyant plumes, J. Fluid Mech. 252 617-646 (1993)

[102] K. Kitamura, F. Kami-iwa, T. Misumi, Heat transfer and fluid flow of natural convection around large horizontal cylinders, Int. J. Heat Mass Transfer 42 4093-4106 (1999)

[103] I.M. O'Gorman, D.B. Murray, G. Byrne, T. Persoons, Natural convection from isothermal horizontal cylinders, Proceedings of the ASME Int. Mech. Engineering Congress, Florida, 913, IMECE2009-11213, Nov. (2009)

[104] O. Reymond, D.B. Murray, T.S. O'Donovan, Natural convection heat transfer from two horizontal cylinders, Exp. Therm. Fluid Sci. vol. 32 pp. 1702-09, (2008)

[105] T. Persoons, I.M. O'Gorman, D.B. Donoghue, G. Byrne, D.B. Murray, Natural convection heat transfer and fluid dynamics for a pair of vertically aligned isothermal horizontal cylinders, Int. J. Heat Mass Transfer, vol. 54 pp. 5163-72, (2011)

[106] Q. Pelletier, D.B. Murray and T. Persoons, Unsteady natural convection heat transfer from a pair of vertically aligned horizontal cylinders, Int. J. Heat Mass Transfer vol. 95 pp. 693-708 (2016)

[107] S. Grafsrønningen , A. Jensen, Natural convection heat transfer from two horizontal cylinders at high Rayleigh numbers, International Journal of Heat and Mass Transfer 55 5552-5564 (2012)

[108] S. Grafsrønningen , A. Jensen, Natural convection heat transfer from three vertically arranged horizontal cylinders with dissimilar separation distance at moderately high Rayleigh numbers, International Journal of Heat and Mass Transfer 57 519-527 (2013)

[109] Y.G. Park, M.Y. Ha, H.S. Yoon, Study on natural convection in a cold square enclosure with a pair of hot horizontal cylinders positioned at different vertical locations, Int. J. Heat Mass Transfer vol. 65, pp. 696-712 (2013)

[110] D. Fiscaletti, D. Angeli, L. Tarozzi, G.S. Barozzi, Buoyancy-induced transitional flows around an enclosed horizontal cylinder: An experiment, Int. J. Heat Mass Transfer, vol. 58 pp. 619-31, (2013)

[111] J.P. Kuehner, A.M. Hamed, J.D. Mitchell, Experimental investigation of the free convection velocity boundary layer and plume formation region for a heated horizontal cylinder, Int. J. Heat Mass Transfer, vol. 82 pp. 78-97, (2015)

[112] J.P. Kuehner, J.R. Pflug, F.A. Tessier Jr., A.M. Hamed, F.J. Moiso Marin, Velocity measurements in the free convection flow above a heated horizontal cylinder, Int. J. Heat Mass Transfer, vol. 55 pp. 4711-23, (2012)

[113] A. Bar-Cohen and W. M. Rohsenow, Thermally optimum spacing of vertical, natural convection cooled, parallel plates, J. Heat Transfer 106, 116-123 (1984)

[114] A. Bejan, Convection Heat Transfer, p. 157, Problem 11. Wiley, New York (1984)

[115] S. H. Kim, N. K. Anand and L. S. Fletcher, Free convection between series of vertical parallel plates with embedded line heat sources, J. Heat Transfer 113, 108 115 (1991)

[116] N. K. Anand, S. H. Kim and L. S. Fletcher, The effect of plate spacing on free convection between heated parallel plates, J. Heat Transfer 114, 515-518 (1992)

[117] W. Nakayama, H. Matsushima and P. Goel, Forced convective heat transfer from arrays of finned packages. In Cooling Technology for Electronic Equipment (Edited by W. Aung), pp. 195-210. Hemisphere, New York (1988)

[118] R. W. Knight, J. S. Goodling and D. J. Hall, Optimal thermal design of forced convection heat sinks-analytical, J. Electronic Packaging 113, 313-321 (1991)

[119] R. W. Knight, J. S. Goodling and B. E. Gross, Optimal thermal design of air cooled forced convection finned heat sinks - experimental verification, IEEE Trans. Components, Hybrids Manufacturing Technol. 15, 754-760 (1992)

[120] H. Matsushima, T. Yanagida and Y. Kondo, Algorithm for predicting the thermal resistance of finned LSI packages mounted on a circuit board, Heat Transfer Jap. Res. 21, 504-517 (1992)

[121] A. Bejan and A. M. Morega, Optimal arrays of pin fins and plate fins in laminar forced convection, J. Heat Transfer 115, 75-81 (1993)

[122] H. Sun, R. Li, E. Chénier, G. Lauriat and J. Padet, Optimal plate spacing for mixed convection from an array of vertical isothermal plates, Int. J. of Thermal Sciences 55, 16-30, (2012)

[123] J. Nocedal, S. J. Wright. Numerical Optimization, second edition, Springer series in Operations Research and Financial Engineering (2000)

[124] G. B. Dantzig. Reminiscences about the origin of linear programming, Technical report SOL 81-5 (1981)

[125] G. Sierksma. Linear and Integer Programming: Theory and Practice, Second Edition. CRC Press. p. 1. ISBN 978-0-8247-0673-9 (2001)

[126] A. M. Turing. Computing machinery and intelligence, Mind vol. 59 no. 236, pp. 433-460 (1950)

[127] Fraser, Alex; Burnell, Donald. Computer Models in Genetics. New York: McGraw-Hill. ISBN 0-07-021904-4 (1970)

[128] I. Rechenberg, Evolutionsstrategie. Stuttgart: Holzmann-Froboog. ISBN 3-7728-0373-3 (1973)

[129] H.-P. Schwefel, Numerische Optimierung von Computer-Modellen (PhD thesis) (1974)

[130] J. H. Holland. Hierarchical descriptions of universal spaces and adaptive systems. In A. W. Burks (Ed.), Essays on cellular automata, pp. 320 353. Urbana: University of Illinois (1970)

[131] J. H. Holland. Adaptation in natural and artificial systems, Ann Arbor. MI: University of Michigan Press (1975)

[132] K. A. De Jong, Analysis of the Behaviour of a Class of Genetic Adaptive Systems. PhD thesis, University of Michigan (1975)

[133] J. J. Grefenstette. Optimization of control parameters for genetic algorithms, IEEE Transactions on Systems, Man, and Cybernetics, SMC vol. 16 no. 1, pp. 122-128 (1986)

[134] M. Pelikan, D. E. Goldberg, and E. Cant-Paz, Bayesian optimization algorithm, population sizing, and time to convergence. Illinois Genetic Algorithms Laboratory, University of Illinois, Tech. Rep., (2000)

[135] A. Piszcz and T. Soule, Genetic programming: Optimal population sizes for varying complexity problems. Proceedings of the Genetic and Evolutionary Computation Conference, pp. 953-954, (2006)

[136] F. G. Lobo and D. E. Goldberg, The parameter-less genetic algorithm in practice. Information Sciencesâ”Informatics and Computer Science, vol. 167, no. 1-4, pp. 217-232, (2004)

[137] F. G. Lobo and C. F. Lima, A review of adaptive population sizing schemes in genetic algorithms. Proceedings of the Genetic and Evolutionary Computation Conference, pp. 228-234, (2005)

[138] T.-L. Yu, K. Sastry, D. E. Goldberg, and M. Pelikan, Population sizing for entropy-based model building in genetic algorithms. Illinois Genetic Algorithms Laboratory, University of Illinois, Tech. Rep., (2006)

[139] G. R. Harik and F. G. Lobo, A parameter-less genetic algorithm. Proceedings of the Genetic and Evolutionary Computation Conference, pp. 258-265, (1999)

[140] Z. M. Jaroslaw Arabas and J. Mulawka, GAVaPSâ”a genetic algorithm with varying population size. Proceedings of the IEEE International Conference on Evolutionary Computation, pp. 73-78, (1995)

[141] A. E. Eiben, R. Hinterding, and Z. Michalewicz, Parameter control in evolutionary algorithms. IEEE Transactions on Evolutionary Computation, vol. 3, no. 2, pp. 124-141, (1999)

[142] C. Poloni, A. Giurgevich, L. Onesti and V. Pediroda. Hybridization of a multi-objective genetic algorithm, a neural network and a classical optimizer for a complex design problem in fluid dynamics. Int. J. Heat and Mass Trans. vol. 186, pp. 403-420 (2000)

[143] Y. Weilin, H. Hongyan and H. Wanjin, Design Optimization of Transonic Compressor Rotor Using CFD and Genetic Algorithm. ASME Turbo Expo 2006: Power for Land, Sea, and Air vol. 6: Turbomachinery, Parts A and B (2006)

[144] J. Doyle, R. Hartfield and C. Roy, Aerodynamic Optimization for Freight Trucks using a Genetic Algorithm and CFD. 46th AIAA Aerospace Sciences Meeting and Exhibit. (2008)

[145] R. Hilbert, G. Janiga, R. Baron and D. ThÃ©venin, Multi-objective shape optimization of a heat exchanger using parallel genetic algorithms. Int. J. Heat and Mass Trans. vol. 49, pp. 2567-2577 (2006)

[146] K. Foli, T. Okabe, M. Olhofer, Y. Jin and B. Sendhoff, Optimization of micro heat exchanger: CFD, analytical approach and multi-objective evolutionary algorithms. Int. J. Heat and Mass Trans. vol. 49, pp. 1090-1099 (2006)

[147] G.N. Xie, B. Sunden and Q.W. Wang, Optimization of compact heat exchangers by a genetic algorithm. Int. J. Heat and Mass Trans. vol. 28, pp. 895-906 (2008)

[148] S. Forrest. Genetic algorithms: principles of natural selection applied to computation. Science, vol. 261, pp. 872-878 (1993)

[149] J. Koza, B. Forest, A. David and K. Martin. Genetic Programming III: Darwinian Invention and Problem Solving. Morgan Kaufmann Publishers, (1999)

[150] J. Koza, K. Martin, M. Streeter, W. Mydlowec, J. Yu and G. Lanza. Genetic Programming IV: Routine Human-Competitive Machine Intelligence. Kluwer Academic Publishers, (2003)

[151] ANSYS Fluent Documentation, (2014)

[152] R.I. Issa, Solution of Implicitly Discretized Fluid Flow Equations by Operator Splitting. J. Comput. Phys., vol. 62 pp. 40-65, (1986)

[153] I. Dermidzic, Z. Lilek, M. Peric, A collocated finite volume method for predicting flows at all speeds. International journal for numerical methods in fluids, vol 16, 1029-1050 (1993)

[154] F. Menter, T. Esch, Elements of industrial heat transfer predictions, COBEM, 16th Brazilian Congress of Mechanical Engineering, (2001)

[155] F.R. Menter, Two-Equation Eddy-Viscosity Turbulence Models for Engineering Applications. AIAA Journal, 32(8):1598-1605, (1994)

[156] A. Bejan, A.D. Kraus, Heat Transfer Handbook, John Willey Sons, (2003)

[157] Deb K., Agrawal S., Pratap A., and Meyarivan T., A Fast Elitist Non-Dominated Sorting Genetic Algorithm for Multi-Objective Optimization: NSGA-II, Kanpur Genetic Algorithms Laboratory (KanGAL) Indian Institute of Technology Kanpur Kanpur, PIN 208 016, India KanGAL Report No. 200001

[158] Srinivas, N. and Deb, K. Multi-Objective function optimization using non-dominated sorting genetic algorithms, Evolutionary Computation, vol. 2(3), pp. 221-248 (1995)

[159] Shared hierarchical academic research computing network (Sharcnet). `https://www.sharcnet.ca/Software/Ansys/16.2.3/en-us/help/wb_dx/dxBEMtemp11.html`

[160] Zitzler, E. and Thiele, L. Multiobjective optimization using evolutionary algorithms - A comparative case study. In Eiben, A. E., Bäck, T., Schoenauer, M., and Schwefel, H.-P., editors, Parallel Problem Solving from Nature, pp. 292-301, Springer, Berlin, Germany (1998)

[161] Rudolph, G. Evolutionary search under partially ordered sets. Technical Report No. CI-67/99, Dortmund: Department of Computer Science/LS11, University of Dortmund, Germany (1999)

[162] Zitzler, E., Deb, K., and Thiele, L. (in press) Comparison of multiobjective evolutionary algorithms: Empirical results. Evolutionary Computation, 8.

[163] Knowles, J. and Corne, D. The Pareto archived evolution strategy: A new baseline algorithm for multiobjective optimisation. Proceedings of the 1999 Congress on Evolutionary Computation, Piscatway: New Jersey: IEEE Service Center, 98-105 (1999)

[164] Irish Centre for High-End Computing website, infrastructure details. `https://www.ichec.ie/infrastructure/`

[165] Irish Centre for High-End Computing website, ANSYS Fluent information. `https://www.ichec.ie/infrastructure/software/FLUENT`

[166] Irish Centre for High-End Computing website, Fionn server specifications. `https://www.ichec.ie/infrastructure/fionn`

[167] M.M. Zdravkovich, Flow around circular cylinders. Part 1: Fundamentals, Oxford University Press, (1997)

Appendix A

Thermal plume oscillations visualization

The video of the simulation conducted to capture the flow and heat transfer interactions between two cylinders thermal plumes can be visualized at the adress below. The pictures presented in Fig. 5.12 have been taken from this video.

The video depicts the formation, development and swaying of the thermal plume arising from the heated cylinders initially placed in water at rest, for the most investigated case $Ra = 3.35 \times 10^6$ and $S = 3D$.

`https://drive.google.com/open?id=0B0Q2curze67ORnN3V2VKb08yVTQ`

Appendix B

Results from the shape optimization investigation

B.1 Three fins shape optimization over a four dimensional search-space

The additional two-dimensional projections of the 4-D search-space studied in Section 6.3.3.3 are presented in Fig. B.1.

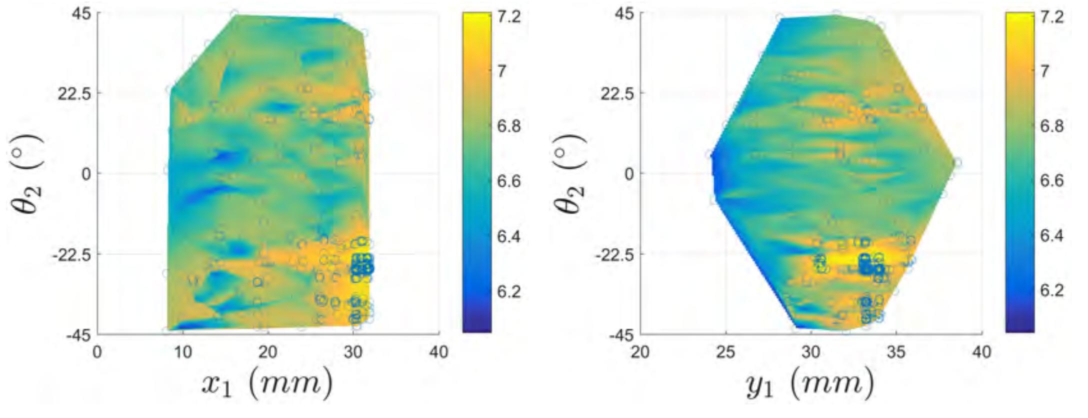

(a) Projection on the (x_1, θ_2) 2-D sub-space (b) Projection on the (y_1, θ_2) 2-D sub-space

Figure B.1: Overall heat transfer rate q' results interpolated and projected on different two-dimensional sub-spaces of the search space, case #4, population size equal to 100. The circle markers corresponds to raw evaluations.

B.2 Three fins shape optimization over a five dimensional search-space

The 2-D sub-spaces of the 5-D search-space studied in Section 6.3.3.4 are presented in Fig. B.2 and B.3.

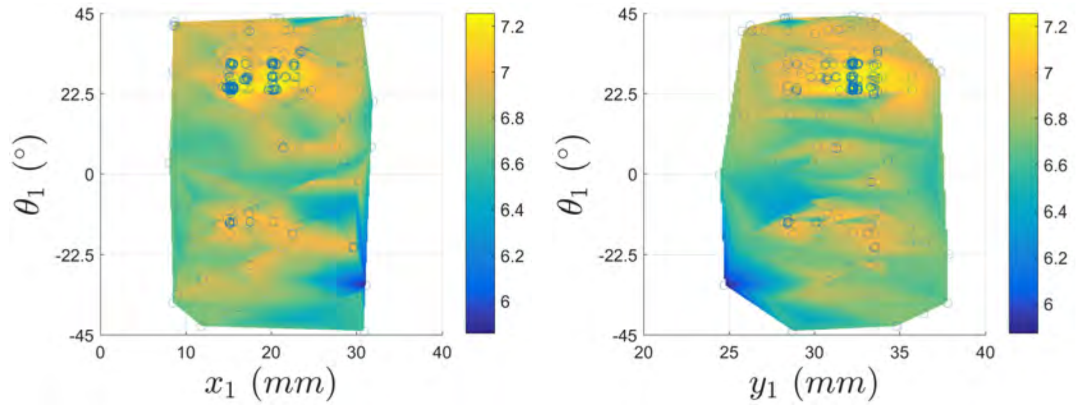

(a) Projection on the (θ_1, x_1) 2-D sub-space (b) Projection on the (θ_1, y_1) 2-D sub-space

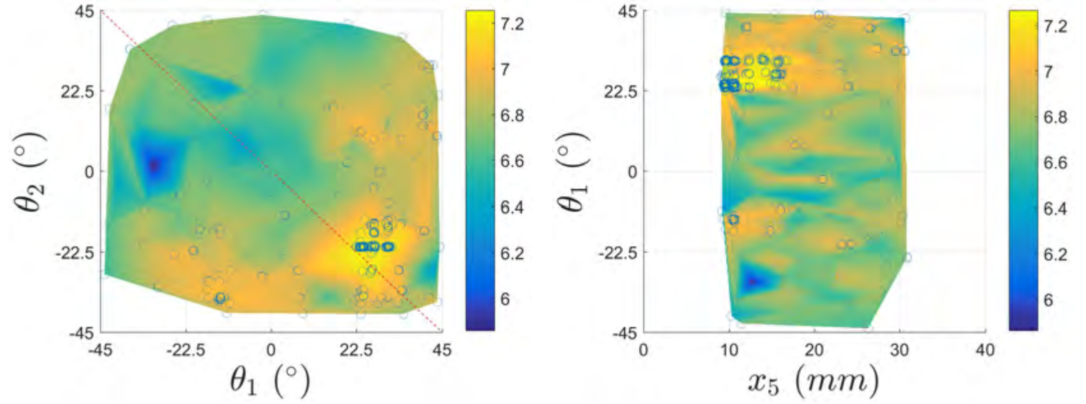

(c) Projection on the (θ_1, θ_2) 2-D sub-space (d) Projection on the (θ_1, x_5) 2-D sub-space

Figure B.2: Overall heat transfer rate q' results interpolated and projected on different two-dimensional sub-spaces of the search space, case #5, population size equal to 80. The circle markers corresponds to raw evaluations.

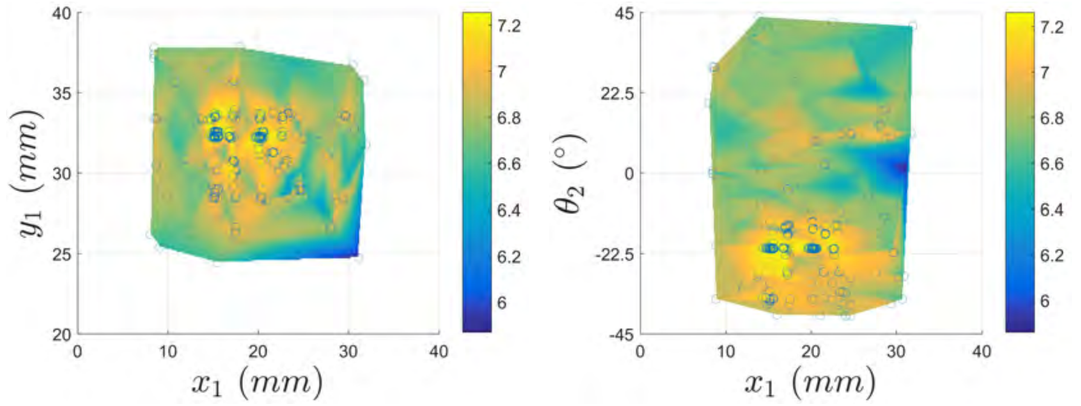

(a) Projection on the (x_1, y_1) 2-D sub-space (b) Projection on the (θ_2, x_1) 2-D sub-space

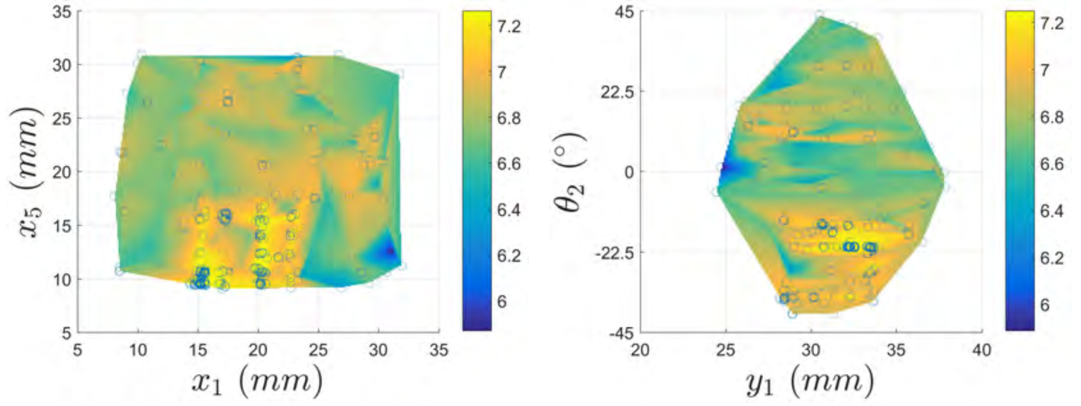

(c) Projection on the (x_1, x_5) 2-D sub-space (d) Projection on the (θ_2, y_1) 2-D sub-space

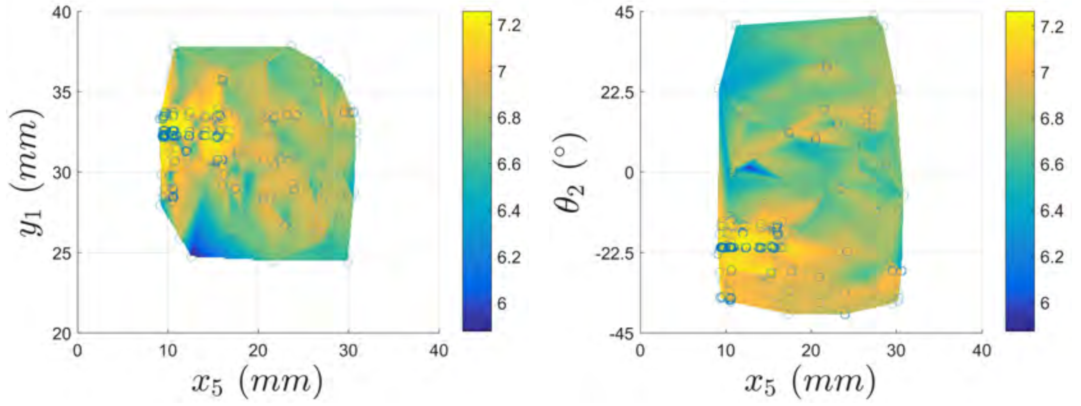

(e) Projection on the (y_1, x_5) 2-D sub-space (f) Projection on the (x_5, θ_2) 2-D sub-space

Figure B.3: Overall heat transfer rate q' results interpolated and projected on different two-dimensional sub-spaces of the search space, case #5, population size equal to 80. The circle markers corresponds to raw evaluations.